Accretion states and thermonuclear bursts in neutron star X-ray binaries

Every second tens of kilograms of extremely hot plasma fall onto each square centimeter of the surface of tens of neutron stars in our Galaxy. This is the consequence of a process known as accretion, by which matter falls onto a celestial body attracted by its gravity. Accretion onto a compact object, neutron star or black hole, is one of the most efficient ways of converting rest-mass energy into radiation and gives rise to extremely powerful X-ray sources. It provides a unique way to increase the spin rate and mass of the compact object after its birth and can also affect the surrounding interstellar medium by means of relativistic jets or outflows associated with the accretion process. There are different ways in which accretion onto a compact object can proceed. Different physical configurations of the accretion flow give rise to different accretion states, as witnessed by the changing spectral and variability properties of the X-ray emission. Another consequence of accretion onto neutron stars are thermonuclear explosions, which provide a direct view of their photosphere and a unique opportunity to constrain the properties of ultra-dense matter.

I present in this thesis a broad view of the high energy phenomena associated with neutron star low-mass X-ray binaries, based on the work that I have carried out at the University of Amsterdam during the past four years. I have focused on the X-ray emission of these systems, studying the luminosity of their different accretion states, a number of peculiar thermonuclear bursts and rapid variability phenomena associated with the innermost regions of the accretion flow.

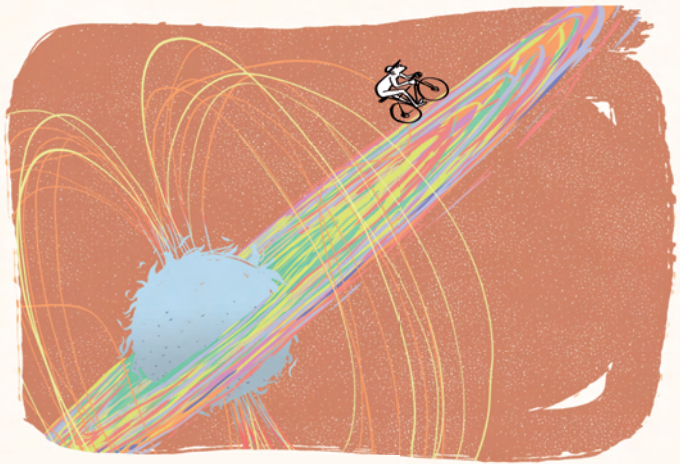

Manuel Linares

Accretion states and thermonuclear bursts in neutron star X-ray binaries

Accretion states and thermonuclear bursts in neutron star X-ray binaries

Manuel Linares

Accretion states and thermonuclear bursts in neutron star X-ray binaries

Find this book online at:
http://dare.uva.nl/dissertations/

Contact the author at:
manulinares@gmail.com

Cover illustration: Jaume Lloses (http://jaudrau.blogspot.com/)

PhD Thesis, University of Amsterdam.

Manuel Linares Alegret, 2009.

Accretion states and thermonuclear bursts in neutron star X-ray binaries

ACADEMISCH PROEFSCHRIFT

ter verkrijging van de graad van doctor
aan de Universiteit van Amsterdam
op gezag van de Rector Magnificus
prof. dr. D. C. van den Boom
ten overstaan van een door het college voor promoties
ingestelde commissie,
in het openbaar te verdedigen in de Aula der Universiteit
op woensdag 16 september 2009, te 14:00 uur.

door

Manuel Linares Alegret

geboren te Barcelona, Spanje

Promotiecommissie:

Promotor:	Prof. dr. M. van der Klis
Overige leden:	Prof. dr. R. P. Fender
	Prof. dr. W. Hermsen
	Prof. dr. E. P. J van den Heuvel
	Prof. dr. M. Méndez
	Prof. dr. R. A. M. J. Wijers
	dr. R. Wijnands

Faculteit der Natuurwetenschappen, Wiskunde en Informatica

The research reported in this thesis was carried out at the Astronomical Institute "Anton Pannekoek", at the Universiteit van Amsterdam, The Netherlands.

A mi padre, a mi madre y a mi hermana.
Por ser como sois y hacerme lo que soy.

To my father, my mother and my sister.
For being who you are and making me who I am.

Why don't you write books people can read?

Nora Joyce to her husband James (1882-1941)

In science one tries to tell people, in such a way as to be understood by everyone, something that no one ever knew before. But in poetry, it's the exact opposite.

Paul Dirac (1902-1984)

Manuscript: something submitted in haste and returned at leisure.

Oliver Herford (1863-1935)

Nothing great in the world has ever been accomplished without passion.

Friedrich Hebbel (1813-1863)

Write drunk; edit sober.

Ernest Hemingway (1899-1961)

Contents

1 Neutron stars in binary systems

Every second tens of kilograms of extremely hot plasma fall onto each square centimeter of the surface of tens of neutron stars in our Galaxy. This is the consequence of a process known as accretion, by which matter falls onto a celestial body attracted by its gravity. Accretion onto a compact object, neutron star or black hole, is one of the most efficient ways of converting rest-mass energy into radiation and gives rise to extremely powerful X-ray sources. It provides a unique way to increase the spin rate and mass of the compact object after its birth and can also affect the surrounding interstellar medium by means of relativistic jets or outflows associated with the accretion process. There are different ways in which accretion onto a compact object can proceed. Different physical configurations of the accretion flow give rise to different accretion states, as witnessed by the changing spectral and variability properties of the X-ray emission. Another consequence of accretion onto neutron stars are thermonuclear explosions, which provide a direct view of their photosphere and a unique opportunity to constrain the properties of ultra-dense matter. In this Chapter I give an overview of these phenomena, to the study of which this thesis is devoted.

1.1 Neutron stars

After ending their life in a supernova explosion, stars that are born with a mass about eight to forty times larger than our Sun leave behind one of the most fascinating astrophysical objects: a neutron star. Neutron stars might also be formed in binary systems through a different mechanism, the accretion induced collapse of a white dwarf. Unlike regular stars, neutron stars do not generate heat in the core by means of thermonuclear reactions. The internal structure and composition of an accreting neutron star can be summarized as follows. In order of decreasing distance from the center, we

find: a thin atmosphere, a metal-poor ocean, a metal-rich solid crust and a core mostly made of neutrons that contains most of the total mass. A typical neutron star has a mass between one and two times that of the Sun, and a radius between five and fifteen kilometers. The core features the highest bulk densities in the present universe, up to a few times 10^{15} g cm^{-3}, higher than those present in atomic nuclei. Precise measurements of the neutron star mass and radius can reveal how compressible matter is at these extreme densities and can be compared with theoretical predictions of the equation of state. The magnetic field can also reach extreme values in neutron stars, up to 10^{15} G in the so-called magnetars. Neutron stars are only slightly larger than their Schwarzschild radius (which is about four kilometers for a 1.4 Solar mass neutron star), and their surface gravitational field is as strong as some 10^{11} times that on Earth. These properties make neutron stars unique physical laboratories and an exciting target of astrophysical research.

Neutron stars show a rich phenomenology and manifest themselves in a number of ways throughout the whole electromagnetic spectrum. Rotation-powered neutron stars emit pulses throughout the whole spectrum, but it is the emission of pulses in the radio band that led to their discovery forty years ago by Hewish et al. (1968). Young neutron stars radiate their internal heat while they cool down and can be observed in the soft X-ray band (Kaspi et al. 2006). Transient high-energy bursting sources (soft gamma repeaters) and persistent X-ray pulsars that spin down rapidly (anomalous X-ray pulsars) are thought to be manifestations of the same type of object: a neutron star with an ultra-strong magnetic field, or magnetar (Woods & Thompson 2006). Finally, accretion of mass in a binary system gives rise to X-ray binaries, opening another high-energy window to neutron stars and giving rise to a number of interesting phenomena, as detailed in the following sections.

1.2 X-ray binaries

A large fraction of the stars in our Galaxy are born in double or multiple systems. In the Galactic bulge and in globular clusters the stellar densities are so high that close encounters between stars are frequent and pairs of stars may form through a number of mechanisms. Soon after the birth of X-ray astronomy (Giacconi et al. 1962) it was realized that the brightest sources in the X-ray sky were powered by accretion onto a compact object in interacting binary systems (e.g. Shklovsky 1967; Pringle & Rees 1972). The observed short-timescale variations in their X-ray luminosity were one of the main reasons to propose this scenario, in which a neutron star (NS) or a black hole (BH) accretes matter from its companion star. Given that the accretion flow

can extend down to the deepest parts of the gravitational potential well of the compact object, where the escape velocities are close to the speed of light, X-ray binaries are one of the few types of system where we can in principle test the theory of general relativity in the strong field regime. We can distinguish two main types of X-ray binary, low-mass and high-mass X-ray binaries, depending on whether the mass of the companion star is lower or higher than about two solar masses. In high-mass X-ray binaries the mass transfer is mostly due to the strong stellar wind of the (early type) companion star. See Tauris & van den Heuvel (2006) for a review on formation and evolution of X-ray binaries.

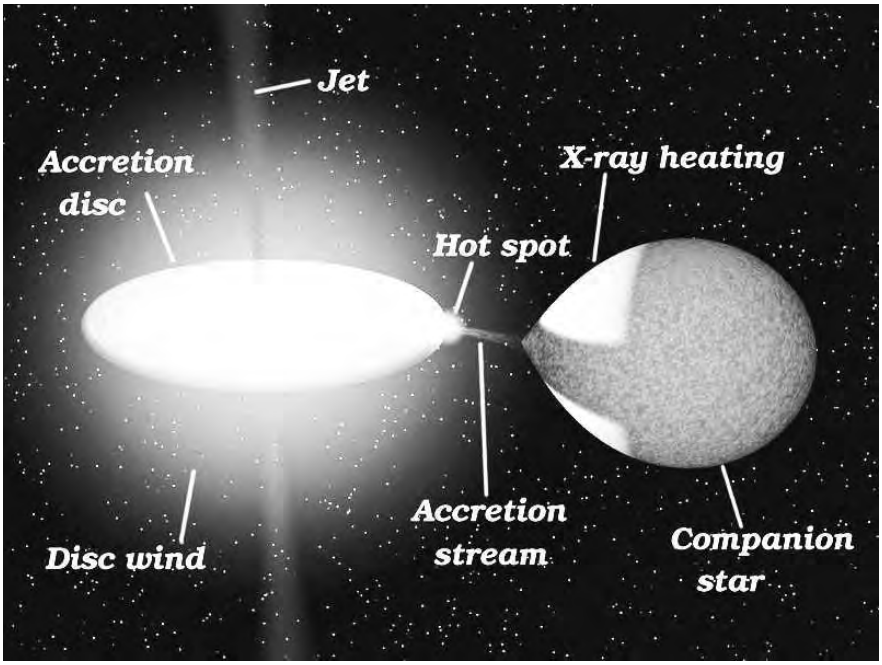

Figure 1.1: Graphic illustration of a low-mass X-ray binary system, with its main features labeled (Hynes, 2001).

In low-mass X-ray binaries (LMXBs), the subject of this thesis, the compact object and its companion star orbit so closely that matter is stripped off the outer layers of the latter and becomes bound to the compact object (Figure 1.1). As the companion expands or the orbit shrinks, the companion star fills and overflows its Roche lobe, the volume within which matter is bound to it. The matter transferred to the Roche lobe of the compact object possesses angular momentum and forms an accretion disk. As this matter loses angu-

lar momentum and approaches the compact object, its gravitational energy is converted into kinetic energy, thermalized and radiated away in the form of X-rays. Sco X-1 was the first such system to be discovered and it is, after the Sun, the brightest X-ray source in the sky. Nowadays more than 200 LMXBs are known (Liu et al. 2007), most of which contain a neutron star. Hasinger & van der Klis (1989) distinguished two classes among neutron star LMXBs, Z and atoll sources, by studing their correlated X-ray spectral and variability properties. Z sources are more luminous than atoll sources and accrete persistently, with one exception (Homan et al. 2007). Atoll sources can be persistent or transient, show numerous type I X-ray bursts and, on average, harder spectra.

1.2.1 Accreting millisecond pulsars

Eleven years ago the first LMXB showing X-ray millisecond pulsations was discovered by Wijnands & van der Klis (1998), presenting the first direct proof of an accreting neutron star having both millisecond spin period and dynamically important magnetic field. At the moment of writing a total of ten such accreting millisecond pulsars (AMPs) have been found in transient systems (see contributions in Wijnands et al. 2008, for a recent overview). Not only are they thought to be the long sought progenitors of radio millisecond pulsars (Bhattacharya & van den Heuvel 1991, for a review), but they also constitute an excellent test bed to study the accretion flow in NS-LMXBs and its interaction with the neutron star (Fig. 1.2; see also Patruno et al. 2009).

The main open question concerning AMPs is what makes them X-ray pulsars, when most NS-LMXBs are not. Although many NS-LMXBs are known to harbor a neutron star with millisecond spin period thanks to the oscillations seen during type I X-ray bursts ("burst oscillations"; see e.g. Strohmayer et al. 1996b; Chakrabarty et al. 2003), in general they do not show millisecond pulsations in their persistent emission. However, seven members of the AMP family show clear and strong pulsations during outburst, while the remaining three have shown intermittent episodes of pulsations (see Altamirano & Casella 2008, and references therein). The typical pulsed fraction in AMPs ranges from 5 to 10 %, whereas in non-pulsing NS-LMXBs the current upper limits are between 0.3 and 0.8 % (Vaughan et al. 1994; Dib et al. 2004). As mentioned above, the pulsations observed in AMPs imply that the neutron star has a magnetic field strong enough ($\sim 10^8$-10^9 G) to channel the accretion flow and create thereby an asymmetric emission pattern (two hot spots in the simplest case; see Figure 1.2). The question is then, why do the rest of NS-LMXBs not show pulsations? One option is that spin and magnetic axes are aligned in the non-pulsing systems and misaligned in AMPs, or that

pulsations are smeared out in non-pulsing NS-LMXBs by an optically thick cloud surrounding the neutron star (Titarchuk et al. 2002). A different physical mechanism was proposed by Cumming et al. (2001) invoking screening of the magnetic field in "classical", non-pulsing, NS-LMXBs by a time-averaged mass accretion rate higher than that of AMPs. Five of the ten currently known AMPs are studied in this thesis, from three different points of view: their fast X-ray varibility, their luminosity and accretion states and their burst oscillations (see Section 1.6 and Chapters 2, 3, 4, 5 and 9).

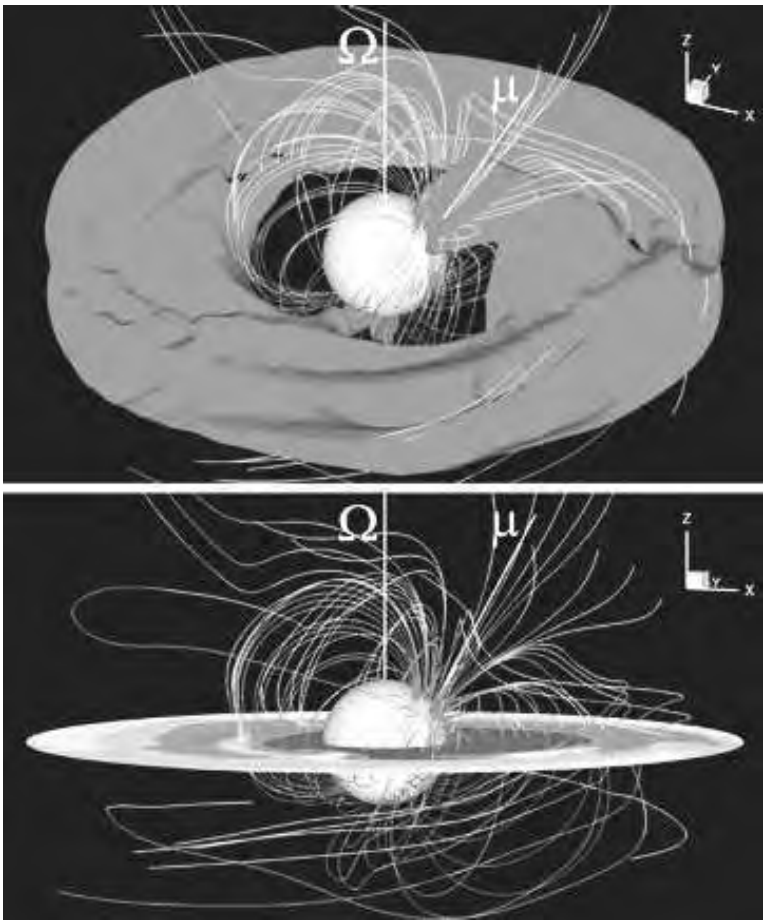

Figure 1.2: Three-dimensional magnetohydrodynamic simulations of accretion onto a magnetized star, by Long et al. (2008). Two views are shown of matter flowing to a star with a dipolar magnetic field misaligned with the rotation axis. The top panel shows one of the density levels. The bottom panel shows the equatorial plane with different density levels. The field lines are shown in both panels.

1.3 Accretion flows and accretion states

The energy available to be radiated when accreting mass at a rate $\dot{M}$ onto a compact object of mass M and radius $R_\star$, sometimes referred to as accretion luminosity, is simply the difference between the gravitational potential at infinity, far from the compact object, and the gravitational potential at the surface (or event horizon in the case of a black hole):

$$L_{acc} = GM\dot{M}/R_\star \tag{1.1}$$

(where G is the gravitational constant). The way in which this energy is radiated constitutes an extensive and active area of astrophysical research, that can be summarized as the study of accretion flows around compact objects. Understanding the spectral, timing and polarization properties of the emergent flux and the exact fraction of L_{acc} emitted at different times in terms of the physical and geometrical properties of the accretion flow is one of the key objectives of this field. After the seminal work of Shakura & Syunyaev (1973), the structure and radiative properties of accretion disks around compact objects have been extensively studied (see e.g. Figure 1.3, from De Villiers et al. 2003). The widely accepted picture in LMXBs (at least in some states) is that of a geometrically thin, optically thick accretion disk that emits a spectrum sum of multiple black body components, each representing an annulus in the disk. The closer to the central compact object, the more gravitational energy is released in the disk and the higher is the temperature of the associated black body. Assuming an optically thick disk one can apply the Stefan-Boltzmann law to derive the following approximate expression for the disk temperature at a given radius R, for an inner disk radius R_{in} (Frank et al. 2002).

$$T(R) \approx \left\{ \frac{3GM\dot{M}}{8\pi R^3 \sigma} \left[1 - \left(\frac{R_{in}}{R} \right)^{1/2} \right] \right\}^{1/4} \tag{1.2}$$

Integrating the resulting black body spectra from the outer disk radius, R_{out}, to R_{in} and taking $R_{out} \to \infty$, $R_{in} \to R_\star$, yields an estimate of the maximum total disk luminosity:

$$L_{disk,max} \approx GM\dot{M}/2R_\star = L_{acc}/2 \tag{1.3}$$

Both the total disk luminosity and its temperature are directly related to the amount of matter flowing through the disk, or mass accretion rate. When the mass accretion rate through the disk is high its innermost parts reach temperatures of tens of millions degrees Kelvin (photon energies of a few keV) so that the emerging flux spectrum peaks in the soft X-ray band. This is what

characterizes the soft states of LMXBs (also called "banana" states in atoll sources), together with the low amplitude and high frequencies of the X-ray variability.

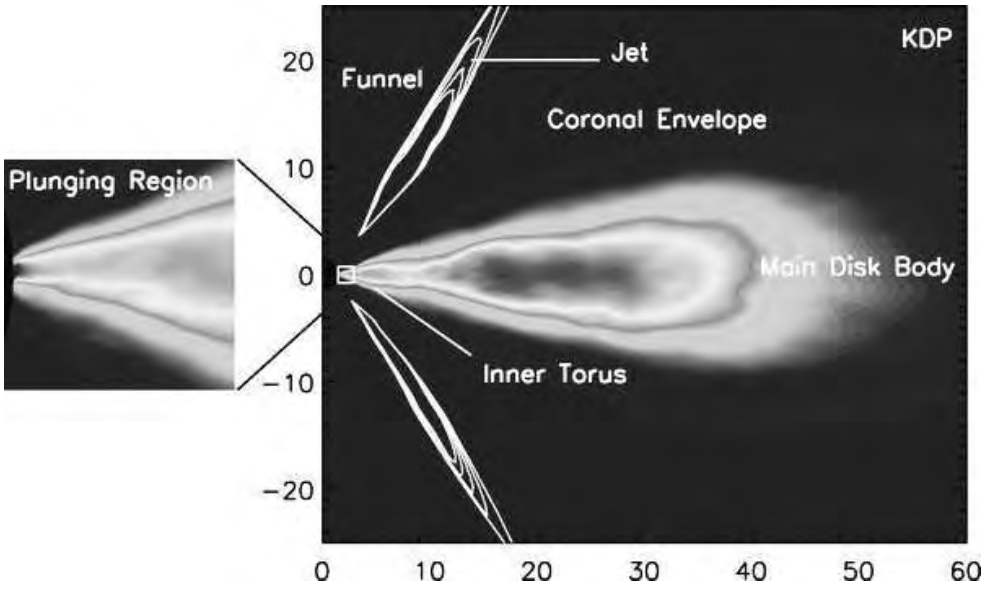

Figure 1.3: Three-dimensional magnetohydrodynamic general relativistic simulations of the accretion flow around a spinning black hole, after De Villiers et al. (2003). The grey scale shows density levels in linear scale. Distances are in gravitational radii. The main dynamical features of the system are labeled, and the jet is outlined by contours of positive radial momentum. The box on the left is a close-up showing the plunging region from just outside the marginally stable orbit to the black hole horizon.

It was soon realized that thermal emission alone is not enough to explain the energy spectra of X-ray binaries (Tananbaum et al. 1972). Many systems that during a given observation show the characteristics of the soft state outlined above (i.e. "they are in the soft state" at a given time), can show a completely different behavior at a different epoch. When they are in the hard state (a.k.a. "extreme island state" in atoll sources), LMXBs emit a large fraction of their bolometric luminosity (more than 50% in some cases) above 20 keV, showing strong hard X-ray tails in their spectrum that can extend up to several hundreds of keV. Hard states show strong X-ray variability, with characteristic frequencies much lower than those present in soft states. New forms of accretion flow different from the standard Shakura-Sunyaev disk were proposed to explain these states (Narayan 1996; Blandford & Begelman 1999; Falcke et al.

2004). Compton up-scattering of the soft X-rays produced in the disk and/or neutron star surface is thought to play an important role in the production of high energy photons. When soft photons are up-scattered in a "hot flow" by a thermal population of electrons, the emerging hard X-ray spectrum depends among other parameters on the temperature and optical depth of the electron gas. Therefore, hard X-ray spectra can also give important information on the physics of accretion, although the geometry and detailed radiative properties of the accretion flow responsible for the hard X-ray emission, the "Comptonizing medium", are still under debate.

Another important and well-debated subject concerning accretion flows around compact objects is the location of the inner edge of the disk in different accretion states of LMXBs. The 'standard' picture, supported by the higher variability frequencies observed during the soft state, is that of a disk that is truncated far from the compact object in the hard states (see e.g. Done et al. 2007) and that reaches the vicinity of the compact object in the soft states. However, recent observations of black hole systems in the hard state may contradict this scenario (Miller et al. 2006). If one measures the compact object mass and has strong evidence that the accretion disk is truncated at the innermost stable circular orbit, measuring the inner disk radius places direct constraints on the spin of the compact object through general relativity. Fitting the emitted continuum or disk reflection spectral components are two possible ways to perform such measurements (e.g. Shafee et al. 2006; Miller et al. 2009).

1.4 Thermonuclear bursts

In NS-LMXBs a large fraction of the accretion flow finally plunges onto the neutron star surface, where the infalling matter is piled up and compressed (Figure 1.4). Due to the high densities and temperatures present there, the accreted matter is subject to thermonuclear reactions, in the form of steady burning or through unstable ignition. The latter phenomenon gives rise to an intense burst of X-rays, was discovered in 1975 (Grindlay et al. 1976; Belian et al. 1976) and it is known as a type I X-ray burst (Hoffman et al. 1978). It outshines briefly but by a large amount the power liberated by accretion, offering a direct view of the neutron star photosphere. The ignition is thought to be sensitive to the heat coming from deep in the neutron star crust (Cumming et al. 2006), hence type I X-ray bursts are potential tools to study the physics of matter at extreme densities.

Type I X-ray bursts show a variety of total energy outputs and durations, set by the mass, thickness and composition of the burning layer: 10^{39}-10^{40}

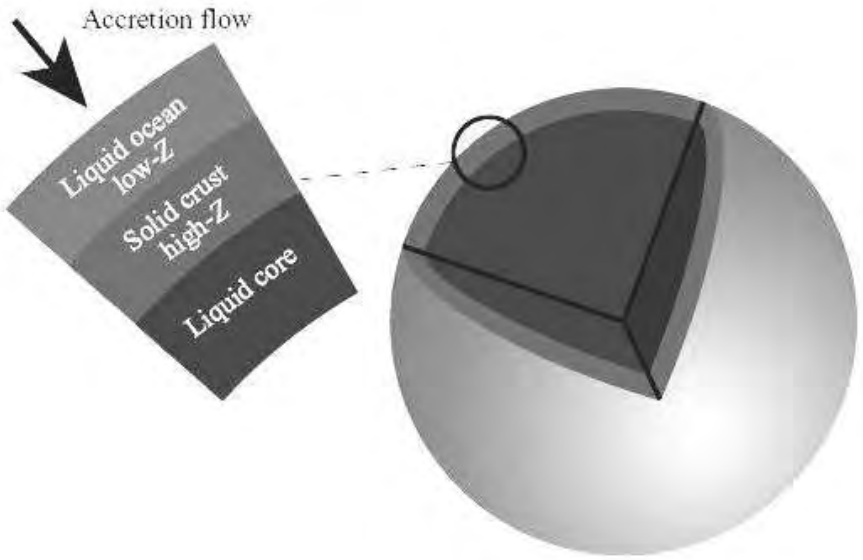

Figure 1.4: Neutron star structure in a nutshell. As the accreted matter piles up it is compressed until the density and temperature at the base of the accreted layer, deep in the liquid ocean, reach the ignition conditions and a thermonuclear runaway occurs. Illustration from C. J. Horowitz.

ergs in the case of "normal" bursts (∼5-50 s long), $\sim 10^{41}$ ergs in the case of long, pure helium bursts (∼10-30 min long) and $\sim 10^{42}$ ergs in the so-called superbursts, which last for several hours and are associated with the ignition of a layer of carbon (see Lewin et al. 1993; Strohmayer & Bildsten 2006, for reviews). They also show nearly coherent and sinusoidal luminosity variations, the so-called burst oscillations, which are thought to trace within a few Hz the neutron star spin frequency (Strohmayer et al. 1996b). Detailed study of the burst energies, recurrence times and mass accretion rate on the neutron star surface gives a unique tool to constrain the different thermonuclear burning regimes that operate at high densities and temperatures.

1.5 X-ray timing and spectral studies

Electromagnetic waves are the main carriers of astronomical information, and we can study them in four basic ways: by looking at their spatial structure or

distribution (imaging), through their polarization properties (polarimetry), by measuring their energy distribution (spectroscopy) and by analyzing their time variability (timing). This thesis is based on X-ray timing and spectroscopic studies of NS-LMXBs that employ the 0.5–200 keV energy range and cover a wide range of timescales, from milliseconds to years. In order to characterize the X-ray spectra of NS-LMXBs I use two distinct methods: i) a photometric analysis, using X-ray intensities and hardness ratios (i.e., count rates and ratios of count rates in several energy bands) and ii) spectral decomposition, i.e., modelling the X-ray spectrum to obtain spectral parameters and measure the energy flux. The main technique used in this thesis to study the time variability in the X-ray flux is the Fourier analysis of evenly spaced count rate time series. A time varying signal is thereby decomposed into a set of sine waves expressed as Fourier amplitudes, the latter in general complex numbers. The modulus of these Fourier amplitudes is squared to give a set of real-valued Fourier power-frequency pairs: a power spectrum. An excellent review of Fourier techniques in X-ray timing is given in van der Klis (1995b), and complementary details can be found in Vaughan et al. (1994). For details of these spectral and timing techniques as used throughout this thesis I refer to Sections 2.2, 3.3, 4.2, 5.2, 7.2.2, 7.2.1, 8.2 and 9.2.

1.5.1 The Rossi X-ray Timing Explorer

The Rossi X-ray Timing Explorer (*RXTE*; Bradt et al. 1993; Swank 1999) was launched on December 30, 1995, from the NASA Kennedy Space Center into a circular orbit at an altitude of 580 km, corresponding to an orbital period of about 96 minutes. *RXTE* opened a new window to X-ray binaries thanks mainly to its unprecedented time resolution. It covers time scales from microseconds to years in a broad spectral range, from 2 to 200 keV. It was designed for a lifetime of two to five years, yet at the moment of writting *RXTE* has been active for almost fourteen years, overlapping with many other X-ray satellites, and the current plan of operations extends to September 2010. This makes *RXTE* one of the most long-lived and best calibrated X-ray missions (Jahoda et al. 2006; Miller 2009).

RXTE carries three scientific instruments onboard (Fig. 1.5): the proportional counter array (PCA, Jahoda et al. 1996, 2006), the high energy X-ray timing experiment (HEXTE, Rothschild et al. 1998) and the all-sky monitor (ASM, Levine et al. 1996). The ASM observes ∼80% of the sky during each orbit with a spatial resolution of $3' \times 15'$. It consists of three Scanning Shadow Cameras, each with a field of view (FOV) of $6^\circ \times 90^\circ$ and an effective area of ∼30 cm^2. It is sensitive to the 1.5–12 keV energy range and has a time resolution of 1/8 seconds. ASM lightcurves from about 350 sources are made

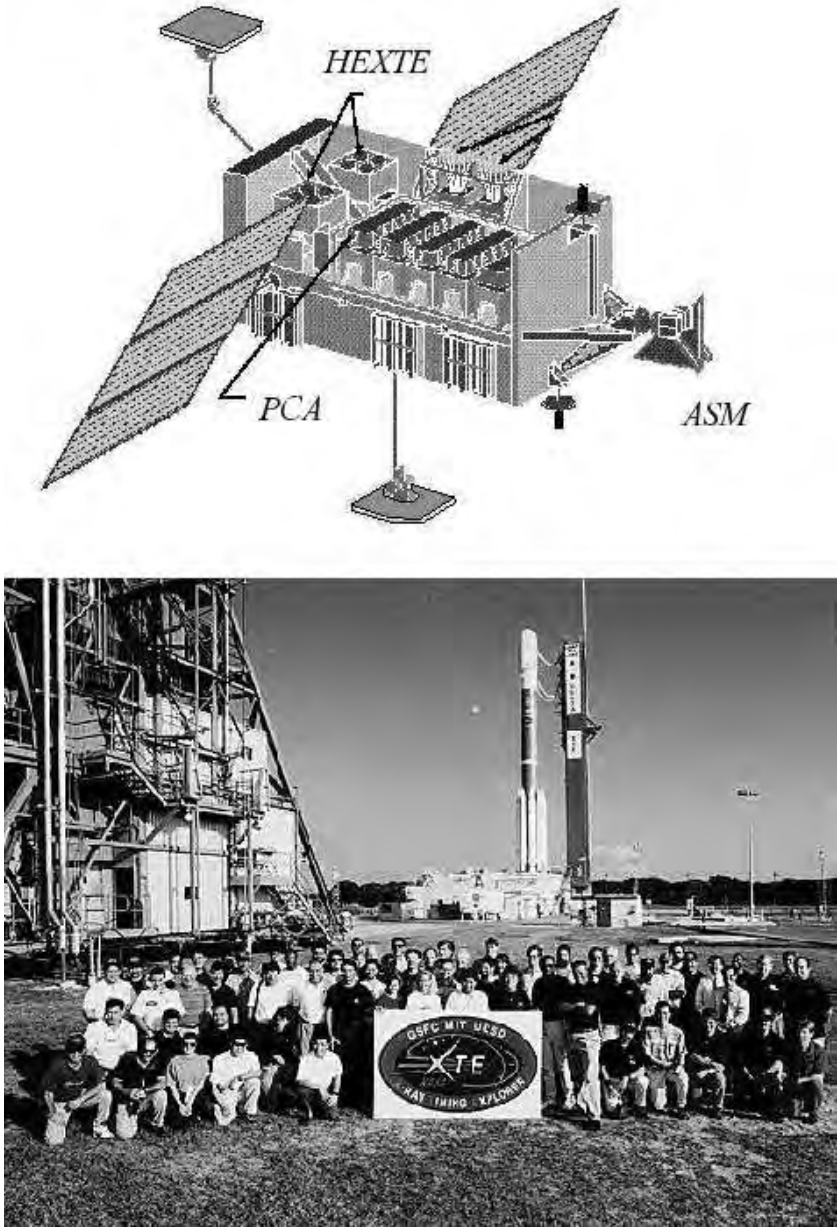

Figure 1.5: *Top: RXTE* and its three scientific instruments (see text). *Bottom: RXTE* team picture taken before launch at the Kennedy space center, in December 1995.

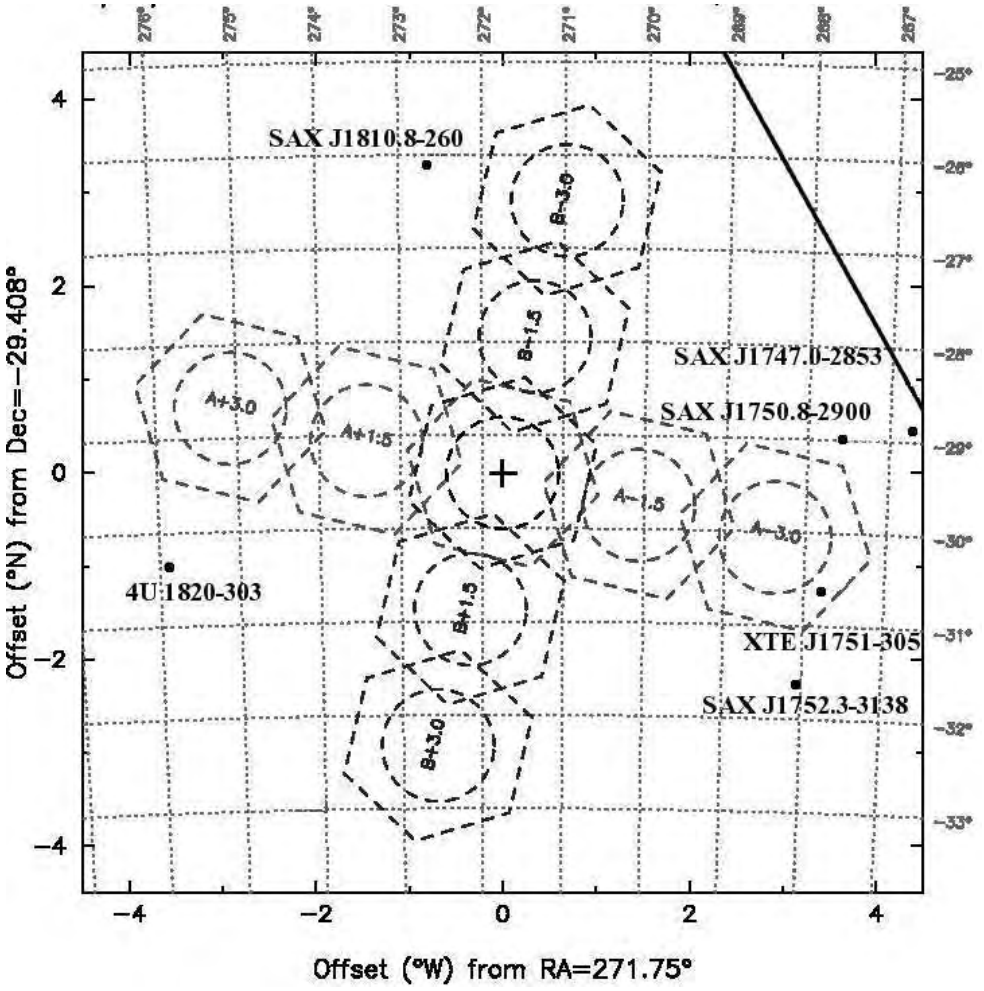

Figure 1.6: Sky map centered on the accreting millisecond pulsar XTE J1807–294 (cross). The hexagonal contour centered on XTE J1807–294 shows the field of view of the PCA and HEXTE instruments on board *RXTE*, and the circle (with one degree radius) shows the approximate full width at half maximum of the collimator response. The contours centered 1.5 and 3 degrees away from XTE J1807–294 show the eight possible off-source (or "rocking") positions of both HEXTE clusters (A and B, as indicated). Other neutron star low-mass X-ray binaries in the field are shown with black dots, and the Galactic plane is indicated with a thick diagonal line. From `http://heasarc.gsfc.nasa.gov/cgi-bin/Tools/HEXTErock/HEXTErock.pl`.

public by the ASM team (`http://xte.mit.edu/ASM_lc.html`), which offer a useful tool to follow the long term (days to years) evolution of X-ray binaries. The PCA consists of five Xenon proportional counter units (PCUs) that cover the 2–60 keV energy range with a time resolution of ∼1 μs and an energy resolution of 17 % (at 6 keV). Its total collecting area is ∼6250 cm^2, when all five PCUs are active. The HEXTE consists of eight NaI scintillation detectors, sensitive to 15-250 keV photons with a time resolution of 8 μs and an energy resolution of 15 % at 60 keV, grouped into two clusters of detectors (clusters A and B). Each cluster has an effective area of 800 cm^2 and can change its pointing position (or "rock") in mutually perpendicular directions, thereby providing measurements of the background around the observed target (see Figure 1.6). Both pointed instruments aboard *RXTE*, PCA and HEXTE, are co-aligned and have a FOV of ∼1° (FWHM). The interested reader is referred to Appendix A for a detailed description of the PCA and HEXTE data reduction procedures.

1.5.2 The Swift Gamma-ray Burst Mission

The *Swift* Gamma-ray Burst Mission (Gehrels et al. 2004, Fig. 1.7) was launched on November 20, 2004, from the NASA Kennedy Space Center into a ∼600 km high and ∼90 min long orbit. *Swift* is a multi-wavelength observatory mainly dedicated to the study of Gamma-ray burst science. The name of the mission refers to its rapid slew capability. After detecting a burst in the sky it can slew automatically within less than 90 seconds so that all instruments can point to the location of the burst. *Swift* has been increasingly available for non-gamma-ray-burst observations since its launch in 2004 and its capabilities yield important contributions to the whole high-energy astrophysics field.

Swift carries three scientific instruments: the burst alert telescope (BAT), the X-ray telescope (XRT) and the ultraviolet/optical telescope (UVOT). The BAT (Barthelmy et al. 2005) is a coded mask instrument with a detecting area of ∼5200 cm^2, a relatively large FOV (∼1.4 sterad) and a ∼4 arcmin angular resolution. It is sensitive to the 15–150 keV energy range. The XRT (Burrows et al. 2000) is a focusing X-ray telescope with a 110 cm^2 effective area, 23.6×23.6 arcmin FOV, 18 arcsec resolution (half-power diameter), and 0.2–10 keV energy range. The XRT uses a grazing incidence Wolter 1 telescope to focus X-rays onto a single CCD detector. The UVOT (Roming et al. 2005) is a 30 cm Ritchey-Chretien reflector telescope, sensitive to the 170–650 nm range and co-aligned with the XRT, with a FOV of 17×17 arcmin.

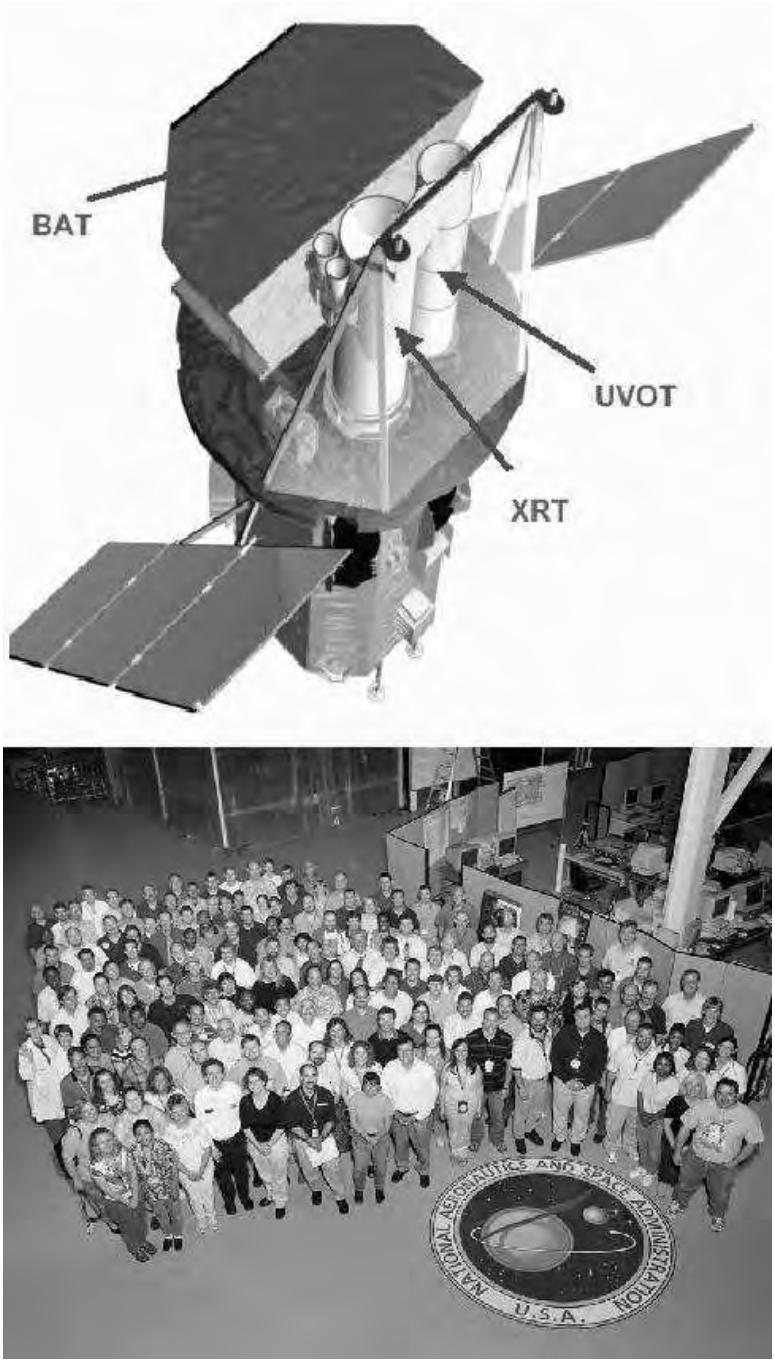

Figure 1.7: *Top: Swift* and its three scientific instruments (see text). *Bottom: Swift* team picture taken at the Goddard space flight center, in May 2004.

1.6 A guide to this thesis

This thesis is devoted to the study of neutron star low-mass X-ray binaries, focusing on their X-ray emission, the luminosity of their different accretion states, rapid variability phenomena and on the study of thermonuclear bursts. It is divided in three parts. Part I (Chapters 2, 3 and 4) presents my study of the aperiodic X-ray variability and spectral properties of three accreting millisecond pulsars. In Chapter 2, I report the discovery of simultaneous kHz quasi-periodic oscillations in the X-ray flux of XTE J1807–294 and discuss their possible connection with the neutron star spin (going back to this discussion in Chapter 8). I also find correlations between the characteristic variability frequencies that are clearly shifted with respect to most other NS-LMXBs, an intriguing phenomenon only seen previously in the first-discovered AMP, SAX J1808.4-3658. Chapter 3 presents the completely atypical behavior that I found in the AMP IGR J00291+5934, which showed the strongest variability and the lowest characteristic frequencies seen thus far in a NS-LMXB. In Chapter 4 I report our X-ray timing and spectral analysis of yet another AMP, SWIFT J1756.9–2508, which unveiled a typical atoll source behavior. Part II (Chapters 5 and 6) contains a thorough analysis of the luminosity of NS-LMXBs in different states, and a systematic comparison of the luminosity, spectral and timing properties of a large sample of sources. Chapter 5 reveals that hard states of atoll sources can be much more luminous than previously thought (up to at least $\sim$15% of the Eddington luminosity) and, on the other hand, soft states can show very low luminosities (down to $\sim$1% of the Eddington luminosity). In Chapter 6, I study the most luminous NS-LMXBs, the Z sources, and compare in detail their spectral and timing properties to those of atoll sources. Part III (Chapters 7, 8 and 9) contains my work on thermonuclear bursts from accreting neutron stars. The discovery and detailed analysis of a rare type of thermonuclear event known as long X-ray burst is presented in Chapter 7. Chapter 8 presents accretion- and nuclear-powered phenomena all observed together in IGR J17191–2821: kHz quasi-periodic oscillations, type I X-ray bursts and burst oscillations. Finally, in Chapter 9, I bring together accreting millisecond pulsars and thermonuclear bursts by reporting the discovery of burst oscillations in the AMP HETE J1900.1-2455, and discuss the implications of the observed burst oscillation properties for intermittency in AMPs.

Part I

Accreting millisecond pulsars: broadband timing and spectral properties

Probleme kann man niemals mit derselben Denkweise lösen, durch die sie entstanden sind.

Problems cannot be solved by the same level of thinking that created them.

Albert Einstein (1879-1955)

2 Discovery of kHz QPOs and shifted frequency correlations in the accreting millisecond pulsar XTE J1807–294

Manuel Linares, Michiel van der Klis, Diego Altamirano, Craig B. Markwardt

The Astrophysical Journal, 2005, 634, 1250

Abstract

We report the discovery of twin kHz QPOs in the X ray flux of XTE J1807–294, the fourth accreting millisecond pulsar (AMP). This is the second AMP exhibiting twin kHz QPOs. In contrast to the first case, SAX J1808.4–3658, the frequency separation $\Delta\nu$ between the kHz QPOs is consistent with the pulse frequency (190.6 Hz), not with half that value, confirming for the first time from pulsation measurements the inference, based on burst oscillations, that 'slow rotators' (spin frequency less than 400 Hz) have $\Delta\nu$ approximately equal to the spin frequency. While the QPOs move in frequency together over a range of more than 200 Hz, $\Delta\nu$ remains constant with an average value of 205±6 Hz. Variability components were found in the 5–130 Hz range similar to those seen in other LMXBs. The correlations between the QPO and noise frequencies are also similar to those in other sources, but shifted by a factor of 1.59 in kHz QPO frequencies, similar to the factor 1.45 shift found for SAX J1808.4–3658. Our results argue in favor of a spin-related formation mechanism for twin kHz QPOs and against a spin-related cause of the shift in the frequency correlations.

2.1 Introduction

The accretion-driven millisecond X-ray pulsar (AMP) family is gradually growing. Since the discovery of its first member (SAX J1808.4–3658, Wijnands & van der Klis 1998) six more have been added: XTE J1751–305, XTE J0929–314, XTE J1807–294, XTE J1814–338 and recently IGR J00291+5934 and HETE J1900.1–2455 (respectively: Markwardt et al. 2002; Remillard 2002; Markwardt et al. 2003a; Markwardt & Swank 2003; Galloway et al. 2005; Vanderspek et al. 2005). All of these are in transient low-mass X-ray binaries (LMXBs) showing faint outbursts (peak count rate 10–100 mCrab) every few years that last a few weeks. Their pulse frequency (i.e., the neutron-star spin frequency) lies in the range 185–599 Hz and the orbital period is between 40 minutes and 2.5 hours. See Wijnands (2005) for an updated observational review.

XTE J1807–294 is the fourth-discovered accreting millisecond pulsar. The source was detected first on February 13^{th}, 2003, in periodic scans of the Galactic bulge region using the Proportional Counter Array (PCA) instrument on board the Rossi X-ray Timing Explorer (RXTE). These scanning observations show a rising flux, with the epoch of maximum X-ray flux (count rate of ~ 58 mCrab) occurring between February 19^{th} and 22^{nd} (Markwardt et al. 2003b). On February 21^{st}, 2003, in the first pointed observation of the source by the PCA, 190.6 Hz pulsations were detected, confirming this source as an accreting millisecond pulsar (Markwardt et al. 2003b). An orbital period of $\sim$40 minutes was determined by Markwardt et al. (2003a), still the shortest among AMPs. A pulse analysis of the outburst was performed by Markwardt (2004).

XTE J1807–294 had the longest outburst among the AMPs observed up to now. It was followed with the PCA for five months, although after a few weeks the source became too weak to measure its aperiodic variability. As noted in Falanga et al. (2005a), the X-ray flux decay did not show a break to a faster decline, such as in the other AMPs (Wijnands 2005) and attributed in those objects to the propeller effect (e.g., Gilfanov et al. 1998). Falanga et al. (2005a) described the energy spectrum as a sum of a disk blackbody and a thermal Comptonization component, without evidence of spectral lines or reflection. No optical or infrared counterpart has been reported to date. Assuming a distance of 8kpc, Campana et al. (2005) placed an upper limit of $4{\times}10^{31}$ erg s^{-1} on the unabsorbed 0.5–10 keV quiescent luminosity.

Studying the power spectra of LMXBs is one of the most direct ways of analyzing the accretion flow in these systems. In particular the high-frequency power-spectral features constitute a probe of the innermost regions of the accretion disk, where gravitational fields are extreme (see van der Klis 2000,

2006, for reviews). The first discovered AMP, SAX J1808.4–3658 (Wijnands & van der Klis 1998), in its 2002 outburst provided surprising information on the relation between the neutron-star spin and the kHz QPOs and confirmed expectations concerning the burst oscillations. While the burst oscillations (cf. Strohmayer et al. 1996b) occurred at the pulse, and inferred spin, frequency (Chakrabarty et al. 2003), the separation $\Delta\nu$ between the kHz QPO frequencies was consistent with *half* the pulse frequency (Wijnands et al. 2003). Although based on only a single simultaneous detection of twin kHz QPOs, this result carried important consequences for our understanding of LMXBs, as it falsifies simple spin-orbit beat-frequency models, yet requires an intimate link between spin and kHz QPOs. This led to several new proposed models for the nature of the interaction between disk flow and neutron-star spin (Wijnands et al. 2003; Lamb & Miller 2003; Kluźniak et al. 2004; Lee et al. 2004) replacing, modifying or adding to earlier proposed models (e.g., Miller et al. 1998; Stella & Vietri 1998; Abramowicz et al. 2003). So far, all sources with inferred spin frequencies $\nu_{spin} > 400$ Hz ('fast rotators') have $\Delta\nu \approx \nu_{spin}/2$ and the ones with $\nu_{spin} < 400$ Hz ('slow rotators') have $\Delta\nu \approx \nu_{spin}$.

Several correlations have been found between the frequencies of power-spectral components in Z and atoll sources (the two main types of neutron-star LMXBs; Hasinger & van der Klis 1989), as well as among black hole candidate systems. Initially, the WK relation (Wijnands & van der Klis 1999a) and the PBK relation (Psaltis et al. 1999) were identified. Including several more correlated components, this set of correlations was synthesized into a 'universal scheme of correlations' among atoll sources by van Straaten et al. (2003). Comparing AMPs to other atoll sources, van Straaten et al. (2005) found that the correlations in two of the AMPs are shifted relative to those of the other atoll sources. The simplest description of the shifts was that the two kHz QPOs had frequencies a factor ~ 1.5 lower than in the other sources.

In this paper we analyze all the RXTE PCA data on XTE J1807–294, and report the discovery of pairs of simultaneous kHz QPOs. The separation $\Delta\nu$ between the seven pairs of kHz QPOs we detect is consistent with the pulse frequency, and confirms for the first time from pulsations that the slow rotators have a kHz QPO frequency separation that is approximately equal to the neutron star spin frequency. Finally, including also the low-frequency variability components in our study, we find a shift in the frequency correlations by a factor $\sim$1.5, similar to that seen in SAX J1808.4–3658.

Table 2.1: Observations used for the timing analysis.

Set	ObsID	Start date	Det. [a]	PDS [b]	Count rate (s^{-1}) [c]	Bkg. (s^{-1}) [d]
					Total – Per PCU	Total – Per PCU
A	80145-01-02-00	2003Mar05	3-4	126	266 – 70	102 – 27
	80145-01-04-03	2003Mar16				
B	80145-01-02-03	2003Mar06	3-5	99	308 – 78	108 – 27
	80145-01-02-02	2003Mar06				
	80145-01-02-01	2003Mar06				
	80145-01-03-03	2003Mar07				
C	80145-01-01-03	2003Mar01	4-5	104	391 – 91	115 – 27
	80145-01-01-04	2003Mar01				
	80145-01-01-00	2003Mar02				
D	80145-01-01-01	2003Feb28	5-5	67	399 – 80	135 – 27
	80145-01-03-02	2003Mar07				
E	80145-01-02-06	2003Mar11	2-4	124	215 – 74	84 – 29
F	70134-09-02-00	2003Feb27	2-5	169	267 – 84	89 – 28
	70134-09-02-01	2003Feb27				
	80145-01-02-04	2003Mar10				
G	80145-01-03-01	2003Mar12	3-4	87	238 – 70	92 – 27
H	80145-01-03-00	2003Mar09	2-4	154	261 – 77	92 – 27
	80145-01-02-05	2003Mar13				

[a] Minimum and maximum number of active detectors during the observations.

[b] Total number of averaged power density spectra (PDS), each one made from a data segment of 128 seconds.

[c] Time averaged count rate not corrected for the background.

[d] Time averaged background count rate estimated with the standard model for bright sources, version 2.1e, provided by the PCA team at GSFC.

2.2 Observations and Data Analysis

We used all the RXTE PCA data from XTE J1807–294 available in NASA's High Energy Astrophysics Science Archive Research Center taken between February 27^{th} and July 29^{th}, 2003.

For the color analysis we used the Standard 2 data, which have a 16-s time resolution and 129 energy channels. We divided the channels into four bands in a way that is often used for neutron-star sources: band A: 2.0–3.5 keV, band B: 3.5–6.0 keV, band C: 6.0–9.7 keV, band D: 9.7–16.0 keV. The count rates in these precise bands were estimated by interpolating linearly between the corresponding energy channels. The background was estimated using the standard bright source background models. From the counts in each band, we computed the colors and intensity as: hard color=D/C, soft color=B/A, intensity=A+B+C+D. We then normalized colors and intensity to the Crab values nearest in time (Kuulkers et al. 1994) and in the same PCA gain epoch (e.g., van Straaten et al. 2003).

The timing analysis was done using the GoodXenon data, with the original $1\mu s$ time resolution data rebinned into 1/8192-s bins, and including all 256 energy channels. We performed fast Fourier transforms (FFTs) of 128-s data segments, fixing the frequency resolution and the lowest available frequency to ∼0.008 Hz; the highest available Fourier frequency (Nyquist frequency) was 4096 Hz. No background subtraction or dead-time correction was made prior to the FFTs. The resulting power spectra were "weeded" (the pulsar spike at $\sim$ 190 Hz was removed at full frequency resolution) and a Poisson level was subtracted. Following Klein-Wolt (2004) we first estimated the Poisson noise using the Zhang et al. (1995) formula and then (after inspecting the ∼3000–4000 Hz range and finding no unexpected features) shifted it to match the level between 3072–4096 Hz, where no intrinsic power should be present, but only counting statistics noise (this shift was in all cases smaller than 0.15% of the previously estimated Poisson level). Then we normalized the power spectra using the rms normalization (van der Klis 1995b). Several observations with similar power spectra and colors were averaged into sets labeled A–H in order to improve the statistics (see Table 2.1). The sets were ordered by increasing kHz QPO frequencies.

To fit the overall broad-band power spectra we use a fit function consisting of the sum of several Lorentzians in the so-called "ν_{max} representation", described in Belloni et al. (2002). In this representation, if ν_0 is the Lorentzian's centroid frequency and Δ its HWHM (half width at half maximum), $\nu_{max} = \sqrt{\nu_0^2 + \Delta^2}$ gives the characteristic frequency of the feature (near the centroid if it is narrow and near the half-width if it is wide). The

quality factor $Q = \nu_0/2\Delta$ is a measure for the coherence of the variability feature. Its strength is given by the integral power whose square root, in the normalization we use, is the fractional rms amplitude of the variability. Four to five Lorentzian components were needed, all of them significant to more than 3σ, with one exception noted in Table 2.3. In some cases in order to avoid a meaningless negative coherence, Q was fixed to zero, which is equivalent to fitting a zero-centered ($\nu_0 = 0$) Lorentzian. From now on, consistent with previous work (e.g., Belloni et al. 2002; van Straaten et al. 2003; van der Klis 2006) we refer to these components as L_i, where the L stands for Lorentzian and 'i' is the label identifying the component ('b' for break, 'u' for upper kHz, 'ℓ' for lower kHz, 'h' for hump, 'LF' for low frequency QPO). Following this notation we call L_i's characteristic frequency ν_i and its coherence Q_i. In order to measure the kHz QPO centroid frequencies and their frequency difference $\Delta\nu$, we performed exactly the same fits to the same data sets, now representing the Lorentzians' frequency by their centroid frequency $\nu_{i,0}$. While of course the two representations are mathematically equivalent, refitting was necessary to calculate the correct error bars for the frequencies. We split the sets in the original observations (see Table 2.1) and checked wether this led to a better measurement of $\Delta\nu$. Only in one case the statistical significance of the kHz QPOs increased (obs. 80145-01-03-00 in set H; $\Delta\nu$=197.8±7.6 was closer to ν_{spin}) but in the final analysis we conservatively used the original datasets. Hereafter, when we talk about frequencies this refers always to characteristic frequencies (ν_{max}) as given above; whenever centroid frequencies (ν_0) are intended this is explicitly stated.

Power law functions were fitted to the ν_i vs. ν_u relations (where 'i' is one of the labels mentioned above) in order to quantify the correlations between these frequencies. For this, we used the FITEXY routine of Press et al. (1992) that takes into account errors in both coordinates and fitted straight lines to the $\log \nu_i$ vs. $\log \nu_u$ relations.

To quantify the shifts in the XTE J1807–294 correlations and compare them with the shifts in the other AMPs we used the same method as van Straaten et al. (2005): we took as a reference the atoll sources 4U 0614+09, 4U 1608–52, 4U 1728–34 and Aql X-1, and included only the frequency sets with $\nu_u <$ 600 Hz (as noted in van Straaten et al. 2005), the behavior of the power spectral components above that value becomes more complex; see also Section 2.4). We multiplied the upper kHz QPO frequencies of XTE J1807–294 by a factor f, which we varied between 0.01 and 5 with steps of 0.001. In each step we fitted a power law to the XTE J1807–294 and atoll source points together. The step with the best χ^2 gives us the optimal shift factor. We also calculated the shift factors in ν_i, following exactly the same procedure, but multiplying

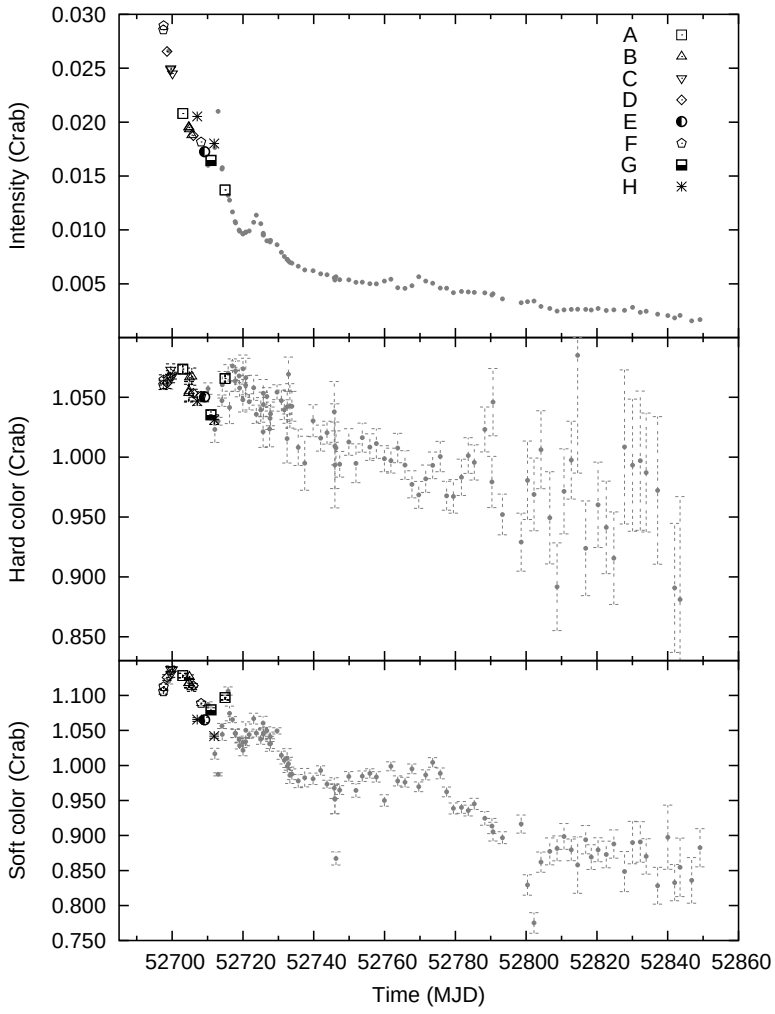

Figure 2.1: Intensity, hard color and soft color (defined in text) versus time for all the observations. Symbols identify the observations used for the timing analysis as indicated. The peak count rate ($\sim$ 58 mCrab) occurred near February 21^{st} (MJD 52691). No strong timing features were detected after March 23^{th} (MJD 52721) because the count rate was too low.

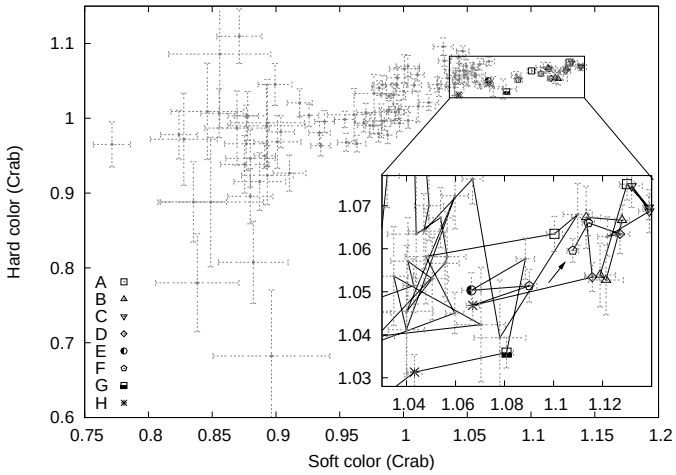

Figure 2.2: Color-color diagram with a zoom into the area used for timing. Symbols identify the observations used for the timing analysis as indicated. The arrow points at the first observation and the solid line indicates the path followed in time.

the ν_i instead of ν_u by a factor f. In the above mentioned atoll sources there were only very few detections of L_{LF}. Therefore, to obtain some information about the shift in this component, we took as a reference the L_{LF1} component of the low luminosity bursters 1E 1724–3045 and GS 1826–24 (van Straaten et al. 2005), and again applied the same procedure.

2.3 Results

Fig. 2.1 shows the light curve for all the observations, as well as the evolution in time of the soft and hard colors (for definitions see Section 2.2). As noted in Falanga et al. (2005a) three peaks in the intensity occurred on March the 9^{th}, 14^{th} and 25^{th}; a peak on March the 30^{th} was instrumental (caused by a flare in PCU4) and removed in the current analysis. The overall trend in the colors is a gradual decline following a slight increase during the first two days of observations. The color-color and color-intensity diagrams are shown in Figs. 2.2 and 2.3, respectively. The region of the color diagrams spanned by the observations, as well as the overall shape of the power spectra (see below), is reminiscent of the island state in atoll sources (see van der Klis 2006). As can be seen from Figs. 2.1-2.3, there is a tendency for the colors to decrease with increasing QPO frequencies (from set A to set H), but the correspondence is not monotonic.

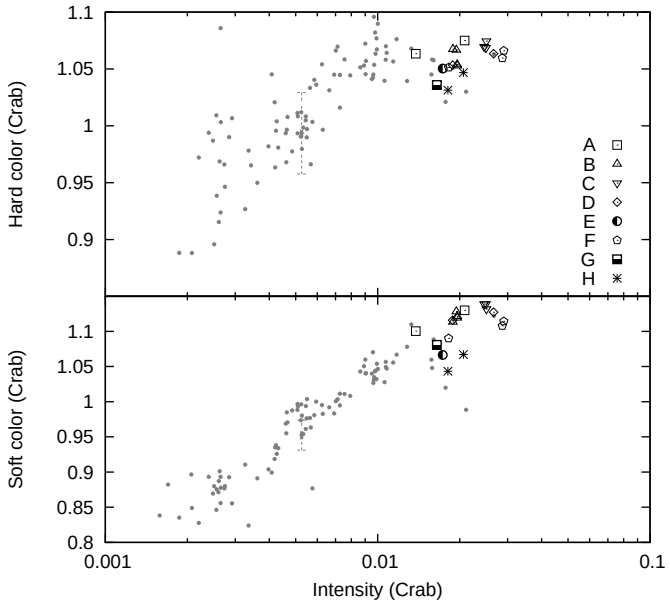

Figure 2.3: Color-intensity diagrams. Symbols identify the observations used for the timing analysis as indicated. Typical error bars are shown.

Two simultaneous kHz QPOs (see Fig. 2.4) were detected in seven of the eight datasets used in this paper; the best-fit centroid frequencies of these QPOs are listed in Table 2.2 together with centroid frequency differences and ratios. As discussed below, the identity of the Lorentzian below L_u is not clear in set A as it could be fitting either L_ℓ or L_{hHz}, or both, so we did not include this value in the analysis of the kHz QPO centroid frequencies. The measured differences $\Delta\nu$ between the kHz QPO centroid frequencies are consistent with being equal to the pulse, and inferred spin, frequency of 190.6 Hz (see Fig. 2.5), with no evidence for variations over the range the QPOs were detected. The weighted average of the seven values for $\Delta\nu$ was 205.1±6.4 Hz, slightly (2.3σ) higher than the pulse frequency.

The broad-band power spectra of the eight sets of observations can be seen in Fig. 2.6, with their multilorentzian fits. The χ^2/d.o.f. of the fits were between 155/168 and 192/143. The best-fit parameters of the power spectral components are presented in Table 2.3.

The multilorentzian fits to the power spectra comprise a broad component at low frequencies (5–10 Hz), L_b (see Section 2.2 for nomenclature); two components at intermediate frequencies, one of them narrow at somewhat lower

frequency and the other one wider and at higher frequency, respectively: L_{LF} (15–40 Hz) and L_h (25–130 Hz); and two narrow components at high frequencies (the kHz QPOs), L_ℓ and L_u with characteristic frequencies 100–370 Hz and 340–570 Hz, respectively. In two of the sets (E and G) L_h was not detected, while in set H it has a frequency of ∼130 Hz and could also be identified as L_{hHz} (see van Straaten et al. 2002, 2003, 2005, for a description of this component in atoll sources and AMPs — the values of the correlation parameters given below do not change significantly when calculated excluding ν_h in set H). The L_ℓ of the two lowest frequency sets (A and B) are wider than the rest (Q∼0.5 compared with Q∼ 1.5) and in set A L_ℓ lies slightly below the ν_ℓ vs. ν_u correlation (see Fig. 2.7), suggesting that we may be looking at a blend between L_ℓ and L_{hHz}. In set A we find a narrow Lorentzian (Q=8) at higher frequency (27 Hz) and a wider one (Q=1.4) at lower frequency (16 Hz). We call the higher-frequency one L_h and the lower-frequency one L_{LF}; note that this implies $Q_{LF} < Q_h$ for this data set. This choice has only a small effect on the numbers reported below and does not affect our conclusions. In the sets where L_h was not detected (E and G), Q_{LF} is also low, which might indicate that L_h and L_{LF} are blended.

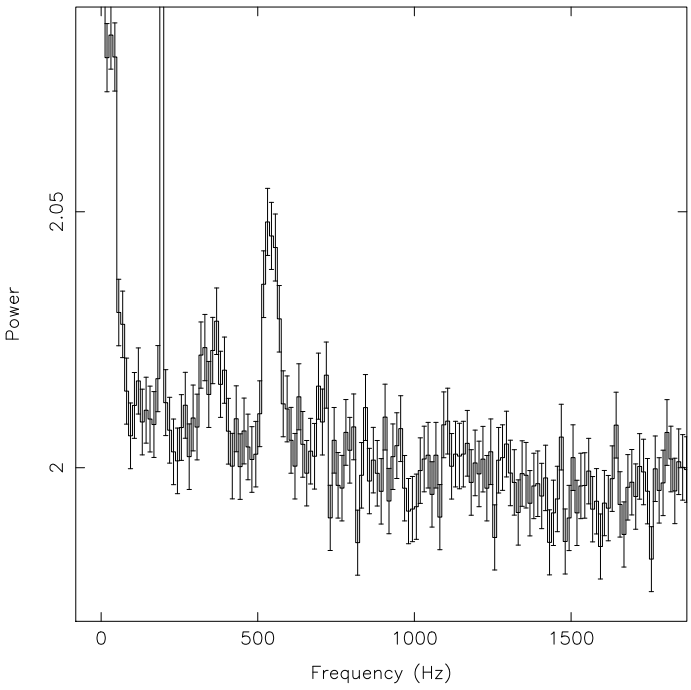

Figure 2.4: Twin kHz QPOs in the power specrum of obs. 80145-01-03-00 (in dataset H). Note the pulsar spike just below 200 Hz.

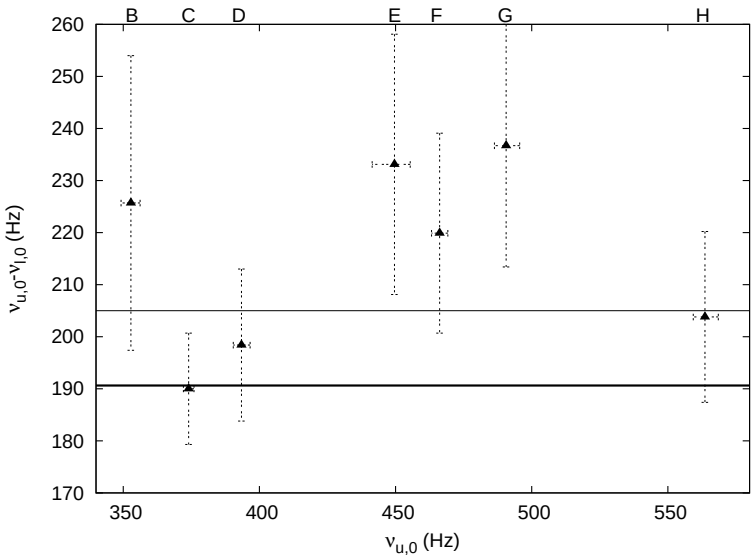

Figure 2.5: kHz QPO frequency separation $\Delta\nu$ plotted vs.upper kHz QPO centroid frequency $\nu_{u,0}$. The thick line indicates the pulse frequency, the thin line the average separation and the letters above the frame the datasets used.

Table 2.2: Twin kHz QPO centroid frequencies with their difference and ratio.

Set	$\nu_{u,0}$ (Hz)	$\nu_{\ell,0}$ (Hz)	$\Delta\nu$ [a] (Hz)	$\nu_{u,0}/\nu_{\ell,0}$
B	352.8±3.5	127.1±28.0	225.7±28.3	2.8±0.6
C	374.0±1.9	184.0±10.5	190.0±10.7	2.03±0.12
D	393.4±3.1	195.0±14.3	198.4±14.6	2.02±0.15
E	449.6±7.1	216.5±23.9	233.1±25.0	2.1±0.2
F	466.2±3.0	246.3±19.0	220.0±19.2	1.89±0.15
G	490.6±4.6	253.9±22.8	236.7±23.3	1.93±0.17
H	563.6±4.6	359.9±15.8	203.7±16.5	1.57±0.07

[a] $\nu_{u,0}$-$\nu_{\ell,0}$

The correlations between our measured characteristic frequencies are compared to those in other sources in Fig. 2.7a. As in SAX J1808.4–3658, our source shows correlations that are shifted with respect to those of the atoll sources. Our results are closer to those of SAX J1808.4–3658 than to those of the other sources, but are somewhat different also from that source. The shift factors between the correlations in XTE J1807–294 and those in the atoll

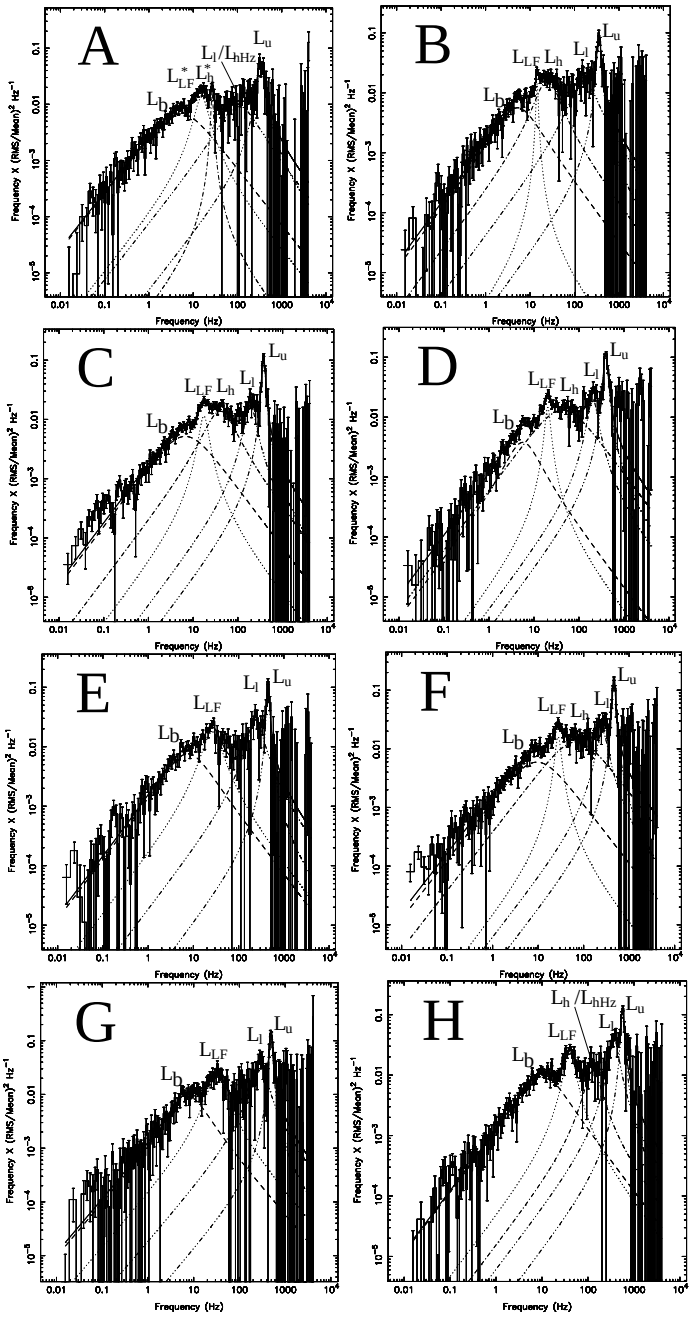

Figure 2.6: Power spectra in power×frequency vs. frequency representation together with the respective fit functions and their Lorentzian components. The pulsar spike was removed before rebinning in frequency.

Table 2.3: Multilorentzian fits to the power spectra.

	Parameter	L_b	L_{LF}	L_h	L_ℓ	L_u	χ^2 d.o.f.
	$\nu_{max}(Hz)$	5.3±0.6	15.6±0.6	26.8±0.5	106±30	337±10	
A	Q	0 (fixed)	1.4±0.3	8^{+15}_{-3}	0.4±0.3	2.8±0.6	180
	rms(%)	14.56±0.8	11.6±1.2	5.4±1.0	15±2	16.7±1.5	148
	$\nu_{max}(Hz)$	5.3±0.7	14.5±0.2	24.7±1.6	163±23	354±4	
B	Q	0.26±0.08	9^{+11}_{-3}	0.73±0.18	0.6±0.3	5.5±1.0	169
	rms(%)	11.8±0.9	4.9±1.0	15.9±1.5	16±2	15.8±1.2	165
	$\nu_{max}(Hz)$	6.7±0.8	17.4±0.4	40±3	191±9	375±2	
C [a]	Q	0 (fixed)	2.0±0.5	0.5±0.2	1.7±0.6	6.3±0.5	192
	rms(%)	12.8±0.9	9.0±1.3	16.2±1.9	12.0±1.4	17.3±0.5	143
	$\nu_{max}(Hz)$	5.7±0.7	20.2±0.4	44±12	202±11	395±3	
D	Q	0.45±0.16	3.6±1.2	0 (fixed)	$2.0^{+1.2}_{-0.7}$	5.1±0.6	129
	rms(%)	8.8±1.4	7.8±1.2	20.3±0.9	12.1±1.9	18.9±0.8	121
	$\nu_{max}(Hz)$	7.5±1.4	26.1±1.6	-	238±25	449±9	
E	Q	0.2 (fixed) [b]	1.0±0.5	-	$1.2^{+1.2}_{-0.6}$	$7.9^{+4.4}_{-1.5}$	132
	rms(%)	14.2±1.7	15±3	-	17±3	15.2±1.8	111
	$\nu_{max}(Hz)$	9.4±1.4	27.6±0.5	69±23	259±16	465±2	
F	Q	0 (fixed)	3.2±1.0	0 (fixed)	1.7±0.7	6.7±0.6	202
	rms(%)	13.6±1.5	8.6±1.2	20.3±1.1	13±2	18.7±0.7	175
	$\nu_{max}(Hz)$	7.8±1.1	32.1±1.5	-	273±19	492±5	
G	Q	0.36±0.11	1.0±0.2	-	1.3±0.6	8±2	155
	rms(%)	14.2±1.2	16.9±1.4	-	20±2	17.3±1.6	168
	$\nu_{max}(Hz)$	10.2±0.8	40.3±1.1	129±19	370±18	565±5	
H	Q	0.22±0.06	1.7±0.3	$1.2^{+1.4}_{-0.7}$	2.0±0.8	6.6±1.4	151
	rms(%)	16.0±0.6	13.7±1.1	12^{+4}_{-3} [c]	17±3	17.1±1.4	142

[a] An extra component could be added to the fit at ∼0.1 Hz, without significant change in the other Lorentzians.

[b] Q fixed to 0.2 for the stability of the fit.

[c] This component was 2.2σ single trial but when added to the fit function it gave a 2.9σ improvement of the chi squared (according to the F-test for additional terms), without significantly changing the rest of the components.

sources, calculated as explained in Section 2.2, are presented in Table 2.4. Note that due to the intrindic dispersion present in the frequency-frequency relations the reduced χ^2 ($\chi^2_r = \chi^2/d.o.f.$) is larger than 2 in three of the four shifts presented. We take this into account when deriving the errors by using $\Delta\chi^2 = \chi^2_r$. The L_b and L_h correlations show shifts in ν_u by factors of 1.46±0.05 and 1.72±0.05, respectively. The lower kHz QPO can be made to match the atoll sources by shifting it by another factor (∼1.08) in ν_u only, but

is also consistent with the option that both ν_u and ν_ℓ are shifted by the same average factor as derived for L_b and L_h (as van Straaten et al. 2005 reported for SAX J1808.4–3658). This can be seen in Fig. 2.7b, where ν_u and ν_ℓ of SAX J1808.4–3658 and XTE J1807–294 have been multiplied respectively by 1.454 (the value found by van Straaten et al. 2005) and 1.59 (the weighted average of the ν_b and ν_h factors; see Table 2.4). The figure clearly shows that with these shifts the ν_ℓ vs. ν_u correlation, and for $\nu_u < 600$ Hz also the ν_b and ν_h vs. ν_u correlations, match those in the other sources.

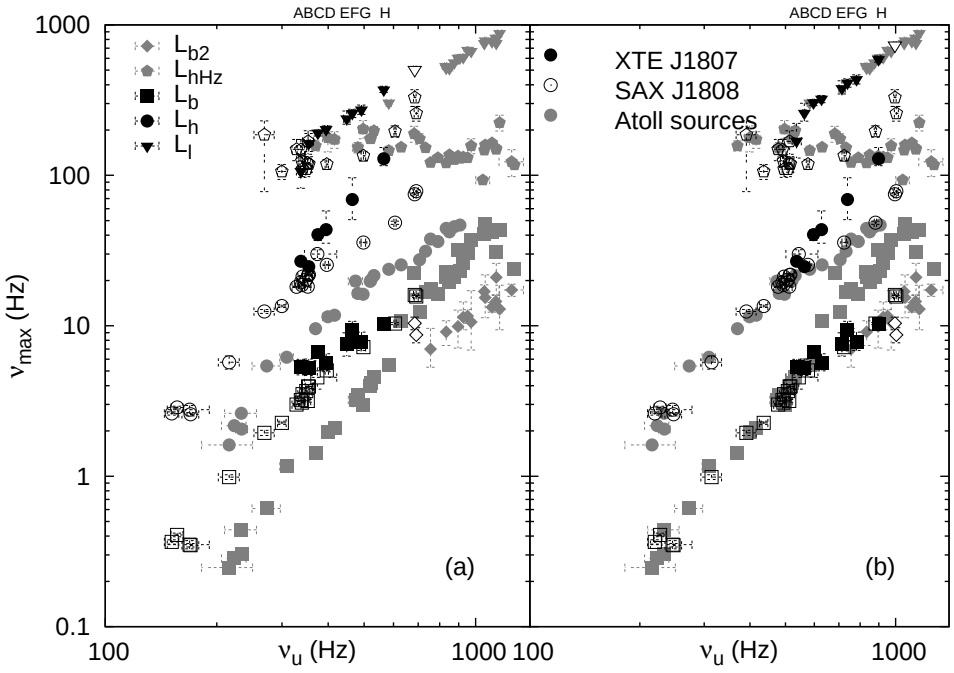

Figure 2.7: Characteristic frequencies of the power spectral components (except ν_{LF}, which is analyzed separately) plotted versus the characteristic frequency of the upper kHz QPO. The black symbols correspond to XTE J1807–294, the open ones to SAX J1808.4–3658 and the grey ones to the atoll sources . Symbols identify the different components as indicated, and the letters above the frame the approximate location of XTE J1807–294 data. The observed frequencies are plotted in (a) while in (b) the XTE J1807–294 points were shifted by a factor 1.59 and the SAX J1808.4–3658 points by a factor 1.454 in both ν_u and ν_ℓ. Note the apparent bifurcations in the L_b and L_h correlations in (b) for $\nu_u > 600$ Hz.

Following van Straaten et al. (2005) and previous works, to prevent crowding

of the figures, the L_{LF} components, with frequencies usually between ν_b and ν_h, are not displayed in Fig. 2.7 but their frequencies are plotted vs. ν_h separately in Fig. 2.8. The ν_{LF} values we find in XTE J1807–294 are high, above 10 Hz, like in SAX J1808.4–3658 (van Straaten et al. 2005) and in 4U 1820–30 (Altamirano et al. 2005), but are somewhat below the power law extrapolated from the low luminosity bursters.

Table 2.4: Shifts in the frequency-frequency relations in XTE J1807–294.

Component	$\chi^2/d.o.f.$	ν_i factor	ν_u factor
L_{LF} [a]	22/17	0.30±0.03	1.73±0.11
L_b	68/22	0.34±0.03	1.46±0.05[b]
L_h	44/20	0.25±0.02	1.72±0.05[b]
L_ℓ [c]	185/21	0.90±0.08	1.08±0.07

[a] This shift was done using the L_{LF1} of the low luminosity bursters as a reference (see text and Figure 2.8).

[b] The weighted average of these two values is 1.59±0.03.

[c] A double shift in this relation (ν_u and ν_ℓ equally shifted) gave a factor 1.31±0.26, with a $\chi^2/d.o.f.$ of 185/21.

Table 2.5: Power law fits to the frequency-frequency relations.

$\nu_i = N \times {\nu_u}^\alpha$	α	$\chi^2/d.o.f.$	$\nu_i = N \times {\nu_u}^\alpha$	α	$\chi^2/d.o.f.$
XTE J1807–294			Atoll sources		
ν_b	1.3±0.2	4/6	ν_b	3.1±0.1	15/14
ν_{LF}	2.2±0.1	14/6	ν_{b2} [a]	1.5±0.4	9/11
ν_h	3.3±0.3	9/4	ν_h	2.5±0.1	29/14
ν_ℓ	1.6±0.1	4/6	ν_ℓ	1.40±0.03	181/14

[a] Five ν_{b2} values measured by van Straaten et al. (2002, 2003) coincide with the L_b track at $\nu_u > 600$ Hz; these were not included in the measurement of the slope of ν_{b2} vs. ν_u.

Table 2.6: Approximate relations between the kHz QPO separation $\Delta\nu$, ν_{burst} and ν_{pulse} in the sources where at least two of these frequencies have been measured. See Table 2.5 in van der Klis 2006 for a more extensive version and complete references.

Source	ν_{burst} (Hz)	ν_{pulse} (Hz)	$\Delta\nu/\nu_{burst}$	$\Delta\nu/\nu_{pulse}$	References
		Slow rotators			
XTE J1807–294	—	191	—	∼1	This paper.
4U 1915–05	272	—	∼1	—	Galloway et al. (2001)
XTE J1814–338	314	314	—	—	Strohmayer et al. (2003)
4U 1702–43	330	—	∼1	—	Markwardt et al. (1999)
4U 1728–34	363	—	∼1	—	Méndez & van der Klis (1999)
		Fast rotators			
SAX J1808.3–3658	401	401	∼1/2	∼1/2	Wijnands et al. (2003)
KS 1731–260	524	—	∼1/2	—	Wijnands & van der Klis (1997)
Aql X-1	549	—	∼1/2	—	van der Klis (2000)[a]
4U 1636–53	582	—	∼1/2	—	Wijnands et al. (1997)
SAX J1750.8–2900	601	—	∼1/2	—	Kaaret et al. (2002)[a]
4U 1608–52	619	—	∼1/2	—	Mendez et al. (1998a,b)

[a]Marginal detection upper kHz QPO.

2.4 Discussion

We found simultaneous twin kHz QPOs in the power spectra of XTE J1807–294. This is the second accreting millisecond pulsar to show twin kHz QPOs. As the spin period of the neutron star can be inferred precisely and with high confidence from the pulse frequency this provides excellent conditions for testing theoretical models of kHz QPOs (see Section 1; van der Klis 2006 for an overview). In SAX J1808.4–3658 the twin kHz QPO centroids were ∼195 Hz apart, consistent with *half* the inferred spin frequency ($\nu_{spin} = 401$ Hz) and not with ν_{spin} as the original beat-frequency models had predicted (see Section 1). In XTE J1807–294, we find instead that the twin kHz QPO separation is near *once* the inferred spin frequency. $\Delta\nu$ is larger than ν_{spin} by 2.3σ. This has previously been seen only in 4U 1636–53 (Jonker et al. 2002) and may be difficult to accomodate in beat-frequency (Lamb & Miller 2001) or relativistic resonance (Kluźniak et al. 2004) models.

In subsequent observations of different sources, a picture is gradually being built up of the relations between the burst oscillation frequency ν_{burst}, the pulse frequency ν_{pulse}, the kHz QPO separation frequency $\Delta\nu$, and the relation of these observed frequencies to the neutron-star spin frequency ν_{spin}. We currently have two cases where $\nu_{burst} \approx \nu_{pulse}$ (and none where these frequencies differ), three examples of $\Delta\nu \approx \nu_{burst}$ and six examples of $\Delta\nu \approx \nu_{burst}/2$ (see Table 2.6). However, so far the only direct information about the relation between ν_{pulse} and $\Delta\nu$ was the one case (SAX J1808.4–3658) where $\Delta\nu \approx \nu_{pulse}/2$. The case of XTE J1807–294 constitutes the first example of $\Delta\nu \approx \nu_{pulse}$. All these findings are consistent with the simple picture that (i) the pulse frequency is always the spin frequency, (ii) the burst oscillations occur always at the spin frequency, and (iii) for $\nu_{spin} < 400$ Hz ('slow rotators'), $\Delta\nu \approx \nu_{spin}$ while for $\nu_{spin} > 400$ Hz ('fast rotators'), $\Delta\nu \approx \nu_{spin}/2$. The strict dichotomy expressed in conclusion (iii) may be due to small sample size; some overlap between the slow and fast rotator groups might well be found in further observations. The model of Lamb & Miller (2003) predicts that kHz QPOs separated by once and half ν_{spin} can occur simultaneously, but this has not yet been observed.

In SAX J1808.4–3658, where twin kHz QPOs were detected only once, several commensurabilities between the centroid frequencies of the kHz QPOs and the spin frequency of the form $\nu_{j,0} = |m\nu_{k,0} - n\nu_{spin}|$ (where $\nu_{i,0}$ indicates the centroid frequency of component L_i, j and k designate u and ℓ or vice versa and m and n are integers) were consistent with the data, with in particular $\nu_{u,0} = |3\nu_{\ell,0} - 2\nu_{spin}|$ a remarkably good match. We searched for this in XTE J1807-294, but with seven detections of kHz QPOs moving over

a 200 Hz range in frequency, no commensurabilities remained consistent with the data as the QPOs moved. The data are also not consistent with a constant ratio between kHz QPO centroid frequencies (Table 2.2). This suggests that, because in SAX J1808.4–3658 only a single twin kHz QPO pair was detected, it was possible for both the commensurability noted by Wijnands et al. (2003) and the 7:4 ratio proposed by Kluźniak et al. (2004) to arise by chance.

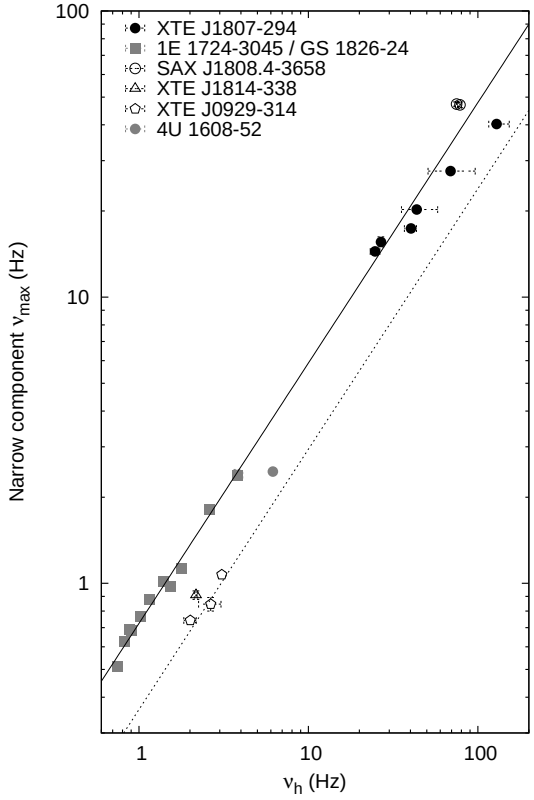

Figure 2.8: Frequencies of L_{LF} versus the frequencies of L_h, for the sources indicated in the plot. The solid line shows the power law fit to the low luminosity bursters 1E 1724–3045 and GS 1826–24. The dotted line represents a power law with the same index and a normalization factor half of that of the solid line.

The correlations between the frequencies of the several power spectral components detected in LMXBs (cf. Section 1) are a relatively new tool to study these systems, and we are still in the process of figuring out their significance and even their phenomenology. The value that we find for the shift in these correlations ($\sim$1.59) is similar to, but significantly different from, both the value of van Straaten et al. (2005) for SAX J1808.4–3658 ($\sim$1.45) and the

small-integer ratio 3/2=1.5 (a value that could suggest a relation with relativistic resonance models; Abramowicz et al. 2003). Yet, the description of the shifts proposed by van Straaten et al. (2005) as the most parsimonious one based on the SAX J1808.4–3658 data (all ν_u and ν_ℓ values are too low by the same factor close to 1.5) provides a remarkable match to the data also for XTE J1807-294 (Fig. 2.7b). In SAX J1808.4–3658 only a single ν_ℓ value was available on which to base the conclusion that ν_ℓ was shifted by the same factor as ν_u. In XTE J1807-294, blindly applying the same 1.59 shift (derived from the ν_b and ν_h vs. ν_u correlations) to the seven well-distributed ν_ℓ and ν_u values, produces a very good match to the atoll-source ν_ℓ vs. ν_u relation.

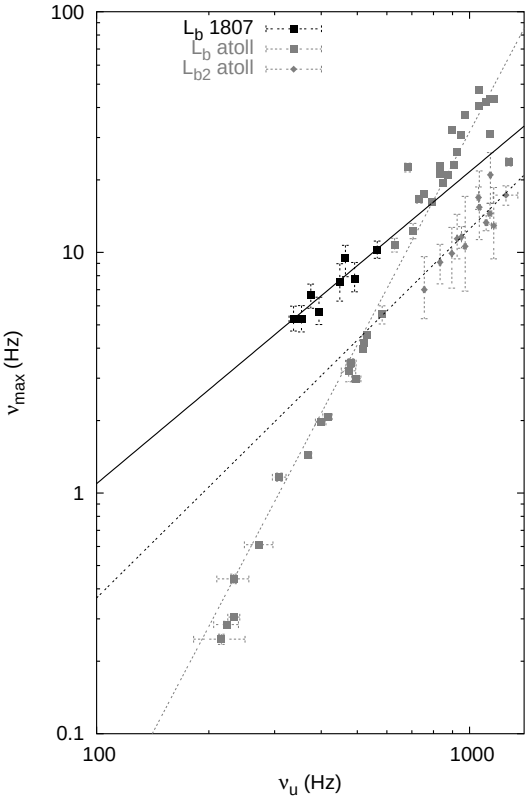

Figure 2.9: Characteristic frequencies of L_b and L_{b2} for the atoll sources 4U 0614+09, 4U 1608–52, 4U 1728–34 and Aql X-1 and for XTE J1807–294, plotted versus ν_u. The fits to the relations are shown as a solid black line (XTE J1807–294), a dashed black line (ν_{b2} of the atoll sources) and a dashed grey line (ν_b of the atoll sources). Five points with doubtful identification were excluded (see Table 2.5).

Altamirano et al. (2005) recently reported a similar shift in the frequency

correlations of the atoll source 4U 1820–30, but by a factor of ∼1.17. This suggests that the mechanism responsible for the shifts may also be present in non-pulsing sources and that the shift factor in ν_u may be sometimes far from 1.5. Nevertheless, the small sample size of the 'shifted' sources makes it too early for final conclusions. Descriptions involving different shift factors for different components, and involving shifts of other components than the kHz QPOs are still possible and, indeed, formally required by our fit results (see Table 2.4). A clear complication is the nature of the shifted correlation diagram (Fig. 2.7b) at $\nu_u > 600$ Hz. There, the band-limited noise component labeled L_b in XTE J1807–294 follows the L_{b2} track of the atoll sources, and the L_h track lies above that for the atoll sources or SAX J1808.4–3658. Power law fits to the ν_i vs. ν_u relations of XTE J1807–294 and the atoll sources (Table 2.5), show that the slope of the ν_b vs. ν_u relation in XTE J1807–294 is much less steep than in the other atoll sources, and actually consistent with that of the ν_{b2} points (see Fig. 2.9), and that the ν_h points define a *steeper* relation in XTE J1807–294 than in the other sources. The overall impression created by all of this in Fig. 2.7b is that of a bifurcation in both the ν_b and the ν_h vs. ν_u relations when ν_u exceeds 600 Hz. Perhaps such a bifurcation could be related to the increasing separation between general-relativistic azimuthal and radial epicyclic frequencies when approaching the compact object (e.g., Abramowicz et al. 2003), or to the onset of some form of rotational splitting (cf. Titarchuk & Muslimov 1997), but at this stage this must remain conjectural.

Further analysis of other AMPs and atoll sources is needed to gain a better insight into the frequency correlation shifts. Only a few useful power spectra were obtained up to now for XTE J1751–305, XTE J0929–314 and XTE J1814–338 and no twin kHz QPOs were seen in them. The recent second outburst of XTE J1751–305 (Grebenev et al. 2005; Swank et al. 2005) or forthcoming outbursts of other new or known AMPs can help to give us a more complete view of this shift phenomenon. In any case, our results for XTE J1807–294 when combined with those for SAX J1808.4–3658, strongly support a spin-related mechanism for kHz QPO production and strongly suggest a spin-independent cause of the shift in the frequency correlations. The former is due to the first detection of twin kHz QPOs separated by the spin frequency in a confirmed slow rotator, and the latter to the fact that similar shifts are observed in the frequency correlations of at least two AMPs with very different spin frequencies.

Acknowledgments: We thank the referee for valuable comments. ML likes to thank M. Klein-Wolt, T. Maccarone, S. Migliari and R. Wijnands for instructive discussions, and M. Falanga for providing an early copy of his manuscript.

3 An accreting millisecond pulsar with black hole-like X-ray variability: IGR J00291+5934

Manuel Linares, Michiel van der Klis, Rudy Wijnands

The Astrophysical Journal, 2007, 660, 595

Abstract

IGR J00291+5934 is one of the seven accreting millisecond pulsars (AMPs) discovered so far. We report on the aperiodic timing and color analysis of its X-ray flux, using all the *RXTE* observations of the 2004 outburst. Flat-top noise and two harmonically related quasi-periodic oscillations, all of them at very low frequencies (0.01–0.1 Hz), were present in the power spectra during most of the outburst as well as a very high fractional variability (∼50 %). These properties are atypical not only for AMPs but also for neutron star low-mass X-ray binaries (LMXBs) in general. There are instead some remarkable similarities with the variability observed in black hole systems, reinforcing the connections between these two types of LMXB, as well as some interesting differences. We note finally that the results of this paper are difficult to reconcile with interpretations where any break frequency of power density spectra scales inversely with the mass of the central object at an accuracy sufficient to distinguish between the masses of neutron stars and black holes in LMXBs.

3.1 Introduction

Most low-mass X-ray binaries (LMXBs) contain rapidly spinning neutron stars (NSs), which only in a few cases become apparent as millisecond X-ray pul-

sars. This growing sub-class of accreting millisecond pulsars (AMPs; see Wijnands 2005 for a review) consists of dim transients that typically go in outburst during a few weeks once every few years (so far the only exception is HETE J1900.1–2455, still active at the moment of writing, more than a year after its discovery). AMPs are thought to be the evolutionary link between neutron star LMXBs and millisecond radio pulsars, according to the so-called recycling scenario (Bhattacharya & van den Heuvel 1991, for a review). Eight years after the first of the AMPs was discovered (SAX J1808.4–3658, Wijnands & van der Klis 1998) it is still unknown why these systems show pulsations and the rest of neutron star LMXBs do not, although some explanations have been put forward (e.g. screening of the magnetic field, Cumming et al. 2001; smearing of the pulsations, Titarchuk et al. 2002).

Aperiodic variability in the X-ray lightcurves of black hole and neutron star LMXBs (BH/NS-LMXBs), such as broadband noise or quasi-periodic oscillations (QPOs), offers a powerful tool to study the accretion flow in its inner region, where the bulk of the radiation is thought to originate and where gravitational fields are extreme (van der Klis 2000, 2006). Using this tool NS-LMXBs were classified according to their correlated timing and energy spectral behavior into Z and atoll sources (Hasinger & van der Klis 1989). As noted several years ago (e.g. van der Klis 1994), very similar physical mechanisms are expected to drive the accretion process in BH- and NS-LMXBs, and the difficulties in finding unequivocal signatures of a black hole or a neutron star in the energy or power spectral properties of LMXBs are a natural consequence of this fact. Several attempts to find direct BH signatures have been made based on the spectral properties at high energies (Sunyaev et al. 1991; but see also di Salvo et al. 2004 or Barret et al. 2000) or in the power spectral properties at high frequencies (Sunyaev & Revnivtsev 2000; but see also Klein-Wolt et al. 2004). On the other hand, apart from pulsations and type I X-ray bursts, twin variable-frequency kilohertz quasi-periodic oscillations (twin kHz QPOs) are now considered a NS signature (van der Klis 2006). NS-LMXBs are also known to be fainter than BH-LMXBs at radio wavelengths (Migliari & Fender 2006), and BH-LMXBs are generally fainter in X-rays when they are in quiescence (Garcia et al. 2001).

We present in this work the results of the aperiodic timing and X-ray color analysis of one of the seven known AMPs, IGR J00291+5934. We show the exceptional behavior of this source in its 2004 outburst, more similar with respect to aperiodic X-ray variability to a BH-LMXB than to the presently known NS-LMXBs: IGR J00291+5934 was variable at very low frequencies with a very high fractional amplitude. However, previously identified NS signatures were also present in the highest frequencies. In Section 3.2 we briefly

review some information on this source and in Sections 3.3 and 3.4 we describe our analysis and give its results, respectively. Section 3.5 contains our final remarks and conclusions.

3.2 IGR J00291+5934

On December 2^{nd}, 2004, IGR J00291+5934 was discovered with *INTEGRAL* during one of the Galactic plane scans (Eckert et al. 2004). Follow up observations with *RXTE* revealed coherent pulsations at 598.88 Hz (Markwardt et al. 2004b), making it the fastest spinning AMP known. The pulse frequency exhibited a sinusoidal modulation with a period of 147.4 minutes (∼2.45 hr) indicative of the orbital motion of the pulsar in the binary system (Markwardt et al. 2004a). Optical (Fox & Kulkarni 2004), radio (Pooley 2004; Fender et al. 2004a; Rupen et al. 2004) and infrared (Steeghs et al. 2004) counterparts were identified and a recurrence time of ∼3 yr was suggested by Remillard (2004), based on *RXTE*'s all-sky monitor data. Positive spin frequency derivatives were reported by Falanga et al. (2005c) and Burderi et al. (2005). Several estimates of the distance to the source have been made, ranging from ∼3 to ∼10 kpc (Shaw et al. 2005; Galloway et al. 2005; Falanga et al. 2005c; Jonker et al. 2005; Burderi et al. 2005).

3.3 Observations and Data Analysis

We used all the pointed PCA observations of the 2004 outburst of IGR J00291+5934, performed by *RXTE* between December 3d. and 20th (see Table 3.1). An intermediate polar[1] was also inside the PCA's field of view: V709 Cas (which has a spin period of ∼313 seconds; Haberl & Motch 1995; Norton et al. 1999; Falanga et al. 2005b). Hereinafter we refer to this system as the IP. All necessary caveats were taken in both color and timing analysis in order to avoid contamination from this foreground source, as explained below.

After filtering out unsuitable data according to the recommended criteria[2] we extracted count rates from Standard 2 data, with 16 s time resolution,

[1]Intermediate polars (Patterson 1994, for a review) are a sub-class of accreting white dwarfs with a magnetic field strong enough to channel the accretion flow onto the magnetic poles (thereby emitting X-rays pulsed at the spin period) but unable to lock the rotation of the white dwarf with the orbital motion (as is the case for the so-called polars). Chance placed two semidetached binaries emitting X-ray pulses inside the PCA field of view, one of them containing a white dwarf and the other a neutron star.

[2]Elevation from the Earth greater than 10 degrees and pointing offset lower than 0.02 degrees; see PCA digest at `http://heasarc.nasa.gov/docs/xte/pca_news.html` or, e.g., van Straaten et al. (2003).

Table 3.1: Log of the observations.

Set	ObsID[a]	Date[b]	Detectors[c]	Count Rate [d] (c/s)	1024-s PDS[e]	Total / Bkg. [f] (c/s)
A1	90052-03-01-00	0.9	3.0	308.9±0.0	1	232.9 / 61.2
	90052-03-01-14	2.7	3.0	262.5±15.0	2	
	90052-03-01-04	3.6	3.0	240.4±4.7	12	
	90052-03-01-05	4.0	3.2	256.4±33.7	8	
	90052-03-01-06	4.6	4.0	300.4±8.9	3	
	90425-01-01-08	4.9	3.3	236.5±29.0	7	
	90425-01-01-02	5.1	5.0	347.8±6.3	3	
	90425-01-01-01	5.2	5.0	351.1±0.0	–	
	90425-01-01-03	5.3	5.0	369.0±0.0	–	
	90425-01-01-09	5.6	3.0	209.1±4.4	3	
	90425-01-01-07	5.9	3.5	225.5±31.6	12	
	90425-01-01-10	6.5	2.9	180.5±53.6	14	
	90425-01-01-12	6.7	3.0	188.2±11.5	2	
A2	90425-01-01-110	7.0	3.3	192.6±41.2	13	166.6 / 59.2
	90425-01-01-11	7.2	3.0	166.9±1.1	2	
	90425-01-01-15	7.3	3.0	168.3±2.1	2	
	90425-01-01-13	7.5	3.2	174.3±21.3	15	
	90425-01-02-07	7.6	3.0	156.7±0.0	1	
	90425-01-02-08	7.7	3.0	174.6±15.2	2	
	90425-01-02-000	7.9	3.2	167.3±22.2	12	
	90425-01-02-00	8.1	3.0	148.2±2.4	4	
	90425-01-02-15	8.2	3.0	150.3±2.4	2	
	90425-01-02-04	8.3	3.0	144.6±3.8	2	
	90425-01-02-05	8.4	3.0	142.6±2.6	3	
	90425-01-02-16	8.5	3.0	141.5±4.5	10	
B	90425-01-02-02	8.7	3.0	127.9±0.0	1	94.1 / 53.9
	90425-01-02-030	8.9	3.0	126.6±5.4	12	
	90425-01-02-03	9.1	3.0	117.5±3.7	5	
	90425-01-02-09	9.2	3.0	112.6±3.5	2	
	90425-01-02-100	9.4	2.8	102.3±14.0	15	
	90425-01-02-10	9.6	3.0	126.0±0.0	1	
	90425-01-02-11	9.7	3.0	99.9±0.0	1	
	90425-01-02-120	9.9	2.8	91.8±9.2	12	
	90425-01-02-12	10.1	2.8	81.9±10.7	5	
	90425-01-02-13	10.3	3.0	85.9±2.7	3	
	90425-01-02-14	10.4	2.6	77.7±13.9	11	
	90425-01-02-17	10.6	2.0	65.7±7.2	2	
	90425-01-02-06	11.5	3.0	72.5±3.8	5	
	90425-01-02-01	11.6	2.0	52.1±0.0	1	
	90425-01-02-18	11.9	3.3	74.0±17.6	10	
	90425-01-02-20	13.2	3.0	58.1±0.0	1	
C[g]	90425-01-02-25	14.1	4.0	72.4±0.4	2	63.6 / 63.6
	90425-01-02-26	14.4	2.0	40.0±0.0	1	
	90425-01-02-24	14.5	4.0	77.4 ±3.7	3	
	90425-01-02-19	14.5	3.0	72.8±0.0	1	
	90425-01-02-27	14.6	5.0	91.5±0.0	1	
	90425-01-03-00	14.9	3.3	63.5±8.1	9	
	90425-01-03-01	15.3	3.0	56.1±2.5	8	
	90425-01-03-02	16.0	4.0	72.7±1.7	2	
	90425-01-03-03	16.2	3.0	55.2±1.5	6	
	90425-01-03-04	17.3	3.4	66.0±10.1	7	
	90425-01-03-05	17.9	4.0	71.9±2.1	6	
	90425-01-03-06	18.2	3.0	54.8±2.0	5	

[a] In the first 5 obs. (P90052) GoodXenon modes were used for timing while in the rest (P90425) event modes E_125us_64M_0_1s were used.

[b] Observation start date in days since MJD 53341 (December 2^{nd}, 2004, the discovery date).

[c] Average number of active detectors.

[d] Average and standard deviation of the ∼2.5–30 keV count rate, including all active detectors and not corrected for background.

[e] Number of power density spectra extracted from the observation, each of them 1024 s long.

[f] Set averages of total and background ∼2.5–30 keV count rates (background estimated from set C; see Section 3.3).

[g] Set C contains mainly background/foreground observations.

in the following bands (in keV): A: 2.0–3.5, B: 3.5–6.0, C: 6.0–9.7, D: 9.7–16.0, and we computed soft (B/A) and hard (D/C) colors and intensity (A+B+C+D). The instrumental background was subtracted according to the standard faint-source background models and the colors and intensity normalized to the Crab values nearest in time (Kuulkers et al. 1994) and in the same PCA gain epoch (e.g., van Straaten et al. 2003). Using WebPimms and the spectrum reported by Falanga et al. (2005b), and taking into account the ∼0.3 deg. offset between the IP and our source, we estimate a foreground 2–16 keV count rate from the IP of ∼3.6 c/s/PCU (to be compared with the peak rate in our observations of ∼76 c/s/PCU), which matches approximately the observed intensity during our last dataset (∼5 c/s in PCU2), when IGR J00291+5934 had presumably ceased activity (see Section 3.4, Figure 3.1). The effect of this contaminating flux is probably strongest on the colors, which are sensitive to subtle changes in the energy spectrum. For that reason we consider only the color-color diagram of the first half of the outburst, where the flux from the IP is less than 20% of the background subtracted total (see Section 3.4.1).

GoodXenon and Event modes were used for the timing analysis (see Table 3.1), rebinned in both cases to a 1/8192-s time resolution (Nyquist frequency of 4096 Hz) and including only the counts in the ∼2.5–30 keV range (absolute channels 5–71; this choice optimizes the S/N). We performed fast Fourier transforms in 1024-s data segments, reaching thereby Fourier frequencies down to ∼0.001 Hz. Two observations were shorter than 1024 s (90425-01-01-01 and 90425-01-01-03) so we performed and analyzed a 512-s FFT in each of them. No background subtraction or dead-time correction were made prior to the FFTs and the Poisson noise power was subtracted from the resulting power density spectra, following Klein-Wolt (2004): we first estimated the Poisson noise using the expression proposed by Zhang et al. (1995) and then (after inspecting the ∼2–4 kHz range and finding no unexpected features) shifted it to match the level between 2000–4096 Hz, where no intrinsic power is expected to be present, but only counting statistics noise (this shift was in all cases smaller than 0.06% of the previously estimated Poisson level). We then normalized the power spectra in the so-called rms normalization (van der Klis 1995b). For this normalization purpose, in order to take into account the foreground flux contributed by the IP, we used the count rates in the tail of the outburst (when the AMP reaches its quiescent state; set C; see Fig. 3.1) to estimate the average background and foreground rate during the data segments used for timing. In order to improve the statistics we averaged observations successive in time and with power spectra consistent within errors, thereby dividing the outburst data into four sets (Table 3.1, Fig 3.1). The integrated power was calculated between 0.01 and 100 Hz in order to avoid contamination

from the IP's variability (see Section 3.4.2).

We fitted the power spectra with a fit function composed of a sum of Lorentzians in the "ν_{max} representation"[3], excluding the first four frequency bins to preclude the IP's variability. In some cases, in order to avoid a meaningless negative coherence, Q was fixed to zero, which is equivalent to fitting a zero-centered Lorentzian. From now on, following previous work (Belloni et al. 2002; van Straaten et al. 2003; van der Klis 2006; Altamirano et al. 2005; Linares et al. 2005) we refer to these components as L_i, where the L stands for Lorentzian and 'i' is the label identifying the component (such identification is given in Sections 3.4.2 and 3.5.2). Following this notation we call L_i's characteristic frequency ν_i and its coherence Q_i. Five to seven Lorentzians were necessary to fit the power spectra, as described in detail in the next section.

3.4 Results

3.4.1 Colors and intensity

The time evolution of the count rate and colors can be seen in Fig. 3.1. The lightcurve shows two clearly different slopes in a semi-logaritmic plot, indicating two different exponential decay timescales. As noted in previous works (e.g. Wijnands 2005), this is common behavior among AMPs, with XTE J1807–294 the only known exception (Linares et al. 2005; Falanga et al. 2005a). We fitted the first two parts of the (2.0–16.0 keV) lightcurve (A1+A2 and B) and found e-folding times of 7.9 ± 0.3 and 2.45 ± 0.05 days, similar to the ones reported in Falanga et al. (2005c) from the *INTEGRAL* 20–100 keV lightcurve.

Overall the source spectrum was hard compared to that of other AMPs (van Straaten et al. 2005; Linares et al. 2005) and it softened at both high (6.0–16.0 keV) and low (2.0–6.0 keV) energies during the first ∼9 days decay (see time evolution of soft and hard color in Fig. 3.1). The resulting track in the color-color diagram in this first half of the outburst is shown in Figure 3.2. After the first 9 days (sets B and C in our analysis), the IP contributes with a significant fraction of the flux ($\gtrsim$20% if all the flux in C comes from the IP) and the increase of the colors is likely due to that (intermediate polars are thought to be the hardest X-ray emitting cataclysmic variables; see e.g. de Martino et al. 2004).

[3]In this representation (Belloni et al. 2002), if ν_0 is the Lorentzian's centroid frequency and Δ its HWHM (half width at half maximum), $\nu_{max} = \sqrt{\nu_0^2 + \Delta^2}$ gives the characteristic frequency of the feature (near the centroid if it is narrow and near the half-width if it is wide). The quality factor $Q = \nu_0/2\Delta$ is used in this representation as a measure of the coherence of the variability feature. Its strength is given by the integral power (0–∞) whose square root, in the normalization we use, is the fractional rms amplitude of the variability.

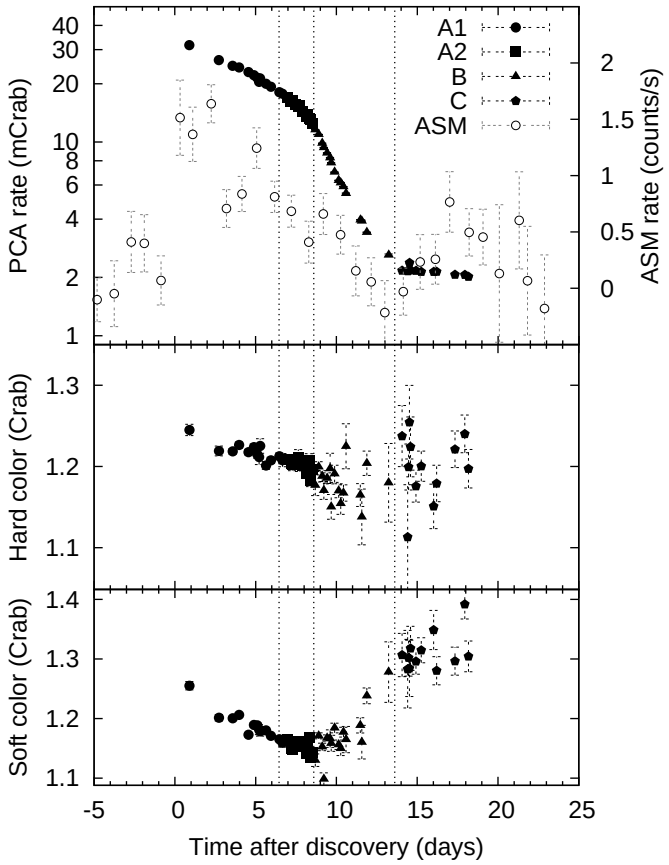

Figure 3.1: Time evolution of colors and intensity during IGR J00291+5934's December 2004 outburst. The upper panel shows the lightcurve from both ASM (1.5–12 keV, daily average; open circles) and pointed PCA (2–16 keV, observation average; filled symbols) data. Vertical dotted lines show the borders between averaged data sets A1, A2, B and C. The increase in colors after day ∼10 is likely due to foreground contamination (see text).

3.4.2 Aperiodic timing

The power spectra (Fig. 3.3) on first inspection show an overall shape characteristic of low (luminosity) and hard (spectra) states of atoll sources, usually called island and extreme island states (where spectral hardness and total rms increase and luminosity and variability frequencies decrease when going

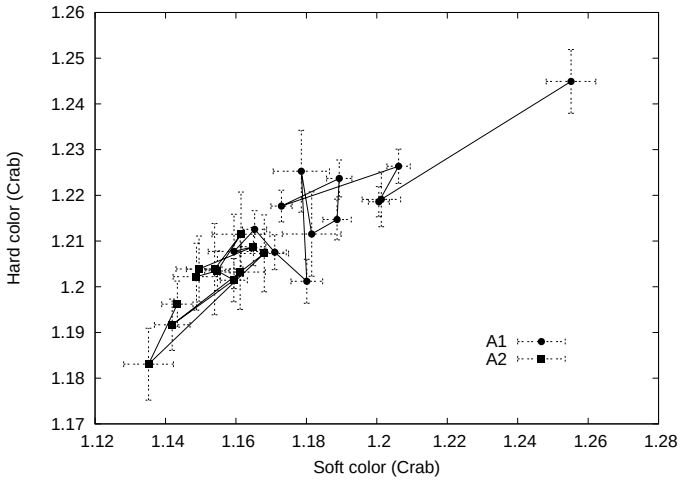

Figure 3.2: Color-color diagram of data sets A1 and A2, where the colors are not yet dominated by the intermediate polar in the field of view. The upper right point corresponds to the first pointed observation and the line connects observations successive in time.

from the island to the extreme island state). However, the overall (0.01–100 Hz) fractional rms amplitude is in the ∼42–58 % range (Fig. 3.6, Table 3.2), much higher than any value reported to date for a NS-LMXB (see e.g. Olive et al. 1998; Barret et al. 2000; Belloni et al. 2002). Five to six Lorentzian components were used to fit these power spectra. The best fit parameters are displayed in Table 3.2. The fit functions comprise i) one broad Lorentzian at 0.03–0.05 Hz accounting for the flat-top noise and its break (L_b for "break"; see Sec. 3.3 for nomenclature) ii) two QPOs between 0.02 and 0.05 Hz (L_{QPO} and its subharmonic, $L_{QPO/2}$) and iii) three zero-centered Lorentzians with characteristic frequencies covering the 0.5–0.8 Hz, 3–5.5 Hz and 25–70 Hz ranges (possibly L_h, $L_{\ell ow}$ and L_u, respectively; see Section 3.5.2 for further discussion). All components are significant at a $> 3\sigma$ level except L_{QPO} and $L_{QPO/2}$ in dataset B.

The flat-top noise present in these observations can be alternatively described with a sum of two broad Lorentzians, one of them giving the first break and the other describing a further steepening above that break (a "wing" above the break in Frequency×Power representation; see Figure 3.5). For completeness we report the parameters of those fits in Table 3.3. These fits are better from a statistical point of view (4.7σ, 2.3σ and 3σ improvement in set A1, A2 and B, respectively, according to the F-test) and give a more detailed description of the structure around the break, but are more difficult to com-

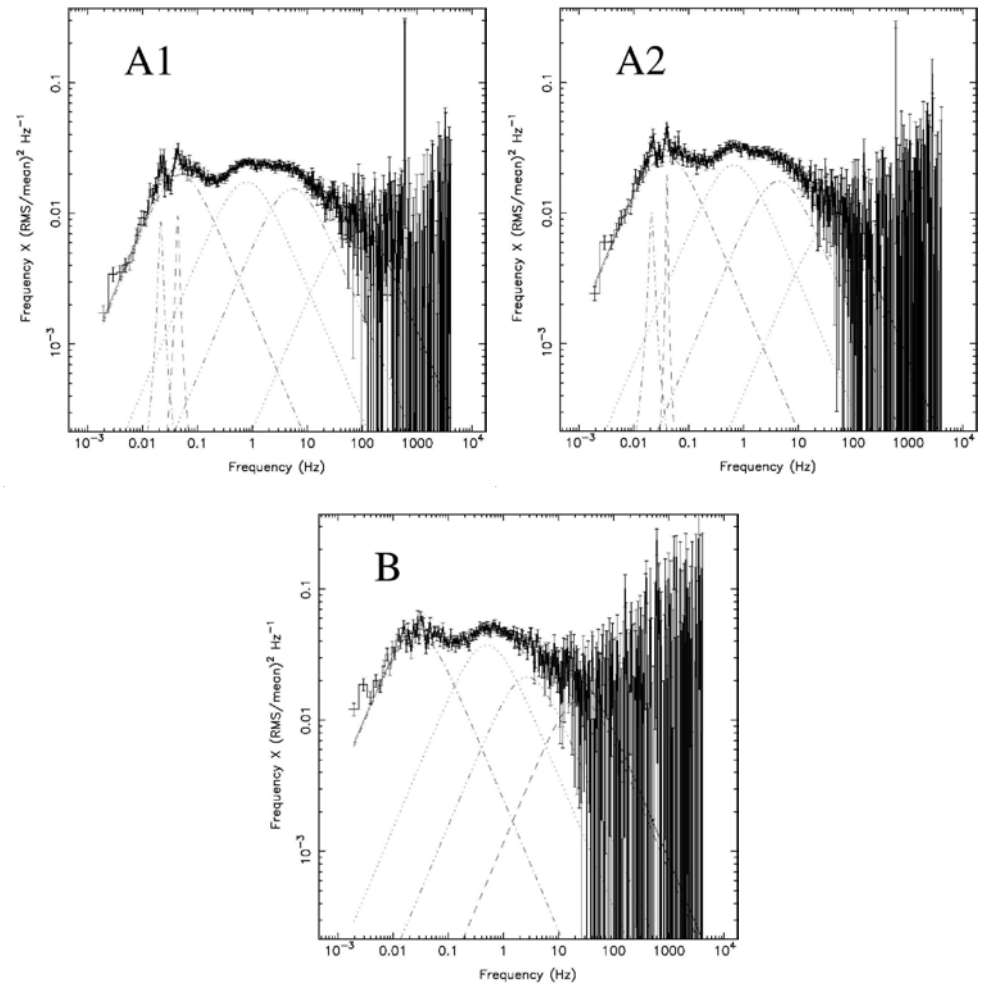

Figure 3.3: Power spectra in Power×Frequency vs. Frequency representation. Also shown are the respective fit functions and their Lorentzian components. The spin frequency of the neutron star shows as a spike at ∼600Hz.

pare with other sources (where usually single-Lorentzian or broken power-law breaks are measured). Therefore, we use the frequencies of the first described six-Lorentzians fit function when comparing with frequencies of other sources (see Section 3.5).

Assuming the IP did not drastically vary its behavior synchronously to the AMP's outburst phases, we can reject the possibility that an appreciable part of the variability above 0.01 Hz comes from the IP. This is shown qualitatively

Table 3.2: Best fit parameters from 6-Lorentzian model and integrated rms variability.

Set	Parameter	L_b	$L_{QPO/2}$	L_{QPO}	L_h	$L_{\ell ow}$	L_u	χ^2/d.o.f.	rms (%)
A1	$\nu_{max}(Hz)$	$(4.9\pm0.2)\times10^{-2}$	$(2.15\pm0.05)\times10^{-2}$	$(4.43\pm0.10)\times10^{-2}$	0.79±0.03	5.5±0.2	70±10	357/325	41.7±0.4
	rms (%)	24.6±0.3	4.8±0.8	4.5±0.7	23.4±0.2	22.1±0.2	15.5±0.4		
	Q	$(4\pm4)\times10^{-2}$	5.5±3.2	6.2±2.2	0 (fixed)	0 (fixed)	0 (fixed)		
A2	$\nu_{max}(Hz)$	$(3.9\pm0.1)\times10^{-2}$	$(2.11\pm0.09)\times10^{-2}$	$(4.03\pm0.06)\times10^{-2}$	0.66±0.02	4.4±0.3	37.6±7.2	335/326	47.3±0.6
	rms (%)	29.3±0.3	5.5±1.0	4.4±0.6	27.1±0.3	23.5±0.4	15.6 ± 0.7		
	Q	0 (fixed)	5.1±2.5	16±6	0 (fixed)	0 (fixed)	0 (fixed)		
B	$\nu_{max}(Hz)$	$(2.8\pm0.1)\times10^{-2}$	–	–	0.50±0.03	2.7±0.4	25.0±7.7	418/332	57.8±1.2
	rms (%)	37.5±0.3	–	–	34.4±0.4	25.9±1.0	21.2±1.4		
	Q	0 (fixed)	–	–	0 (fixed)	0 (fixed)	0 (fixed)		

Table 3.3: Best fit parameters from 7-Lorentzian model.

Set	Parameter	L_{1b}	$L_{QPO/2}$	L_{QPO}	L_{2b}	L_h	$L_{\ell ow}$	L_u	χ^2/d.o.f.
A1	$\nu_{max}(Hz)$	$(1.6\pm0.3)\times10^{-2}$	$(2.25\pm0.05)\times10^{-2}$	$(4.36\pm0.08)\times10^{-2}$	$(7.8\pm0.8)\times10^{-2}$	0.71±0.03	5.3±0.2	66.3±9.3	327/322
	rms (%)	12.8±2.1	6.5±2.1 (2.3σ)	8.3±1.6	17.8±1.7	24.0±0.2	22.3±0.2	15.6±0.4	
	Q	0.53±0.17	3.6±1.6	2.9±1.0	0.44±0.11	0 (fixed)	0 (fixed)	0 (fixed)	
A2	$\nu_{max}(Hz)$	$(1.8\pm0.4)\times10^{-2}$	$(2.19\pm0.08)\times10^{-2}$	$(3.98\pm0.05)\times10^{-2}$	$(6.5\pm0.9)\times10^{-2}$	0.63±0.03	4.3±0.3	36.7±6.9	323/322
	rms (%)	18.7±3.4	5.8±2.0 (1.8σ)	6.1±0.9	21.0±3.1	27.6±0.3	23.7±0.4	15.7±0.7	
	Q	0.3±0.1	5^{+9}_{-2}	7.8±2.5	0.3±0.1	0 (fixed)	0 (fixed)	0 (fixed)	
B	$\nu_{max}(Hz)$	$(1.8\pm0.3)\times10^{-2}$	–	–	$(5.0\pm1.3)\times10^{-2}$	0.56±0.03	3.1±0.5	27^{+12}_{-7}	403/330
	rms (%)	29.5±4.1	–	–	25.2±4.7	34.5±0.7	24.9±1.1	20.7±1.5	
	Q	0 (fixed)	–	–	0 (fixed)	0 (fixed)	0 (fixed)	0 (fixed)	

Within this function two Lorentzians are used to fit the break in the flat-top noise, L_{1b} and L_{2b} (see Sec. 3.4.2).

by the lack of power above ∼0.01 Hz in the power spectrum of the last dataset (Figure 3.4), when the AMP is back to quiescence. Quantitatively, if e.g., L_{QPO} came from the IP it had an rms amplitude of ∼27% of the IP's flux in set A1, and fell below the detection level in set C. A similar quantitative argument can be made for all variability components, as the integrated power between 0.01 and 100 Hz in set C was zero within errors. We split the energy range into four contiguous bands (channels 5–9, 10–15, 16–25, 26–71: 2.5–4 keV, 4.5–6.5 keV, 6.9–10.6 keV and 11.0–30.0 keV, respectively) and found no significant variations with energy in the strength, width or frequency of the detected QPOs or noise components. On the other hand a clear time evolution of both the QPOs and the broad-band noise is detected as shown in Fig. 3.6: the (0.01–100 Hz) fractional rms variability increased during the outburst (from 41.7 to 57.8%), while the frequencies of the QPOs and the other components decreased (from ∼0.79 to ∼0.50 Hz for L_h).

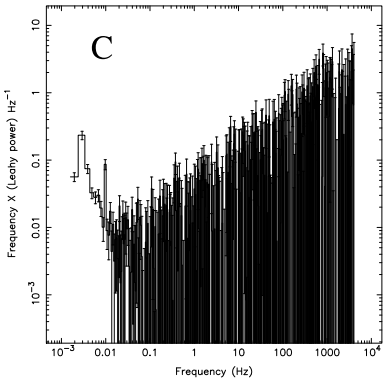

Figure 3.4: Power spectra of the background/foreground dominated set, in Power×Frequency vs. Frequency representation. The spin frequency of the white dwarf in the field of view is visible at ∼0.003Hz (312.8s), as well as its second harmonic. Both periodicities have been already detected in this system in the 0.1–2.4 keV *ROSAT* energy band (Haberl & Motch 1995; Norton et al. 1999).

3.5 Discussion

3.5.1 Exceptional island state

Our analysis of the fastest spinning AMP, IGR J00291+5934, reveals the exceptional behavior of this source in its 2004 outburst compared to the rest of NS-LMXBs: very strong X-ray variability at very low Fourier frequencies. Its

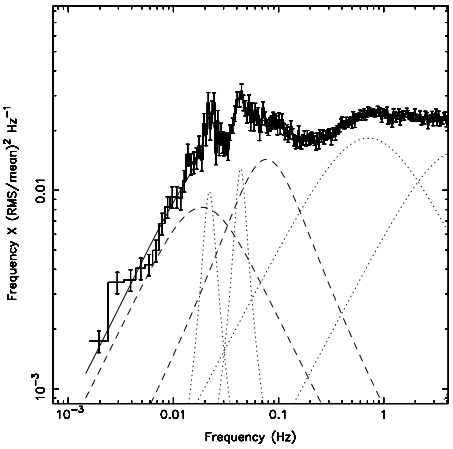

Figure 3.5: Zoom into the low-frequency part of the power spectrum of set A1, showing an alternative function which uses two broad lorentzians (dashed lines) to fit the break. See Section 3.3 for details.

power spectra showed flat-topped noise (i.e. approximately flat below a certain "break" frequency and decreasing above that) with extremely low break frequencies (∼0.04 Hz), as well as very high integrated fractional rms variability (∼50 %). These break frequencies are about two orders of magnitude lower than those observed in Z sources and about one order of magnitude lower than those previously found in extreme island (low-hard) states of atoll sources (e.g, Barret et al. 2000; Belloni et al. 2002)[4]. The measured fractional rms amplitude of the variability is the highest found so far for in a NS-LMXB. Both the break frequencies and fractional variability observed in IGR J00291+5934 are instead similar to those detected in low-hard states of BH-LMXBs (though the frequencies are low even for the lowest BH-LMXB range; see next section for a more detailed comparison). It has been noted (van Straaten et al. 2005; Linares et al. 2005) that AMPs hardly "make it to the soft state" and instead remain in (low-hard) island or extreme island states. The (2.5–25.0 keV) peak luminosity of IGR J00291+5934 (between 0.5 and 5.5 % of the Eddington luminosity according to the flux measured by Galloway et al. 2005 and the different distance estimates, see Sec. 3.2) was similar to that of other transient NS-LMXBs when they show "canonical" extreme island states, which seems to indicate that the exceptional state of our source was not purely a consequence of an exceptionally low accretion rate.

[4] A reanalysis of GS 1826–238 data in Barret et al. (2000) led to a break frequency above 0.1 Hz.

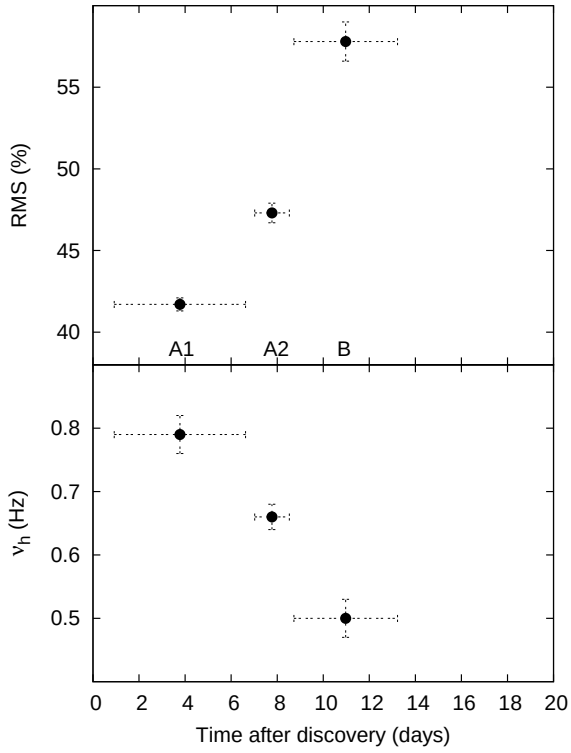

Figure 3.6: Integrated (0.01–100 Hz) fractional rms amplitude and characteristic frequency of the "hump" in the power spectra (L_h) for the three first datasets. Error bars in the X axis indicate the time interval of each dataset.

The lack of high frequency variability ($\gtrsim$100 Hz) during the outburst of IGR J00291+5934 might be related to a combination of a dynamically important magnetic field (needed in AMPs in order to produce the observed pulsations) and a fast spin (spin frequency of $\sim$600 Hz in the case of IGR J00291+5934) that could prevent the accretion disk from reaching the innermost regions, where the highest dynamical frequencies are present. This could in turn be related to the strong overall variability that we measured. If, as has been argued (e.g. Churazov et al. 2001; Gilfanov et al. 2003), the disk sets the variability frequencies and the comptonizing medium (corona, boundary layer, spreading layer, ADAF or similar) sets the variability amplitude, then a disk truncated at a large radius could provide both low dynamical frequencies and strong *fractional* variability, as its flux contribution would be

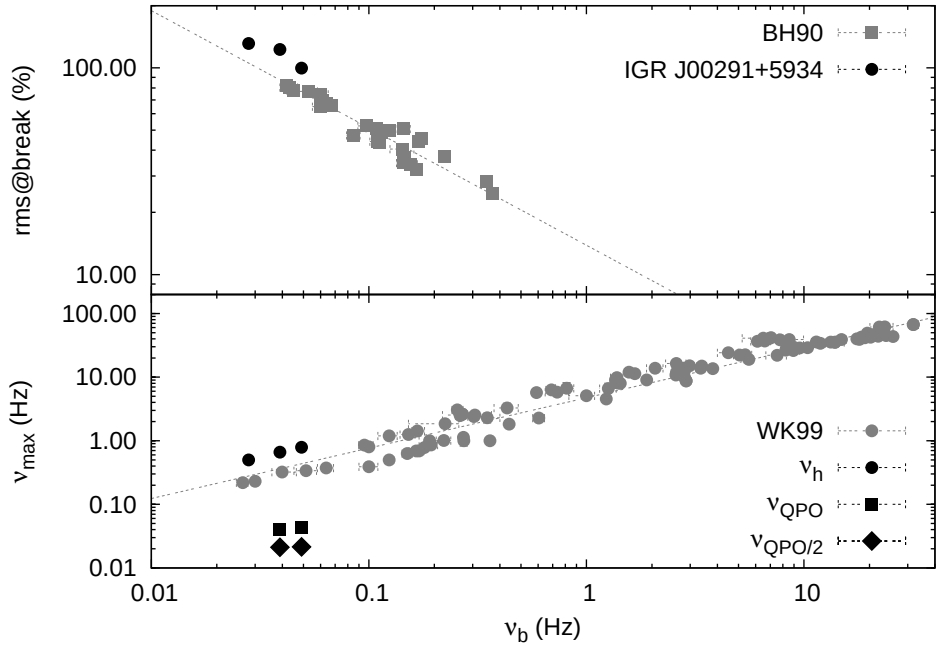

Figure 3.7: *(Top:)* Correlation between rms level at the break of the power spectra and the frequency of this break (after Belloni & Hasinger 1990, BH90: Cyg X-1, grey squares). *(Bottom:)* Correlation between the frequencies of L_b and L_h, after Wijnands & van der Klis (1999a). The lines indicate the best power law fits to the original correlations and the points that come from our work are shown in black.

relatively low and hence so would be the decrease that this flux would cause in the relative amplitude of the variability. We note, however, that in standard descriptions (e.g. Ghosh & Lamb 1978) the inner disk radius does not depend on the spin rate, and if the so-called propeller mechanism is responsible for clearing out the inner disk annulus this would be in contradiction with the reported spin-up (Falanga et al. 2005c; Burderi et al. 2005), as the expelled matter would remove angular momentum from the neutron star. The interaction between a rapidly spinning magnetized neutron star and an accretion disk is a complex problem. Most of the work so far concerns the "classical" slow X-ray pulsars (Lamb et al. 1973; Ghosh & Lamb 1978) and only recently the AMP case has received more attention (Psaltis & Chakrabarty 1999; Rappaport et al. 2004).

An anticorrelation in the flat-topped noise of Cyg X-1 was discovered by Belloni & Hasinger (1990) linking the rms level of the flat top with the break frequency: the lower the break frequency, the higher is the flat-top (in rms

normalization). In Figure 3.7 (top) we see how IGR J00291+5934 extends this relation to the lowest frequencies and the highest rms levels, even when comparing with the BH system Cyg X-1 (see Belloni et al. 2002, for an update of this correlation and comparison with other neutron star systems, which are all at frequencies >0.1 Hz, and the BH-LMXB XTE J1118+480, which is contiguous with but still at slightly higher frequecies than our NS-LMXB IGR J00291+5934).

3.5.2 IGR J00291+5934 vs. BH-LMXBs

The similarities between IGR J00291+5934 and BH-LMXBs in low-hard states are illustrated in Figure 3.8, where a power spectrum of IGR J00291+5934 is compared to one of XTE J1118+480 and one of XTE J1550–564 (e.g. Revnivtsev et al. 2000; Cui et al. 1999, respectively). The flat-top noise has very similar power, break frequency and QPOs. There are also obvious yet interesting differences: as previously noted in a study of low states of BH/NS-LMXBs the NS power spectra show more power at high frequencies ($\gtrsim$10 Hz) than the BH ones (Sunyaev & Revnivtsev 2000). In this extreme case, however, the differences between the power spectra of IGR J00291+5934 and XTE J1118+480 start at ∼0.2 Hz, where the NS power spectrum rises and the BH one starts to fall (see Fig. 3.8). The power spectrum of XTE J1550–564 has a very similar shape to that of IGR J00291+5934 and XTE J1118+480, but shifted towards higher frequency and lower rms. It also shows a prominent bump at ∼1–10 Hz (similar to what is seen in IGR J00291+5934 at slightly lower frequency) followed by a steep decline above ∼10 Hz (characteristic of BH systems; see Klein-Wolt & van der Klis 2006 for an extensive study and further discussion). In contrast to the ones studied in Sunyaev & Revnivtsev (2000) this NS-LMXB shows no significant power above ∼100 Hz.

We found two low-frequency QPOs at ∼0.02 and ∼0.04 Hz, similar to the ones seen in BH- and other NS-LMXBs in low-luminosity states (Casella et al. 2005; van Straaten et al. 2005). Their centroid frequency ratios were 2.06±0.06 and 1.91±0.06 in A1 and A2 respectively, indicating an harmonic relation. In general this kind of QPO is associated with low-luminosity states and therefore it requires a relatively low mass accretion rate in the inner regions of the disk. Several attemps have been made to investigate the nature of these low-frequency QPOs, e.g. in the context of shot-noise models (Vikhlinin et al. 1994) or thermal-viscous instabilities (Chen & Taam 1994). In any case our work shows clearly that neither the presence of a solid surface nor a magnetic field affects this phenomenon so that the same physical mechanism must be at work in NS and BH systems in order to produce this common feature: harmonically related QPOs superposed on a break in the flat-top noise at

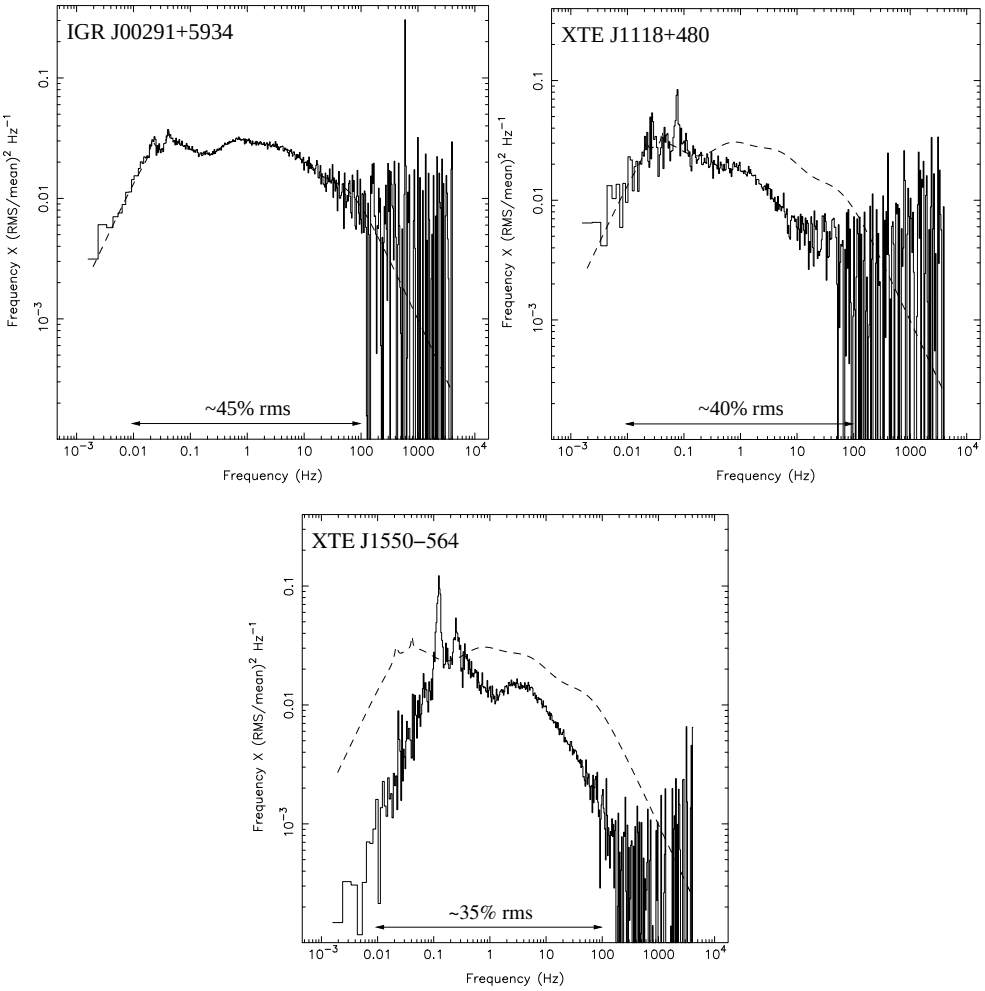

Figure 3.8: Power spectra of the accreting millisecond pulsar IGR J00291+5934 and of two black hole low-mass X-ray binaries in the low state (XTE J1118+480, Revnivtsev et al. 2000; XTE J1550–564, Cui et al. 1999). The power spectrum of IGR J00291+5934 corresponds to sets A1, A2 and B of our analysis. The energy band of XTE J1550–564's power spectrum (∼2–13 keV) is different than the one used in the other two cases (∼2.5–30 keV). The fractional rms variability (0.01–100 Hz) is shown on each plot. The mimetism between the neutron star and the black hole candidates is obvious, although there are also interesting differences (see Section 3.5.2).

very low frequencies.

Wijnands & van der Klis (1999a) found a correlation between the break frequency and the frequency of the "hump" present in the power spectra of atoll,

Z sources, black hole candidates and AMPs (L_h or sometimes an associated QPO, L_{LF}). We find that the frequency of the first zero-centered Lorentzian detected above the break in the power spectra of IGR J00291+5934 also satisfies this WK correlation (Figure 3.7, bottom) which leads us to identify it as L_h. The fact that ν_{QPO} and $\nu_{QPO/2}$ fall much below this relation (on top of the break as discussed) suggests that they are not directly related to the low frequency QPOs (L_{LF}, $L_{LF/2}$) measured sometimes on top of the "hump". Interestingly, the same happens for XTE J1118+480 and XTE J1550–564: the QPOs on top of the break fall clearly below the WK correlation, whereas L_h follows it.

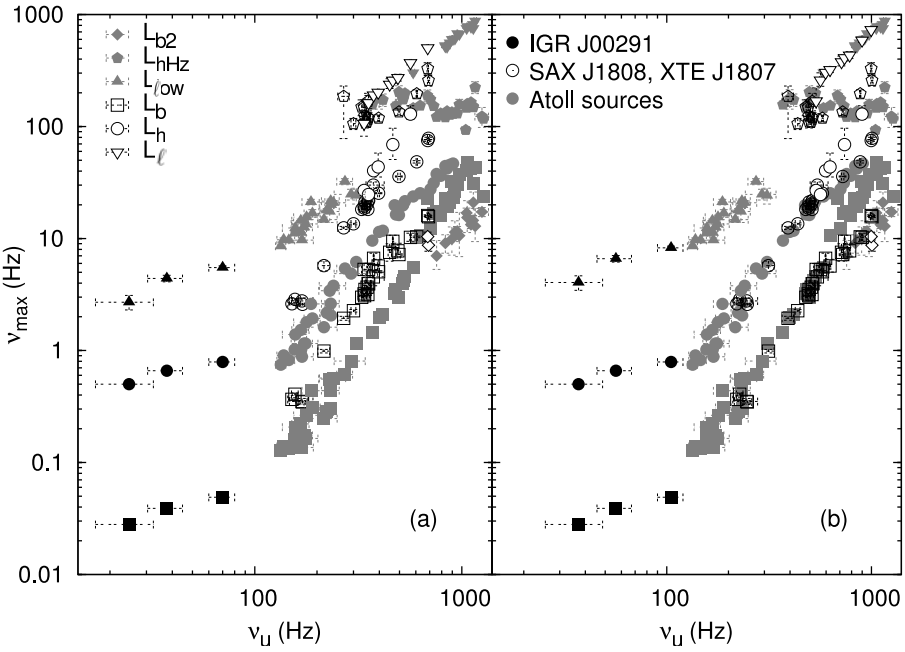

Figure 3.9: Frequency-frequency correlations in neutron star low-mass X-ray binaries. IGR J00291+5934 (black symbols at $\nu_u \lesssim 100$ Hz) is compared with two accreting millisecond pulsars showing shifts in these correlations (SAX J1808.4–3658 and XTE J1807–294, open symbols) and with non-pulsing atoll sources (grey symbols, after van Straaten et al. 2002). In a) the characteristic frequencies of power spectral components (identified by the symbols on the left) are plotted versus the frequency of the upper kilohertz QPO (or L_u). In b) ν_u and ν_ℓ of SAX J1808.4–3658 and XTE J1807–294 have been multiplied by the reported shift factors, whereas a factor of 1.5 has been used for IGR J00291+5934.

The relations between the characteristic frequencies of several variability components of Z and atoll sources and the frequency of the upper kilohertz QPO, ν_u, were studied and synthesized by van Straaten et al. (2003) (Figure 3.9). Shifts in these frequency-frequency correlations were found in two AMPs by van Straaten et al. (2005) and Linares et al. (2005, in SAX J1808.4–3658 and XTE J1807–294, respectively), in a way that was best explained by the upper and lower kHz QPOs having frequencies (ν_u, ν_ℓ) lower than the ones measured in atoll sources by a factor $\sim$1.5. The component $L_{\ell ow}$ plotted in Figure 3.9 is the broad component present below L_u (the component with the highest characteristic frequency) in extreme island states of low-luminosity atoll sources (including bursters and AMPs; van Straaten et al. 2002, 2003, 2005). We tentatively identify the two highest frequency variability components in IGR J00291+5934 as L_u and $L_{\ell ow}$, as these are the only broad variable-frequency components detected in extreme island states of NS-LMXBs above L_h, and plot the frequencies of L_b, L_h and $L_{\ell ow}$ against that of L_u (Figure 3.9a). As can clearly be seen in Figure 3.9, the frequencies of IGR J00291+5934 also vary in correlation to one another, but with slopes much less steep than those found in atoll sources and AMPs at higher frequencies. In order to compare IGR J00291+5934 with the two shifted AMPs, we multiply ν_u and $\nu_{\ell ow}$ by a trial factor of 1.5 (Figure 3.9b). The tracks traced by IGR J00291+5934 seem to connect better with the ones at higher frequencies in the shifted version of the frequency-frequency plots, but of course the difference in slopes remains. We conclude that a radical change in the slope of these correlations appears to occur at frequencies $\nu_u \lesssim$100 Hz. It is unclear at this point to what extent this is universal to LMXBs or specific to IGR J00291+5934. It will be interesting to study the behavior of our source in future outbursts to see if at $\nu_u \gtrsim$ 100Hz its components follow the usual correlations or not.

3.5.3 Mass scaling for break frequencies

This work also sheds some light on another interesting issue regarding broad-band noise in power spectra. Break frequencies are often used to estimate masses of accreting black holes with the argument that timescales in the accretion disk scale linearly with the mass of the central object and therefore the observed frequencies should scale inversely (e.g., Uttley et al. 2002). From the theoretical point of view this argument is weakened by our poor knowledge of what produces the broad-band noise and which timescale sets its break frequency (viscous, dynamical, related with the size of the disk, with shot lifetime; see e.g. Priedhorsky et al. 1979; Manmoto et al. 1996; Poutanen & Fabian 1999; Merloni et al. 2000; Churazov et al. 2001). From the observa-

tional point of view the application of this argument using break frequencies (ν_b) of the flat-top noise (L_b) observed in low-hard states of LMXBs is clearly challenged by IGR J00291+5934, as it harbors a neutron star and shows break frequencies lower than the ones observed in most of the more massive stellar-mass black holes. Although ν_b of Cyg X-1 in the low-hard state was used in the past to infer masses of super-massive black holes, recent advances in active galactic nuclei (AGN) X-ray timing indicate that most AGN are in a state similar to the high-soft state of BH-LMXBs (Uttley & McHardy 2005). Any power spectral feature that is used in such mass-scaling arguments should i) have a rather stable frequency (like perhaps the hectohertz Lorentzian in NS systems, van Straaten et al. 2002; see also Pottschmidt et al. 2003) or ii) be accurately corrected for drifts due to some parameter varying in and between systems (e.g. mass accretion rate; McHardy et al. 2004; Uttley & McHardy 2005) or a combination of i) and ii). In any case the power spectra observed in IGR J00291+5934 refute a simple mass-frequency relation for most of the variability components present in LMXBs.

Acknowledgments: We thank Phil Uttley for stimulating discussions on AGN X-ray variability. We also thank D. Altamirano, M. Klein-Wolt, M. Méndez and A. Patruno for useful discussions, and the anonymous referee for valuable comments that improved the clarity of this paper.

4 Timing and spectral properties of the accreting millisecond pulsar SWIFT J1756.9–2508

Manuel Linares, Rudy Wijnands, Michiel van der Klis, Hans Krimm, Craig B. Markwardt, Deepto Chakrabarty

The Astrophysical Journal, 2008, 677, 515

Abstract

SWIFT J1756.9–2508 is one of the few accreting millisecond pulsars (AMPs) discovered to date. We report here the results of our analysis of its aperiodic X-ray variability, as measured with the Rossi X-ray Timing Explorer during the 2007 outburst of the source. We detect strong (∼35%) flat-topped broadband noise throughout the outburst with low characteristic frequencies (∼0.1 Hz). This makes SWIFT J1756.9–2508 similar to the rest of AMPs and to other low luminosity accreting neutron stars when they are in their hard states, and enables us to classify this AMP as an atoll source in the extreme island state. We also find a hard tail in its energy spectrum extending up to 100 keV, fully consistent with such source and state classification.

4.1 Introduction

Nine years after the discovery of the first accreting millisecond pulsar (AMP), the number and variety of this type of neutron star low-mass X-ray binary (NS-LMXB) continues to grow. The idea that a neutron star could be spun up by accretion torques in the bosom of a LMXB (Alpar et al. 1982; Bhattacharya & van den Heuvel 1991) was confirmed in 1998, when the first millisecond pulses

were seen from a LMXB (Wijnands & van der Klis 1998). Besides coherent pulsations, two types of quasi-periodic millisecond X-ray variability have been seen in AMPs: twin kilohertz quasi-periodic oscillations (kHz QPOs) in SAX J1808.4–3658 and XTE J1807–294 (Wijnands et al. 2003; Linares et al. 2005) and burst oscillations also in SAX J1808.4–3658 and in XTE J1814–338 (Chakrabarty et al. 2003; Strohmayer et al. 2003). Together, these phenomena place important constraints on kHz QPO and type I X-ray burst models, offering a new insight onto accretion physics (van der Klis 2006, for a recent review). As far as low frequency variability is concerned, the fastest spinning AMP, IGR J00291+5934, showed the strongest broadband noise with the lowest characteristic frequencies observed to date in a NS-LMXB (Linares et al. 2007).

Even though AMPs have provided new input to better understand accretion onto low magnetic field NSs, important questions about their physics remain open. For instance, if the magnetic field of the neutron star in AMPs disrupts and channels the accretion flow, thereby producing the observed pulsations, it is not clear yet why the strength or configuration of such magnetic field should differ drastically from that of non-pulsating NS-LMXBs (see Cumming et al. 2001, for a possible explanation). In this context it is interesting to note that in three systems millisecond X-ray pulsations have been seen to appear in and disappear from the persistent emission, producing predominant (HETE J1900.1–2455; Galloway et al. 2007) intermittent (SAX J1748.9–2021; Altamirano et al. 2008b) or very rare (Aql X-1; Casella et al. 2008) episodes of pulsations. This implies that the AMP within them is only active or visible during a relatively small fraction of the time, which may provide a link with non-pulsating NS-LMXBs.

On June 7^{th}, 2007, a new X-ray transient was discovered (Krimm et al. 2007a) with the burst alert telescope (BAT) onboard *Swift*. Subsequent *RXTE* observations revealed that this was the eighth discovered AMP, with a pulse frequency of ∼182 Hz and an orbital period of ∼54 minutes (Markwardt et al. 2007b; Markwardt & Krimm 2007; Krimm et al. 2007b). The outburst lasted about two weeks and a possible infrared counterpart was identified (Burderi et al. 2007). No radio pulsations were found in quiescence at 8.7 and 1.4 GHz (Possenti et al. 2007; Hessels & Stappers 2007).

In the present work we analyze the aperiodic variability of the source and compare it with other AMPs and with atoll sources (a low-luminosity class of NS-LMXB, see Hasinger & van der Klis 1989). Using both PCA and HEXTE data we also measure its 2–200 keV energy spectrum. We are thereby able to classify SWIFT J1756.9–2508 as an atoll source and to characterize its accretion state.

Table 4.1: Log of the observations.

Set	ObsID	Date[a]	Detectors[b]	Count Rate [c] (c/s)	512-s PDS[d]
A	93065-01-01-02	54265.2	2.0	111.0±1.4	6
	93065-01-02-00	54266.0	2.0	102.3±3.8	16
B	93065-01-02-01	54267.0	2.0	95.3±0.9	4
	92050-01-01-01	54267.1	3.0	136.7±1.0	6
	92050-01-01-00	54267.4	1.7	75.3±21.1	24
	92050-01-01-02	54268.1	2.5	109.3±20.9	12
C	92050-01-01-03	54269.0	2.0	71.3±1.3	6
	92050-01-01-04	54269.2	2.0	68.8±4.2	5
D	92050-01-01-06	54270.2	2.0	46.0±2.2	10
	92050-01-01-07	54270.6	2.4	62.4±12.6	20
E	92050-01-01-10	54271.6	2.0	49.4±0.9	3
	92050-01-01-11	54271.8	2.0	50.0±2.2	4
	92050-01-01-12	54271.9	3.0	67.0±1.6	5
	92050-01-01-09	54271.9	1.0	20.9±0.3	5
	92050-01-01-08	54272.4	1.3	28.6±11.1	19
	92050-01-01-13	54273.0	2.0	47.4±1.2	5
	92050-01-02-00	54273.5	1.0	21.8±0.6	11

[a]Observation start date in MJD.

[b]Average number of active detectors.

[c]Average and standard deviation of the ∼2–35 keV PCA count rate, including all active detectors and not corrected for background (which we estimate from set E to be ∼22.3 c/s/PCU; see Section 4.2).

[d]Number of power density spectra extracted from the observation, each of them 512 s long.

4.2 Observations and Data Analysis

We used all pointed *RXTE* observations of SWIFT J1756.9–2508 (Table 4.1). The observations started on June 14^{th}, 2007, and were all performed with an ∼0.3° pointing offset in order to avoid contamination from the nearby (∼0.9° away) bright source GX 5-1. After applying standard screening criteria[1] we extracted energy spectra from PCA (using only PCU2) and HEXTE (using cluster B) data and power spectra from PCA data, using all active PCUs.

After checking that no strong source falls within the field of view of HEXTE-cluster B[2], we extracted source and background spectra from standard mode data. The background spectrum was obtained by averaging both rocking positions. We applied dead-time correction and created response matrices taking into account the above mentioned pointing offset.

[1]See `http://heasarc.nasa.gov/docs/xte/abc/screening.html`. A conservative filter on the time after SAA passage (>15 min) and the ELECTRON2 rate (<0.1 c/s) was applied before extracting the energy spectra.

[2]According to HEXTErock: `http://heasarc.gsfc.nasa.gov/cgi-bin/Tools/HEXTErock/HEXTErock.pl`.

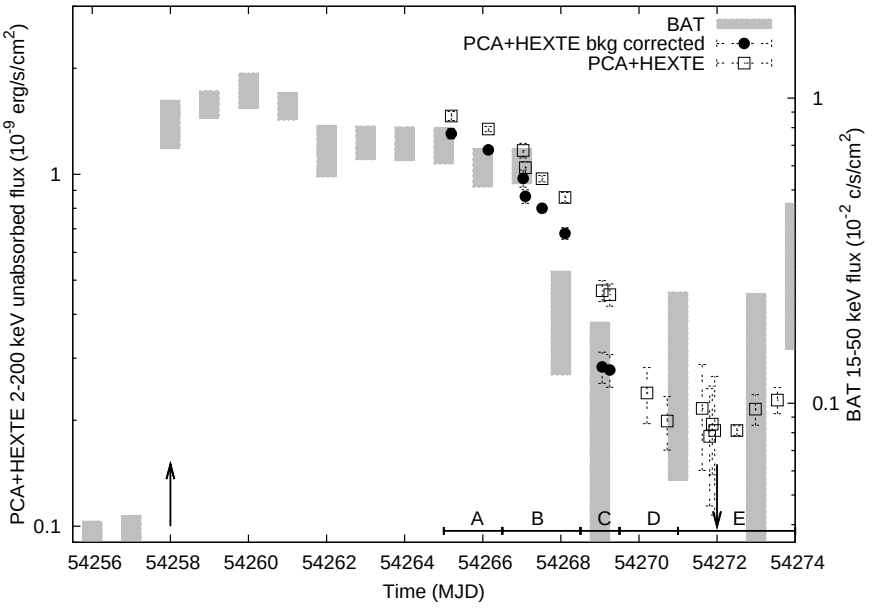

Figure 4.1: Light curve of the outburst of SWIFT J1756.9–2508, showing 2–200 keV and 15–50 keV fluxes measured with *RXTE*-PCA&HEXTE and *Swift*-BAT, respectively. Filled circles show fluxes after removing the Galactic ridge contribution (see Section 4.2 for details), while for open squares only the instrumental background was subtracted. The upward arrow indicates the discovery date (June 7^{th}, 2007; Krimm et al. 2007a) and the downward arrow the date of the first non-detection with *Swift*-XRT (June 21^{st}, 2007; Campana et al. 2007). Data sets A-E used in this work are shown with their corresponding labels along the bottom axis.

A first estimate of the PCU2 background was given by the PCA background model for faint sources. Given that the source lies in the direction of the Galactic bulge and from the observed flux in the last part of the outburst (or "tail", set E, see below) it is clear that there is additional (non-instrumental) background flux, most likely originating in the Galactic ridge (note that the source was not detected by Campana et al. 2007, with the *Swift*-XRT on June 21^{st}, within set E). The presence of an iron line at ∼6.5 keV whose energy, width and flux remained constant as the overall flux decreased also suggests that the Galactic ridge is the main source of contaminating flux. In order to take this into account and under the assumption that both instrumental and astronomical backgrounds remain constant during the observations, we obtained the average spectrum of the tail of the outburst and subtracted it from every PCU2 spectrum. This final empirical background estimation is

independent of PCA background modelling. The iron line was not present in the resulting spectra. We created response matrices for the ∼0.3° off-axis pointing.

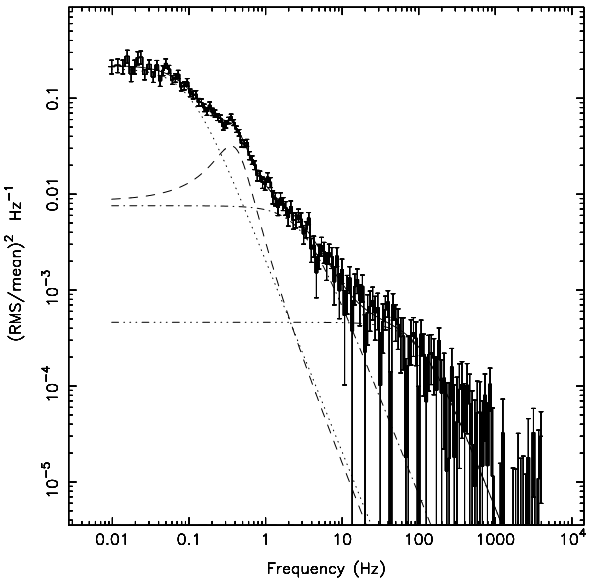

Figure 4.2: Average power spectrum of sets A and B in Power vs. Frequency representation, together with the four Lorentzians function used in the fits.

A detailed modelling of the energy spectra is beyond the scope of this paper, and probably difficult due to the faintness of the source, so we opted for the following phenomenological approach. We fitted the joint PCA+HEXTE spectra with an absorbed blackbody plus power law model using XSPEC v.11 (Arnaud 1996), allowing for a constant factor (weighted mean 0.68±0.03) to account for the difference in effective areas between PCA and HEXTE. The equivalent hydrogen column density was fixed to $5.4{\times}10^{22}$ cm^{-2}, the value measured by Krimm et al. (2007b) from the *Swift* X-ray telescope (XRT) spectrum. Figure 4.1 displays the evolution of the 2–200 keV unabsorbed flux and the BAT 15–50 keV lightcurve, showing the rise, decay, duration and peak flux of the outburst as well as the data sets used in the timing analysis (see below).

In order to study the low-frequency variability, we performed fast Fourier transforms (FFTs) on 512 s event mode data segments keeping the original 125 μs time resolution. The power spectra thereby cover the ∼0.02–4000 Hz frequency range. We used PCA channels 0 to 79 (∼2.0–35.0 keV) excluding

the highest (background-dominated) channels to increase the signal-to-noise ratio, and averaged all power spectra within each observation. No dead time nor background correction was made before the FFTs and the Poisson noise level was subtracted according to Klein-Wolt (2004) (using the Zhang et al. 1995, formula and shifting the resulting level to match the 2000–4000 Hz range, where no intrinsic power is expected). When looking for changes in frequency and power of the broadband noise (see Sec.4.3) we averaged observations successive in time and with power spectra consistent within errors in order to improve the statistics. The outburst was divided into five contiguous data sets (labeled A-E; see Table 4.1 and Figure 4.1). In set C low statistics only allows us to constrain the break frequency and the flat-top power level. In data set D the source was too faint to measure accurately its energy or power spectrum (about 2.5 c/s/PCU), and as discussed above data set E is background dominated. Power spectra were "rms-normalized" (van der Klis 1995b) using the count rate observed in set E as background count rate.

We fitted the broadband power spectra with a sum of four Lorentzians in ν_{max} representation (Belloni et al. 2002)[3], three of which were zero-centered. Following previous notation (Belloni et al. 2002; van Straaten et al. 2003; Linares et al. 2007), we call the different Lorentzians L_i and refer to their characteristic frequencies as ν_i, where the label "i" identifies the variability feature (see Section 4.3).

Table 4.2: Parameters of the 4-Lorentzian fits to sets A and B.

Parameter	L_b	L_h	$L_{\ell ow}$	L_u	χ^2/d.o.f.
Set A					
ν_{max} (Hz)	0.12±0.01	0.45±0.03	3.1±0.9	53±30	167/150
rms (%)	17.7±0.8	13.1±1.6	17.9±1.3	21±3	
Q	0 (fixed)	0.9±0.3	0 (fixed)	0 (fixed)	
Set B					
ν_{max} (Hz)	0.09±0.01	0.39±0.02	3.1±0.6	141±41	142/150
rms (%)	18.3±0.8	15.1±1.5	21.0±0.9	34±3	
Q	0 (fixed)	0.7±0.2	0 (fixed)	0 (fixed)	

See Section 4.2 for details of the fit function and notation. All errors are 1σ.

[3] $\nu_{max} = \sqrt{\nu_0^2 + \Delta^2}$ gives the characteristic frequency of the variability feature, where ν_0 is the Lorentzian's centroid frequency and Δ its HWHM. The quality factor $Q = \nu_0/2\Delta$ is a measure of the coherence of the feature. Its strength is given by the integral power (0–∞) whose square root, in the normalization we use, is the fractional rms amplitude of the variability.

Table 4.3: Parameters of the spectral fits.

ObsID	Ph.I.	P.L. norm	kT (keV)	χ^2/d.o.f.	2–200 keV unabs. Flux ($erg/s/cm^2$)
Set A					
93065-01-01-02	1.85±0.02	$(13.0\pm0.6)\times10^{-2}$	0.5±0.2	43/61	$(13.0\pm0.4)\times10^{-10}$
93065-01-02-00	1.84±0.02	$(11.0\pm0.6)\times10^{-2}$	0.7±0.1	53/61	$(11.7\pm0.2)\times10^{-10}$
Set B					
93065-01-02-01	1.92±0.04	$(11.0\pm0.9)\times10^{-2}$	0.5±0.1	59/61	$(9.7\pm0.5)\times10^{-10}$
92050-01-01-01	1.94±0.04	$(11.0\pm1.1)\times10^{-2}$	0.6±0.4	61/61	$(8.7\pm0.4)\times10^{-10}$
92050-01-01-00	1.88±0.02	$(9.6\pm0.5)\times10^{-2}$	0.6±0.1	70/61	$(8.0\pm0.2)\times10^{-10}$
92050-01-01-02	1.90±0.03	$(9.1\pm0.6)\times10^{-2}$	0.7±0.1	83/61	$(6.8\pm0.3)\times10^{-10}$
Set C					
92050-01-01-03	2.03±0.05	$(6.4\pm0.6)\times10^{-2}$	0.5±0.1	73/61	$(2.8\pm0.3)\times10^{-10}$
92050-01-01-04	1.98±0.06	$(4.7\pm0.7)\times10^{-2}$	0.4±0.2	41/61	$(2.8\pm0.3)\times10^{-10}$

NOTE.– In all fits the column density was fixed to 5.4×10^{22} cm^{-2} (Krimm et al. 2007b). The power law (P.L.) is characterized by the photon index (Ph.I.) and the normalization, which corresponds to the photon flux density at 1 keV. In five cases the B.B. normalization was not significant but in all 8 observations it gave a $2-4$ σ improvement in the fit, according to the f-test for additional terms. All errors are 1σ.

4.3 Results and Discussion

Figure 4.2 shows the broadband power spectrum of SWIFT J1756.9–2508. Its overall shape is typical of island and extreme island states (IS/EIS) of atoll sources (see e.g. Barret et al. 2000; Belloni et al. 2002), as well as similar to low (luminosity) and hard (spectrum) states of black hole X-ray binaries (e.g. XTE J1118+480; Revnivtsev et al. 2000, XTE J1550–564; Cui et al. 1999). Furthermore, the integrated (0.01–100 Hz) fractional rms variability was very high (∼35%), also characteristic of such low-hard (Comptonized) states. This allows us to classify this AMP as an atoll source, something common to all the other AMPs known to date (Wijnands 2005). The low characteristic frequencies of the variability (see below) indicate that SWIFT J1756.9–2508 was in the EIS during its 2007 outburst (see van der Klis 2006, for an overview of states).

The most prominent variability feature is a strong, band-limited and flat-topped noise component (L_b, for "break"), with a break or cutoff at a frequency ν_b∼0.1 Hz. This break frequency lies in the low frequency end of the range usually observed in NS-LMXBs. We also detect a narrower (Q∼0.8) component at higher frequencies (∼0.4 Hz). The correlations between characteristic frequencies of power spectral features are a useful tool to identify such features (Wijnands & van der Klis 1999a; Psaltis et al. 1999; van Straaten et al. 2005).

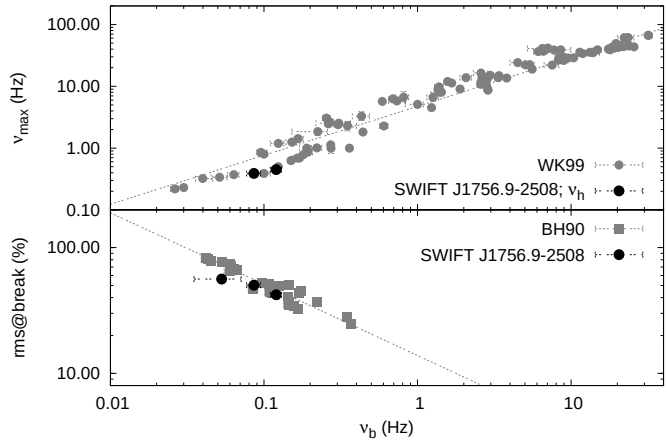

Figure 4.3: *Upper panel:* Correlation between the characteristic frequencies of L_b and L_h, after Wijnands & van der Klis (1999a) (see Belloni et al. 2002, for a discussion and extension of this correlation). *Lower panel:* Correlation between the frequency of the break in the power spectrum and the power level at the break frequency (Belloni & Hasinger 1990). SWIFT J1756.9–2508 follows both of them (see Sec. 4.3 for details).

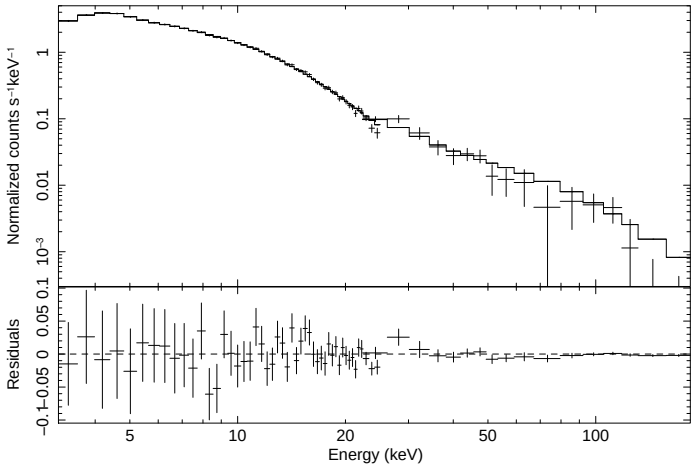

Figure 4.4: PCA+HEXTE energy spectrum of observation 93065-01-02-00, in set A, together with its fit function. Residuals are shown in the lower panel.

The narrow component at ∼0.4 Hz follows the correlation found by Wijnands & van der Klis (1999a) between ν_b and the frequency of the "hump" (L_h) present above L_b in both black hole and neutron star systems (see Figure 4.3), and we therefore identify it as L_h. The next component in order of increasing frequency has a characteristic frequency of 3.1 Hz, close to (but a bit lower than) what we would expect from extrapolating the relation between $L_{\ell ow}$ and L_b found in atoll sources (van Straaten et al. 2002, 2003). This leads us to tentatively identify it as $L_{\ell ow}$. The highest frequency component that we find in the power spectrum of SWIFT J1756.9–2508 is most likely L_u, also present in the same frequency range in IS/EIS of atoll sources. A less likely candidate is the so-called "hecto-Hertz" Lorentzian, as that component seems to be present only when the variability is at higher frequencies, with ν_b more than one order of magnitude higher (van Straaten et al. 2002). All parameters from the fits to sets A and B are shown in Table 4.2.

In disk accreting X-ray binaries as the flat-topped noise shifts down in frequency its flat top becomes higher. In other words, the rms level at the break of the power spectrum is anticorrelated with the frequency of that break. This was found by Belloni & Hasinger (1990) in Cyg X-1 and extended to other BH and NS systems by Belloni et al. (2002). SWIFT J1756.9–2508 also follows this anticorrelation, as can be clearly seen from Figure 4.3.

The broadband 2–200 keV spectra from all observations within sets A, B and C were reasonably well fitted (reduced $\chi^2 < 1.5$ for 61 degrees of freedom) with the adopted (Sec. 4.2) model (see Figure 4.4). The resulting parameters are shown in Table 4.3. A hard tail extending up to ∼100 keV was present in the energy spectra during most of the outburst, similar to island states of other atoll sources (di Salvo et al. 2004). As can be seen from Figure 4.5, the resulting power law index increases when the outburst decays. Several models have been proposed for the emission process at work in the transition from outburst to quiescence, including pulsar shock emission and thermal emission from the neutron star (Campana et al. 1998a, for a review). Our data are not sensitive enough to yield precise tests of such models, and in general sensitivity limits and time constrains make this task a difficult one.

We do not detect a significant change in the fractional rms of L_b with energy in the studied energy range, suggesting that the spectrum of this component is flat. Previous work has shown that in LMXBs the X-ray luminosity does not uniquely determine the characteristic frequencies of the variability (Ford et al. 2000; van Straaten et al. 2005; van der Klis 2006) so that another parameter must act to decouple luminosity and variability frequencies. Figure 4.5 shows that as the outburst decays and the inferred mass accretion rate drops the fractional rms variability seems to increase, whereas the frequency of the break

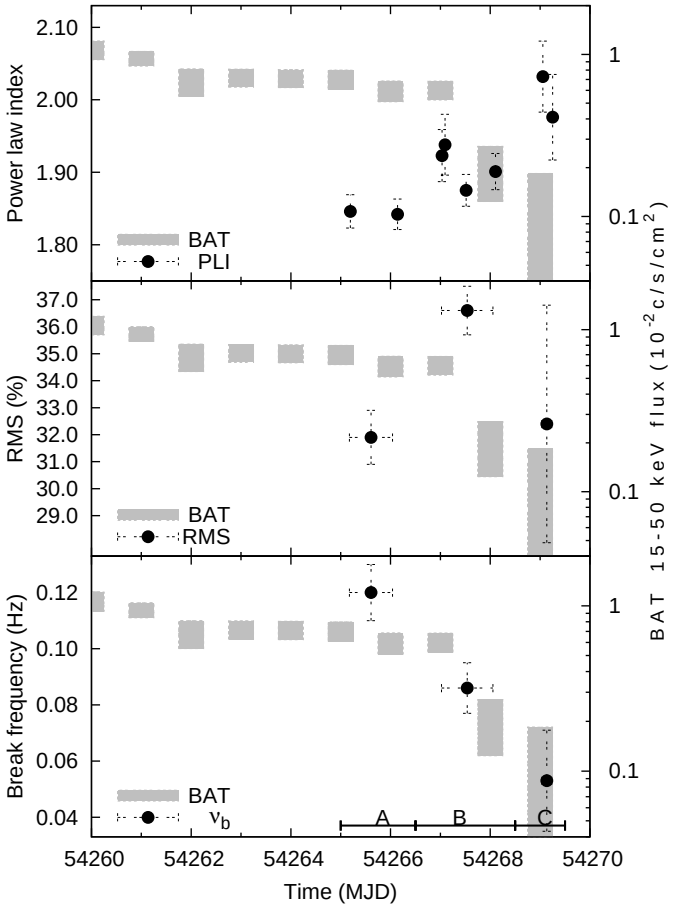

Figure 4.5: Time evolution of spectral index *(top)*, integrated (0.01–100 Hz) fractional rms *(middle)* and frequency of the break in the power spectrum *(bottom)*. The BAT light curve is shown in grey and the data sets used are indicated along the bottom axis.

decreases. The same behavior has been observed e.g. in IGR J00291+5934 (Linares et al. 2007). A successful model for broadband noise in LMXBs should explain both this short-term correlation between luminosity and break (or "cutoff") frequency and the long-term luminosity-frequency decoupling discussed above.

Acknowledgments:
Swift-BAT transient monitor results provided by the *Swift*-BAT team (`http://swift.gsfc.nasa.gov/docs/swift/results/transients/`).

Part II

Accretion states and luminosity of neutron star low-mass X-ray binaries

How many legs does a dog have if you call the tail a leg?
Four; calling a tail a leg doesn't make it a leg.

Abraham Lincoln (1809-1865)

5 Accretion states of neutron stars: luminosity, variability and spectra of atoll sources.

Manuel Linares and Michiel van der Klis

The Astrophysical Journal, 2009, submitted

Abstract

The X-ray spectrum of neutron stars that accrete from low-mass companions varies on a wide range of timescales. We study in this work the most numerous class of neutron star low-mass X-ray binaries, the so-called atoll sources. Using more than a decade of *Rossi X-ray Timing Explorer* data, we perform a systematic study of the luminosity, timing and spectral properties of nine atoll sources across different source states. We include the hard X-ray emission in our spectral fits in order to obtain broadband luminosities. We measure the cutoff of the flat-topped variability spectrum over more than two decades in frequency, as well as the frequencies of the kilohertz quasi-periodic oscillations. We show that soft states can have luminosities as low as 1% of the Eddington luminosity, while the luminosity of hard states can be as high as 15% Eddington. State transitions, which feature large changes in variability frequencies, occur at fairly constant luminosities within each of the studied sources. Nevertheless, the state transition luminosity can be different in a given source at different epochs, and differs by more than one order of magnitude among different systems. The transient systems within our sample can mimic the canonical behavior of black hole transients during an outburst. However, we show that contrary to black holes they can transit from the hard to the soft state at luminosities lower than those of the soft to hard transition.

By comparing the spectral and timing properties in each source we find an anticorrelation between the hardness of the X-ray spectrum and the variability frequencies. Furthermore, we show that for constant variability frequency, luminosity and hardness are positively correlated across different sources. This luminosity-hardness correlation is clearly at odds with the common perception that harder sources are less luminous, and holds for luminosities between 0.5% and 30% Eddington. We put these new results in the context of models of accretion flows around compact objects, and propose an explanation for the luminosity-frequency decoupling and the luminosity-hardness correlation that involves changes in the inner disk temperature.

5.1 Introduction

Low-mass X-ray binaries (LMXBs), the most numerous class of bright X-ray sources, are powered by accretion from a low-mass donor star onto a neutron star (NS) or a black hole (BH). Mass is transferred through Roche lobe overflow and forms an accretion disk (Pringle & Rees 1972; Shakura & Syunyaev 1973) that often extends down to deep in the gravitational potential well, a few Schwarzschild radii from the center. Other forms of accretion flow are known to exist in LMXBs, and are essential to interpret those observations that show only traces of the predicted thermal emission from the accretion disk. Their structure and radiative properties are still a matter of debate (Narayan 1996; Blandford & Begelman 1999; Falcke et al. 2004) yet it is generally agreed that Compton up-scattering of thermal photons contributes considerably to the emerging spectrum.

Twenty years ago Hasinger & van der Klis (1989) found two classes of NS LMXBs when studying the correlation between their X-ray spectra and variability: "Z" and "atoll" sources. Named after the shapes they trace out in color-color diagrams (Sec. 5.2), these two classes differ in their luminosity; near the Eddington limit [1] (at luminosity L_{Edd}) in Z sources and below $\sim$50 % L_{Edd} in atolls. Moreover, atoll sources can show harder X-ray spectra, which usually change on longer timescales than in Z sources. Three exceptional systems have exhibited both Z and atoll source behavior (Cir X-1, Oosterbroek et al. 1995; XTE J1806–246, Wijnands & van der Klis 1999b and most recently XTE J1701–462, Homan et al. 2007) suggesting that mass accretion rate, $\dot{M}$,

[1] The Eddington luminosity depends among other parameters on the composition of the accreting matter (Lewin et al. 1993). For a $1.4 M_{\odot}$ NS, at a gravitational redshift of $1 + z = 1.31$, $L_{Edd} = 1.6(2.7) \times 10^{38}$ erg s^{-1} for solar composition (pure helium). While keeping in mind that the nature and composition of the donor star are uncertain in many LMXBs, we use throughout this paper a value of 2.5×10^{38} erg s^{-1}.

is the main parameter that sets the different behaviors of Z and atoll sources. The fundamental question remains, however, of which processes make Z and atoll sources different and how precisely their differences arise.

Atoll sources show multiple X-ray variability components in their power spectra, ranging from millisecond to kilosecond timescales, which change in strength and frequency whithin every studied source, giving rise to different *timing states*. Kilohertz quasi-periodic oscillations (kHz QPOs), present in both Z and atoll sources, produce the fastest luminosity variations in accreting systems and have received wide attention since they were discovered (van der Klis et al. 1996; Strohmayer et al. 1996a). Several broad and peaked components are present at lower frequencies, between millihertz and several hundred Hertz. In a way analogous to BH X-ray binaries, the energy spectra of atoll sources can be classified into three broad classes or *spectral states*: hard states, soft states and intermediate states (Sec. 5.3 for more details and the relation with the traditional "banana" and "island" terminology). Since the first studies of X-ray spectra and variability of NS-LMXBs (Hasinger & van der Klis 1989) some timing properties (such as the frequency, strength or mere presence of certain variability components) have been found to correlate with spectral indicators (such as colors or hardness ratios, Sec. 5.2.2), suggesting that spectral and timing states are intimately related.

The X-ray luminosity of transient and persistent atoll sources varies considerably on timescales longer than about one day. The role of luminosity in setting (or being set by) the spectral and variability properties outlined above (i.e. the precise relation between timing/spectral states and luminosity) has remained elusive during the last two decades. For instance, although in a given source the kHz QPO frequency correlates with X-ray intensity (or count rate) within less than $\sim$1 hr (Strohmayer et al. 1996b), these two quantities are not correlated on longer timescales Ford et al. (1997); Méndez et al. (1999). This is known as the *parallel track* phenomenon, as the combination of short time scale correlation, observational windowing and long term lack of correlation gives rise to parallel lines in a frequency versus intensity diagram. Ford et al. (2000) showed that in different sources kHz QPOs can have the same frequencies at 2–50 keV luminosities that differ by more than two orders of magnitude. This creates patterns in a frequency versus luminosity diagram reminiscent of (but covering a much wider range in luminosity than) the parallel lines from a single source. The physical origin of both phenomena may or may not be the same. It should be noted that Méndez et al. (1999) and Ford et al. (2000) used the 2–16 keV and 2–50 keV energy ranges in their works, respectively, and therefore could not discard the possibility that a variable and sizable fraction of the bolometric flux was being radiated outside that energy band. More re-

cently, Gladstone et al. (2007) analyzed the ∼2–50 keV spectra of a sample of atoll sources and suggested that these show two types of spectral transitions, one that follows a vertical track on a color-color diagram and occurs at 2% of the Eddington luminosity and a diagonal one at 10% Eddington. By studying two transient atoll sources Lin et al. (2007), proposed a hybrid spectral model to explain the emission in different states, and discussed the implications for $\dot{M}$ and the radiative efficiency in the hard state.

During more than a decade the *Rossi X-ray Timing Explorer (RXTE)* has accumulated a wealth of data from many LMXBs. The broad band spectral coverage (from ∼2 to 200 keV) together with the unprecedented range of variability timescales accessible to *RXTE* (∼10 yr to ∼1μs) make this a unique dataset to study accretion physics in LMXBs. Using these data we performed a systematic and homogeneous analysis of the luminosity, timing and spectral properties of a sample of atoll sources in order to investigate the relations between these properties. We find that, while the broadband luminosity and the variability frequencies are decoupled on timescales longer than one week, the hardness of the energy spectrum is in one-to-one correspondence with the variability frequencies in each source, which shows up as a global anticorrelation between spectral hardness and variability frequencies that breaks down in both soft and hard states. Furthermore, we find a positive correlation between luminosity and spectral hardness at given variability frequency. We present these results in Section 5.3 and discuss the main implications of this work in Section 5.4. Section 5.2 and Appendix A describe our analysis method.

5.2 Observations and Data Analysis

5.2.1 Atoll sources

With the main goal of investigating how spectral and timing states relate to luminosity, we compiled a sample of atoll sources that satisfy the following requirements: i) they present different states, as witnessed by previous work; ii) they have been extensively observed with *RXTE*, allowing a detailed study of their properties in the different states and state transitions, iii) their distance is well constrained and therefore a good estimate of their bolometric luminosity is achievable and iv) together they cover a wide range in luminosity. This yielded a total of nine sources. We used all *RXTE* pointed observations, taken over more than a decade, that were publicly available at the start of this project. We list the sources that form our sample in Table A.1, together with a summary of their properties and the *RXTE* datasets used in this work.

5.2.2 Spectral analysis and bolometric luminosity

We extracted the Crab normalized and dead time corrected count rate (intensity) in the 2.0–16.0 keV energy band, in 16 s bins. We searched for type I X-ray bursts and instrumental spikes or dropouts in the resulting 16 s lightcurves and excluded these events from the subsequent spectral and timing analysis. In order to obtain a model independent measurement of the spectral properties we calculated colors (hardness ratios) using four contiguous energy bands, in 16 s steps and then averaged per observation. We refer to Appendix A.1 for a detailed description. The soft color (SC) gives a model independent (but n_H dependent) measurement of the average spectral slope in the 2.0–6.0 keV range. The hard color (HC) gives a model independent (and n_H independent, for the relatively low absorption to the sources in our sample) measurement of the spectral index in the 6.0–16.0 keV energy range. We refer to the HC herein as "spectral hardness" or "hardness". We constructed color-color diagrams (CDs) to study the spectral evolution of each source and following previous work (Hertz et al. 1992; Kuulkers et al. 1994; Homan et al. 2002) we measured the position along the atoll tracks displayed on the CDs with the parameter S_a. To do so we projected every data point onto a spline drawn along the atoll track and defined a hard vertex ($S_a \equiv 1$) and a soft vertex ($S_a \equiv 2$), so that soft and hard states have $S_a > 2$ and $S_a < 1$, respectively (see Fig. 5.1 for the precise location of the vertices). By means of this method we can characterize the spectral state or position in the CD with a single parameter and compare it among the sample of sources.

We performed simultaneous fits of background and deadtime corrected PCA and HEXTE energy spectra (Appendix A.1 and A.2 for details of extraction) of each observation using XSPEC (Arnaud 1996, Version 11.3.2). We included the 3–25 keV range from the PCA spectra and the 20–200 keV range from the HEXTE spectra (to avoid in both instruments the lowest and highest energy channels, which are ill-calibrated and background-dominated, respectively). We included a multiplicative constant in the model and allowed it to vary when fitting the HEXTE spectra to account for the relative error in the effective areas of PCA and HEXTE. We obtain thereby fluxes referred to the PCA. In all cases we fix the equivalent hydrogen column density to the values reported in the literature (listed in Table A.1), as the energy range of the PCA is not well suited for constraining the absorption. Following a similar approach to that of Lin et al. (2007) we use a spectral model consisting of two thermal components (bb and diskbb) and a power law. The hard states of 1608 and 1705 did not require two thermal components so we use a simple diskbb + power law model to fit their spectra. From the best fit model we obtained the unabsorbed flux in the 2–200 keV energy band and calculated the

luminosity using the most reliable and up to date distance measurements (see Table A.1 and references therein). Given the large uncertainties that would be introduced by extrapolating the spectral model below the PCA energy band, our 2–200 keV luminosity is the most robust estimate of the bolometric luminosity that can be obtained from *RXTE* data. We tried a more physical model for the hard X-ray emission (comptt, which describes Comptonization of soft photons in a hot plasma) and verified that the fluxes thereby obtained are consistent within the errors with those of our adopted model. We stress that we perform these spectral fits with only the aim of estimating the luminosity and not to study details of spectral formation in our sources. For details of the spectral decompositions in atoll sources we refer to the recent works of Done et al. (2007); Lin et al. (2007). We finally stress that given the systematic uncertainty on the distance measurements (typically ∼15% for those derived from type I X-ray bursts; see Table A.1 and references therein) the typical fractional systematic uncertainty on the luminosity is ∼30%.

5.2.3 Timing analysis

We performed Fourier transforms on 256 s-long data segments using high time resolution PCA light curves including all energies below ∼ 35 keV. We thereby access variability frequencies in the range ∼4 mHz–4 kHz. We rms-normalized the resulting power spectra and subtracted the Poisson noise contribution (see App. A.1 for details). After inspecting by eye all the power spectra, we measured the following parameters from the power spectra (as discussed further below) in order to characterize the timing state of the sources in each observation: i) break frequency of the flat-topped noise, ii) frequency of the upper kHz QPO, iii) slope of the very low frequency noise and iv) fractional rms amplitude of the variability integrated in two frequency bands: 0.01–1 Hz and 1–100 Hz.

In those observations where flat-topped broadband noise is present we fitted a broken power law model to the power spectrum in order to measure the cutoff or *break frequency*, ν_b, of the flat-topped noise, fixing the pre-break slope to zero (see Fig. 5.2 for an overview). We added one or two Lorentzians to the fit model to account for other variability components often present at frequencies higher than ν_b (L_h and $L_{\ell ow}$, where L stands for Lorentzian, "h" for hump and "ℓow" for low-frequency; see van Straaten et al. 2002, 2005 for details). When fitting the flat-topped noise we used a variable frequency range to accomodate the changes in ν_b, including only the relevant ∼1 to ∼2 decades in frequency around the break. Table A.2 shows the number of observations of each source where we were able to measure ν_b using this method.

We searched for kHz QPOs in the 300–1300 Hz frequency range of all obser-

vations taken when the sources were in soft or transitional states (banana or island states) and we used a simple or double Lorentzian fit function to obtain their frequency. kHz QPOs are known to change their frequency on timescales much shorter than the typical time span of one *RXTE* observation (e.g. Berger et al. 1996; Ford et al. 1997; Paltani et al. 2004). Therefore this method yields an average value of the QPO frequency during the observation, which is suited to our goal of characterizing the timing state of the source. In the observations where we detected two kHz QPOs we readily identified the higher frequency component with the upper kHz QPO and the lower frequency component with the lower kHz QPO. Based on the relation between their frequencies (ν_u and ν_ℓ for the upper and lower kHz QPO, respectively) and the spectral hardness (as traced by the HC; see Sec. 5.2.2 and Fig. 5.3) we were able to identify the large majority of the kHz QPOs detected as single peaks. The number of ν_u measurements obtained from twin and single kHz QPO detections is shown in Table A.2.

We searched all the observations taken in the soft state for red noise at the lowest frequencies (often called very low frequency noise, VLFN). We fitted a simple power law in the 0.01–1 Hz frequency range and obtained thereby the VLFN index (slope of the best fit power law). The fit results are somewhat sensitive to the presence of variability components at the high end of the frequency range spanned by the VLFN (i.e. between 0.1 and 1 Hz; see e.g. Reerink 2005). Only in five observations we detected simultaneously VLFN and flat-topped noise, which in those cases had $\nu_b \gtrsim 30$ Hz, i.e., near the maximum observed break frequency. To get a model independent measure of the variability present in all the states we calculated the fractional rms amplitude of the variability in two frequency bands: 0.01–1 Hz (r_L), and 1–100 Hz (r_H). We constructed rms-rms diagrams using r_H and r_L and, in direct analogy with CDs (Sec. 5.2.2), we measured the position along the resulting tracks projecting each point onto a spline. Using these various measurements we characterized the timing state of each of the sources for each observation. This characterization is robust: it uses variability components that can be unambiguously identified (flat-topped noise, upper kHz QPO and red noise) and model independent measurements of the strength of the variability (r_L and r_H).

5.3 Results

Based on our systematic analysis of luminosity, spectral and timing properties of atoll sources and on the results that will be presented in this Section, we divide the accretion states of atoll sources into three main classes: soft states,

hard states and intermediate states. These three classes are named after the average slope of the hard X-ray spectrum (Sec. 5.2.2) but, as shown by previous work (Hasinger & van der Klis 1989; van Straaten et al. 2000) and detailed hereafter, they also differentiate the timing state of the sources. However, as explained in Secs. 5.3.2 and 5.3.3, the relation between spectral/timing states and luminosity is not one-to-one. Soft states (S_a>2) and hard states (S_a<1) are frequently called in the literature "banana" states and "extreme island" states, respectively. Intermediate states were originally named "island" states due to their patchiness in CDs, which (as already noted by Hasinger & van der Klis 1989) was partly due to observational windowing. The transient sources in our sample show rapid (within a few days) state transitions during which their spectral and timing properties are like those of the persistent sources in the intermediate state. Together with the typical *RXTE* sampling (daily observations in the best case but more sparse in most cases), this results in sparsely populated intermediate state branches in the transient systems. On the contrary, some of the persistent sources are in intermediate states most of the time, which results in densely populated intermediate state branches (Sec. 5.3.2). We refer alternatively to these states (1<S_a<2) as transitional or intermediate state.

5.3.1 Variability and spectra

A summary of our correlated spectral and timing analysis is presented in Figure 5.1, which shows color-color diagrams (CDs) of all the studied sources. The observations where we detect flat-topped broadband noise, an upper kHz QPO or VLFN in the power spectrum are highlighted in each CD in green, blue and red, respectively. One can readily see the regions of the CD where each of these variability components is present. Namely, flat-topped noise (green) appears in hard and intermediate (extreme island and island) states, kHz QPOs (blue) are present in intermediate and soft states (only in soft states with relatively low SC, in the region of the CD called "lower-left banana") and the VLFN (red) dominates the power spectra of most soft state observations. Table A.2 shows the total number of detections of these three variability components in each source, as well as the observed range of variability frequencies. In all nine sources we measure values of the VLFN index between ∼0.8 and ∼3, and find no correlation with luminosity, SC or HC, so we do not consider this quantity further in this analysis.

By comparing the results of our timing and spectral analysis we find a *frequency-hardness anticorrelation within individual sources*. The break frequency of the flat-topped noise, ν_b, anticorrelates with the HC over nearly three orders of magnitude in frequency (Figure 5.2; Figure 5.4, top right).

The frequencies of both the upper and lower kHz QPOs, ν_u and ν_ℓ, also anticorrelate with the HC (Fig. 5.3 and bottom right panel of Fig. 5.4). Of course, ν_u and ν_ℓ follow different tracks in a frequency-hardness diagram (as shown by Fig. 5.3), which in practically all cases allows us to identify the upper kHz QPO in those observations where the lower kHz QPO is not detected (Sec. 5.2.3). The steepness of the ν_b-HC tracks increases at the highest HC values ($\sim$1.1; i.e. when the sources reach the hard or extreme island state). For the kHz QPOs we find instead a steepening of the ν_u-HC and ν_ℓ-HC anticorrelations when the sources reach the soft state (Fig. 5.3, which also shows a steepening of the ν_u-HC relation towards the hard state in some of the sources). We also find that the highest (ν_u) and the lowest (ν_b) characteristic frequencies of the rapid X-ray variability are correlated with each other, as witnessed by previous work based mostly on averages of several observations (van Straaten et al. 2005; Linares et al. 2005; Altamirano et al. 2005) and as expected if both frequencies are anticorrelated with the spectral hardness. The overall strength of the variability, measured by its fractional rms amplitude, decreases gradually within each source as the spectral hardness decreases. This can be clearly seen in Figure 5.5, which displays the integrated 1–100 Hz rms fractional variability for each point of the CD. When looking at the full sample, however, we find that different values of the fractional rms amplitude occur at the same spectral hardness (e.g. between 10% and 25% for HC $\simeq$0.9).

5.3.2 Luminosity and spectra

Active atoll sources feature broadband (2–200 keV) luminosities in the range 0.1–50% L_{Edd} (3×10^{35}–1×10^{38} erg s^{-1}). Figure 5.6 shows hardness-luminosity diagrams (HLDs) for all nine sources. The two transient systems, 1608 and Aql, show a similar luminosity range during their outbursts, with maximum[2] luminosities of $\sim$20% L_{Edd} and $\sim$30% L_{Edd}, respectively, and cover almost the entire luminosity range of the full sample of sources (luminosity ranges are shown in Table A.2). The HC is independent of the interstellar absorption and traces clearly the changes in spectral state. Three systems (1608, Aql and 1705) show a bimodal distribution in HC, i.e., they are most of the time in the soft state or in the hard state. The luminosity of 1705 varies by more than an order of magnitude (between $\sim$1% and $\sim$40 % L_{Edd}), which adds to the similarities between 1705 and the two transient systems. Two systems (0614 and 1728) are anchored in the intermediate state, and they maintain roughly

[2]As witnessed by previous work based on deeper observations (Campana et al. 1998b; Jonker et al. 2003; Linares et al. 2008a), the luminosity of the transients drops to $\sim 10^{35}$–10^{34} erg s^{-1} after such episodes of intense accretion, and decays to 10^{33}–10^{32} erg s^{-1} in quiescence (van Paradijs et al. 1987; Wijnands et al. 2004; Cackett et al. 2006).

constant luminosities that differ by one order of magnitude (∼0.8% and ∼8 % L_{Edd} for 0614 and 1728, respectively). Figure 5.6 also shows that 1636 moves (in a quasi-regular cycle, see Belloni et al. 2007 and references therein) along two branches in the HLD: an intermediate state branch produced by changes in its spectral hardness and a soft state branch mainly due to luminosity changes. The remaining three systems (1820, 1735 and GX 3+1) are predominantly in soft states, although 1820 has visited the intermediate and hard states on a few occasions (Bloser et al. 2000; Altamirano et al. 2005). We note that the soft state branches clearly defined in at least five of the nine sources (Fig. 5.6), while relatively constant in HC in a given source, span a wide range in spectral hardness across sources, with HC values between ∼0.5 and ∼0.8. On the other hand the hard state branches, traced out clearly by 1608, Aql and 1705, have a similar value of HC=1.1±0.1. Our work also shows that hard states can be as luminous as ∼15% L_{Edd} and hence the term "low-hard state", often used in the literature and inspired by the relatively low count rates observed in the soft X-ray band during hard states, can be misleading. It is also worth noting that the intermediate state forms a nearly vertical track in all the studied systems, indicating that the broadband luminosity remains approximately constant when the sources transit between the soft and the hard state, or vice versa. However, the SC increases in the intermediate states when going from soft to hard states, with the exception of only 0614. Figure 5.6 also shows that the intermediate state luminosity (i.e., the location of the vertical track) in different systems differs by more than one order of magnitude, from ∼0.5 to ∼14 % L_{Edd} (a much wider range than was previously thought; e.g. Maccarone 2003). The reported distance uncertainties for the two systems at the high and low end of this luminosity range are ∼15% (Table A.1) and can not account for the large dispersion in intermediate state luminosity. This implies that the wide range in intermediate state luminosity of different sources is most likely produced by an intrinsic parameter that differs between sources, as already suggested by Ford et al. (2000) (See Sec. 5.4.3).

In Figure 5.7 we show the broadband luminosity of each source throughout its CD. In the case of 1608, Aql X-1 and 1705, the most luminous hard states present luminosities as high as *or higher than* the least luminous soft states. The two transients, 1608 and Aql, feature underluminous regions in the bottom-left part of the soft state branch (i.e. in the lower left banana) compared to the rest of that branch. As explained in Section 5.2, we determine the spectral state with a single parameter, S_a, which measures the position along the atoll track (from $S_a<1$ in hard to $S_a>2$ in soft states; Fig. 5.1) and allows a direct comparison between sources. Figure 5.9 shows the relation between the broadband luminosity and S_a. A correlation between S_a and luminosity is

visible in soft and hard states (except in the soft state of 1728 and GX 3+1). During intermediate or transitional states, however, S_a and luminosity are in general not correlated (see also Galloway et al. 2008b). Interestingly, even though these two parameters are widely used in the literature as tracers of $\dot{M}$, this lack of correlation implies that in intermediate states $\dot{M}$ is not simply related to both S_a and luminosity (further discussion in Sec. 5.4.1).

5.3.3 Luminosity and variability

As explained in Section 5.3.4, detailed analysis of individual outbursts of the transient atoll sources reveals correlations on timescales shorter than about one week between broadband luminosity and break frequency. In order to search the full sample for longer timescale correlations, we split our measurements into consecutive seven days intervals (when available). We found no strong correlation between frequencies and luminosity in the resulting intervals. We repeated the same procedure using continuous series of observations (defined as having gaps between observations of less than two days), and again found no obvious ν-L correlations.

The rms-rms diagrams displayed in Figure 5.8 show the evolution of the power spectrum as its characteristic frequencies change. We can distinguish two branches: i) a "steady" branch where r_L is low and approximately constant ($r_L \lesssim 5\%$) while r_H increases from a few percent to $\sim$10–15% and ii) a "variable" branch where r_H has reached a high ($\sim$20–25%) and roughly constant value while r_L increases. The steady branch corresponds to high characteristic variability frequencies and soft spectra whereas the variable branch corresponds to low frequencies and hard states. As can be clearly seen from the color scale in Figure 5.8, and in direct analogy with the spectral states shown in the CDs (Fig. 5.7), the same timing states can occur at very different luminosities. The relations between the characteristic variability frequencies, ν_u and ν_b, and the fractional amplitude of the variability are shown in Figure 5.10. In general these two measures of the X-ray variability are anticorrelated, in agreement with the well known power decay towards high frequencies (and soft states). We find, however, that this anticorrelation breaks down for 1820, 1735 and 1636 at the highest upper kHz QPO frequencies (Fig. 5.10, bottom panels; see also Sec. 5.4.3). The case of 1820 is of particular interest as it features a correlation between ν_u and both r_L and r_H when $\nu \gtrsim 1000$Hz, where all other sources (with the possible exception of 1735) show an anticorrelation. This increase of variability amplitude when ν_u reaches its highest values is due to the appearance in 1820 and 1735 of a strong "peaked noise" component at a few tens of Hz. This component is reminiscent of the flaring branch oscillation observed in Z sources and it arises in the two highest luminosity sources

within our sample, which suggests a link between the soft states of the highest luminosity atoll sources and Z sources.

In Figure 5.4 (left) we show the values of ν_b and ν_u plotted versus the luminosity. Clearly, in the whole dataset variability frequencies and luminosity are not correlated, neither within a single source nor across different sources. Three sources, 1608, Aql X-1 and 1705, present a similar feature in the ν_b-luminosity diagram (Fig. 5.4, top left): when ν_b<1Hz their maximum luminosity is correlated with ν_b (showing up as a lower-right envelope in their ν_b-luminosity diagrams). This constitutes another similarity between 1705 and the two transient systems (Sec. 5.3.2). Summarizing, although spectral hardness and variability frequencies are in one-to-one correspondence within each individual source, the same hardness-frequency pairs can occur at luminosities that differ up to one (for a given source) or two (across different sources) orders of magnitude (Fig. 5.4; Sec. 5.3.1). We stress that similar shifts between sources are observed in a frequency-[2–50 keV]-luminosity diagram and in a frequency-[2–200 keV]-luminosity diagram (Ford et al. 2000; this work). We therefore conclude that it is not just the energy radiated in the hard X-ray band (50–200 keV) that "decouples" the variability frequencies and luminosity (Sec. 5.4.3).

Even though the mutual relations between spectral hardness, variability frequencies and luminosity appear complex when considering the ensemble of systems and states, we have discovered a very systematic aspect to these relations that was not yet known. In Figure 5.4 (right) the frequency-hardness tracks subtended by different sources are offset from one another. Looking now at the left panels of Figure 5.4 one can see that the frequency-luminosity tracks are also offset, and in the same order as in the right panels. These systematic differences between sources lead to a strikingly simple relation between luminosity and spectral hardness at a given timing state, in the form of a positive *luminosity-hardness correlation across different sources*. We select observations with ν_u∼1000 Hz and show their luminosity versus spectral hardness in Figure 5.11. The luminosity-hardness relation of all observations with ν_b∼30 Hz is also shown. In both cases luminosity and hardness are clearly correlated over nearly two orders of magnitude in luminosity. The frequencies thereby selected are in the high end of both ν_b and ν_u ranges and correspond to $1.8 \lesssim S_a \lesssim 2.2$, i.e., to the "lower-left banana". A similar luminosity-hardness correlation is present when selecting lower variability frequencies, somewhat less strong but still significant. We show this by plotting in Figure 5.11 luminosity versus hardness for those observations with ν_u∼500 Hz and those with ν_b∼1 Hz. This correlation is therefore strongest in soft, thermal dominated states where variability timescales are short, but occurs in all states where

variability frequencies can be measured.

5.3.4 Time evolution

To illustrate how the broadband luminosity, the spectral properties and the variability change during the course of an outburst, we show in Figures 5.12 and 5.13 a detailed view of these quantities along two outbursts of the two transient systems studied herein (1608 and Aql X-1). Figure 5.12 (left) shows the luminosity, colors, characteristic frequencies and fractional rms variability of the 2002 outburst of 1608. The source started in the hard state as can be seen from the values of the HC, then transited to the soft state while it was not being observed by *RXTE* and started a smooth luminosity decline. Around MJD 52540 a series of five state transitions started that lasted about 20 days, until the source went back to quiescence. The break frequency during the initial hard state tracks the luminosity changes (the corresponding track in the frequency-luminosity plane can be seen in blue in the upper part of Figure 5.12). All the observed transitions in this outburst occur at a similar luminosity of ∼0.4–0.5 % L_{Edd}. In the 2005 outburst (Fig. 5.12, right) instead all transitions occur at higher luminosity, the two soft-to-hard transitions (S→H) occur around 1% L_{Edd} and the H→S ones at a still higher luminosity of ∼3% L_{Edd}. It is also interesting to note that the H→S transition is *anticipated* by an increase of the break frequency (as well as of the SC and luminosity). The flat-topped noise disappears when HC reaches its minimum and the source reaches the soft state. After the source transits back to the hard state (within about four days), the break frequency decreases continuously for about twenty days, i.e., on a similar timescale to that observed after BH state transitions (Kalemci et al. 2004). Aql X-1 behaved in the same way during its 1999 and 2000 outbursts (Fig. 5.13). In both outbursts the initial H→S transitions are preceded by an increase in luminosity, SC and break frequency. The luminosity of these transitions (around ∼10% L_{Edd} or above) is higher than the luminosity of the S→H transition (between ∼1 and ∼3% L_{Edd}; see also Maccarone & Coppi 2003; Tudose et al. 2009) that occurs later on in the outburst, in a way analogous to BH transients (Homan & Belloni 2005).

5.4 Discussion

5.4.1 Luminosity and mass accretion rate

We present in Figure 5.14 a sketched summary of the luminosity and variability evolution along each of the three states of atoll sources: soft, hard and

intermediate. It also shows the luminosities at which these states are observed along the full sample of sources (Fig. 5.6). The two transients (1608 and Aql X-1) and 1705 are the only systems that fully sample the hard state, which as pointed out by Barret & Olive (2002) and Muno et al. (2002c) results in a "Z"-shaped track on the CD. However, these three atoll sources can be clearly distinguished from Z sources by their lower luminosity, harder average spectra and stronger variability (van Straaten et al. 2003), which shows that (as already pointed out by Hasinger & van der Klis 1989) CD morphology *per se* is not sufficient to classify an LMXB. As explained in Sec. 5.3.2, 1608, Aql X-1 and 1705 show two distinct and populated branches in the HLD and SaLD, corresponding to hard and soft states, and a less densely populated intermediate state branch. This suggests that the transitional state is unstable, that each of these two branches corresponds to a stable configuration of the accretion flow and that the movements along each branch are produced by changes in the $\dot{M}$ of such stable configurations (Done et al. 2007). However, 1636, 0614 and 1728 show intermediate states that are instead densely populated, which indicates that the inner accretion flow in the intermediate state is not intrinsically unstable in these systems. The fact that the three systems with the longest orbital periods show the largest long term luminosity changes (Table A.2) supports the picture that large disks are colder in the outer parts and tend to be unstable (Lasota 2001). Some atoll sources are mostly in soft states (1820, 1735 and GX 3+1 in our sample; Figs. 5.6 and 5.9, lower panels; Table A.2), which could be due to a sustained high mass transfer rate that has maintained the accretion disk hot and bright during more than a decade of *RXTE* observations.

The approximately constant luminosities that we observe during state transitions imply that such transitions involve mainly a redistribution of the flux at different energies, so that the total radiated energy does not change by large amounts in intermediate or transitional states. If $\dot{M}$ increases during the hard to soft transition (as e.g. the burst properties of 1636 suggest, van der Klis et al. 1990) the net efficiency in converting $\dot{M}$ into 2–200 keV radiation must decrease in order to keep a constant luminosity. This would imply, however, that hard states are more radiatively efficient than soft states, in clear contradiction with the high efficiency usually attributed to soft (a.k.a "thermal" or "disk-dominated") states. An alternative is that two accretion flows operate simultaneously and only the mass accretion rate through the disk, $\dot{M}_d$, increases during the H→S transition while the mass accretion rate in the corona, $\dot{M}_c$, decreases accordingly so as to keep a constant *total* $\dot{M}$ (Esin et al. 1997; Meyer-Hofmeister et al. 2005; Done et al. 2007, see also 5.4.3.2). Several mechanisms have been proposed to produce the switch between hard and soft

states, from a disk-instability induced transition (Mineshige 1996), disk evaporation into a corona (Meyer-Hofmeister et al. 2005), the ejection of the corona into a transient jet (supressing the steady jet, Fender et al. 2004b) or the onset of an ADAF (Narayan & Yi 1995). The mechanism responsible for such state transitions must account for i) approximately constant luminosities in a single transition, a narrow range of luminosities in a given source at different epochs and a wide range of luminosities across sources (Secs. 5.3.2, 5.3.4 and Table A.2), ii) densely populated intermediate states in non-transients and sparsely populated intermediate states in transients (with the same timing and spectral properties; Sec. 5.3) and iii) variability frequencies that increase when going from the hard to the soft state (Fig. 5.4, right, Sec. 5.3.1). Our work also shows that a successful model for the accretion flow in the hard state must be able to explain luminosities as high as 15% L_{Edd} (as in 1705 or 1820), and that disk dominated (soft) states can have luminosities as low as 1% L_{Edd} (as is the case of 0614 or 1608, Fig. 5.9). As noted in Section 5.3.2, distance uncertainties do not affect these conclusions. Clearly, soft states of atoll sources are not necessarily more luminous than hard states. Hard and soft states show overlapping ranges in luminosity, both in a given source and across sources. Hence the terms "*low*-hard state" and "*high*-soft state" are misleading and should be abandoned.

5.4.2 Comptonization and variability frequencies

It is widely agreed that the hard X-ray flux in LMXBs is produced by Compton up-scattering of soft thermal photons within a population of hot electrons. The location and geometry of the comptonizing medium is a matter of debate (corona, ADAF, base of the jet, boundary layer...). Our work gives an important constraint to model the behavior of this comptonizing medium in atoll sources: the fraction of comptonized flux is anticorrelated with the variability frequencies. This is true not only for QPOs but also for broadband (flat-topped) noise. In other words, the harder the energy spectrum, the longer the variability timescales (see Fig. 5.4, right). A similar phenomenon has been seen in some BH systems (Vignarca et al. 2003; Titarchuk & Fiorito 2004; Titarchuk & Shaposhnikov 2008), indicating that this constitutes a basic property of accretion flows around compact objects.

Linares et al. (2007) showed that NS-LMXBs can have variability frequencies lower than BH systems, contrary to the common belief that characteristic variability timescales of LMXBs scale linearly with the mass of the accreting compact object. In this work we show that the main tracer of such frequencies is the spectral hardness. It is interesting to note in this respect that the accreting millisecond pulsar Linares et al. (2007) studied, IGR J00291+5934,

featured an X-ray spectrum harder than any of the sources studied herein (HC>1.2 Crab). In terms of the hardness-frequency anticorrelation presented in this work (Sec. 5.3.1), this can explain the anomalously low frequencies observed in this object ($\nu_b \simeq 0.02$ Hz). We also stress that, if the X-ray luminosity tracks $\dot{M}$, the observed break frequencies are not correlated with $\dot{M}$ (Fig. 5.4, left). Therefore, if the characteristic frequency of the BH system Cyg X-1 used to infer AGN masses (Uttley & McHardy 2005; Axelsson et al. 2005) changes due to the same process as the characteristic frequencies of atoll sources, then it is imperative to identify and understand this process before using variability frequencies to measure the mass of super massive BHs.

If the variability frequencies are set by the orbital frequency at the inner edge of the disk, this relation between hardness and frequencies is consistent with a scenario in which the disk recedes when the sources transit from the soft to the hard state, leaving an optically thin inner accretion flow (Narayan & Yi 1995; Done et al. 2007). In this framework the inner accretion flow (or "corona") must yield a higher flux in hard X-rays (more Compton upscattered photons) when the disk is truncated far out. Therefore a larger fraction of the soft seed photons produced in the disk and/or NS surface must be intercepted by the corona before reaching the observer, which poses strong constraints on the geometry of the flow (Maitra et al. 2009). Our results on the frequencies and luminosities during state transitions (Fig. 5.4, Table A.2) imply that, if the "receeding disk" scenario applies, the same change in inner disk radius should occur at luminosities between $\sim$0.5 and $\sim$15 % L_{Edd}.

5.4.3 Decoupling variability and luminosity

Our work shows that, even when including the hard X-ray band (up to 200 keV), the same kHz QPO frequencies can be present in a given source at luminosities that differ by a factor of $\sim$2 (see 0614, 1820, 1728 and 1636 in lower left panel of Fig. 5.4) or a factor of $\sim$8 in the case of 1608. This is a consequence of the parallel track phenomenon in individual sources operating throughout the present work (see Sec. 5.1). Considering the full sample of atoll sources, one can readily see that the same kHz QPO frequencies are observed over a range of two orders of magnitude in luminosity. This is often known as the parallel track phenomenon across sources in reference to the tracks in a frequency-luminosity diagram displayed by different sources (Ford et al. 2000). We stress that different NS masses and accreted material compositions will change L_{Edd} by a factor of $\sim$3.5 at most (for a NS mass between 1 and 2 $M_\odot$), much less than the two orders of magnitude range in luminosities actually observed. As a consequence of the spectral hardening that occurs when upper kHz QPO frequencies decrease (Fig. 5.4, lower right) such tracks become vertical when

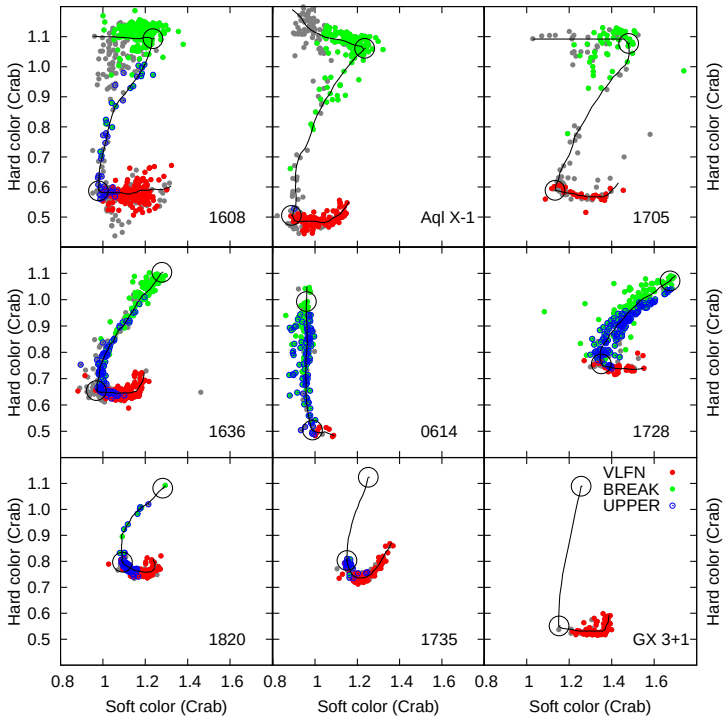

Figure 5.1: Color-color diagrams of the nine atoll sources studied. Green points mark observations where we measure the break frequency of the flat-topped broadband noise, small blue open circles mark our detections of upper kHz QPOs, red points show those observations where VLFN is present and grey points the cases where none of these phenomena were present. There were only five instances where flat-topped noise and VLFN occurred in the same power spectrum (Sec. 5.2.3). Observations combining either VLFN or flat-topped noise with upper kHz QPO show up as blue circles with red or green iinterior, respectively. The hard ($S_a \equiv 1$) and soft ($S_a \equiv 2$) vertices are marked with a large black open circle on the upper and lower part of the atoll track, respectively (Sec. 5.2.2).

considering the broadband luminosity instead of the soft X-ray intensity or the 2–50 keV luminosity (as in Ford et al. 2000). At $\nu_u \gtrsim 1000$ Hz, however, a "bending" of the tracks towards high luminosities is apparent in some of the sources (Fig. 5.4, lower left; the same sources stand out in Fig. 5.10, see Sec. 5.3.3). In summary, when considering all observations taken over more than ten years, there is no correlation between luminosity and kHz QPO frequency in any of the sources.

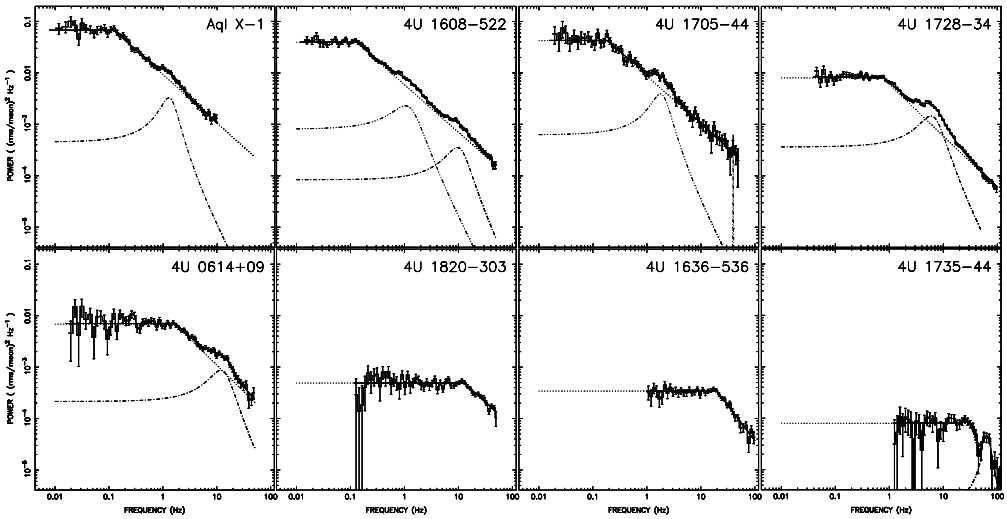

Figure 5.2: Overview of flat-topped noise present in hard and intermediate states (Sec. 5.2.3). Representative power spectra are shown together with their fit functions, with break frequencies spanning more than two decades. It should be noted that the break frequency of each individual system varies over a similar range (see Fig. 5.4).

We showed in Section 5.3.3 that the luminosity observed at a given timing state (or variability frequency) in different sources is correlated with the spectral hardness above 6 keV (see Fig. 5.11). This constitutes a new ingredient to model accretion flows in LMXBs. The fact that luminosity and spectral hardness are correlated at a given variability frequency also offers a potential tool to estimate the distance to systems that show no photospheric expansion bursts by only measuring one frequency (ν_u or ν_b), together with spectral hardness and flux. van Paradijs & van der Klis (1994) found an anti-correlation between spectral hardness and luminosity in a sample of LMXBs using the HEAO-1 A4 catalogue. The fact that they average over different states and use a different hardness energy band (13–80 keV) prevents a direct comparison between these results. In the following we discuss several mechanisms to decouple X-ray variability from luminosity, both in a single source and across sources, and for the latter case speculate on how the observed luminosity-hardness correlation may or may not be explained by such mechanisms. In the rest of this Section we adopt the hypothesis that the variability frequencies trace the radius of the inner edge of the disk (R_{in}), and in particular that the frequency of the upper kHz QPO reflects the orbital frequency at R_{in}.

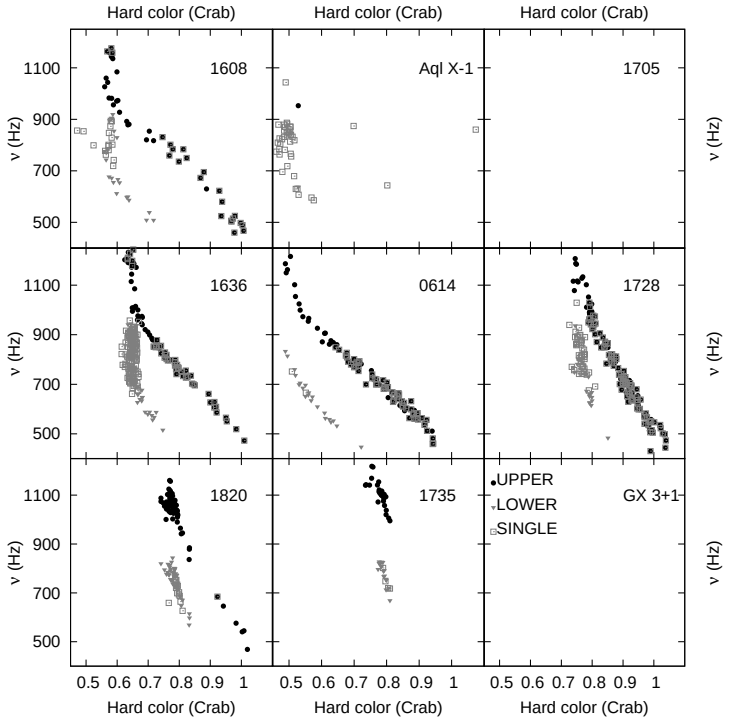

Figure 5.3: kHz QPO frequencies versus spectral hardness. Black dots represent upper kHz QPOs and grey triangles lower kHz QPOs. Squares show initially unidentified (single) kHz QPOs. We can identify most of these as upper or lower kHz QPO based on the distinct tracks clearly visible in this Figure (see also Sec. 5.3.1). In this and the following Figures each point represents one observation. Fragments of these kHz QPO frequency-hardness diagrams were reported for 1608 (Méndez et al. 1999) and 1636 (Di Salvo et al. 2003; Belloni et al. 2007).

5.4.3.1 Relative change in mass accretion rate

van der Klis (2001) proposed a mechanism to decouple variability frequencies from luminosity that involves a single variable ($\dot{M}_d$ in the simplest version) and its value averaged over a certain timescale ($< \dot{M}_d >$). In this model, the observed shifts in kHz QPO frequencies are caused by changes in $\dot{M}_d$, which in turn change the inner radius of the disk and the orbital frequencies therein (as in e.g. Miller et al. 1998; Lamb & Miller 2003). However, the frequencies are not simply set by the instantaneous value of $\dot{M}_d$ but depend on $\dot{M}_d / < \dot{M}_d >$, and therefore on how much $\dot{M}$ differs from its average. The luminosity is

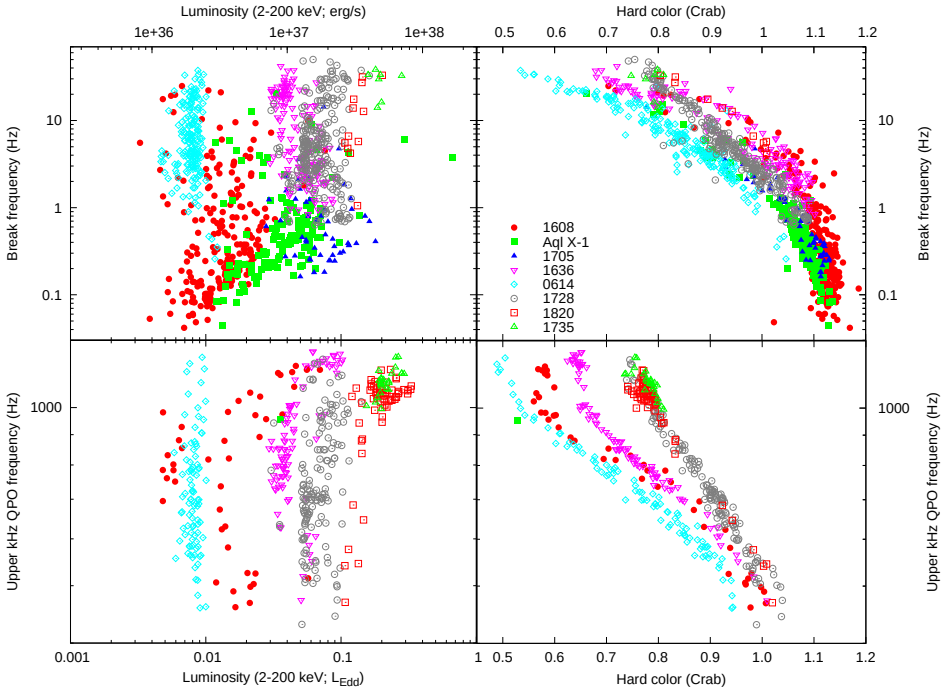

Figure 5.4: *Top right:* Break frequency versus spectral hardness for the eight sources where flat-topped noise is present. *Bottom right:* upper kHz QPO frequency versus spectral hardness for the seven sources that show upper kHz QPOs. The frequency-hardness anticorrelation is visible in both cases, and "saturates" towards soft and hard states (Secs. 5.3.1 and 5.4.2 for details). *Top left:* Break frequency versus luminosity for the eight sources where flat-topped noise is present. *Bottom left:* upper kHz QPO frequency versus luminosity for the seven sources that show upper kHz QPOs (see also Ford et al. 2000). Note that the same range in break frequency (more than two orders of magnitude) is observed at very different luminosities, both in a single source (spanning ∼1 order of magnitude in 1608, Aql X-1 and 1705) and across sources (spanning ∼2 orders of magnitude). See Secs. 5.3.3 and 5.4.3 for details.

assumed to vary in response to both the instantaneous and the time-averaged $\dot{M}_d$. In this way the same frequencies can occur at luminosities different by a factor of up to 10 in one source and up to two orders of magnitude across sources. The physical mechanism used to maintain the same R_{in} over such a wide range in luminosity in this model is a balance between mass accretion $\dot{M}_d$ "pushing" the inner disk inwards and radiation force "pushing" it outwards (as proposed by Miller et al. 1998). Luminosity and $\dot{M}_d$ would balance out so

as to keep R_{in} within a certain range.

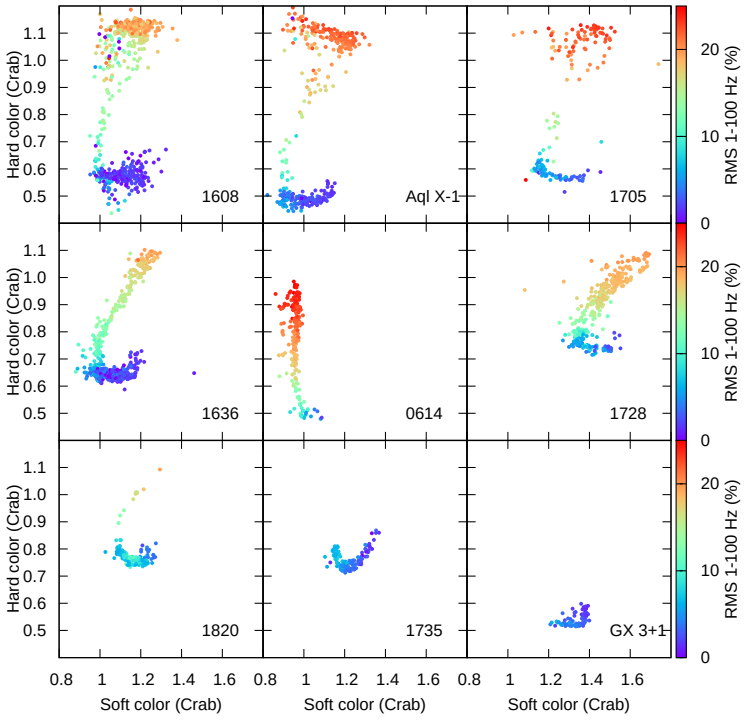

Figure 5.5: "Color-color-color" diagrams of the nine atoll sources studied. The color scale shows the 1–100 Hz fractional rms amplitude of the variability. Hard states are more variable, but hardness does not determine rms.

In this context, we propose that our luminosity-hardness correlation at a given kHz QPO frequency (Sec. 5.3.3) could reflect an underlying correlation between total luminosity and disk temperature. For a fixed inner disk radius, and upper kHz QPO frequency, a hotter disk would produce more luminosity and its high energy tail would increase the observed spectral hardness. As an example, increasing the disk-blackbody temperature by a factor of two in the best-fit spectral model of one of the observations near 1% L_{Edd} (while keeping the inner disk radius and remaining parameters fixed) leads to an increase of a similar factor in the spectral hardness (as defined in Sec. 5.2.2, i.e., in the 6–16 keV band). The steep (T^4) dependence of luminosity on black body temperature can reconcile the observed large range of luminosities with a sensible range of inner disk temperatures. NS mass difference between sources

could slightly affect the luminosity-hardness correlation, but by much less than the range covered by the data. Finally, we note that this interpretation would also explain why the luminosity-hardness correlation is strongest at the highest variability frequencies: in soft states the disk contributes more to the total spectrum, and changes in its temperature can therefore affect more strongly the spectral hardness.

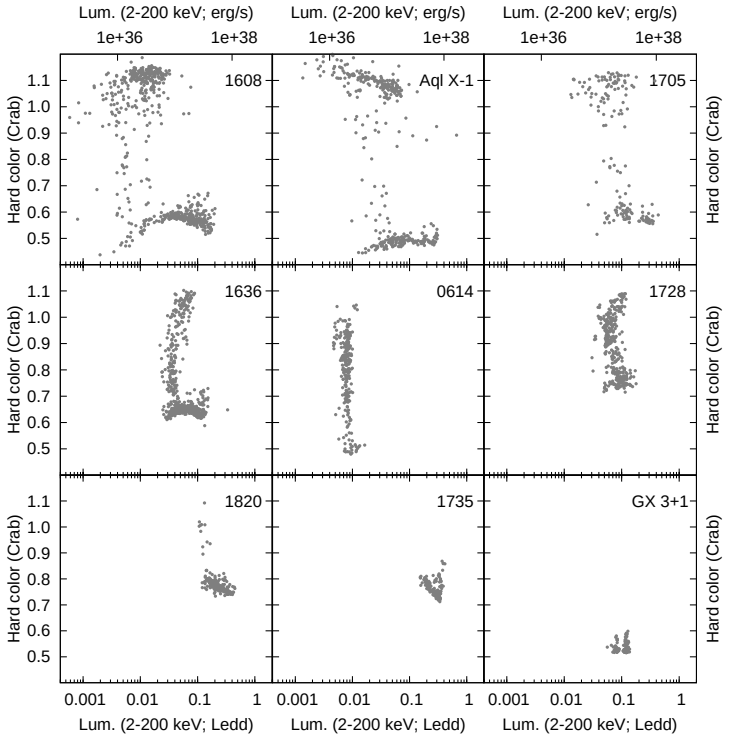

Figure 5.6: Hardness-Luminosity diagrams of the nine atoll sources studied. The luminosity range is indicated in Eddington units (lower axis) and erg s^{-1} (upper axis). Hard and soft state branches are approximately horizontal while intermediate states trace out vertical tracks.

5.4.3.2 Two flows, bolometric corrections, jets and anisotropy

If $\dot{M}_d$ is in one-to-one correspondence with the variability frequencies, one of the proposed ways to explain the different luminosities at which such frequencies are observed is by means of an additional accretion flow that varies the total $\dot{M}$ for a given $\dot{M}_d$ (e.g. Wijnands et al. 1996; Ford et al. 2000, see also

Sec. 5.4.3.1). However, if changes in the mass accretion rate of such spherical inflow (or "corona"; $\dot{M}_c$) are responsible for the variability-luminosity decoupling one expects a comparable decrease in the fractional amplitude of the kHz QPOs towards high luminosities, in disagreement with observations (Méndez et al. 2001).

Emission outside the *RXTE* 2–200 keV band can constitute another sink of energy and a way to decouple X-ray luminosity from variability frequencies (as noted e.g. by van der Klis 1995a). For instance, Thompson et al. (2008) point out that in some particular states about 30% of the bolometric luminosity can reside in the soft X-ray band, below the PCA energy range. Radiation of a variable fraction of the bolometric luminosity in the soft X-rays and UV band may therefore account for the frequency-luminosity decoupling in a given source, but expected bolometric correction factors being a factor 2 or 3 at most (Migliari & Fender 2006; in't Zand et al. 2007), it can hardly account for the more than two orders of magnitude difference in 2–200 keV luminosity between different sources in the same accretion (spectral/timing) state.

Based on the interaction between the jet and surrounding medium Gallo et al. (2005); Heinz et al. (2007) argue that the time-averaged jet power in some X-ray binaries is comparable to their X-ray luminosities. Although such estimates are still subject to large uncertainties, mechanical energy leaving the system in the form of a jet and at a variable rate gives another potential mechanism to decouple the radiated energy from the mass accretion rate through the disk and from the variability frequencies (Méndez et al. 1999). When considering a sample of sources, however, we see that the difference in jet power should be as high as two orders of magnitude in order to explain the observed frequency-luminosity relation. Moreover, if the low X-ray luminosity systems have large jet power this would be in contradiction with their low radio luminosities (Migliari & Fender 2006).

For a number of reasons, accretion flows in LMXBs are expected to radiate anisotropically. The emission of a flat accretion disk will have a $cos\ i$ angular dependence, based purely on the change in projected area (where i represents the angle between the line of sight and the perpendicular to the disk). Beloborodov (1999) proposed a scenario in which Thomson scattering in an outflowing disk atmosphere collimates most of the soft X-ray emission along the disk axis. Jets are known to exist and emit in the radio, IR and perhaps X-ray band in hard states of LMXBs (Fender 2006; Russell et al. 2007; Falcke et al. 2004). Their emission is strongly beamed if they move away from the compact object at relativistic speeds. We refer hereinafter to the apparent luminosity (calculated from the measured flux and assuming anisotropy) as simply "luminosity", and to the total (integrated over all solid angles) energy

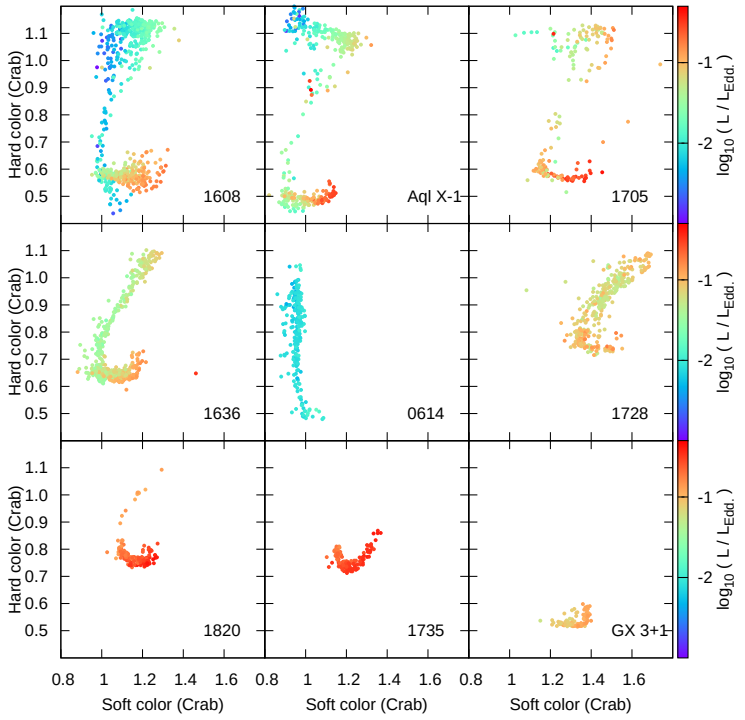

Figure 5.7: "Color-color-color" diagrams of the nine atoll sources studied. The color scale shows the 2–200 keV luminosity, in Eddington units and logarithmic scale. The luminosity ranges from 2.5×10^{35} erg s^{-1} (0.1% L_{Edd}) to 1.3×10^{38} erg s^{-1} (50% L_{Edd}). In a given source hard states are *on average* less luminous, but HC does not determine luminosity , and hard states in some sources (e.g. 1820, 1705) can be more luminous than soft states in other sources (e.g. 0614, 1608).

per unit time that escapes the system in the form of radiation as "radiated power". In all the cases mentioned above the (apparent) luminosity will depend on the inclination angle [3] so that systems with the same radiated power, when seen at low inclination will appear more luminous than those seen at high inclination. This provides a plausible mechanism to decouple variability frequencies and luminosity: if $\dot{M}_d$ sets *both* variability frequencies and radiated power (e.g. because $\dot{M}_d$ sets R_{in}, and this sets variability frequencies), then systems with the same radiated power and variability frequencies will show large differences in luminosity when viewed at different inclinations. As an

[3] We assume in this context that the disk is in the plane of the orbit and the jet axis is perpendicular to the disk, so that the inclination of the system is unambiguously defined.

example, applying the formula for the (de)boosting factor of a continuous jet given by (Fender 2006), assuming a jet velocity of $0.8c$ and a radiated power of 5% L_{Edd} we estimate that the observed luminosity at an inclination between 0 and 80 degrees would be between 3 and 45 % L_{Edd}. Two words of caution are necessary here: i) this formula gives a rough estimate and the problem obviously deserves detailed modelling (see e.g. Maitra et al. 2009) and ii) this scenario predicts that high inclination systems should be systematically underluminous for a given state, which so far has not been observed.

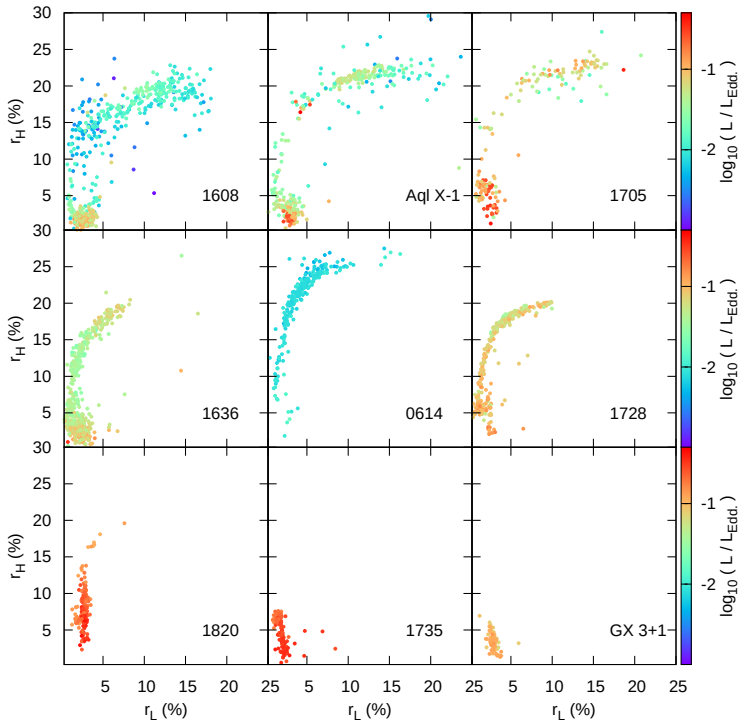

Figure 5.8: RMS-RMS diagrams of the nine atoll sources studied. The color scale shows the 2–200 keV luminosity, in Eddington units and logarithmic scale. The luminosity ranges from 2.5×10^{35} erg s^{-1} (0.1% L_{Edd}) to 1.3×10^{38} erg s^{-1} (50% L_{Edd}). See Section 5.3.3 for details.

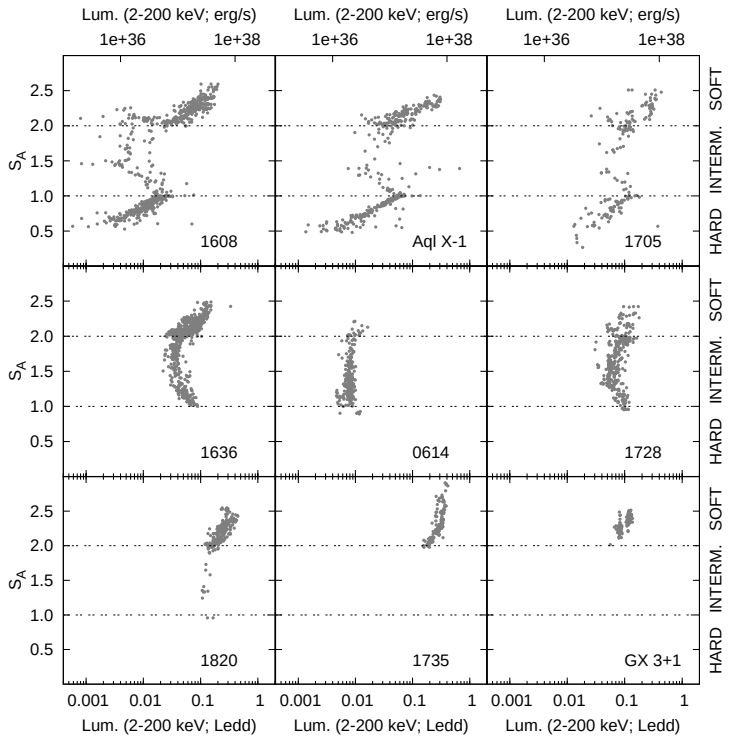

Figure 5.9: Color coordinate representing the position along the atoll track, S_a, versus luminosity (in the same units as Fig. 5.7). The S_a ranges corresponding to soft, hard and intermediate states are separated by the double dashed lines and indicated on the right-hand axis. Luminosity and S_a are in general anticorrelated in soft and hard states, but not in intermediate states.

5.5 Summary and conclusions

We have performed a systematic analysis of the luminosity, variability and spectral properties of a large sample of atoll sources in order to study how accretion flows around weakly magnetic neutron stars relate to the different observed accretion states, and how these relate to luminosity. In the following we summarize the main results and conclusions that arise from this work.

- State transitions and intermediate states are one and the same state: they share the same spectral and timing properties as well as luminosity range. The only difference is how populated these states are: some persistent sources have spent most of the last decade in the intermediate

state, whereas transient sources (which have the longest orbital periods; Table A.1) are predominantly in hard or soft states and show rapid transitions between them. We conclude that the inner accretion flow is not necessarily unstable during state transitions. It is most likely an "external" parameter (perhaps disk size) that determines how long a source stays in the intermediate state.

- The luminosity during a given state transition in a given transient is approximately constant, yet the intermediate state luminosity spans more than one order of magnitude when considering the full sample.

- Hard states are not necessarily *low*: they can show luminosities as high as 15% L_{Edd}. Similarly, high luminosities are not a defining property of soft states: they can feature luminosities down to 1% L_{Edd}.

- Variability frequencies are anticorrelated with spectral hardness in each of the studied sources. Our results show this *frequency-hardness* anticorrelation for the upper kHz QPO and break frequencies present in the power spectra of atoll sources. Similar results have been found in BH systems, suggesting that this is a common property of accretion flows around compact objects.

- By considering a fixed timing state we have discovered a *correlation between luminosity and spectral hardness* across different sources, which therefore links luminosity with spectral and timing properties. This constitutes a new ingredient for accretion flow models, which so far face trouble in explaining the very different luminosities at which similar accretion states take place. We argue that strongly beamed X-ray emission and different viewing angles could explain the difference in luminosity for a given value of the variability frequencies. We also propose a new explanation for the luminosity-frequency decoupling that involves different inner disk temperatures for a fixed inner disk radius.

Acknowledgments:
The research presented here used NASA's *HEASARC* and observations obtained thanks to a number of *RXTE* proposers. It is a pleasure to thank P. Casella, J. P. Lasota, D. Maitra, M. Méndez, S. Migliari, R. Rothschild, S. Suchy, P. Uttley and R. Wijnands for uncountable and useful discussions during several stages of this work.

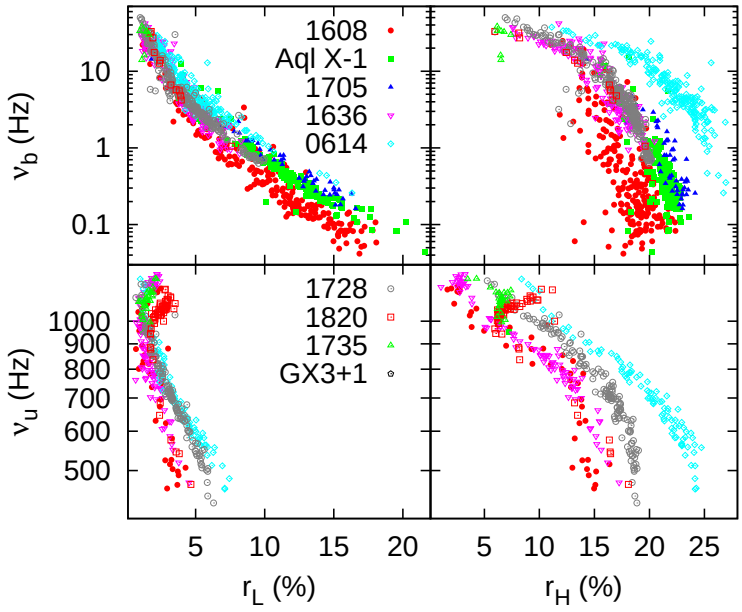

Figure 5.10: Break (*top*) and upper kHz QPO (*bottom*) frequencies versus the fractional rms amplitude of the variability in the low (*left*) and high (*right*) frequency bands. Note the ν_u-r_L and ν_u-r_H positive correlations in 1820 on top of the obvious general anticorrelation between frequencies and rms.

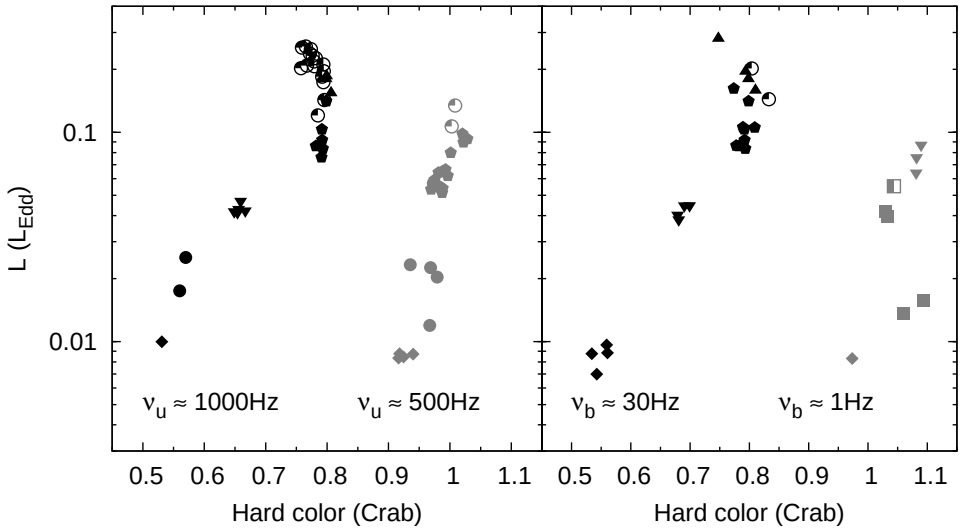

Figure 5.11: Luminosity-hardness correlation across sources for a given timing state (Secs. 5.3.3 and 5.4.3). *Left:* Observations with upper kHz QPO frequency near 1000 Hz and 500 Hz. *Right:* Observations with break frequency near 30 Hz and 1 Hz.

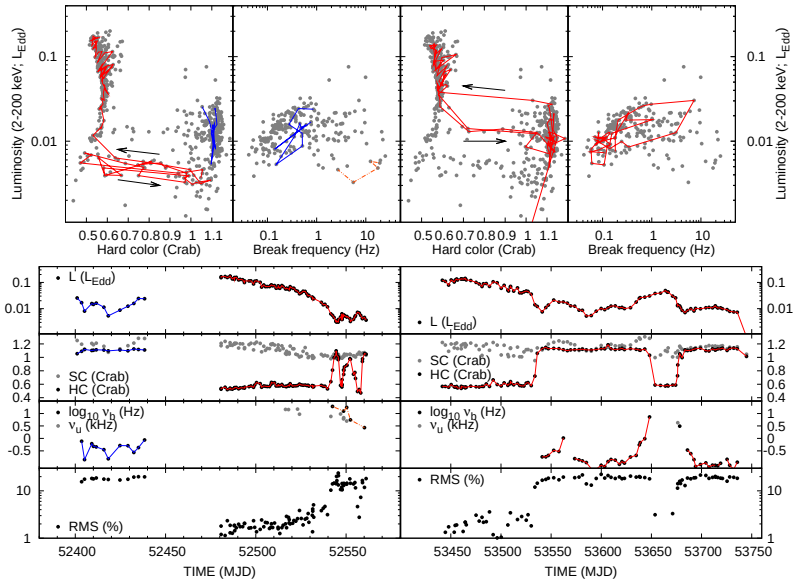

Figure 5.12: 2002 and 2005 outbursts of 4U 1608 showing the time evolution of the luminosity, colors, variability frequencies and 1–100 Hz rms variability. Hardness- and break frequency-luminosity diagrams are also shown in the upper panels. Arrows indicate the state transitions (Sec. 5.3.4).

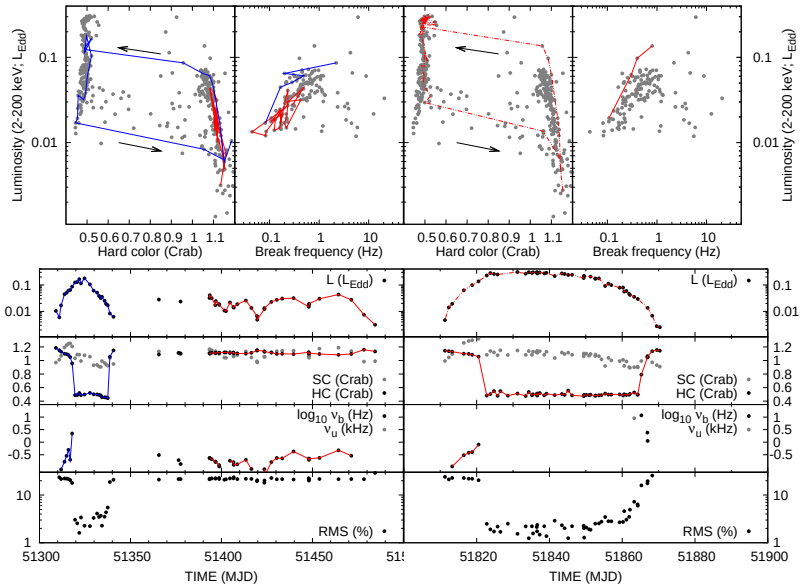

Figure 5.13: 1999 and 2000 outbursts of Aql X-1 showing the time evolution of the luminosity, colors, variability frequencies and 1–100 Hz rms variability. Hardness- and break frequency-luminosity diagrams are also shown in the upper panels. Arrows indicate the state transitions (Sec. 5.3.4).

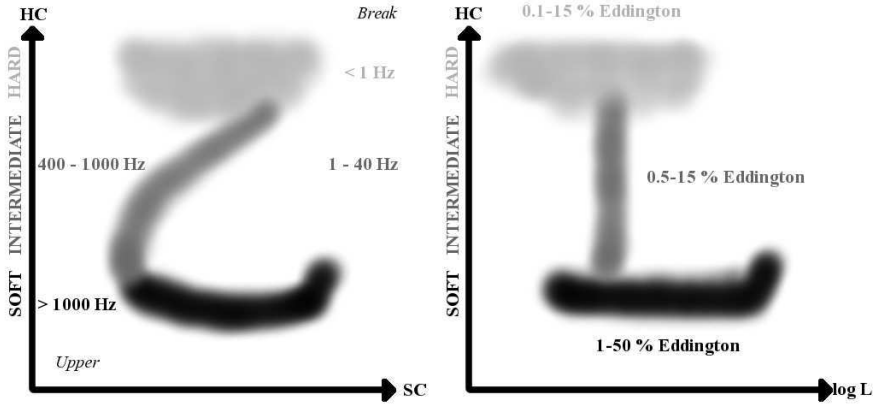

Figure 5.14: Summary of the atoll tracks in the color-color (CD; *left*) and hardness-luminosity (HLD; *right*) diagrams (SC: soft color; HC: hard color; L: 2–200 keV luminosity; see Section 5.2.2 for details). Soft, intermediate and hard states are shown in black, dark grey and light grey, respectively. The ranges spanned by the break frequency and the upper kHz QPO frequency in different states *of individual sources* are displayed on the CD (*left*). The luminosity ranges spanned by each state *in the full sample of sources* are displayed on the HLD (*right*). Both the upper kHz QPO and break frequencies are anticorrelated with the spectral hardness in each source (see Sec. 5.3.1 and Fig. 5.4). For a fixed value of these frequencies, luminosity and hardness are correlated across different sources (Sec. 5.3.3 and Fig. 5.11).

6 Accretion states of neutron stars: comparing luminosity, variability and spectra of Z and atoll sources

Manuel Linares and Michiel van der Klis

in preparation

Abstract

Neutron stars in low-mass X-ray binaries accrete mass at very different rates, from less than 1% of the Eddington rate in the weakest atoll sources to near or above the Eddington rate in the so-called Z sources. We present a study of the luminosity, spectral and timing properties of two Z sources, GX 17+2 and GX 340+0, across their different states. We also perform a detailed comparison between these properties and those of a large sample of atoll sources. We find intrinsic differences in the transition between the normal and flaring branches in both Z sources. Namely, GX 17+2 shows stronger variability in that state than GX 340+0. On the other hand, on the horizontal branch GX 340+0 is more strongly variable than GX 17+2. Atoll sources in hard states can show harder spectra and stronger variability than Z sources, yet the ranges in spectral hardness and fractional rms variability amplitude largely overlap in the two types of source. We finally point out that the normal-to-flaring branch vertex shows a similar luminosity in GX 17+2 and GX 340+0, which argues against a systematic difference in mass accretion rate between these two types of Z source.

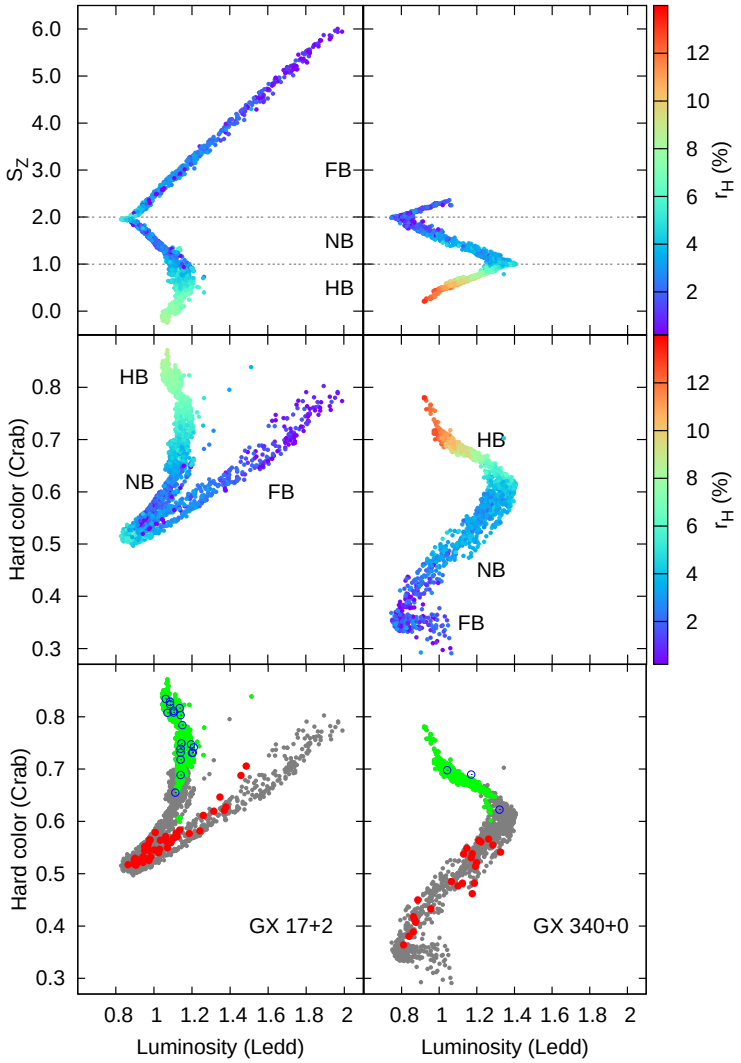

Figure 6.1: *Top panel:* Z coordinate, S_Z, versus 2–50 keV luminosity for GX 17+2 *(left)* and GX 340+0 *(right)*. The color scale shows the 1–100 Hz fractional rms amplitude of the variability. The S_Z ranges that correspond to different states are indicated with horizontal dashed lines. Note the S_Z-luminosity correlations on the FB and HB and the S_Z-luminosity anticorrelation on the NB. Each point corresponds to 256 s of data. *Middle panel:* Hardness-luminosity diagrams of GX 17+2 *(left)* and GX 340+0 *(right)*, in 256 s steps. The different branches or states are indicated and the color scale shows the fractional rms amplitude of the 1–100 Hz variability. *Bottom panel:* Hardness-luminosity diagrams, where grey points show all the 256 s segments analyzed in this work. Those segments where the HBO fundamental was detected are overplotted with green filled points. Red points and blue open circles show the observations where we detect the NBO/FBO and upper kHz QPO, respectively.

6.1 Introduction

Accretion onto compact objects is one of the most efficient ways of converting rest-mass energy into radiation and gives rise to one of the most powerful classes of object in our Galaxy, the low-mass X-ray binaries (LMXBs). These are neutron stars (NSs) or black holes that accrete matter from a low-mass star through an accretion disk. Of the two main types of NS-LMXB (Hasinger & van der Klis 1989), Z sources feature higher (near-Eddington) X-ray luminosities than atoll sources. Z sources show, on average, softer spectra than atolls, and conversely atoll sources can show stronger variability. The X-ray spectral and variability properties are correlated in both source types, and define different accretion (spectral & timing) states. In Z sources these different accretion states result in three distinct paths in color-color and hardness-intensity diagrams: the horizontal branch (HB), the normal branch (NB) and the flaring branch (FB). Together, these branches show two characteristic shapes (Fig. 6.1): a "Z" in the Cyg-like sources (after Cyg X-2) and a "ν" in the Sco-like sources (after Sco X-1).

Z sources show a number of variability components: kHz quasi-periodic oscillations (kHz QPOs; mostly observed in the HB and upper NB), horizontal branch oscillations (HBOs; seen in the HB and NB and often accompanied by harmonics), normal branch and flaring branch oscillations (NBOs/FBOs; seen in the NB and FB, at frequencies lower than the HBO when both are present), low-frequency noise (LFN; peaked or broad and present on the HB and NB) and very-low-frequency noise (VLFN; red noise, strongest on the FB). See van der Klis (2006) for a review. Even though the six well-identified Z sources have been actively accreting since their discovery, a remarkable exception was found recently by Homan et al. (2007): a transient source that was in outburst for about one year and a half and showed virtually all canonical Z source behavior at the highest luminosities.

Revnivtsev & Gilfanov (2006) describe the X-ray spectrum of Z sources as the sum of accretion disk and boundary layer emission, whereas Church et al. (2006) propose a model consisting of blackbody radiation from the NS surface together with Comptonized emission from an accretion disk corona. Earlier models were proposed by Psaltis et al. (1995) and Done et al. (2002), specifically for the X-ray emission of Z sources. The frequency of the HBO is known to correlate with the position along the HB (e.g. Jonker et al. 2000). By studying the X-ray timing behavior of the Sco-like Z source GX 17+2, Homan et al. (2002) found that the frequencies of the HBO and upper kHz QPO correlate below $\nu_u \simeq 1000$ Hz and anticorrelate above that value.

Lack of systematic study has prevented a complete understanding of the pre-

cise relation between luminosity and accretion states in LMXBs. By studying this relation in atoll sources, Linares & van der Klis (2009) showed that luminosity and hardness are positively correlated among different sources when they feature the same variability frequencies, and proposed an explanation that involves different inner disk temperatures across sources for the same inner disk radius. This luminosity-hardness correlation contradicts the widespread idea that harder sources are less luminous. In the present work we take the following step towards a complete understanding of the luminosity-state relation by extending our study to two Z sources, which accrete near the Eddington limit. We analyze in an homogeneous way the full *RXTE* dataset of GX 17+2 and GX 340+0, each representing one of the two Z sub-classes described above and each covering all three Z branches well), and measure their luminosity, spectral and timing properties. We then compare the results found for Z and atoll sources.

6.2 Observations and Data Analysis

We included in our analysis all pointed *Rossi X-ray Timing Explorer (RXTE)* observations of the two well sampled Z sources GX 17+2 and GX 340+0 that were publicly available in March 2009. These were taken over nearly twelve years. The total amount of data analyzed herein, after the filters explained below were applied, was ∼620 ksec and ∼470 ksec for GX 17+2 and GX 340+0, respectively.

We extracted background and deadtime corrected count rate (intensity) from Standard 2 data (16 s time resolution) of the *Proportional Counter Array (PCA)* in four energy bands covering the 2–16 keV range. We filtered out type I X-ray bursts and instrumental spikes from the resulting lightcurves, and following the recommended screening criteria we excluded data taken when the sources were close to the Earth (<10°) or off-axis (>0.01°). The background was estimated with *pcabackest* (V. 3.6) and the bright source model. We calculated colors (hardness ratios) in order to measure the slope and evolution of the energy spectrum in a model independent way. The soft (SC) and hard (HC) colors were defined as the ratios of count rates in the following bands (in keVs): SC=[3.5–6]/[2–3.5]; HC=[9.7–16]/[6–9.7]. We then normalized colors and intensity to the Crab values closest in time (and within the same gain epoch, van Straaten et al. 2003; Kuulkers et al. 1994). Finally, we averaged the colors and intensity in each of the 256 s data segments used for the timing analysis (see below). With the resulting colors and intensity we constructed color-color (CD) and hardness-intensity diagrams. Following previous work (Hertz et al. 1992; Kuulkers et al. 1994; Homan et al. 2002), we measured the

position on the Z track by projecting each data point onto a spline subtended along the track. This "Z-coordinate", S_Z, gives a one-dimensional measure of the spectral state, that we define in accordance to previous work as $S_Z \equiv 1$ in the HB-NB vertex and $S_Z \equiv 2$ in the NB-FB vertex.

We selected Event and Single Bit modes with time resolution of 250 μs or better and covering all energy channels below$\sim$100 (i.e. between 2 and $\sim$40 keV, except for data of GX 17+2 from proposals 20053-03 and 92042-01, in which this energy range was not available and we used instead the full PCA range). We performed Fourier transforms on 256 s data segments, with a uniform time resolution of 250 μs and without previous background or deadtime corrections. The Poissonian noise was subtracted from the resulting power spectra following Zhang et al. (1995) and Klein-Wolt (2004), and the powers were rms-normalized (van der Klis 1995b) using the average observation-averaged background rate in the corresponding energy band.

We calculated the fractional rms amplitude of the variability in each power spectrum, in two frequency bands: 0.01–1 Hz (r_L), and 1–100 Hz (r_H). We searched for kHz QPOs in the 300–1300 Hz range of the average power spectrum of all observations (which typically last a few hours) and fitted a single or double Lorentzian model to those observations that showed one or two kHz QPOs in order to measure the characteristic frequency [1] of the upper (ν_u) and lower (ν_ℓ) kHz QPO. We attempted to fit the kHz QPOs in shorter (256 s) steps, but given their moderate amplitude, on these timescales the kHz QPOs were mostly ill-constrained or undetected. We searched for HBOs and LFN in the observations of the HB and fitted them with a model consisting of a power law (to fit the VLFN, although it is weak in those parts of the CD), a broad (zero-centered) Lorentzian to fit the LFN and one Lorentzian that fitted the HBO. The characteristic frequency of the zero-centered Lorentzian gives a measure of the cutoff or break frequency of the LFN (ν_{LFN}). After an initial search with all parameters left free, we fixed the quality factor of the HBO to 4, as this gave a good approximation to the coherence of the feature and improved the overall stability of the fits. Whenever the HBO was detected in an averaged observation, we used the best-fit parameter values as initial guess to fit all individual (256s long) power spectra within the same observation, leaving all parameters free. Even though the LFN, being broader and weaker than the HBO, is not well constrained in the resulting "time-resolved" power spectra, this technique allowed us to measure the frequency of the HBO (ν_{HBO})

[1] We use the "numax" representation (Belloni et al. 2002), where if ν_0 is the Lorentzian's centroid frequency and Δ its HWHM (half width at half maximum), $\nu_{max} = \sqrt{\nu_0^2 + \Delta^2}$ gives the characteristic frequency of the feature (near the centroid if it is narrow and near the half-width if it is wide). The quality factor $Q = \nu_0/2\Delta$ is used as a measure of the coherence of the variability feature.

on timescales much shorter than the typical duration of an observation (ν_{HBO} is known to vary on timescales of minutes, e.g. Jonker et al. 2000). We used in this search the frequency range below 50 Hz in order to characterize the timing state of the sources in the HB (the HBO has been identified at slightly higher frequencies in the upper NB; e.g. Homan et al. 2002, , but it is weaker in that range and it therefore becomes ill-constrained in the time-resolved fits). We searched the 0.01–20 Hz power spectra of all observations in the FB and NB for NBOs/FBOs, and when these components were present we fitted a power law plus Lorentzian model and obtained thereby the characteristic frequency of the NBO/FBO (ν_{FBO}). In order to compare the Z source timing properties with those of atoll sources, we study the evolution of r_L, $_H$ and ν_u (which were also measured in atoll sources, Linares & van der Klis 2009) along the three branches of the Z track. We also look in detail at the behavior of the HBO and LFN, which can be directly compared to the flat-topped noise of atoll sources.

Hard X-ray components from Z sources have been detected in the hardest part of the HB, but contrary to atoll sources they carry less than ∼8% of the 0.1-200 keV flux (Di Salvo et al. 2000; di Salvo et al. 2004). We extracted and inspected *High Energy X-ray Timing Experiment (HEXTE)* background and deadtime corrected 20-200 keV spectra of both sources and detected no significant emission above 50 keV (with one single exception in GX 17+2; see Migliari et al. 2007). We therefore exclude the *HEXTE* data from the remaining spectral analysis. We extracted one PCU2 spectrum for each of the 256 s intervals used for the timing analysis (see above), and corrected for dead time using the average rates during the observation. We grouped the energy channels of the resulting spectra to have a minimum of 20 counts per energy bin, created one response matrix per observation with *pcarsp* (V. 10.1) and subtracted the background spectrum accumulated in each 256 s interval. We finally fitted the energy spectra with XSPEC (Arnaud 1996, Version 11.3.2), using an absorbed disk-blackbody plus broken power law model. In the FB of GX 340+0 the broken power law component was not required so we used instead a simple absorbed disk-blackbody model. We note that we perform these spectral fits with the goal of estimating the luminosity, and not to study in detail the spectral decomposition of the two studied sources (see Psaltis et al. 1995; Done et al. 2002; Church et al. 2006; Revnivtsev & Gilfanov 2006, for a different approach). The column density was held fixed during the fits at the values reported by Christian & Swank (1997) from 0.5–20 keV spectral fits to EXOSAT spectra (1.9×10^{22} cm^{-2} and 6.0×10^{22} cm^{-2} for GX 17+2 and GX 340+0, respectively). We finally obtained the luminosity from the 2–50 keV unabsorbed flux, using the distance estimates obtained by Galloway

et al. (2008b) for GX 17+2 (9.8±0.4 kpc; from analysis of photospheric radius expansion type-I X-ray bursts) and by Christian & Swank (1997) for GX 340+0 (11±3 kpc; from measurements of the absorbing column density as no type-I bursts have been observed from this source thus far). The errors on these distances translate into a ∼50% systematic uncertainty on the luminosity of GX 340+0, and a ∼10% systematic uncertainty on the luminosity of GX 17+2.

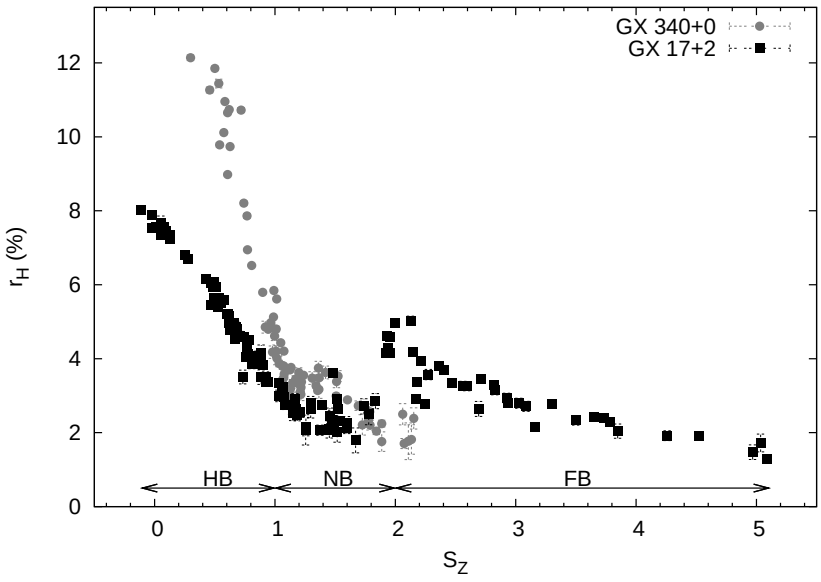

Figure 6.2: Observation-averaged measurements of the fractional rms amplitude in the 1–100 Hz frequency range versus S_Z. Along the HB GX 340+0 is more strongly variable than GX 17+2, although the variability amplitude decays until both sources reach a similar value on the NB. Note the increase in variability amplitude in the NB-FB vertex of GX 17+2.

6.3 Results

We show in Figure 6.1 (lowest two panels) the location in the hardness-luminosity diagram of those power spectra where we detect upper kHz QPOs (blue circles), HBOs (green points) and NBO/FBOs (red points). The HBO and upper kHz QPO are present throughout the HB. We detect upper kHz QPOs in 19 and 4 observations of GX 17+2 and GX 340+0, respectively. In some of these observations (ten in GX 17+2 and one in GX 340+0) only

one kHz QPO was detected, which therefore remained unidentified at first instance. However, like in the case of atoll sources (Linares & van der Klis 2009), upper and lower kHz QPOs trace clearly distinct tracks in hardness-frequency diagrams (where hardness refers to HC), which allowed us to identify them in all cases. The middle panels of Figure 6.1 show the changes in the strength of the 1–100 Hz variability (in the fractional rms amplitude, r_H) as the sources move along the Z track. In the upper panels we plot the Z coordinate, S_Z versus the 2-50 keV luminosity, showing that these two are correlated on the FB and HB but anticorrelated on the NB (Fig. 6.1, top). Looking at the middle and upper panels a systematic behavior is evident in both the HB and the FB, where r_H decreases (drastically on the HB) when the sources move along the Z track in the sense of increasing S_Z. We note that, contrary to r_H, the 0.01–1 Hz variability amplitude (r_L) increases in the FB of GX 17+2 with increasing S_Z. This is because the VLFN, which dominates the variability below ∼1 Hz, becomes stronger there (e.g. Homan et al. 2002).

The evolution of r_H along the Z track of both Z sources is shown in Figure 6.2. On the HB and upper NB ($S_Z \lesssim 1.5$), GX 340+0 features always higher r_H (stronger variability) than GX 17+2. As noted above, r_H decreases drastically along the HB with increasing S_Z in both sources, starting from different values (∼13% at $S_Z \simeq 0.4$ in GX 340+0; ∼9% at $S_Z \simeq$-0.2 in GX 17+2). At the HB-NB vertex ($S_Z \equiv 1$) a sudden transition occurs in the two sources, and the variability amplitude levels off between 2 and 4%. We also find that, in GX 17+2, r_H is higher on the NB-FB vertex ($S_Z \equiv 2$) than in its immediate surroundings, reaching values of more than 5% (Fig. 6.1, middle left panel, and Fig. 6.2). This increase in variability amplitude is due to the appearance of a strong NBO/FBO component (see Homan et al. 2002, and Fig. 6.1). Surprisingly, this is not the case in GX 340+0, which shows instead its strongest NBOs/FBOs on the NB, and a FB much shorter than that of GX 17+2 (Fig. 6.1).

In Figure 6.3 we show the time-resolved measurements (256 s steps) of ν_{HBO}, versus both HC (left panels) and luminosity (right panels). Also shown are the ν_{HBO} values obtained from observation-averaged power spectra (black empty circles). The frequencies obtained with these two methods are consistent. The short timescale measurements show some scatter and "sub-structure", i.e., tracks not visible in the observation-averaged measurements, which could be due to intrinsic deviations from the main track combined with observational windowing or to small systematic errors in the hardness or luminosity measurements at different epochs.

The color-luminosity diagrams of atoll and Z sources are shown in Figure 6.4, which displays both soft (SC) and hard (HC) colors versus the 2–50 keV

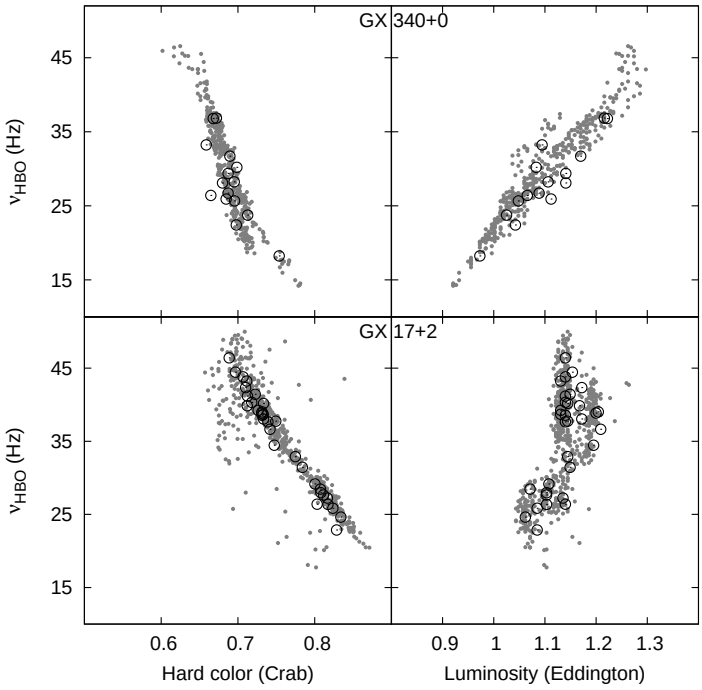

Figure 6.3: Grey filled points show the time-resolved (256 s) measurements of the HBO frequency (ν_{HBO}) versus hardness *(left)* and luminosity *(right)*. The observation-averaged frequencies are shown with black circles. ν_{HBO} and hardness are anticorrelated in both sources, as is the case for atoll sources. ν_{HBO} and luminosity are correlated in GX 340+0 but not in GX 17+2, which shows a more vertical HB in the hardness-luminosity diagram (hence a narrower luminosity range on that branch; see Fig. 6.1).

luminosity. The narrow range in luminosities of the Z sources is readily visible, between 0.8 and 2 times the Eddington luminosity (L_{Edd}; we use throughout this work a value of 2.5×10^{38} erg s^{-1}). This is in contrast with the much wider range (more than two orders of magnitude) in luminosity spanned by atoll sources. Z sources span a range of HC similar to that of atoll sources in soft and intermediate states (Linares & van der Klis 2009), with the exception of the lower NB and the FB of GX 340+0, which are softer than soft states of atoll sources (HC between 0.45 and 0.3, in Crab units; see Fig. 6.4). GX 340+0 features the highest values of the SC, reaching values of ∼2.1 times that of Crab (which correspond to the HB-NB vertex). SC and luminosity are correlated in both Z sources, as is the case for soft and hard states of atoll sources.

In Figure 6.5 we plot the fractional rms amplitude of the variability in the

high and low frequency bands (r_H and r_L, respectively; see Sec. 6.2) versus the luminosity and spectral hardness. In the left panels it is readily visible that the hardness and variability amplitudes occupy overlapping ranges in atoll and Z sources. The lower NB and FB of GX 340+0, however, stand out in the rms-HC diagrams (due to their afore mentioned softer spectra) and show opposite trends in the r_H-HC and r_L-HC relations. Namely, in those states the HC is correlated with r_H but anticorrelated with r_L. Atoll sources in hard states feature substantially harder spectra and stronger variability. In the right panels of Figure 6.5 one can see that the fractional rms of Z sources shows the same range as intermediate and soft states of atoll sources (i.e., 0.5-15%), even though their luminosities can differ by more than one order of magnitude.

The characteristic frequencies of the HBO, LFN and upper kHz QPO are plotted versus the spectral hardness and luminosity in Figure 6.6. For a given HC, the frequencies of GX 17+2 are somewhat lower than those of GX 340+0 and in both studied sources all three frequencies are anticorrelated with the spectral hardness (Fig. 6.6, top right). We show for comparison the values of the break and upper kHz QPO frequencies measured in atoll sources (Linares & van der Klis 2009). The ν_u-HC track of GX 17+2 lies between those of the atoll sources 4U 0614+09 and 4U 1636–536, and the ν_u-HC track of GX 340+0 is below that of 4U 0614+09. Now looking at the bottom right panel of Figure 6.6, the path subtended by the break frequency of atoll sources in the frequency hardness plane lies between those of ν_{HBO} and ν_{LFN} in the Z sources. As already noted by Ford et al. (2000), the same kHz QPO frequencies occur in Z sources, which accrete near the Eddington limit, and in atoll sources, at luminosities two orders of magnitude lower (Fig. 6.5, bottom left). A similar phenomenon is visible in the top left panel of Fig. 6.6: the LFN of Z sources and the flat top noise of atoll sources span the same break frequency range, whereas the luminosities at which these frequencies are observed differ by more than two orders of magnitude.

6.4 Discussion

Atoll sources show a broad range of spectral hardness and luminosity, as witnessed by Figure 6.4. For a fixed value of their variability frequencies, Linares & van der Klis (2009) showed that luminosity and spectral hardness are positively correlated across different sources. This can be explained with an inner disk temperature varying across sources for a given inner disk radius, which would make luminosities higher and increase the spectral hardness as the disk gets hotter. We find that Z sources do not follow this luminosity-hardness cor-

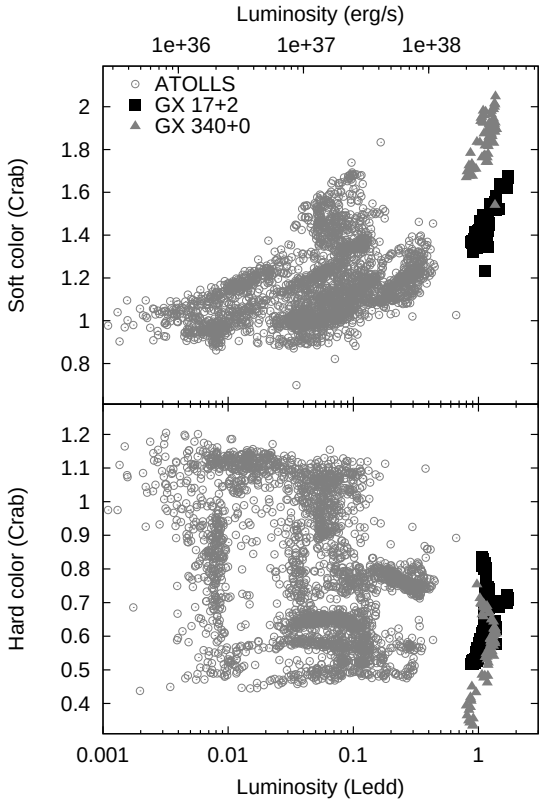

Figure 6.4: Hardness-luminosity planes, showing the sample of nine atoll sources studied by Linares & van der Klis (2009) (grey circles) and the two Z sources studied in this work: GX 17+2 (black squares) and GX 340+0 (grey triangles). Soft (upper panel) and hard (lower panel) colors are plotted versus luminosity. Each point corresponds to one observation. Note the narrow range in luminosities of the two Z sources compared to that of atolls. A general soft color-luminosity correlation is apparent in both types of source, with a relatively large scatter partly due to the different absorption towards the sources.

relation, as they are much more luminous than atoll sources (up to two orders of magnitude) but show the same, or even a lower, spectral hardness when comparing observations with the same variability frequencies (see Figure 6.6). If we take the common working hypothesis that characteristic variability frequencies are set by the inner disk radius, then it is clear that the scenario proposed to explain the luminosity-hardness correlation does not apply to Z sources. At near-Eddington luminosities radiation pressure may change the

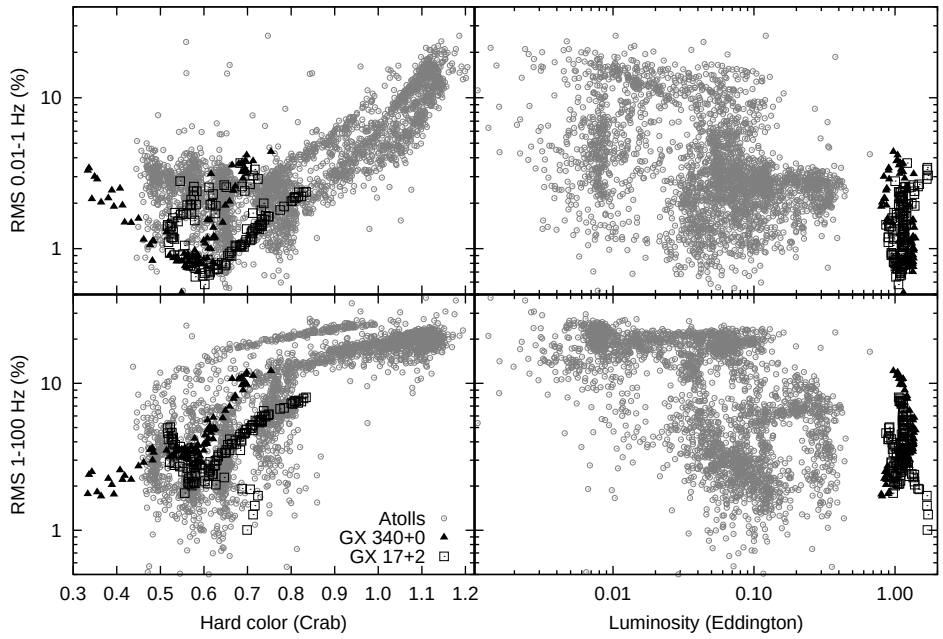

Figure 6.5: Fractional rms amplitude of the variability in the high (1–100 Hz, bottom panels) and low (0.01–1 Hz, top panels) frequency ranges, versus the 6–16 keV spectral hardness (left panels) and 2–50 keV luminosity (right panels). GX 340+0 and GX 17+2 are compared to the atoll sources studied by Linares & van der Klis (2009).

disk structure and emergent spectrum (e.g. because the inner disk is puffed up; e.g. Frank et al. 2002), and that could yield a luminosity-hardness relation different from that proposed for the less luminous atoll sources by Linares & van der Klis (2009). Alternatively, the higher soft photon flux in Z sources could affect the radiative properties of the Comptonizing medium. Therefore, a comparison between their energy spectra must be made with care. Extending this luminosity-state study to the bright atoll sources can bridge the $\sim$0.5–0.8 L_{Edd}luminosity gap between "classical" atoll sources and Z sources, and potentially give new insights in the accretion disk behavior at different luminosities.

The HB of Z sources shows clear similarities with intermediate states of atoll sources (van der Klis 2006, and references therein): broadband noise and kHz QPOs that increase in frequency as the 6–16 keV spectrum softens (HC decreases), variability amplitude that decays in both cases when HC decreases, and the same range of frequencies and HC. There are also a number

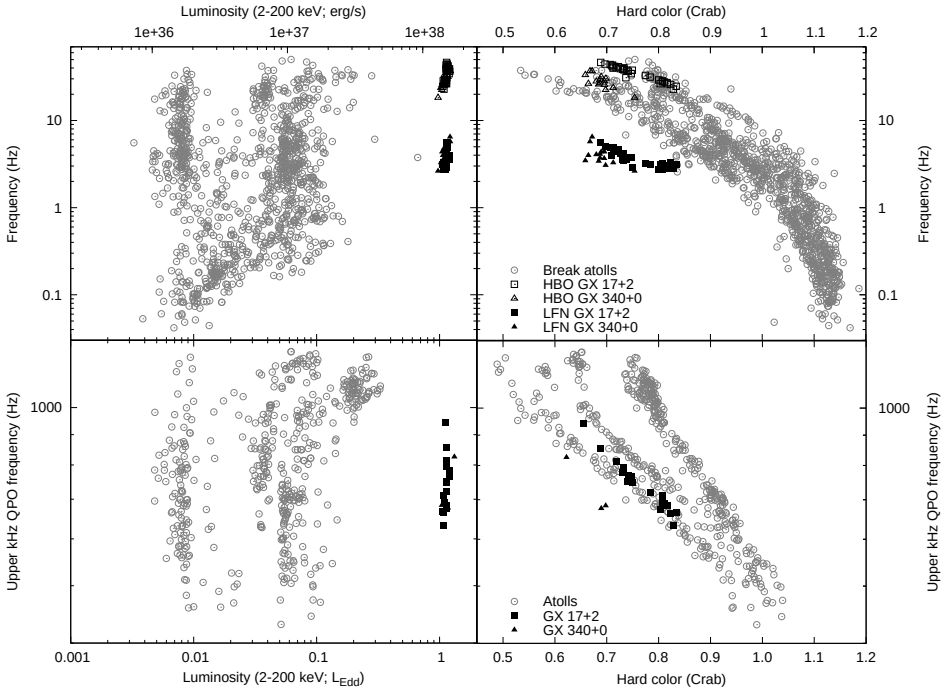

Figure 6.6: Frequencies of the HBO and LFN *(top)* and the upper kHz QPO (*bottom)* of GX 17+2 (black squares) and GX 340+0 (black triangles), plotted versus the spectral hardness. For comparison, the break and upper kHz QPO frequencies measured in atoll sources are shown with grey circles (Linares & van der Klis 2009).

of interesting differences: S_Z and luminosity are strongly correlated along the HB of Z sources, whereas the luminosity-S_a relation is more erratic in atolls (Linares & van der Klis 2009). The luminosities of the HB are of course higher than those of atolls in intermediate states, whereas the variability amplitude spans a similar range. The HB shows typically higher values of the SC than atoll-intermediate states, which is most likely connected to the higher X-ray luminosity (SC and luminosity are positively correlated in both hard and soft states of atoll sources).

It is worth noting that, while we use distance estimates that make no assumption on the luminosity of the different states (Sec. 6.2), we find that the NB-FB vertex of both Z sources shows a similar luminosity of $\sim$0.8 L_{Edd}. This supports the earlier suggestion that some states of Z sources occur always at the same luminosity, but improvements on the distance estimates and analysis

of a larger sample of sources are needed to confirm this. Homan et al. (2007) suggested that Cyg-like Z-source behavior is associated with a higher mass accretion rate than Sco-like behavior, based on the evolution of the intensity of the NB-FB vertex in the transient Z source XTE J1701–407. Unless the distance to GX 340+0 is severely underestimated, the results presented here do not support that hypothesis, which requires a difference of a factor ∼1.5 in the measured luminosities of the NB-FB vertex. The upper FB of GX 17+2 shows luminosities higher than those of GX 340+0, even when considering the distance uncertainties in both systems.

A Details of the $RXTE$ data extraction

This Appendix presents an extensive description of the data reduction procedures used in Chapter 5 in the X-ray spectral and timing analysis of atoll sources.

A.1 PCA

The proportional counter array (PCA, Jahoda et al. 1996, 2006) onboard the *Rossi X-ray Timing Explorer* (Bradt et al. 1993; Swank 1999) consists of five proportional counter units (PCUs) that cover the 2–60 keV energy range with an excellent time resolution (1 μs) and moderate energy resolution (17 % at 6 keV). We used Standard 2 data for the spectral analysis, which has 16 s time resolution and 129 energy channels covering the PCA energy bandpass. We filtered out data taken when the spacecraft was pointing too close to the Earth (elevation<10 deg) or too far from the source (offset>0.02 deg). We extracted dead time corrected count rates in the following energy bands: 2.0–3.5 keV (band A), 3.5–6.0 keV (band B), 6.0–9.7 keV (band C), 9.7–16.0 keV (band D). The count rates in these precise bands were estimated by interpolating linearly between the corresponding energy channels (given by pca_e2c_e05v03.fits). We subtracted the background rates from each band using *pcabackest* (Version 3.6), the latest PCA background models and updated SAA passage history files (`http://heasarc.gsfc.nasa.gov/docs/xte/pca_news.html`). Following the recommended procedure, we use the faint source model when the source count rate is lower than ∼40 c/s/PCU and the bright source model otherwise. From the count rates in each band, we defined the colors and intensity as: hard color=D/C, soft color=B/A, intensity=A+B+C+D. We then normalized colors and intensity to the Crab values nearest in time (Kuulkers et al. 1994) and in the same PCA gain epoch (e.g., van Straaten et al. 2003),

and averaged them in each observation.

We extracted one 2–60 keV energy spectrum per observation from Standard 2 data, using only PCU2 as this has been the most active and best calibrated throughout the whole *RXTE* mission lifetime. Apart from the basic filters explained above we excluded data taken during 15 min after each SAA passage and corrected the on-source exposure time for dead time, following `http://heasarc.gsfc.nasa.gov/docs/xte/recipes/pca_deadtime.html` and using the standard VLE setting. We estimated the background spectrum with *pcabackest* following the same steps explained above. PCA spectra with exposure time lower than three minutes and observations with net 2–60 keV count rate lower than 5 c/s/PCU were excluded from the spectral fitting. We created response matrices using *pcarsp* (Version 10.1), added a 1% systematic error to all channels and grouped them in order to have a minimum of 20 counts per energy bin.

For the timing analysis we selected "event" or "single-bit" modes covering all channels below ∼101 with a time resolution of 122 μs or better. We binned the data in time to obtain light curves with a uniform 122 μs time resolution (Nyquist frequency of 4096 Hz), without subtracting the background contribution. We obtained Fourier transforms from consecutive (and generally contiguous) 256 s long data segments, thereby reaching variability frequencies down to ∼4 mHz. We averaged the resulting power spectra within each observation and subtracted the Poissonian noise using the Zhang et al. (1995) formula. We also applied the prescription of Klein-Wolt (2004), shifting the Poisson level to match the power above 2000 Hz where no source variability is expected but only "counting statistics noise". Finally, we normalized the power spectra in the so-called "rms normalization" (van der Klis 1995b), using the average background rate in the same energy band and time intervals used for the timing analysis. In this normalization, the square root of the power integrated over a certain frequency band gives the fractional rms amplitude of the variability in the same frequency range.

A.2 HEXTE

The high energy X-ray timing experiment (HEXTE, Rothschild et al. 1998) consists of eight scintillation detectors, sensitive to 15–250 keV photons with an energy resolution of 15 % at 60 keV, grouped into two clusters of detectors (clusters A and B). Each cluster can change its pointing position or "rock" in mutually perpendicular directions, thereby providing measurements of the background around the observed target. We extracted one 15–250 keV spectrum per observation from the standard mode data of one of the

clusters in HEXTE. As one of the four detectors in cluster B lost its spectral capabilities in March 1996 (`http://mamacass.ucsd.edu:8080/hexte/status/hexte_status_960307.html`) we use preferentially cluster A for our analysis. However, cluster A was fixed in the on-source position in October 2006 due to rocking anomalies (`http://heasarc.gsfc.nasa.gov/docs/xte/whatsnew/big.html`) and therefore we use only cluster B in the observations taken thereafter, excluding the damaged detector. We checked that the cluster is rocking regularly during the observation and excluded the observations with variable rocking period from the HEXTE analysis. We verified that there are no contaminating sources in the field of view of HEXTE near each of the sources in our sample using the web tool *HEXTErock* (`http://heasarc.gsfc.nasa.gov/cgi-bin/Tools/HEXTErock/HEXTErock.pl`). We separated on-source and background data using *hxtback* and the corresponding rocking period. We corrected both source and background spectra for deadtime using *hxtdead* and added the spectra of all the segments within an observation with *sumpha*. We excluded spectra with on-source exposure time lower than three minutes from the spectral fitting. We created one response matrix for each observation using *hxtrsp*. Finally, we binned the resulting source spectrum to increase the signal to noise ratio with a factor 2 in channels 1–26 and a factor 3 in channels 27–64 (i.e. above $\sim$50 keV; see e.g. Wilms et al. 1999).

A.3 Tables

The atoll sources that form the sample studied in Chapter 5 are listed in Table A.1, together with some of their properties. Table A.2 presents an overview of the X-ray spectral and variability properties and broadband luminosities of all the sources in their different accretion states.

Table A.1: Atoll source sample and observations used in Chapter 5, together with a summary of the main source properties.

Name	Total obs.[d]	Used obs.[e]	n_H (10^{22}cm^{-2})	Distance[a] (kpc)	ν_{spin} (Hz)	P_{orb} (hr.)	Mean burst rate (hr^{-1})[f]	P/T[b]	P.W.[c]
4U 1608–522[g]	700	626	1.5[1]	3.3±0.5[2]	619[17]	12.9/12.0[15]	0.068	T	[19]
Aql X-1[h]	448	409	0.5[3]	5.2±0.8[2]	549[17]	19.0[15]	0.22	T	[20]
4U 1705–44[i]	175	170	1.5[11,12]	8.4±1.2[2]	-	-	0.28	P[j]	[21]
4U 1636–536[k]	686	665	0.3[4,5]	6.0±0.5[14]	582[17]	3.8[15]	0.12	P	[22]
4U 0614+09[l]	264	246	0.4[7]	3.2±0.4[8]	415[18]	0.9[16]	*	P	[23]
4U 1728–34[m]	366	356	3[6]	5.3±0.8[2]	363[17]	-	0.20	P	[24]
4U 1820–303[n]	207	203	0.15[4,9]	7.6±0.4[10]	-	0.19[15]	0.015	P	[25]
4U 1735–44[o]	135	129	0.3[4,11,12]	9.4±1.4[2]	-	4.7[15]	0.087	P	[26]
GX 3+1[p]	103	101	1.7[11]	4.5±1[13]	-	-	0.013	P	[27]

[a] The typical fractional error on the distance derived from photospheric expansion type I X-ray bursts is 15%. For three systems in our sample considerably larger or smaller values of the distance uncertainty have been reported: ∼20% in GX 3+1 (one single burst used in the distance estimate); ∼10% in 4U 1636–536 (bimodal distribution of photospheric radius expansion burst peak flux and considerations on the composition) and ∼5% in 4U1820–303 (globular cluster source). See details in [10],[13],[14].

[b] Persistent/Transient source

[c] Representative previous work on spectral/timing states based on *RXTE*.

[d] Excluding observations with missing data, slews or scans. The proposal and target numbers are listed below.

[e] After applying standard filters (see App. A) and excluding quiescent observations in the transient systems.

[f] Average type I X-ray burst rate measured by Galloway et al. (2008b) from all *RXTE* observations until June 2007.

[g] 10072-05,10093-01,10094-01,30062-01,30062-02,30062-03,30188-01,30419-01,30502-01,40437-01,50052-01,50052-02,50052-04,50052-05,60052-02,60052-03,70058-01,70059-01,70059-03,70069-01,80406-01,90408-01,91405-01,92401-01,93408-01.

[h] 20091-01,20092-01,20098-03,30072-01,30073-01,30073-02,30073-03,30073-04,30073-05,30188-03,40033-10,40047-01,40047-02,40047-03,40048-01,40049-01,40432-01,50049-01,50049-02,50049-03,60054-02,60429-01,70069-03,70426-01,80403-01,90017-01,90017-11,90403-01,91028-01,91414-01,92034-01,92438-01,93405-01.

[i] 20073-04,20074-02,20161-01,40034-01,40051-03,70038-01,70038-03,70038-04,90170-01,91039-01,93060-01.

[j] Similarities with transient systems, see Sec. 5.3.2.

[k] 10072-03,10088-01,30053-02,30056-03,40028-01,40030-03,40031-01,50030-02,60032-01,60032-05,70034-01,70036-01,80425-01,90409-01,91024-01,91152-05,92023-01,92023-02,93406-15.

[l] 10072-02,10095-01,20428-01,30053-01,40429-01,50412-01,60424-01,80037-01,80414-01,90422-01,91425-01,92411-01,93404-01.

[m] 10073-01,10410-01,20083-01,30042-03,40019-03,40027-06,40027-08,40033-06,50023-01,50029-23,50030-03,60029-02,70028-01,90406-01,91023-01,92023-03.

[n] 10074-01,10075-01,10076-01,20075-01,30053-03,30057-01,40017-01,40019-02,60030-01,70030-03,70031-05,80105-07,90027-01,91152-04,91435-01,92030-02.

[o] 10068-06,10072-07,20084-01,30056-02,40030-02,40031-02,40033-07,50025-02,50026-01,50029-34,60042-01,70036-03,91025-01,91152-06,93406-16.

[p] 10069-03,30042-04,30048-01,40023-01,40425-01,60022-01,70065-02,80105-03,90022-05.

[p] Refs. [1]: Penninx et al. (1989); [2]: Jonker & Nelemans (2004, and references therein); [3]: Church & Balucińska-Church (2001); [4]: Dickey & Lockman (1990); [5]: Fiocchi et al. (2006); [6]: Di Salvo et al. (2000); [7]: Juett et al. (2001); [8]: Kuulkers & et al. (2009); [9]: Sidoli et al. (2001); [10]: Kuulkers et al. (2003); [11]: Christian & Swank (1997); [12]: Schulz (1999); [13]: Kuulkers & van der Klis (2000); [14]: Galloway et al. (2006); [15]: Liu et al. (2007, and references therein); [16]: Shahbaz et al. (2008, temptative); [17]: Galloway et al. (2008b, and references therein); [18]: Strohmayer et al. (2008a, to be confirmed); [19]: van Straaten et al. (2003); [20]: Reig et al. (2004); [21]: Olive et al. (2003); [22]: Altamirano et al. (2008c); [23]: van Straaten et al. (2000); [24]: Di Salvo et al. (2001); [25]: Zhang et al. (1998b);[26]: Wijnands et al. (1998); [27]: Reerink (2005).

Table A.2: Summary of X-ray spectral and variability properties and broadband luminosities of atoll sources in their different accretion states.

Source	Soft[a]	Hard[b]	Int.[c]	Breaks[d]	Uppers[e]	VLFN[f]	ν_b (Hz)[g]	ν_u (Hz)[h]	L[i] (% L_{Edd})	L_{int}[j] (% L_{Edd})	L_{av}[k] (% L_{Edd})	rms[l] (%)
4U 1608–522	45%	40%	15%	226	44(21)	156	0.1–25	460–1176	0.001–20	0.5–1.4	4.0	110
Aql X-1	42%	40%	18%	148	1(1)	127	0.1–21	953	0.001–30	1–5	6.5	115
4U 1705–44	35%	38%	26%	54	-	29	0.2–14	-	1–40	5–14	12.0	77
4U 1636–536	65%	-	35%	136	90(37)	242	0.8–42	473–1244	2–20	∼4	6.3	46
4U 0614+09	7%	2%	91%	191	90(35)	9	0.3–38	459–1216	0.4–2	∼0.8	0.8	18
4U 1728–34	15%	3%	82%	249	144(48)	40	0.6–50	430–1207	3–20	4–10	7.9	32
4U 1820–303	86%	1%	13%	12	63(62)	149	1.1–33	467–1160	10–50	11	23.6	32
4U 1735–44	97%	-	3%	7	26(26)	85	14–38	995–1218	12–50	-	28.1	22
GX 3+1	100%	-	-	-	-	84	-	-	5–15	-	10.3	20

[a]Fractional number of observations in which the source was in the soft state.

[b]Same as previous column, for the hard state.

[c]Same as previous column, for the intermediate state.

[d]Number of observations where we detect flat-top noise and measure its break frequency.

[e]Number of observations where we detect the upper kHz QPO and measure its frequency. We indicate between parenthesis the number of twin kHz QPO detections (Sec. 5.2.3).

[f]Number of observations where we detect VLFN and measure its slope.

[g]Range of measured break frequencies.

[h]Range of measured upper kHz QPO frequencies.

[i]Luminosity range. Lower limit in transient systems corresponds to approximate quiescent luminosity.

[j]Range in intermediate state luminosity.

[k]Average luminosity, including all observations.

[l]Fractional rms amplitude of the 2–200 keV luminosity long term variability. Calculated from the record of observation-averaged fluxes, spanning more than ten years.

Part III

Thermonuclear bursts from accreting neutron stars

Poca favilla gran fiamma seconda.

From a little spark may burst a flame.

Dante Alighieri (1265-1321)

7 The *Swift* capture of a long X-ray burst from XTE J1701–407

Manuel Linares, Anna L. Watts, Rudy Wijnands, Paolo Soleri, Nathalie Degenaar, Peter A. Curran, Rhaana L. C. Starling, Michiel van der Klis

Monthly Notices of the Royal Astronomical Society - Letters, 2009, 392, 11

Abstract

XTE J1701–407 is a new transient X-ray source discovered on June 8th, 2008. More than one month later it showed a rare type of thermonuclear explosion: a long type I X-ray burst. We report herein the results of our study of the spectral and flux evolution during this burst, as well as the analysis of the outburst in which it took place. We find an upper limit on the distance to the source of 6.1 kpc by considering the maximum luminosity reached by the burst. We measure a total fluence of 3.5×10^{-6} erg/cm^2 throughout the $\sim$20 minutes burst duration and a fluence of 2.6×10^{-3} erg/cm^2 during the first two months of the outburst. We show that the flux decay is best fitted by a power law (index $\sim$1.6) along the tail of the burst. Finally, we discuss the implications of the long burst properties, and the presence of a second and shorter burst detected by *Swift* ten days later, for the composition of the accreted material and the heating of the burning layer.

7.1 Introduction

The bulge of our Galaxy harbours a large fraction of the known population of accreting compact objects. During one of the regular monitoring observations of that region with the proportional counter array (PCA) onboard the Rossi X-ray timing explorer (*RXTE*) on June 8th, 2008, a new transient X-ray

source was discovered: XTE J1701–407 (Markwardt et al. 2008b). Three days later a follow-up observation with the X-ray telescope (XRT) onboard *Swift* improved the source localization and showed a spectrum that could be fitted with an absorbed power law of index ∼2 (Degenaar & Wijnands 2008). The transient nature, flux level and spectrum of the source are characteristic of X-ray binaries, but the exact class of the binary (high-mass or low-mass) was unkown and the compact object (black hole or neutron star) remained unidentified for more than one month. On July 17th at 13:29:59 UT the burst alert telescope (BAT) onboard *Swift* detected an X-ray flare at a position consistent with that of XTE J1701–407 (Barthelmy et al. 2008). *Swift* began slewing to the source 60 seconds after the trigger and the XRT began observing the field 97 seconds after the initial BAT trigger, detecting a fading X-ray source at the position of XTE J1701–407 (Barthelmy et al. 2008). Markwardt et al. (2008a) suggested that the flare could be caused by a thermonuclear burst based on the early BAT data. By studying the evolution of the XRT spectrum, Linares et al. (2008b) found a clear cooling curve and confirmed the speculation that this was a thermonuclear event, identifying the source as an accreting neutron star (NS) and the system, in all likelihood, as a low-mass X-ray binary (LMXB). As noted by Linares et al. (2008b) this particular event, having a total duration of more than 15 minutes, belongs to the rare subclass of long duration bursts (Cumming et al. 2006).

After the long X-ray burst the source continued in outburst[1] and *RXTE* kept observing it. A refined *Swift*-XRT position (Starling & Evans 2008), a search for an IR counterpart (Kaplan & Chakrabarty 2008) and the discovery of kHz quasi-periodic oscillations (QPOs; Strohmayer et al. 2008b) were all reported during the following two weeks. On July 27th BAT detected another X-ray flare from XTE J1701–407 (Sakamoto et al. 2008). The soft spectrum and duration (∼10 s) of the flare indicated that this was a type I X-ray burst (`http://gcn.gsfc.nasa.gov/notices_s/318166/BA/`), and hereafter we refer to it as the short burst (even though from the BAT data the total duration is somewhat uncertain). At the moment of writing the source is still active, more than two months after the start of the outburst.

In this Letter we present our analysis of the bursting behaviour of this source. Long bursts are rare, and therefore probe quite unusual burning regimes. Their duration is between that of normal Type I X-ray bursts (durations ∼ 10–100 s, triggered by unstable burning of H/He) and superbursts

[1]To clarify the terminology we stress that in the context of LMXBs an outburst is powered by accretion and lasts for weeks to years whereas a type I X-ray burst, or "burst", results from unstable thermonuclear burning on the surface of a NS and lasts for ∼10 seconds to ∼hours.

(durations ∼ hours, triggered by unstable burning of C). There are two scenarios in which such bursts could occur, both requiring the build-up and ignition of a thick layer of He. One possibility is that the system is ultracompact, so that it accretes nearly pure He (Cumming et al. 2006). The other possibility is that unstable H burning at low accretion rates builds up He (Peng et al. 2007; Cooper & Narayan 2007). While several examples of the first type are now known (see for example in't Zand et al. 2007; Falanga et al. 2008 and references therein), the second class - which probe the boundaries of H burning stability - have so far proved much rarer (Chenevez et al. 2007). In this Letter we will demonstrate that XTE J1701–407 is a good candidate for membership of this second class.

7.2 Observations and Data Analysis

We analysed all the 27 pointed *RXTE*-PCA observations of XTE J1701–407 taken until August 10th, 2008 (ID 93444-01; See Table 7.1). We also analysed the *Swift*-XRT data taken during and after the long burst (on July 17th, obsids 00317205000 and 00317205001). *Swift* observed XTE J1701–407 again on July 27th, triggered by the BAT detection of the short burst (Sec. 7.1). We also included this XRT observation (obsid 00318166000) in our analysis, which started ∼109 seconds after the trigger but did not detect the burst. In the following two sections we provide the details of our analysis. All errors given in Section 7.3 correspond to the 1 σ confidence level.

7.2.1 Swift

We ran the XRT pipeline (v. 0.12.0) on all the *Swift* observations. For the spectral analysis we created exposure maps and ancilliary files and used the latest response matrices (v011) provided by the *Swift*-XRT team. We grouped the spectra to a minimum of 20 counts per bin, applyied a systematic error of 2.5% (Campana et al. 2008) and fitted the 0.5–10 keV spectra within Xspec (Arnaud 1996, v. 11). In our fits (see models below) we fixed the absorbing column density to the average value found from X-ray fits to the persistent emission: 3.5×10^{22} cm^{-2} (Degenaar & Wijnands 2008; Markwardt et al. 2008b).

Observation 00317205000 started on July 17th, 2008 at 13:31:36.9 UT (Sec. 7.1) and lasted for a total of about one kilosecond. All the XRT data were collected in windowed timing (WT) mode, except for the initial ∼8 seconds which were taken in photon counting (PC) mode. We divided the observation into nine contiguous intervals of increasing length in order to compensate

Table 7.1: Log of the *RXTE* observations.

ObsID	Date (MJD)	Effective exposure (s)	Source count rate (c/s/PCU2)	2–50 keV unabsorbed flux ($erg\ s^{-1}\ cm^{-2}$)
93444-01-01-00	54626.8	700	18.3	3.57e-10 ± 2.7e-11
93444-01-01-01	54627.9	2393	20.3	3.87e-10 ± 2.4e-11
93444-01-02-00	54633.3	1873	37.9	6.24e-10 ± 7.4e-11
93444-01-02-01	54634.4	2382	29.4	5.13e-10 ± 9.5e-11
93444-01-02-02	54635.3	1751	26.6	4.76e-10 ± 1.3e-11
93444-01-03-01	54638.8	3183	20.2	3.84e-10 ± 1.5e-11
93444-01-03-02	54639.9	3004	19.5	3.71e-10 ± 1.3e-11
93444-01-03-00	54640.9	3183	19.3	4.09e-10 ± 2.6e-11
93444-01-04-00	54665.1	3176	39.9	6.28e-10 ± 6.2e-11
93444-01-04-01	54669.3	1709	41.7	6.61e-10 ± 5.3e-11
93444-01-04-02	54671.0	3199	43.2	6.77e-10 ± 4.5e-11
93444-01-05-00	54673.0	1725	37.0	5.82e-10 ± 6.6e-11
93444-01-05-01	54674.7	1790	41.8	6.25e-10 ± 5.6e-11
93444-01-05-02	54677.5	3458	36.1	5.4e-10 ± 4.8e-11
93444-01-05-03	54678.6	3189	33.9	5.12e-10 ± 5.5e-11
93444-01-06-02	54679.7	3115	34.6	5.17e-10 ± 4.8e-11
93444-01-06-00	54680.3	2032	32.1	4.84e-10 ± 2.3e-11
93444-01-06-03	54681.9	3426	26.3	4.01e-10 ± 3.8e-11
93444-01-06-04	54682.8	6859	14.0	2.44e-10 ± 5.6e-11
93444-01-06-01	54683.9	3275	11.1	2.3e-10 ± 2.6e-11
93444-01-06-05	54684.9	1809	9.8	1.75e-10 ± 3e-11
93444-01-06-06	54685.8	1538	9.7	1.71e-10 ± 3.4e-11
93444-01-07-00	54686.3	2460	10.8	1.99e-10 ± 2.1e-11
93444-01-07-06	54687.0	575	12.6	2.25e-10 ± 3e-11
93444-01-07-01	54687.4	2671	11.4	2.89e-10 ± 1.4e-11
93444-01-07-07	54687.4	2142	11.3	1.97e-10 ± 2.8e-11
93444-01-07-02	54688.4	2327	11.6	2.71e-10 ± 1.2e-11

for the flux decay and maintain an approximately constant total number of counts in each interval (between ∼1500 and ∼2500). About 830 seconds after the start of the observation a data gap of ∼3300 seconds occurred, after which the XRT continued to observe the source for another ∼35 seconds. This last data segment allows us to estimate the persistent flux after the X-ray burst. We extracted source and background spectra for each interval using circular regions with radii of ∼30 and ∼15 pixels, respectively, and fitted the resulting spectra using an absorbed black body model (reduced χ^2 between 0.7 and 1.1).

We performed fast Fourier transforms on 2s segments of XRT-WT data taken during the long burst in order to search for rapid variability. For that purpose we used the energy range 0.5–10 keV, keeping the original time resolution and thereby sampling the ∼0.5–280 Hz frequency range.

Both post-burst observations (00317205001 and 00318166000) allow us to

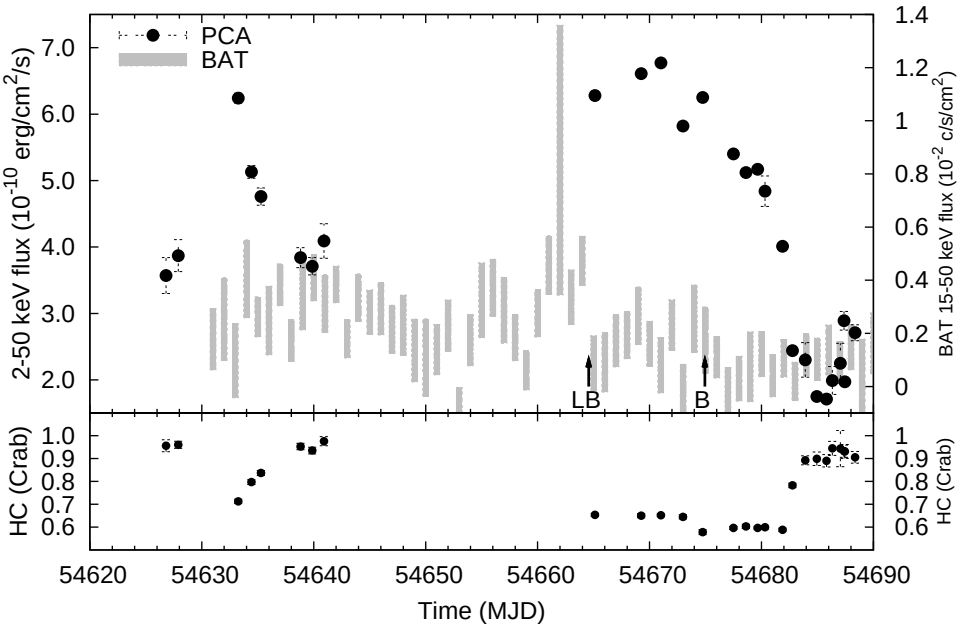

Figure 7.1: Time evolution of the 2–50 keV unabsorbed flux *(top, filled dots)* and the hard colour *(bottom)* during the outburst of XTE J1701–407, as measured by the *RXTE*-PCA. Arrows indicate the times of the long (LB) and short (B) X-ray burst. The 15–50 keV flux measured by *Swift*-BAT is shown as well *(top, grey rectangles)*.

characterize the persistent soft X-ray emission of XTE J1701–407. For the PC data we used an annular extraction region with radii 10–25 pixels in order to account for pile-up. The energy fraction enclosed by the resulting annuli was about 20%, and such energy loss was taken into account when creating the ancilliary files. Finally, including also the WT data, we fitted the energy spectra with an absorbed power law model (reduced χ^2 of 1.1 and 1.2).

7.2.2 RXTE

We analysed all the pointed *RXTE* observations of the source made until August 10th. After applying standard filters we extracted energy spectra from Standard 2 data collected by PCU2 and corrected them for background using the latest PCA background models. We generated reponse matrices and fitted the spectra within Xspec in the 3.0–25.0 keV band, after applying a 1% systematic error, with a black body plus power law model corrected for

absorption (see Sec. 7.2.1). The resulting fits had reduced χ^2 between 0.5 and 1.4 (for 45 degrees of freedom). We extracted a hardness ratio ("hard colour" hereafter) for each observation, defined as the count rate in the 9.7–16.0 keV band divided by that in the 6.0–9.7 keV band and normalized by that of the Crab. Furthermore, we extracted a background and deadtime corrected HEXTE (cluster B) energy spectrum from each observation, but found no significant source emission above 50 keV in any of them.

7.3 Results

7.3.1 Outburst

The overall lightcurve is shown in Figure 7.1, together with the evolution of the hard colour. The outburst shows two peaks at a similar flux, $(6.2, 6.8)\times10^{-10}$ erg/cm^2/s. The BAT transient monitor lightcurves[2] indicate that the source was active during the three weeks where no *RXTE* pointed observations were obtained, at a flux level similar to that measured during the first two weeks of outburst (see Fig. 7.1). The hard colour traces directly the changes in spectral state along the outburst, with a clear tendency: when the source is bright its spectrum is soft whereas the spectrum is harder at the lowest fluxes. However, it is interesting to note that as is the case for many other NS-LMXBs the correspondence between flux and hardness is not one-to-one (van der Klis 2006). Together with the presence of kHz quasi-periodic oscillations (Strohmayer et al. 2008b), the peak luminosity and the spectral evolution (Fig. 7.1) show that XTE J1701–407 is a new member of the atoll source class (Hasinger & van der Klis 1989). Both X-ray bursts occur at relatively high fluxes (see Table 7.2) and soft spectra (low hard colour).

By interpolating linearly between the available datapoints we integrate the lightcurve and find a total outburst fluence up until August 10th of 2.6×10^{-3} erg/cm^2. More than half of this energy (1.6×10^{-3} erg/cm^2) was radiated before the long burst occurred, whereas the fluence between long and short bursts was about 5×10^{-4} erg/cm^2.

From our spectral fits to the post-burst XRT observations (Sec. 7.2.1) we measure 2–10 keV fluxes of $(4.0 \pm 0.9) \times 10^{-10}$ erg/cm^2/s (July 17th) and $(5.6\pm1.0)\times10^{-10}$ erg/cm^2/s (July 27th), which are consistent with the fluxes in the same band obtained from the nearest (within one day) PCA observations. In both cases the photon index was $\sim$2. Furthermore, we estimate unabsorbed 1–2 keV fluxes of 2.3×10^{-10} erg/cm^2/s (July 17th) and 3.5×10^{-10} erg/cm^2/s (July 27th) and add them to the unabsorbed 2–50 keV fluxes measured with

[2] `http://swift.gsfc.nasa.gov/docs/swift/results/transients/`.

Table 7.2: Properties of both type I X-ray bursts detected from XTE J1701–407.

	Long	Short
BAT rise time (s)	50	5
Duration[a] (min)	21	?
Peak flux[b] (10^{-8} erg/s/cm^2)	8.4	∼4.9
Total fluence[c] (10^{-6} erg/cm^2)	3.5	?
Persistent flux[d] (10^{-10} erg/s/cm^2)	8.6±0.9	9.8±1.0

[a]From start of rise to 1% of peak flux.
[b]Bolometric.
[c]Including fluence in BAT (Markwardt et al. 2008a) and during XRT data gap.
[d]Unabsorbed 1–50 keV.

the PCA within one day of the bursts (6.3×10^{-10} erg/cm^2/s for both bursts; see Fig. 7.1). These 1–50 keV fluxes (Table 7.2) are the closest we can safely get to the bolometric persistent flux at the times of the bursts, but we note that the uncertainties in the absorbing column density and the extrapolation to the 0.01–1 keV energy range could change the bolometric flux by a factor of ∼2 (see e.g. discussion in in't Zand et al. 2007).

7.3.2 X-ray bursts

From the flux and spectral parameters reported by Markwardt et al. (2008a) we estimate a bolometric unabsorbed peak flux of 8.4×10^{-8} erg/cm^2/s for the long burst. By assuming that the peak luminosity was equal to or lower than that typical of photospheric expansion type I X-ray bursts (∼3.8×10^{38} erg/s Kuulkers et al. 2003) we can place an upper limit on the distance to the source of 6.1 kpc. On the other hand, if we use the Eddington limit for a mix of H and He (∼1.6×10^{38} erg/s for a hydrogen fraction X=0.7) as a limit for the peak luminosity the upper limit on the distance becomes 4.0 kpc. The rise time in the BAT lightcurve was about 50 seconds, the peak occurred about ten seconds after the trigger (`http://gcn.gsfc.nasa.gov/notices_s/317205/BA/`) and the total duration, assuming that the burst finished when it reached 1% of the peak flux, was about 21 min. The fluxes in the post-burst XRT observation, taken more than two hours after the peak of the long burst, are similar to the flux we measure in the last interval (∼1 hour after the peak, Sec. 7.2.1), confirming that the source had returned to the persistent level.

Figure 7.2 shows the results of our time-resolved spectroscopy of the tail of the long burst. The flux decays by almost two orders of magnitude and the temperature decreases from 1.72±0.05 keV to 0.88±0.02 keV during the burst tail (see also Linares et al. 2008b). XRT did not observe the peak of

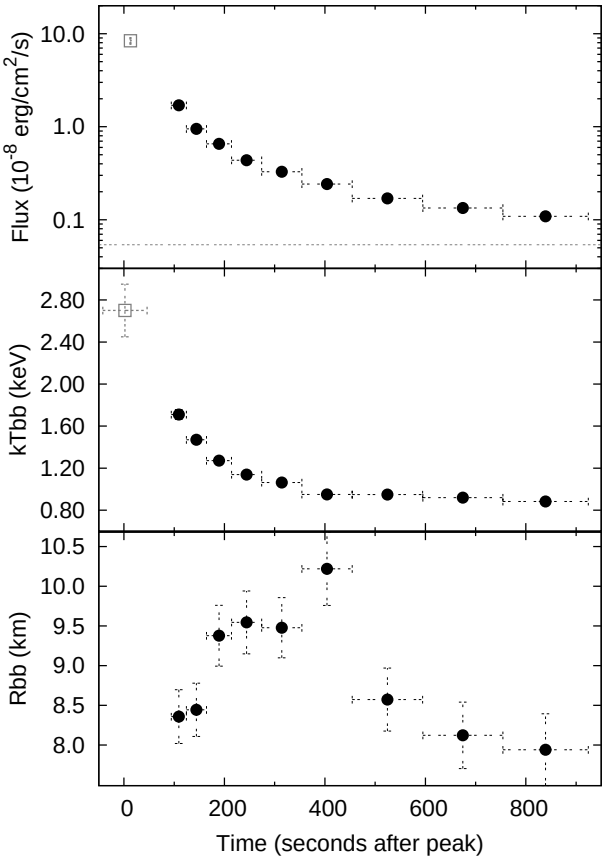

Figure 7.2: Time evolution of the bolometric flux *(top)*, black body temperature *(middle)* and black body radius *(bottom)* along the long X-ray burst. Filled dots correspond to our *Swift*-XRT measurements whereas empty squares show *Swift*-BAT results (Markwardt et al. 2008a). The horizontal dotted line on the top panel indicates the persistent flux. Error bars in the x axis represent the averaged intervals. The distance upper limit of 6.1 kpc has been used to obtain the black body radius.

the burst, and no spectral variations were seen in BAT data of that period (Markwardt et al. 2008a). Therefore the question of whether or not the burst showed photospheric radius expansion cannot be addressed. Going back to our XRT measurements, the radius of the black body appears to increase between ∼200 s and ∼500 s after the peak (Fig. 7.2). However, the large error affecting this parameter, the uncertainties on the underlying model (NS atmosphere in a dramatically-non-steady state) and the absence of an associated drop in the

black body temperature imply that this cannot be taken as concrete evidence of a physical increase in emitting area.

Table 7.3: Spectral evolution during the tail of the long burst. The best-fit spectral parameters and bolometric fluxes obtained from the time-resolved spectroscopy of the long burst are shown (see Sec. 7.3.2). Errors are 1-σ.

Interval nr.	Start[a] time (s)	End[a] time (s)	Rate[b] (c/s)	Temperature (keV)	Radius[c] (km)	Bolometric flux $(erg\ s^{-1}\ cm^{-2})$[d].
1	94	124	88.5	1.72 ± 0.05	8.4 ± 0.3	$(1.7\pm0.2)\times10^{-8}$
2	124	164	58.7	1.47 ± 0.04	8.5 ± 0.3	$(9.5\pm1.1)\times10^{-9}$
3	164	214	42.7	1.27 ± 0.03	9.5 ± 0.4	$(6.6\pm0.6)\times10^{-9}$
4	214	274	31.7	1.14 ± 0.03	9.6 ± 0.4	$(4.4\pm0.4)\times10^{-9}$
5	274	354	24.6	1.06 ± 0.02	9.6 ± 0.4	$(3.3\pm0.3)\times10^{-9}$
6	354	454	17.6	0.95 ± 0.02	10.3 ± 0.5	$(2.4\pm0.2)\times10^{-9}$
7	454	594	12.9	0.95 ± 0.02	8.7 ± 0.4	$(1.7\pm0.2)\times10^{-9}$
8	595	754	9.9	0.92 ± 0.02	8.2 ± 0.4	$(1.3\pm0.1)\times10^{-9}$
9	754	924	7.9	0.88 ± 0.02	8.0 ± 0.5	$(1.1\pm0.1)\times10^{-9}$
10	4138	4173	3.7	0.83 ± 0.12	6.4 ± 2.0	$(5.4\pm4.0)\times10^{-10}$

[a] In seconds since the burst peak.
[b] Average source count rate in the 0.7–10 keV band.
[c] Calculated using 6.1 kpc.
[d] The errors on the flux take into account the range (3.3–3.6 $\times10^{22}cm^{-2}$) of absorbing column densities reported (Markwardt et al. 2008a; Degenaar & Wijnands 2008).

We fit the flux decay of the long burst measured by the XRT and find that a simple power law with an index of -1.62±0.04 and normalization $(3.0\pm0.6)\times10^{-5}$ erg/cm^2/s gives a remarkably good description of the data (reduced χ^2 of 1.2; see Fig. 7.3). A simple or double exponential decay do not fit the data satisfactorily (reduced χ^2 of 22 and 7, respectively). We note that power law cooling is consistent with the expectations from models for long bursts (Cumming & Macbeth 2004).

The bolometric fluence measured by XRT during the long burst, after subtracting the persistent flux level, is 2.2×10^{-6} erg/cm^2. We integrate the flux decay along the data gap (Sec. 7.2.1) and estimate a fluence of 4.4×10^{-7} erg/cm^2 during that period. Adding the reported BAT fluence (Markwardt et al. 2008a) we find a total burst fluence of 3.5×10^{-6} erg/cm^2, which using the 6.1 kpc upper limit on the distance corresponds to a maximum radiated energy of 1.6×10^{40} erg.

We searched the XRT power spectra obtained during the tail of the long burst (Sec. 7.2.1) and found no strong pulsations or QPOs. This non-detection is not surprising given i) the distribution of burst oscillation frequencies (Galloway et al. 2008b) combined with our Nyquist frequency (∼280 Hz) and ii)

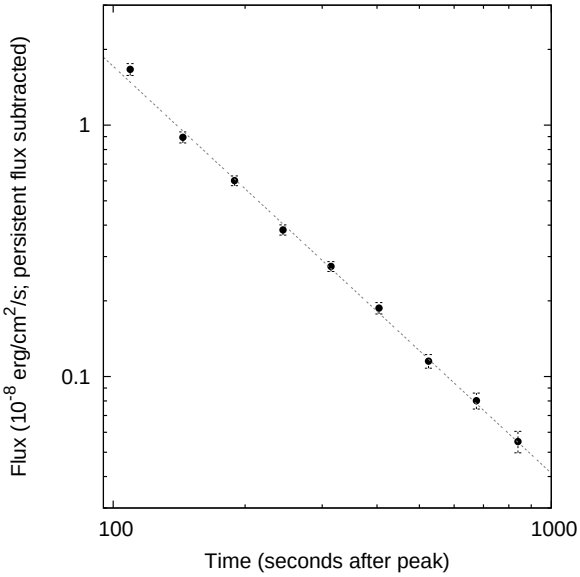

Figure 7.3: Fit to the long burst flux decay with a power law of index ∼1.6, together with the values of the baseline-subtracted bolometric flux.

the relatively low count rate collected by the XRT: for the maximum rate of ∼90 c/s, a 3σ detection of a 2 Hz wide QPO in a 2s FFT would require a fractional rms of at least ∼ 25% (van der Klis 1995b), much higher than the values usually measured (Galloway et al. 2008b).

7.4 Discussion

Theoretical modelling of long bursts suggests that they involve the build-up and ignition of a thick layer of He. One possibility is that the binary is ultracompact, so that the accreted fuel is almost pure He. At low accretion rates, and in the absence of heating from steady H burning, the temperature remains low and ignition can be delayed until a thick layer of He has built up (in't Zand et al. 2005; Cumming et al. 2006). Although He burning is quick, the cooling time is long because of the thickness of the layer in which the heat is deposited. Long bursts can also be triggered in systems accreting a mix of H and He if the source accretes at low rates, close to the point where H burning stabilises (Fujimoto et al. 1981; Peng et al. 2007; Cooper & Narayan 2007). In this case weak H flashes can build up He, which ignites sporadically, resulting in a long burst. Layer thickness again results in a long cooling time: but the

presence of H in the burning mix may also prolong nuclear energy generation.

Using the measured fluxes F from Table 7.2 and the upper limit on the distance d that we obtained from the long burst, we infer an upper limit on the global accretion rate $\dot{M} \approx 4\pi d^2 RF/GM$ of $3.7{\times}10^{-10}$ $M_\odot$ yr^{-1} (for a neutron star mass $M = 1.4M_\odot$ and radius $R = 10$ km) around the times of the two bursts. Assuming isotropy, this corresponds to an upper limit on the local accretion rate $\dot{m}$ of $1.9{\times}10^3$ g/cm^2/s, (2.5% of the Eddington rate for an Eddington luminosity of $1.6{\times}10^{38}$ erg/s). This accretion rate is close to the rate where H burning is expected to transition to stability (Fujimoto et al. 1981; Peng et al. 2007; Cooper & Narayan 2007), so we need to examine both scenarios for the generation of the long burst.

The BAT rise time of the long burst, ≈ 50 s, is much longer than most of the pure He bursts examined by in't Zand et al. (2007) and Falanga et al. (2008). This points to it being a mixed H/He type burst, triggered by H ignition, although we note that burst lightcurves can change considerably depending on the energy range where they are observed (see Chelovekov et al. 2006; Molkov et al. 2005).

We next consider the ignition conditions. The long burst had a total energy output of at most $E_b = 1.6 \times 10^{40}$ ergs (6.1 kpc distance). The corresponding ignition column depth $y = E_b(1+z)/4\pi R^2 Q_{\rm nuc}$, where z is the redshift, R the neutron star radius and $Q_{\rm nuc} = 1.6 + 4X$ MeV/nucleon the nuclear energy release, given an H fraction X at ignition (Galloway et al. 2008b). Assuming $z = 0.31$ (the redshift for a 1.4 $M_\odot$, 10 km radius neutron star) we derive an ignition depth $y = 3.9 \times 10^8$ g/cm^2 for solar abundances (X=0.7) and $y = 1.1 \times 10^9$ g/cm^2 for pure He (X=0). Ignition of pure He at this column depth would require a heat flux from the deep crust of $\gtrsim 2$ MeV/nucleon at 1% Eddington accretion rates (Figure 22, Cumming et al. 2006). This is higher than the crustal energy release of ~ 1.5 MeV/nucleon calculated by Haensel & Zdunik (1990, 2003), but close to the value of ~ 1.9 MeV/nucleon recently found by Gupta et al. (2007); Haensel & Zdunik (2008). Recent results by Horowitz et al. (2008) demonstrate that even larger amounts of heat may be released in the crust of an accreting neutron star. However, the high heat requirements certainly put some strong constraints on the pure He accretion scenario. Using the maximum local accretion rate calculated above ($1.9{\times}10^3$ g/cm^2/s), these ignition conditions predict minimum recurrence times $\Delta t_{\rm rec} = y(1+z)/\dot{m}$ of $\sim$10 days (X = 0) and $\sim$3 days (X = 0.7). The data provide only weak constraints on the time without bursts that elapsed before the long burst (we estimate that the source was in the field of view of BAT for about 20% of the two months analysed herein), but these numbers are at least compatible with the time since the start of the outburst.

The presence of a short, weaker burst at similar accretion rates is perhaps the strongest piece of evidence pointing to mixed H/He fuel. The short burst has a relatively slow rise time, ≈ 5 s, similar to that expected for mixed H/He bursts. The fact that it has a lower peak flux than the long burst also implies some H content: if the system were a pure He accretor we would expect both bursts to reach similar peak fluxes since He bursts, whether long or short, are expected to exhibit photospheric radius expansion (Cumming 2004). In the H-triggered burst scenario it is possible to have bursts with quite different properties at very similar accretion rates, as H burning transitions to stability (Cooper & Narayan 2007).

XTE J1701–407 increases the number of known NS-LMXBs in the interesting low accretion rate bursting regime. The balance of evidence suggests that it may be a good probe of thermonuclear burning near the boundary of stable H ignition. However, further observations, in particular better constraints on recurrence times and burst energetics, are required to confirm this picture. Identification of the companion star and determination of the orbital parameters may also be able to confirm whether or not the system is ultracompact.

Acknowledgements: ML would like to thank C. Markwardt and A. Cumming for stimulating discussions and N. Rea, E. Martínez and Ll. Guasch for their encouraging comments. RLCS acknowledges support from STFC.

8 Type I X-ray bursts, burst oscillations and kHz quasi-periodic oscillations in the neutron star system IGR J17191-2821

Diego Altamirano, Manuel Linares, Alessandro Patruno, Nathalie Degenaar, Rudy Wijnands, Marc Klein-Wolt, Michiel van der Klis, Craig B. Markwardt, Jean Swank

Monthly Notices of the Royal Astronomical Society, 2009, submitted

Abstract

We present a detailed study of the X-ray energy and power spectral properties of the neutron star transient IGR J17191–2821. We discovered four instances of simultaneous pairs of kilohertz quasi-periodic oscillations (kHz QPOs) and five thermonuclear type-I X-ray bursts. We found that the frequency difference between kHz QPOs is between 315 Hz and 362 Hz. We also detected burst oscillations at ~ 294 Hz during three of the X-ray bursts. Finally, we report on a faint and short outburst precursor, which occurred about two months before the main outburst. Our results on the broadband spectral and variability properties allow us to firmly establish the atoll source nature of IGR J17191–2821.

8.1 Introduction

Neutron star low–mass X-ray binaries (NS-LMXBs) have been extensively observed with the *Rossi X-ray Timing Explorer* (RXTE) during the last 13 years. These observations have led to important discoveries, such as persistent and intermittent pulsations in accretion-powered millisecond X-ray pulsars, nearly coherent oscillations during X-ray bursts and strong quasi-periodic variability on millisecond time-scales (the so called kilohertz quasi-periodic oscillations; kHz QPOs).

In neutron star LMXBs, the kHz QPOs are relatively narrow peaks in the power spectrum. They appear (sometimes) in pairs, are usually called L_u and L_ℓ (u and ℓ stand for upper and lower, respectively, based on their frequency). These QPOs are thought to reflect motion of matter around the neutron star at the inner edge of the accretion disk (see, e.g. Miller et al. 1998). While it is often assumed that at least one of them reflects the Keplerian frequency at the inner edge of the accretion disk (see e.g. review by van der Klis 2006), models have to still satisfactorily explain the presence and characteristics of both of them. Up to date, kHz QPOs with similar characteristics have been detected in about 30 neutron star sources.

Direct detection of coherent or nearly coherent pulsations is the only available method to measure the neutron star spin period in LMXBs. Ten NS-LMXBs out of more than 100 known (Liu et al. 2007) have shown coherent millisecond pulsations in their persistent emission; these systems are known as accretion-powered millisecond X-ray pulsars (AMXPs; see Wijnands 2005, for a review of the first six AMXPs discovered; for the last four see Kaaret et al. 2006, Krimm et al. 2007b, Casella et al. 2008 and Altamirano et al. 2008a). Sixteen sources to date (including the one presented in this paper) have shown nearly coherent millisecond oscillations during thermonuclear Type-I X-ray bursts (Watts et al. 2008a, 2009b). As the X-ray burst evolves, the oscillation frequency typically increases by a few Hz, approaching an asymptotic value (ν_{BO}) which is stable for a given source from burst to burst. This asymptotic frequency is thought to trace within a few Hz the spin frequency of the neutron star (Strohmayer et al. 1996b). In some AMXPs ν_{BO} is more stable in individual bursts. The AMXPs SAX J1808–3658 (Chakrabarty et al. 2003), XTE J1814–338 (Strohmayer et al. 2003), Aql X-1 (Casella et al. 2008) and most recently HETE J1900.1–2455 (Watts et al. 2009b) have all shown $\nu_s \simeq \nu_{BO}$, strongly supporting this connection between ν_{BO} and ν_s.

Since the discovery of burst oscillations and two simultaneous kHz QPOs in neutron star LMXBs, it was suggested that there was a relation between the neutron star spin frequency, ν_s, and the kHz QPO frequency difference

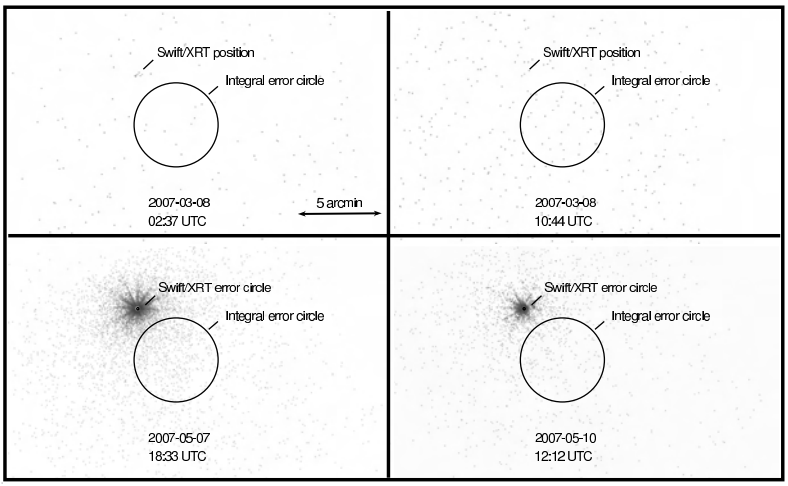

Figure 8.1: Swift/XRT images of IGR J17191–2821. The INTEGRAL error circle for the position is plotted in each case. The scale is the same for all panels. The source showed an outburst precursor or flare on March 8^{th}, as it was detected at 02:37 UT (upper-left panel) and undetected at 10:44 UT (upper-right panel). The source was in outburst in May (lower panels). See Section 8.3.1 for more details.

$\Delta\nu = \nu_u - \nu_\ell$. Although the frequency of the QPOs was found to vary ($150 \lesssim \nu_\ell \lesssim 900$ Hz and $350 \lesssim \nu_u \lesssim 1200$ Hz), at first instance $\Delta\nu$ was consistent with being constant[1] and equal to the asymptotic burst oscillation ν_{BO} (see, e.g., Strohmayer et al. 1996b). This was the main motivation for beat-frequency models such as the sonic-point model (Miller et al. 1998), which proposed that ν_u reflects the Keplerian frequency at the inner edge of the disk, and that ν_ℓ was the beat between ν_u and ν_s. As new observations revealed more sources showing both ν_{BO} and twin kHz QPOs, the relation became more complex (see Méndez & Belloni 2007 and van der Klis 2008 for a detailed historical overview). As a summary, NS-LMXBs are often classified as *fast* or *slow* rotators, depending on whether the spin frequency is higher or lower than ~ 400 Hz, respectively (Muno et al. 2001). It was found that generally the fast rotators follow $\Delta\nu \simeq \nu_s/2$, while slow rotators follow $\Delta\nu \simeq \nu_s$ (see Wijnands et al. 2003; Linares et al. 2005, and references therein). This of course implies that there is no one-to-one relation between the two quantities.

The question of whether $\Delta\nu$ and ν_s are physically related is still under debate. While current data might still be compatible with a bimodal rela-

[1] At least in those source in which ν_{BO} was known. For example, $\Delta\nu$ in the neutron star LMXB Sco X-1 is known to vary (see, e.g. van der Klis et al. 1997).

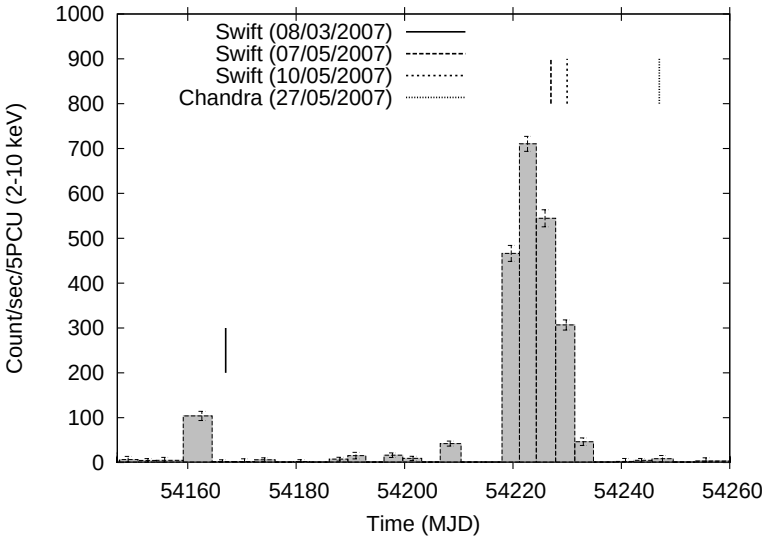

Figure 8.2: Light curve of IGR J17191–2821 as seen by the PCA bulge scan monitor program (Swank & Markwardt 2001). The times of the Swift and Chandra observations are marked with vertical lines.

tion, recent results suggest that this might not be the case. For example, Méndez & Belloni (2007) suggested that $\Delta\nu$ and ν_s are unrelated and that the division between fast and slow rotators may be just an effect of the low number of sources showing both phenomena (see also Yin et al. 2007). Recently, Strohmayer et al. (2008a) reported the discovery of burst oscillations at 414.7 Hz in the LMXB 4U 0614+091; if confirmed, these results would imply a spin frequency that is inconsistent with either $\Delta\nu \simeq \nu_s/2$ or $\Delta\nu \simeq \nu_s$ relations.

8.1.1 IGR J17191-2821

IGR J17191–2821 was discovered by the IBIS/ISGRI instrument aboard INTEGRAL during observations of the galactic bulge monitoring (Kuulkers et al. 2007b) conducted between the 2^{nd} and the 4^{th} of March, 2007 (Turler et al. 2007). The source was detected in the 20–40 and the 40-80 keV bands with significances of 10.4 and 4σ, and fluxes of 8.9 ± 0.9 and 5.8 ± 1.4 mCrab, respectively. The position of the source was first reported as (RA,DEC) = (259°.77, –28°.35) (J2000) with an accuracy of 2.5 arcmin.

On the 3^{rd} of March 2007, RXTE Galactic bulge scans (Swank & Markwardt 2001) detected a source at a position consistent with that reported by Turler et al. (2007) at an intensity of 10 ± 1 mCrab in the 2-10 keV band (Swank et al. 2007). Three days later, a follow-up RXTE observation found the source at

flux levels of about 0.5 mCrab; a day later the source was not detected, with a 3σ upper limit of 1.2 mCrab. 8 years of Galactic bulge scans were reanalyzed for contributions from a source at the position of IGR J17191–2821, but no flares brighter than 2 mCrab were found. These non-detections showed that this source is active relatively infrequently (Swank et al. 2007).

During further Galactic bulge scan observations on April 29^{th} and May 2^{nd} of 2007, IGR J17191–2821 was detected again, but at a level of 30 and 70 mCrab (2–10 keV). This suggested that the previous detection was a flare or outburst precursor. Several Astronomical Telegrams at this time communicated on the discovery of Type I X-ray bursts (Klein-Wolt et al. 2007b; Markwardt et al. 2007a), burst oscillations (Markwardt et al. 2007a) and several episodes of kHz QPOs (Klein-Wolt et al. 2007c).

In this work, we present an intensive study of Type I X-ray burst characteristics, burst oscillations and kHz QPOs of this newly discovered neutron star LMXB IGR J17191–2821.

8.2 Observations and data analysis

8.2.1 Light curves, color diagrams and timing analysis

We use data from the Rossi X-ray Timing Explorer (RXTE) Proportional Counter Array (PCA; for instrument information see Zhang et al. 1993; Jahoda et al. 2006). To study the long-term (days/months) L_x behavior of the source, we used the PCA monitoring observations of the galactic bulge (Swank & Markwardt 2001). These observations are performed nine months of the year (as parts of the months of November, December, January and June are excluded due to solar constraints). The PCA bulge scans are capable of distinguishing a source position error of about 15 arcmin. The bulge scan light curves are given in the $\sim 2-10$ keV energy band.

To study the short-term (minutes or less) variability, we use PCA pointed observations. For IGR J17191–2821 there were 18 observations in one data set (92052-10) containing ~ 2.5 to ~ 10 ksec of useful data per observation. We use the 16-s time-resolution Standard 2 mode data to calculate X-ray colors. Hard and soft color are defined as the 9.7–16.0 keV / 6.0–9.7 keV and 3.5–6.0 keV / 2.0–3.5 keV count rate ratio, respectively, and intensity as the 2.0–16.0 keV count rate. Type I X-ray bursts were removed, background was subtracted and deadtime corrections were made. Colors and intensities were normalized by those of the Crab Nebula (see Kuulkers et al. 1994; van Straaten et al. 2003, see table 2 in Altamirano et al. 2008c for average colors of the Crab Nebula per PCU).

For the Fourier timing analysis we used the Event mode E_125us_64M_0_1s. Leahy-normalized power spectra were constructed using data segments of 128 seconds and 1/8192 s time bins such that the lowest available frequency is 1/128 Hz and the Nyquist frequency 4096 Hz. No background or deadtime corrections were performed prior to the calculation of the power spectra. Unless stated explicitly, in our fits we only include those Lorentzians whose single trial significance exceeds 3σ based on the error in the power integrated from 0 to ∞. For the kHz QPOs, we report the centroid frequency ν_0, the full width at half maximum (FWHM) and the rms amplitude. The quoted errors use $\Delta\chi^2 = 1.0$. The upper limits quoted in this paper correspond to a 95% confidence level ($\Delta\chi^2 = 2.7$).

8.2.2 Energy spectra of the persistent emission

For the PCA, we used the Standard 2 data of PCU 2, which was active in all observations. The background was estimated using the PCABACKEST version 6.0 (see FTOOLS). We calculated the PCU 2 response matrix for each observation using the FTOOLS routine PCARSP V10.1. For the HEXTE instrument, spectra were accumulated for cluster B (as cluster A stopped rocking in October 2006), excluding the damaged detector and averaging both rocking directions to measure the background spectrum. Dead time corrections of both source and background spectra were performed using HXTDEAD V6.0. The response matrices were created using HXTRSP V3.1. For both PCA and HEXTE, we filtered out data recorded during, and up to 30 minutes after passage through the South Atlantic Anomaly (SAA). We only used data when the pointing offset from the source was less than 0.02 degrees and the elevation of the source respect to the Earth was greater than 10 degrees. Using XSPEC V11.3.2i (Arnaud 1996), we fitted simultaneously the PCA and HEXTE energy spectra using the 3.0–25.0 keV and 20.0–200.0 keV energy bands, respectively. We used a model consisting of a disk blackbody and a power law, absorbed with an equivalent Hydrogen column density of 0.3×10^{22} cm^{-2} (Klein-Wolt et al. 2007a), which gave a good fit in all the observations ($\chi^2/dof < 1.1$).

8.2.3 Type I X-ray bursts

We searched the Standard 1 mode data (2–60 keV, 0.125 seconds time resolution, no energy resolution) of the 18 observations. We found 5 Type I X-ray bursts (see Table 8.1).

We searched each burst for coherent pulsations using the Z_n^2 statistic (Strohmayer & Markwardt 1999). We computed Z_1^2 (i.e. assuming that the

signal is sinusoidal) throughout the bursts using a sliding 2 seconds window with a step of 0.125 sec. The Z_1^2 statistic has the same statistical properties as a Leahy normalized power spectrum, which means that for a purely random Poisson process, the powers follow a χ^2 distribution with 2 degrees of freedom (Strohmayer & Markwardt 1999). We searched the 30–4000 Hz frequency range in the 2–60 keV band and in narrower energy bands (Sec. 8.3.2).

We also created energy spectra every 0.25 sec from the Event mode (E_125us_64M_0_1s) data of all the PCUs that were on during the burst. Given the high count rates during the peak of the bursts, we corrected each energy spectrum for dead-time using the methods suggested by the RXTE team[2]. For each energy spectrum, we created the corresponding response matrix using the latest information available on the response of the instrument at the relevant times. As is common practice, we used as background the energy spectrum of the persistent emission taken seconds before each burst. (We used 100 sec of the persistent emission to calculate the spectrum. However, we found no significant differences in the fits when the persistent-emission before or after the burst was used, or when using data-segments of different lengths -between 100 and 500 seconds-). We used a black-body model to fit the resulting burst spectra[3].

8.3 Results

8.3.1 Position of the source

Swift observed the source twice on March 8^{th} 2007 (at 02:37 UT for a total of $\sim$ 800 sec, and at 10:44 UT for a total of $\sim$ 1600 sec – both observations where performed in in PC mode). These are the only Swift observations performed

[2] `http://heasarc.gsfc.nasa.gov/docs/xte/recipes/pca\_deadtime.html`

[3] We assumed that the X-ray spectra after the persistent emission has been subtracted are Planckian and that the observed luminosity of the source is:

$$L = 4\pi\sigma T^4 R^2,$$

so the unabsorbed bolometric X-ray flux may be determined using

$$F_{bol} = \sigma T^4 (R/D)^2,$$

where σ is the Stefan-Boltzmann constant, T is the black-body temperature, R the neutron star photosphere radius, and D the distance to the source. The ratio $(R/D)^2$ is the normalization of the black-body model we used (*bbodyrad* – see Xspec manual for details). We note that X-ray burst spectra are generally well described by black-body emission, however, the emission from the neutron star and its environment (e.g. accretion disk) is expected to be more complex than simple black-body emission (see, e.g., van Paradijs 1982; London et al. 1984; Kuulkers et al. 2003, and references therein).

before the bright outburst (see Section 8.3.4). The observations were taken in Photon Counting mode and did not show a source *within* the INTEGRAL error circle with an upper limit of 0.0021 cnts s^{-1} (at a 95% confidence level). Assuming a galactic absorption of 3.4×10^{21} cm^{-2} and a photon index of 1.8, this countrate translates into an upper limit of $\sim 8.7 \times 10^{-14}$ erg s^{-1} cm^{-2} on the unabsorbed flux (approximately 0.004 mCrab in the 2-10 keV range). We found a source in the first Swift observation (i.e. on March 8^{th} at 2:37 UT) located at a distance of about 3.5 arcminutes from the INTEGRAL position. Its coordinates are (RA, DEC) = (259.8114, -28.3005) (J2000), with an error of $\sim$ 9 arcsec. We measured an average count rate of 0.0087 cnts s^{-1}, which corresponds to an unabsorbed flux of 3.6×10^{-13} erg s^{-1} cm^{-2} or 0.02mCrab (2-10 keV, assuming the same Nh and photon index as above). In the second Swift observation this source is not significantly detected (a total of three photons within a 10 pixel source error circle and zero from a background region 3 times as large). We place a 95% confidence upper limit on the 2-10 keV unabsorbed flux of $\sim 2.0 \times 10^{-13}$ erg s^{-1} cm^{-2} (employing PIMMS[4] for an absorbed power-law spectrum with $N_h = 3.4 \times 10^{21}$ cm^{-2} and a photon index of 1.8, and applying the prescription for low number statistics given by Gehrels 1986). In Figure 8.1 we show the Swift/XRT images of the region around the source for the 2 observations on March 8^{th} (upper panels). For comparison, in the lower panels we show the Swift/XRT images of two observations during IGR J17191–2821 outburst (May 7th and 10th, 2007).

As noted by Klein-Wolt et al. (2007a), the formal INTEGRAL error circle on the position of IGR J17191–2821 would suggest that the faint source we detected with Swift is unrelated to IGR J17191–2821 (its position is 1 arcminute outside the INTEGRAL error circle for the position of IGR J17191–2821, see Figure 8.1). However, given the systematic uncertainties in the INTEGRAL position, both sources are probably one and the same. We note that this is not the first case in which the true position of a transient laid outside the reported INTEGRAL-IBIS/ISGRI error circle (see e.g. Kuulkers et al. 2007a).

8.3.2 Thermonuclear X-ray bursts and the distance to the source

We found 5 Type I X-ray bursts (see Table 8.1). All bursts showed similar temperature, radius and bolometric flux profiles (not shown). The temperature and flux profiles were all single peaked, and reached their maxima within a second. The maximum temperature (kT) was always between 2 and 3 keV and the peak bolometric fluxes were in the $2-3 \times 10^{-8}$ erg s^{-1} cm^{-2} range (Ta-

[4] `http://heasarc.gsfc.nasa.gov/Tools/w3pimms.html`.

ble 8.1). In all cases, the black-body radius remained approximately constant after the peak and was usually constrained between 5 and 10 km (assuming a distance of 11 kpc). None of the bursts showed indications of photospheric radius expansion. By using the highest measured bolometric peak flux of 3×10^{-8} erg s^{-1} cm^{-2} we can estimate an upper limit on the distance. We find a distance $D < 11$ kpc when using the empirically determined Eddington luminosity of 3.79×10^{38} erg s^{-1} (for bursts showing photospheric radius expansion – Kuulkers et al. 2003). Using a more complex approximation[5] and standard values for the mass and the radius of the neutron star (i.e. $M_{NS} = 1.4 M_{\odot}$ and $R = 10$ km), we found $D < 8.6$ and $D < 6.6$ for hydrogen mass fractions of $X = 0$ and $X = 0.7$, respectively. Higher values of R give higher upper limits.

Table 8.1: X-ray bursts in IGR J17191–2821.

Number	ObsID (92052-10)	Start time of the burst (UT, 2007)	Num. of PCUs on	Flux[a] (10^{-8} erg s^{-1} cm^{-2})	Osc. (yes/no)	Osc. rms amplitude[b] (2–17 keV)
1	-01-00	May 4 02:32:06	2	2.5 ± 0.3	yes	$6.9 \pm 0.6\%$
2	-05-00	May 7 02:39:39	2	2.9 ± 0.3	yes	$5.0 \pm 1.0\%$
3	-03-01	May 7 05:51:12	2	2.7 ± 0.3	no	$< 3\%$
4	-06-00	May 8 17:08:53	3	2.6 ± 0.2	yes	$10.2 \pm 1.5\%$
5	-06-01	May 8 20:38:44	2	2.1 ± 0.3	no	$< 3\%$

[a]:Bolometric peak flux.
[b]:Integrated amplitude of the oscillations in the 2–17 keV range.

8.3.3 kHz QPOs

We searched the averaged power spectrum of each observation for the presence of significant kHz QPOs at frequencies $\gtrsim 200$ Hz. In each case, we fitted the power spectra between 200 and 4000 Hz with a model consisting of one or two Lorentzians and a constant to account for the presence of QPOs and Poisson noise, respectively. We found that 12 out of the 17 observations show significant QPOs in the 605-1185 frequency range. In 4 observations we detected 2

[5]The approximation was recently used by Galloway et al. (2008b) to compare a sample of more than a thousand X-ray burst from different sources. The distance is given by:

$$D = 8.6 \cdot \left(\frac{Flux_{Bol}}{3 \cdot 10^{-8} erg\ cm^{-2}\ s^{-1}}\right)^{-1/2} \cdot \left(\frac{M_{NS}}{1.4 M_{\odot}}\right)^{1/2} \cdot \cdot \left(\frac{1+z(R)}{1.31}\right)^{-1/2} \cdot (1+X)^{-1/2} kpc$$

where M_{NS} is the mass of the neutron star in solar masses, X is the mass fraction of hydrogen in the neutron star atmosphere and z(R) is the term that takes into account the gravitational redshift at the photosphere (were $1 + z(R) = (1 - 2GM_{NS}/Rc^2)^{-1/2}$, G is the gravitational constant, c the speed of light and R the radius measured at the photosphere – see Galloway et al. 2008b).

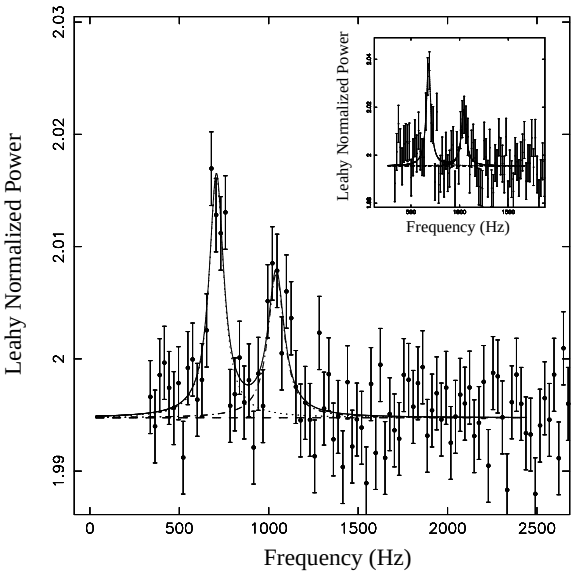

Figure 8.3: kHz QPOs after the shift–and–add. The lower kHz QPO was shifted to the arbitrary frequency of 700 Hz (see Section 8.3.3). Inset: kHz QPOs in observation 92052-10-05-00. See also Table 8.2.

simultaneous kHz QPOs (see Table 8.2). The lower kHz QPO frequency was between 680 and 870 Hz, with single trial significance between 5.7 and 10σ. The upper kHz QPO frequency was between 1037 and 1085 Hz, with single trial significances between 3.0 and 3.7σ. $\Delta\nu$ showed no significant changes and was always consistent with 350 Hz (see Table 8.2).

We tried to better constrain $\Delta\nu$ by using the shift–and–add method as described by Mendez et al. (1998b). We first tried to trace the detected kilohertz QPO using a dynamical power spectrum (e.g. see figure 2 in Berger et al. 1996) to visualize the time evolution of the QPO frequency, but the signal was too weak to be detected on timescales shorter than the averaged observation. Therefore, for each observation we used the fitted averaged frequency to shift each lower kHz QPO to the arbitrary frequency of 700 Hz. Next, the shifted, aligned, power spectra were averaged. The average power spectrum was finally fitted in the range 300–2048 Hz so as to exclude the edges, which are distorted due to the shifting method. To fit the averaged power spectrum, we used a function consisting of two Lorentzians and a constant to fit the QPO and the Poisson noise, respectively. In this case, the averaged $\Delta\nu$ is 332 ± 16 Hz. In Figure 8.3 we show the shift–and-added power spectrum and a representative example of the single observation power spectrum with two kHz QPOs (see inset).

Table 8.2: Observations and kHz QPOs.

ObsID (92052-10)	MJD (days)	Aver. Cts/s[a] /PCU2	PCUs on[b]	Lower kHz QPO ν (Hz)	Lower kHz QPO FWHM (Hz)	Lower kHz QPO rms (%)	Upper kHz QPO ν (Hz)	Upper kHz QPO FWHM (Hz)	Upper kHz QPO rms (%)	$\Delta\nu$ (Hz)
-01-00	54224.09	182	2	–	–	–	–	–	–	–
-02-00	54225.07	170	3-4	870 ± 1	11 ± 1.7	8.5 ± 0.4	1185 ± 50	220 ± 94	9.2 ± 1.5	315 ± 50
-02-01	54225.14	188	3	866 ± 3	38 ± 6	9.2 ± 0.6	–	–	–	–
-03-00	54226.21	172	1-3	881 ± 10	132 ± 23	15 ± 1	–	–	–	–
-05-00	54227.10	142	2-3	681 ± 5	55.2 ± 15	10.3 ± 0.9	1043 ± 10	60^{+27}_{-19}	8.4 ± 1.1	362 ± 11
-03-01	54227.23	148	2	730 ± 1	13.2 ± 2.7	9.7 ± 0.6	1075 ± 12	55^{+32}_{-22}	8.5 ± 1.3	345 ± 12
-04-00	54228.01	156	3	891 ± 3	37.7 ± 7.5	9.4 ± 0.6	–	–	–	–
-04-01	54228.20	151	2-3	838 ± 1	25 ± 4	9.3 ± 0.4	–	–	–	–
-06-00	54228.70	129	2-3	946 ± 20	151^{+66}_{-41}	10.6 ± 1.2	–	–	–	–
-06-01	54228.90	130	2-3	702 ± 3	37 ± 7	10.4 ± 0.6	1037 ± 15	88^{+43}_{-27}	8.8 ± 1.1	335 ± 15
-07-00	54229.06	105	1-2	884 ± 13	108^{+53}_{-31}	15 ± 2	–	–	–	–
-07-01	54229.98	72	2	706 ± 10	83 ± 25	18 ± 2	–	–	–	–
-05-01	54230.04	70	2	682 ± 20	172^{+78}_{-55}	22.4 ± 2.8	–	–	–	–
-08-00	54231.09	46	2	–	–	–	–	–	–	–
-08-01	54231.75	27	2-3	–	–	–	–	–	–	–
-09-00	54232.01	23	3	–	–	–	–	–	–	–
-09-01	54232.08	21	3-4	–	–	–	–	–	–	–

[a]: Background and deadtime corrected averaged count rate for PCU2; this PCU was on during all observations.
[b]: In case the number of active PCUs changed, we report the minimum and maximum number.

8.3.4 Outburst evolution

Figure 8.2 shows the PCA light curve of IGR J17191–2821 as seen by the PCA bulge scan monitor program (Swank & Markwardt 2001). While a precursor of the outburst (see Section 8.1.1) occurred at MJD 54162.6, the full X-ray outburst did not start until 54 days later (i.e. MJD 54216); it lasted for about 30 days.

On MJD 54247 (May 27th, 2007) the source was not detected anymore with RXTE, and a Chandra/HRC-I observation was performed. As reported by Chakrabarty et al. (2007), the source was not detected in the 1.1 ks observation within the 30 arcsec of the Swift/XRT position (see Section 8.3.1). These authors estimated an upper limit on the 0.3–10 keV unabsorbed flux of $< 8.3 \times 10^{-14}$ erg s^{-1} cm^{-2}.

In Figure 8.4 we show the persistent unabsorbed 2-200 keV flux (panel *a*), power law index (panel *b*), strength of the broad band noise (panel *c*) and kHz QPO frequency (panel *d*) as a function of time during the ∼3 weeks of the outburst from which RXTE pointed observations are available. The source reached a maximum flux of $\sim 2.5 \times 10^{-9}$ erg cm^2 s^{-1}. Assuming $D < 11$ kpc (see Section 8.3.2), we place an upper limit on the outburst peak luminosity of 4×10^{37} erg s^{-1}. In panel *a* of Figure 8.4 we also plot the (Type I) X-ray burst bolometric peak fluxes at the time they occurred (as detected by RXTE).

Due to the relatively low count rates collected by the PCA, the average power spectrum of each observation had low statistical quality. However, in the brightest (and softest) observations we found traces of the so-called very low frequency noise (VLFN). A steep power-law rised below 1 Hz towards the lowest frequencies, this VLFN is a typical signature of the so called "banana branch" (soft state) of atoll sources (see, e.g., van der Klis 2006, for a review). When comparing the results showed in the different panels of Figure 8.4, we found that the 5-50 Hz averaged fractional rms amplitude is anti-correlated with the source luminosity, whereas the frequencies of both kHz QPOs showed no obvious trend. The spectral index was clearly anti-correlated with the strength of the variability (i.e, correlates with luminosity). This is similar to what has been found in other atoll sources (see, e.g., van der Klis 2006, for a review), where the strength of the variability and the spectral index trace the changes in the timing and spectral state during the outburst. By studying the time evolution of these two quantities (Fig. 8.4) we found that the source was initially in the soft (banana) state and showed a failed transition to the hard (extreme island) state around MJD 54226. After this, it re-brightened and returned to the soft state. On MJD 54228 (i.e. two days later) the luminosity reached a secondary peak and started to decline, while the source gradually transitioned from the soft (banana) state to the hard (extreme island) state.

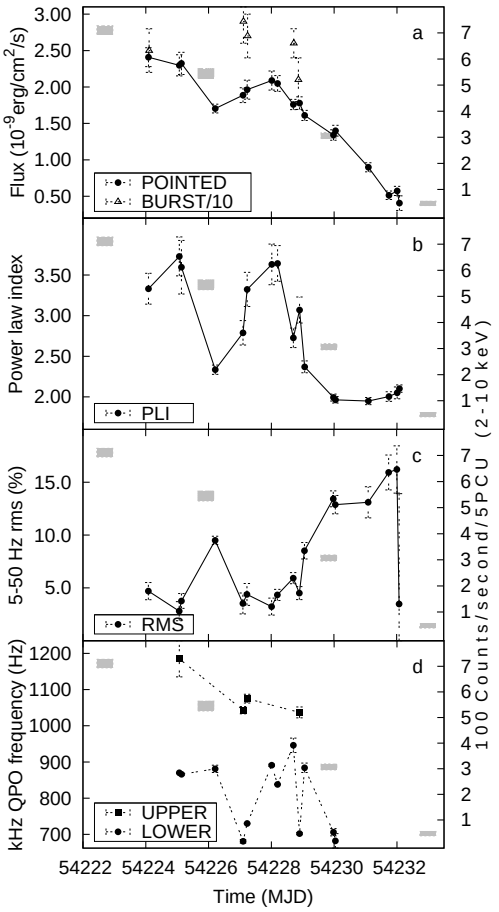

Figure 8.4: Spectral and timing properties along the outburst of IGR J17191–2821. From top to bottom, *a)*: 2-200 keV unabsorbed persistent flux (filled circles) and bolometric peak flux of the type I X-ray bursts detected by the PCA (open triangles; flux values are divided by ten for plotting purposes); *b)*: power law index obtained from the broad band spectral fits; *c)*: fractional rms amplitude of the variability between 5 and 50 Hz in the ∼2.5-45 keV energy band and *d)*: frequencies of the upper (squares) and lower (circles) kHz QPOs detected during the outburst. The grey rectangles show the flux measured by the PCA Galactic bulge scans (right axis; see also Figure 8.2).

Finally IGR J17191–2821 faded below the detection limit of RXTE-PCA. The timing and spectral properties (and evolution) allow us to firmly establish the atoll source nature of IGR J17191–2821.

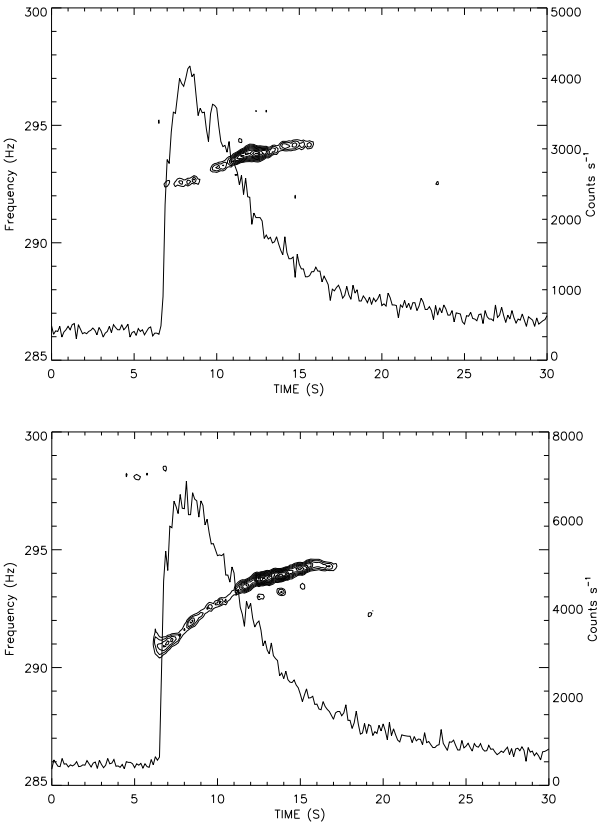

Figure 8.5: Lightcurve and dynamical power spectra (2–60 keV) for bursts 1 and 4 (upper and lower panel, respectively – see also Table 8.1). The dynamical power spectra were created using overlapping 2 s windows, with new windows starting at 0.125 s intervals. We used a Nyquist frequency of 4096 Hz. The contours show Leahy normalized powers between 20 and 60, increasing in steps of 5.

8.3.5 Burst oscillations

By applying the Z_1^2 method (see Section 8.2.3) on the 2–60 keV X-ray burst data, we discovered highly significant nearly-coherent oscillations in 2 of the 5 X-ray bursts (Burst 1 and 4 in Table 8.1). For the remaining 3 bursts, we repeated the Z_1^2 analysis using only data in different energy sub-bands. We found that the oscillations were significantly detected also in burst number 2, but only in the 10–25 keV range. The oscillations are not significantly detected in either burst 3 or 5. Fractional rms amplitudes (averaged over the period the signal was significantly detected) and upper limits are given in Table 8.1. In Figure 8.5 we show the dynamical power spectra of bursts 1 and

4 (upper and lower panels, respectively) in the 2–60 keV range. Maximum Z_1^2 powers of ~ 63 were found in both cases. As can be seen, the frequency of these oscillations increases with time as usually seen for burst oscillations during Type I X-ray bursts (see, e.g., Strohmayer 2001, for a review). During bursts 1 and 4 , the frequency drifts from $\sim$291Hz and $\sim$ 292.5Hz, respectively, until it reaches a frequency between 294 and 294.5 Hz.

8.3.6 The energy dependence of the burst oscillations

We analyzed the energy dependence of bursts 1 and 4 which showed the strongest oscillations – see Table 8.1. We split the data in six energy bands (from 2.5 keV to 17 keV), and calculated the amplitude of the pulsations in each band. To create a pulse profile in each energy band, we selected all the data with a significant pulse detection in the corresponding power spectrum, and explored the $P - \dot{P} - \ddot{P}$ space around a given initial guess value for the pulse period (obtained from the power spectrum). $\dot{P}$ and $\ddot{P}$ were initially set to zero. We note that $\dot{P}$ and $\ddot{P}$ do not represent true spin changes of the neutron star, but comprise all the frequency variations due, primarily, to the burst oscillation drift seen in the data. $\dot{P}$ and $\ddot{P}$ are therefore useful to align the phases of the pulsations (folded in a profile of 32 bins) for each energy band. We then fitted the pulse profiles with two sinusoids representing the fundamental and the 1st overtone of the burst oscillations. The errors on the fractional amplitudes are calculated using a $\Delta\chi^2 = 1$. Upper limits are at a 95% confidence level (i.e. using $\Delta\chi^2 = 2.7$). We found no significant second harmonic in any of the energy bands we chose for either burst, with rms amplitude upper limits in the $2.5 - 17$ keV range of 3.7% and 2.0% for bursts 1 and 4, respectively. The energy dependence of the burst oscillation rms amplitude is shown in Figure 8.6. The fractional amplitude of the fundamental increases slightly with energy; a possible dip in the 5-7 keV band is seen in both bursts. No significant phase lags were detected.

8.4 Discussion

The energy and broadband power spectra of IGR J17191–2821 evolved in a manner consistent with that seen in other neutron star LMXBs: the source is soft when the flux is high and hard when the flux is low, and near the end of the outburst it shows the hardest spectra and strongest variability, with an rms amplitude above 15%. We detected thermonuclear X-ray bursts, some of them showing burst oscillations at $\nu_{BO} \sim 294$ Hz. This ν_{BO} is within the the range observed in other sources (i.e. 45–619 Hz, see, e.g. Watts et al. 2008a,

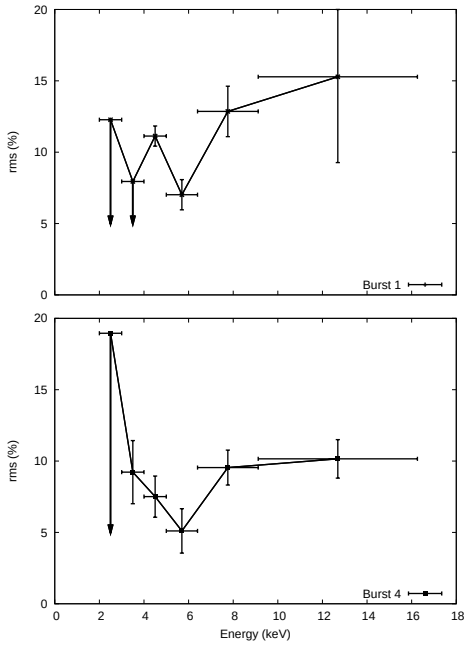

Figure 8.6: Fractional rms amplitude versus energy for the oscillations in X-ray bursts 1 and 4 (See Table 8.1). Arrows mark upper limits at 95% confidence level.

and references within). The energy dependence of the burst oscillations is consistent with a slight increase at higher energies. This is similar to what has been found for burst oscillations in other NS systems (see, e.g., Muno et al. 2003). We also detected several episodes of kHz QPOs. When two were detected simultaneously, the difference in frequency was approximately constant (See Table 8.2). These results allow us to firmly establish the atoll source nature of IGR J17191–2821.

Two months before the main outburst, the source exhibited a very brief (only days) event which was nearly an order or magnitude less luminous. It is unclear what the relation of this event is with respect to the main outburst. However, we note that similar precursors have been seen before (see, e.g., Degenaar & Wijnands 2009). To our knowledge, no systematic search has been performed in order to quantify how common these precursors are and how they can be explained in the commonly used disk-instability models proposed for outbursts of X-ray binaries (see Lasota 2001, for a review).

There are presently 12 LMXBs with reported measurements of $\Delta\nu$ whose spin can be estimated from either burst oscillations or from pulsations in their persistent X-ray emission (van der Klis 2008, for a recent overview). In

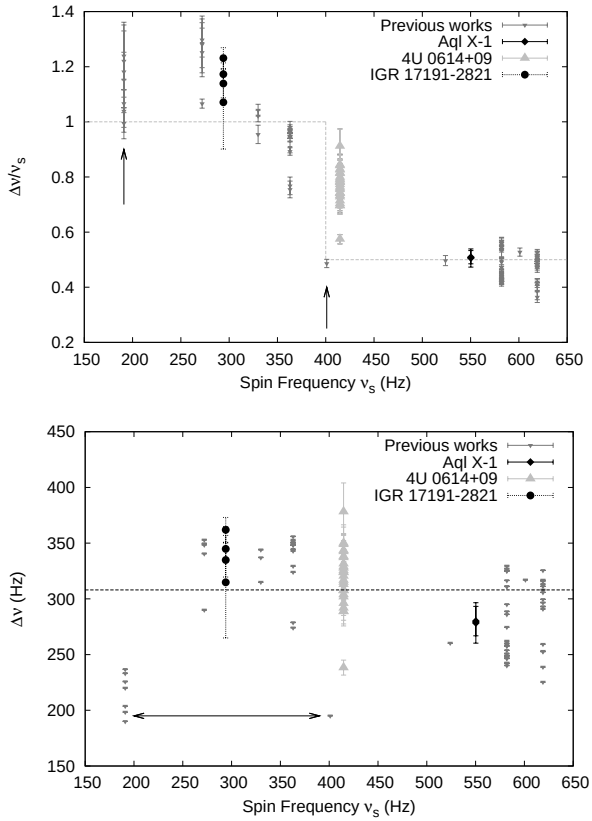

Figure 8.7: In the upper panel we plot the ratio between the individual measurements of $\Delta\nu = \nu_u - \nu_\ell$ and the spin frequency ν_s as a function of ν_s (cf. van der Klis 2006; Méndez & Belloni 2007; van der Klis 2008). Spin frequencies are as estimated from the persistent pulsations observed in AMXPs (marked with the arrows) or from burst oscillations in the non-pulsating sources. The dashed line shows the step function $S(\nu_s) = 1$ for $\nu_s \leq 400$ Hz; $S(\nu_s) = 0.5$ for $\nu_s > 400$ Hz. The lower panel shows the same data as above. The horizontal dashed line corresponds to a constant $\Delta\nu = 308$ Hz (Méndez & Belloni 2007). For 4U 0614+09 we used the tentative burst oscillation frequency of 414.7 Hz (Strohmayer et al. 2008a) and the kHz QPOs measurements reported by van Straaten et al. (2000). For Aql X-1 we used $\nu_s = 550$ Hz (e.g. Casella et al. 2008, and references within) and the tentative $\Delta\nu$ measurements reported by Barret et al. (2008). IGR J17191–2821 data are from this work.

Figure 8.7 (upper panel) we plot $\Delta\nu/\nu_s$ vs. ν_s for all these sources (cf. van der Klis 2006; Méndez & Belloni 2007; van der Klis 2008). The dashed line represents a step function: $\Delta\nu/\nu_s \sim 1$ for the slow rotators (< 400 Hz) and $\Delta\nu/\nu_s \sim 0.5$ for the fast rotators (> 400 Hz). Although most of the data seems to be consistent with this scheme (and our data of IGR J17191–2821

are as well), certainly there are points that do not follow this relation. A clear example is given by the neutron star 4U 0614+09. A tentative $\sim$ 414.7 Hz burst oscillation frequency was recently reported for this source (Strohmayer et al. 2008a, note that we quote this value as tentative given that it has been detected only once, the signal showed no frequency drift as expected from burst oscillations, and it was the first and only detection to date of burst oscillations with the Burst Alert Telescope on board the Swift telescope). As shown in Figure 8.7 this burst oscillation frequency is very close to the discontinuity of the step function (although given the present data, the discontinuity of the step function could be anywhere between $\sim$ 360 and 401 Hz). At the same time, $\Delta\nu/\nu_s$ covers almost the complete 0.5-1 range (van Straaten et al. 2000; Boutelier et al. 2008).

Méndez & Belloni (2007) have recently suggested that $\Delta\nu$ and ν_s are unrelated and that the division between fast and slow rotators may be just an effect of the low number of sources showing both phenomena (see also Yin et al. 2007). In the lower panel of Figure 8.7 we show $\Delta\nu$ and ν_s for the same data plotted in the upper panel. The dashed line in this panel corresponds to the average $\Delta\nu = 308$ Hz suggested by Méndez & Belloni (2007). As can be seen, the $\Delta\nu$ range of most sources overlaps with this constant value, except for the two AMXPs SAX J1808.4–3658 and XTE J1807–294, for which $\Delta\nu$ falls clearly below 300 Hz. The discrepancy is solved, if the data for these two sources are multiplied by a factor of 1.5. This was first suggested by Méndez & Belloni (2007) based on the works of van Straaten et al. (2005) and Linares et al. (2005)[6] . We note that not all AMXPs are affected by the same multiplicative factor (van Straaten et al. 2005), and furthermore, that the factor might be independent of whether the neutron star pulsates or not (Altamirano et al. 2005).

Clearly, the present data are not enough to draw any final conclusions, so the detection of ν_s, ν_{BO} and $\Delta\nu$ in other sources is necessary. The new instrument ASTROSAT (an Indian multiwavelength Astronomy Satellite), which is planned to be launched in 2010, will play a major role, as it is likely to increase the sample of sources with both spin frequency and kHz QPOs measurements.

[6]Previous works have shown that the frequencies of the variability components observed in atoll sources follow a universal scheme of correlations when plotted versus ν_u (see e.g. van Straaten et al. 2002, 2003; Reig et al. 2004; Altamirano et al. 2008c, and references therein). The two AMXPs SAX J1808.4–3658 and XTE J1807–294 show similar relations. However, the relations for these two sources are shifted with respect to those of the other sources (van Straaten et al. 2005; Linares et al. 2005). This shift is between the frequencies of the low-frequency components and ν_u by a factor around 1.5 (1.45 and 1.59 for SAX J1808.4–3658 and XTE J1807–294, respectively) and between ν_ℓ and ν_u by a similar factor.

9 Discovery of burst oscillations in the intermittent accretion-powered millisecond pulsar HETE J1900.1–2455

Anna L. Watts, Diego Altamirano, Manuel Linares, Alessandro Patruno, Piergiorgio Casella, Yuri Cavecchi, Nathalie Degenaar, Nanda Rea, Paolo Soleri, Michiel van der Klis, Rudy Wijnands

The Astrophysical Journal Letters, 2009, 698, L174

Abstract

We report the discovery of burst oscillations from the intermittent accretion-powered millisecond pulsar (AMP) HETE J1900.1–2455, with a frequency ~ 1 Hz below the known spin frequency. The burst oscillation properties are far more similar to those of the non-AMPs and Aql X-1 (an intermittent AMP with a far lower duty cycle), than those of the AMPs SAX J1808.4–3658 and XTE J1814–338. We discuss the implications for models of the burst oscillation and intermittency mechanisms.

9.1 Introduction

There are two ways in which we can measure the spin of rapidly rotating accreting neutron stars: via accretion-powered pulsations (due to magnetic channeling of infalling material), or burst oscillations (coherent pulsations seen during the thermonuclear explosions of accreted fuel that give rise to Type I X-ray bursts). The mechanism that generates the brightness asymmetries

responsible for burst oscillations is not yet known. Once understood, however, it should shed light on the thermonuclear burning process and the composition of the outer layers of the neutron star (Strohmayer & Bildsten 2006; Watts 2008).

Burst oscillations often drift upwards in frequency by a few Hz during a burst. However the stability of the asymptotic frequency for a particular source (Muno et al. 2002a), and the detection of the same frequencies in superbursts as well as Type I bursts (Strohmayer & Markwardt 2002), suggested even at an early stage that burst oscillation frequency might be (to within a few Hz) the spin frequency. This was confirmed in 2003 with the discovery of burst oscillations at or within a few Hz of the spin frequency in the accretion-powered millisecond pulsars (AMPs) SAX J1808.4–3658 and XTE J1814–338 (Chakrabarty et al. 2003; Strohmayer et al. 2003). The near identity of burst oscillation frequency and spin frequency is now the major constraint on models for the burst oscillation mechanism.

The AMPs are particularly useful when investigating the burst oscillation mechanism, since they are the only sources in which we can gauge the effects of the magnetic field and asymmetric fuel deposition. They are also the only stars where we can measure the size and sign of the small offset between the spin and burst oscillation frequency. However both SAX J1808.4–3658 and XTE J1814–338 have burst oscillations with quite atypical properties compared to the other sources (Section 9.3). It is not yet clear whether we are seeing a continuum of behavior (which could be explained by one burst oscillation mechanism) or completely separate classes.

The picture has evolved in the last three years with the discovery of three intermittent AMPs: HETE J1900.1–2455, SAX J1748.9–2021 and Aql X-1 (Kaaret et al. 2006; Galloway et al. 2007; Gavriil et al. 2007; Altamirano et al. 2008a; Casella et al. 2008). Unlike the other AMPs these sources show accretion-powered pulsations only sporadically. What cause the intermittency is also not known, with models including sporadic obscuration of the magnetic poles (Göğüş et al. 2007 and references therein), wandering of the accretion funnel and hence the hot spot around the magnetic pole (Romanova et al. 2003, 2004; Lamb et al. 2008), or magnetic field burial (Cumming et al. 2001; Cumming 2008).

If the magnetic field is what makes the burst oscillations of the AMPs so different from those of the other stars, then an intermittency mechanism that affects the magnetic field may also influence burst oscillation properties. Burst oscillations from the intermittent AMPs (all of which burst) are therefore an important piece of the puzzle. Until now, however, only Aql X-1 has shown burst oscillations, at ≈ 0.5 Hz below the spin frequency (Zhang et al. 1998a;

Casella et al. 2008). The properties of the Aql X-1 burst oscillations are very similar to those of the non-AMPs: however this source has the lowest pulsation duty cycle of any of the intermittent AMPs. In this Letter we report the discovery of burst oscillations from the intermittent AMP HETE J1900.1–2455 (Watts et al. 2009a), and consider the implications for the burst oscillation and intermittency mechanisms.

9.2 Burst analysis

HETE J1900.1–2455 was first detected in June 2005, and has remained in outburst ever since apart from a 3 week period of quiescence in 2007 (Degenaar et al. 2007). It was quickly identified as an AMP with a spin frequency of 377.3 Hz, an orbital period of 83.3 minutes, and a low ($< 0.1 M_{\odot}$) mass companion (Kaaret et al. 2006). It is at a distance of ≈ 5 kpc, determined from Eddington limited X-ray bursts (Galloway et al. 2008b). Accretion-powered pulsations of low fractional amplitude ($\lesssim 3$ %) were detected sporadically during the first two months of outburst, but have not been seen since (Galloway et al. 2007, 2008a). There is some evidence that the intermittent appearance of the accretion-powered pulsations may be related to the occurrence of Type I X-ray bursts, but whether the relationship is causal is not clear (Galloway et al. 2007). From 2005–2008 several X-ray bursts from this source were detected by *HETE-II*, the *Rossi X-ray Timing Explorer* (RXTE) and SWIFT[1]. We searched the bursts detected by both the RXTE Proportional Counter Array (PCA) and the SWIFT Burst Alert Telescope (BAT) for oscillations, but found no significant signal.

9.2.1 Burst oscillations

During routine monitoring on April 2 2009 (08:57 UTC), RXTE detected another X-ray burst with both the PCA and the *High Energy X-ray Timing Experiment* (HEXTE). Timing analysis was conducted using 125 μs time resolution PCA event mode data from the two active PCUs (PCUs 0 and 2). We used all photons in the 2–30 keV range, the band where burst emission exceeds the persistent level. The data were barycentered using the JPL DE405 and spacecraft ephemerides, with the source position of Fox (2005). Some event mode data overruns occurred in the burst peak, leading to short data gaps.

A dynamical power spectrum (Figure 9.1) reveals strong burst oscillations

[1]Galloway et al. (2008a) list most of the bursts detected during 2005-2008. One additional burst during this period was recorded by RXTE on December 5 2007 (05:57 UTC), and there is a candidate burst in slew data on November 27 2007.

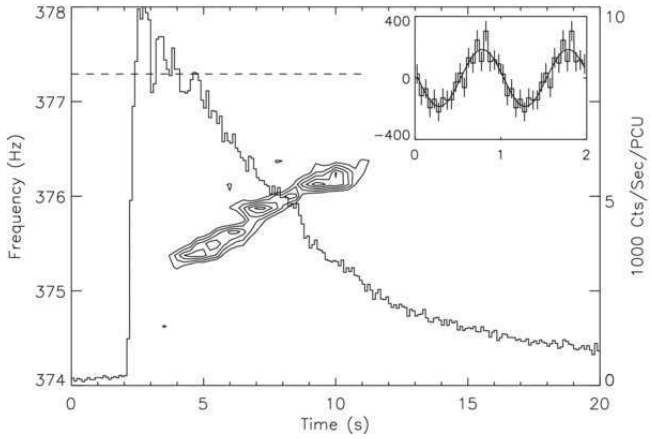

Figure 9.1: Lightcurve and dynamical power spectrum (2–30 keV) for the April 2 2009 burst. The dynamical power spectrum uses overlapping 4 s bins, with new bins starting at 0.25 s intervals. We use a Nyquist frequency of 2048 Hz and an interbin response function to reduce artificial drops in amplitude as the frequency drifts between Fourier bins (Hasinger & van der Klis 1989). The contours show Leahy normalized powers of 20–40, increasing in steps of 5. The dashed line indicates the 377.3 Hz spin frequency. The inset shows the pulse profile of the burst oscillations for the 8s interval where they are detected, folded with the best fit polynomial frequency model (counts per 0.05 cycle phase bin against phase in cycles), with the mean subtracted. The resulting profile is well fit by a simple sinusoid (overplotted) with no requirement for any harmonic content. Two cycles are shown for clarity.

during the initial decay of the burst, drifting upwards by about 1 Hz. Selecting only data after t=4 s in Figure 9.1 (the time of the final data gap), we find maximum Leahy power in the range 17–30 in 4 independent consecutive 2 s bins, an extremely robust detection. The oscillations fall below the detectability threshold when the frequency is 376.3 Hz, 1 Hz below the spin frequency. Although the binary ephemeris cannot be extended to 2009 (the errors are too large), orbital Doppler effects will shift the spin frequency by 0.009 Hz at most (Kaaret et al. 2006), so the offset in the frequencies is secure. A search for accretion-powered pulsations during the observation revealed no significant signals.

To study the pulse profile, we extracted data for the 8s period (t = 4–12s in Figure 9.1) during which the oscillations are detected. We fitted the frequency drift using a polynomial model to maximise the power. Power was maximised with a quadratic drift model, $\nu = \nu_0 + \dot{\nu}_0(t - t_0) + \ddot{\nu}_0(t - t_0)^2$, which yielded a Leahy normalised power of 88 (the best linear model gave a maximum power of 78, and higher order polynomial terms yielded no further

improvement). Using the best fit quadratic frequency model we generated a folded profile. The persistent (non-burst) emission level was estimated from the $\sim$ 1000s prior to the burst. The resulting pulse profile is shown inset in Figure 9.1. The pulse is well fit with a simple sinusoid ($\chi^2/dof = 31/37$), with no need for harmonic content. The fractional amplitude was (3.5 ± 0.3)% Root Mean Square (RMS) (2–30 keV), comparable to the fractional amplitude of the accretion-powered pulsations of this source. The amplitude of the pulsations rises with energy, from (3.1 ± 0.5) % RMS in the 2–5 keV band to (5.5 ± 0.6)% RMS in the 10–20 keV band. The burst oscillations also show hard lags, with the 10–20 keV pulse lagging the 2–5 keV pulse by (0.09 $\pm$ 0.03) cycles.

9.2.2 Burst properties

To study the characteristics of the burst containing the oscillations, we extracted spectra every 0.25s from the PCA Event data (E_125us_64M_0_1s), which has 64 energy channels between 2 and 60 keV. We used data from PCUs 0 and 2, which were operating at the time of the X-ray burst. We generated an instrument response matrix for each spectrum, and fitted it using XSPEC version 11.3.2. We added a 1% systematic error to the spectra and restricted the spectral fits to the energy range 2–25 keV. We extracted spectra using 100s segments before and after the burst, and used them as background in our fits. We fitted each of the 0.25s spectra with an absorbed (`wabs`, Morrison & McCammon 1983) blackbody model (`bbodyrad` model in XSPEC). This approach, which takes account of the contribution of the persistent and background emission, is standard procedure in X-ray burst analysis (see for example Kuulkers et al. 2003).

The simple blackbody fit described above yields a peak luminosity of 3.6×10^{38} ergs s^{-1}, and a total energy of 2.7×10^{39} ergs. The evolution of the temperature T_{bb} and the radius R_{bb} given by the spectral fits resembles those seen in photospheric radius expansion (PRE) bursts (Galloway et al. 2008b), i.e. (i) R_{bb} reaches a local maximum close to the time of the peak flux, (ii) lower values of R_{bb} were measured following the flux maximum and (iii) there is a local minimum in T_{bb} at the same time as the maximum in R_{bb}. This conclusion (and the derived peak flux and fluence) should be treated with care, however, since the χ^2/dof of the spectral fits can reach values as high as 4 or 5. The problem stems from an excess at high energies. Similar issues were reported by Galloway et al. (2008a) for other bursts from this source, and the physical cause is not yet understood. Adding a power law to our model, for example, reduces χ^2/dof to below 2: the evolution of T_{bb} and R_{bb} in this case still suggests a PRE burst. Photospheric touchdown occurs $3.5 - 5$s after the start of the burst, consistent with the first detection of the burst oscillations.

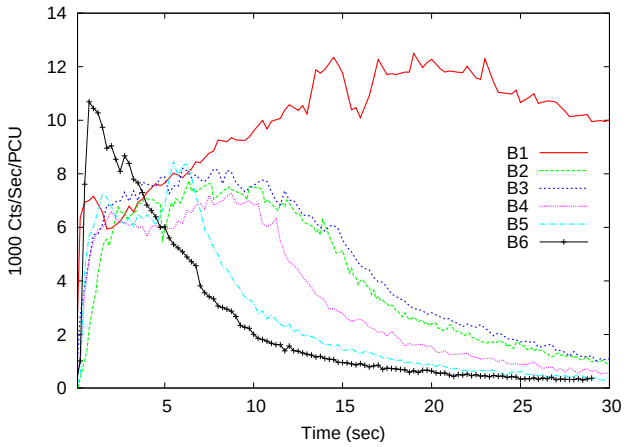

Figure 9.2: 2–25 keV lightcurves for the bursts recorded by the RXTE PCA from 2005-2009. Background and persistent emission have been subtracted and deadtime corrections applied (this was not done in Figure 9.1). The bursts are numbered according to their position in the color-color diagram (Figure 9.4). B6, the burst with the oscillations, has quite a different lightcurve.

The parameters of the April 2 burst do not differ dramatically from those of other bursts from HETE J1900, which also show evidence for PRE subject to uncertainties about the spectral fits (Galloway et al. 2008b,a). The burst with oscillations does not however have the extended or double peak structure exhibited by most of the other bursts (Figure 9.2). The burst lightcurve shows a fast rise, ≈ 0.4 s defined as in Galloway et al. (2008b). The decay can be modelled with a double exponential with decay timescales as of 7.3 s and 8.4 s respectively. Total burst duration is ≈ 60 s (burst end is defined as the time when flux falls to 1% of the peak flux, corrected for persistent emission).

9.2.3 Persistent emission

Figure 9.3 shows the intensity, defined as the countrate in the 2.0–16.0 keV band, for all publicly available observations from 2005-2009. Figure 9.4 shows the corresponding color-color diagram. Data were deadtime corrected, background subtracted, and X-ray bursts removed. For each observation we calculated X-ray colors from the Standard2 data. We defined soft color as the ratio between count rates in the 3.5–6.0 and 2.0–3.5 keV bands and hard color as the ratio between count rates in the 9.7–16.0 and 6.0–9.7 keV bands. We normalized colors and intensity to the Crab values nearest in time (Kuulkers et al. 1994) and in the same PCA gain epoch (see for example van Straaten et al. 2003).

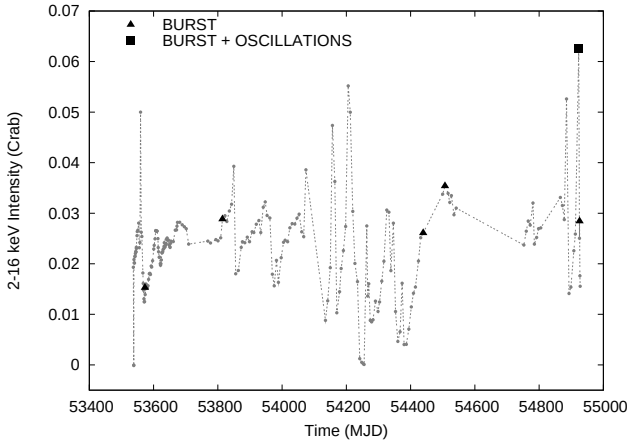

Figure 9.3: Average 2–16 keV intensity per RXTE observation for HETE J1900.1–2455 from 2005 to April 4 2009 (data from March-October 2008 are not yet public). Observations containing bursts are marked in black: triangles (no oscillations), square (oscillations). We include the four confirmed bursts detected by the PCA from 2005-2008 (the candidate slew burst also occurs in the hard state, but is not shown), the burst with oscillations from April 2 2009 and an additional burst detected by the PCA on April 4 2009.

It is clear from Figures 9.3-9.4 that the observation where the burst oscillations were detected was rather unusual. The burst happened when source intensity was at its highest recorded level (≈ 63 mCrab) and when it was in the soft (banana) state. All previous bursts have been detected in harder states. Fitting the PCA spectrum with an absorbed disk-blackbody plus power-law model, and assuming a standard bolometric correction factor of 2 (in't Zand et al. 2007) we find an unabsorbed bolometric flux of 3.5×10^{-9} ergs s^{-1} cm^{-2} (interstellar absorption was fixed to 1.6×10^{21} cm $^{-2}$). At a distance of 5 kpc, this corresponds to 4% of the Eddington luminosity if we assume $L_{\rm Edd} = 2.5 \times 10^{38}$ erg s^{-1}.

9.3 Discussion

What causes burst oscillations is still not understood. Flame spread from a point should lead to asymmetries in the early phase of the burst. However, while this may explain the presence of burst oscillations during the rise, it is not sufficient to explain the continuing presence of large-scale asymmetries in the burst tail once the entire stellar surface has ignited (Strohmayer & Bildsten 2006). This has led to the consideration of alternative models. Non-

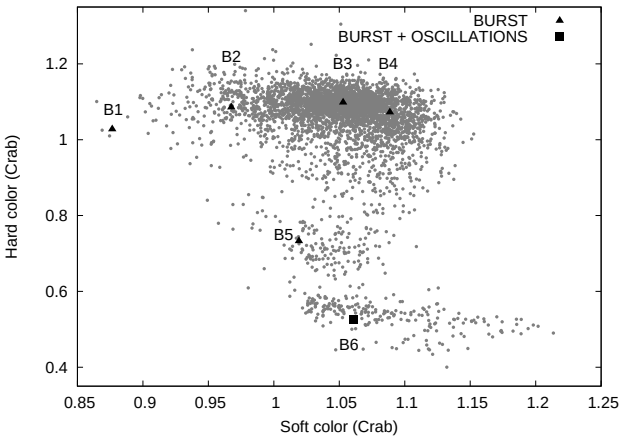

Figure 9.4: Color-color diagram for HETE J1900.1–2455 using all publicly available RXTE data from 2005 to April 4 2009 (excluding observations with intensities below 2 mCrab, see Figure 9.3). The source behaves like a typical atoll source (Hasinger & van der Klis 1989). The grey dots show the colors computed from 160s segments of data. Observations containing bursts are marked in black: triangles (no oscillations), square (oscillations). Lightcurves for the bursts are shown in Figure 9.2.

radial global oscillations in the surface layers of the star, excited by the flame spread, remain a promising possibility (Heyl 2004). In this case the brightness asymmetry would be caused by variations in ocean height associated with the mode. Inertial frame pattern speed can be very close to the spin rate, and cooling of the layers in the aftermath of the burst would naturally lead to frequency drift. The major problem of this model is that it overpredicts the size of the frequency drift compared to observations (Piro & Bildsten 2005; Berkhout & Levin 2008). Alternative possibilities like photospheric modes (Heyl 2004) or shear oscillations (Cumming 2005) also have shortcomings in their present form (Berkhout & Levin 2008). Current efforts to resolve these problems are focusing on the role of the magnetic field, which can dominate the dynamics in the surface layers and is expected to have a large effect on surface modes.

If the magnetic field is the most important factor determining the properties of burst oscillations then this might lead to a natural explanation for the differences in the properties of the burst oscillations of SAX J1808.4–3658 and XTE J1814–338 (hereafter collectively referred to as SX: Chakrabarty et al. 2003; Strohmayer et al. 2003; Watts et al. 2005; Watts & Strohmayer 2006) compared to those of the non-AMPs (Muno et al. 2002a,b, 2003, 2004; Galloway et al. 2008b). These differences can be summarized as follows. (1)

SX show oscillations in all of their bursts, even in the hard state; the non-AMPs do not (oscillations are detected primarily although not exclusively in the soft state). (2) SX show oscillations throughout their bursts (except during PRE); the non-AMPs, in most cases, do not. (3) SX burst oscillations have amplitudes that fall with energy; the non-AMP oscillations have amplitudes that rise. (4) SX burst oscillations have detectable harmonic content; the non-AMPs have none. (5) Frequency drift in SX is either very fast or non-existent; in the non-AMPs it is much slower.

The magnetic field also plays an important role in models for intermittency of accretion-powered pulsations. In the obscuration and accretion stream wander models, the field is always present at the level necessary to channel the flow: but the accretion hot spot either wanders out of the line of sight or is obscured by magnetospheric material. In the magnetic burial model the field strength and geometry change as the field is suppressed by accretion. If magnetic field affects both intermittency and burst oscillations, then studying the latter may enable us to pinpoint the cause of the former.

In Aql X-1 the burst oscillations are similar in properties to those of the non-AMPs: however this source has an exceptionally low duty cycle so its intermittent pulsation episode may have been triggered by an extremely rare event. In HETE J1900.1–2455 the accretion-powered pulsations lasted for much longer. Its burst oscillations, however, also behave like those of the non-AMPs. This has important implications. If hot spot wander or obscuration models for intermittency are correct, then a field strong enough to channel infalling material cannot be the only factor causing the atypical burst oscillations of SAX J1808.4–3658 and XTE J1814–338. Some other factor, such as the presence of a strong temperature gradient around the magnetic pole, must also play a role in the burst oscillation mechanism (Watts et al. 2008b). If on the other hand the field has been buried in HETE J1900.1–2455, then it must be screened to a depth where it is unable to affect the burst oscillation mechanism on the timescale of the burst. Detailed calculations will be required to resolve this issue, but if screening at the burning depth is not possible, then this could point to photospheric rather than oceanic modes as a cause of burst oscillations.

One other point of note is that in both Aql X-1 and HETE J1900.1–2455, burst oscillation frequency remains below spin frequency. Given the similarities in properties it seems probable that this is the case for non-AMPs as well. However it is not the case for SAX J1808.4–3658 and XTE J1814–338. In SAX J1808.4–3658 the burst oscillations are first detected below the spin frequency but rapidly overshoot it, settling ~ 0.1 Hz above the spin frequency in the burst tail (Chakrabarty et al. 2003). In XTE J1814–338 the two fre-

quencies are identical, and in fact burst oscillations and accretion-powered pulsations are coherent and phase-locked (Strohmayer et al. 2003; Watts et al. 2005, 2008b). Any unified model of burst oscillations must be able to explain this diversity in the relationship between burst oscillation frequency and spin.

Samenvatting

You can observe a lot by watching.

In theory, there is no difference between theory and practice. But in practice, there is.

Yogi Berra (1925)

Accretie, het proces waarbij materie op een hemellichaam valt onder de invloed van zwaartekracht, speelt een belangrijke rol in vele onderzoeksgebieden van de astrofysica. De studie van accretiestromen is daarom een breed onderwerp en één van groot belang. In lage massa röntgendubbelsterren (in het Engels 'low mass X-ray binaries' of kortweg 'LMXBs') wordt de accretiestroom gevoed door de materie die van de lage massa donorster wordt overgedragen en geleidelijk naar binnen spiraliseert in de richting van het compacte object. Accretie op een neutronenster is één van de meest efficiënte manieren om rustmassa in straling om te zetten en vormt extreem krachtige bronnen van röntgenstraling.

Type-I röntgenuitbarstingen, thermonucleaire explosies op het oppervlak van accreterende neutronensterren, zijn een veel voorkomend gevolg van accretie op een neutronenster en bieden de unieke mogelijkheid om de eigenschappen van ultra-dichte materie te bestuderen.

Dit proefschrift geeft een breed beeld van hoog-energetische verschijnselen die geassocieerd zijn met accreterende neutronensterren in LMXBs. Het is gebaseerd op waarnemingen die zijn uitgevoerd met twee momenteel actieve observatoria, de Rossi X-ray Timing Explorer en de Swift Gamma-ray Burst missie. De technieken die in dit werk voornamelijk gebruikt worden zijn X-ray timing en spectroscopie.

In het eerste deel van mijn proefschrift presenteer ik resultaten die verkregen zijn door het bestuderen van drie accreterende milliseconde pulsars

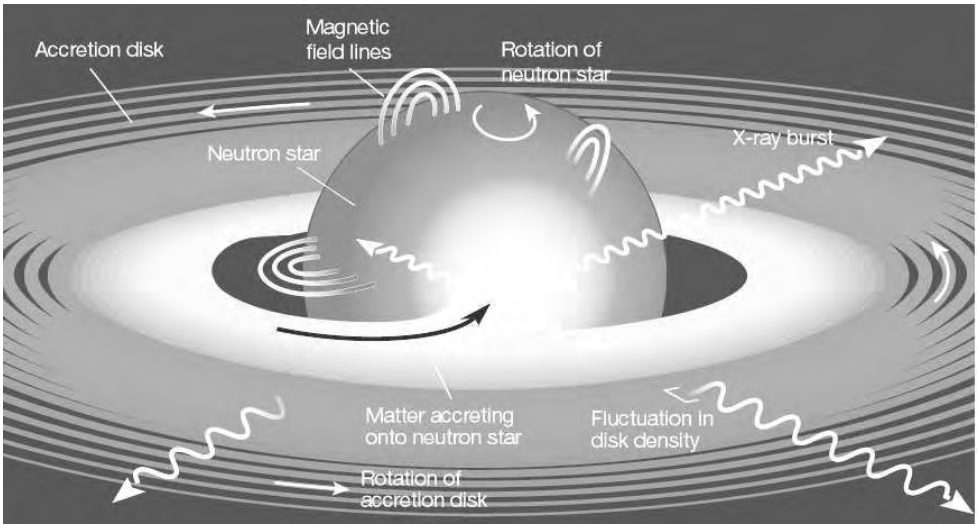

Figuur 1: Schematisch overzicht van een accretieschijf rondom een zwak gemagnetiseerde neutronenster en een aantal mogelijke bronnen van röntgenvariabiliteit: rotatie van de schijf en dichtheidsfluctuaties, rotatie van de neutronenster en type-I röntgenuitbarstingen. Bron: Wagoner (2003).

(AMPs), een speciale klasse van neutronensterren in LMXBs die milliseconde röntgenpulsaties in hun persistente emissie vertonen. De ontdekking van kHz quasi-periodieke oscillaties (kHz QPOs) met een frequentie verschil nabij de spinfrequentie in één van de AMPs behoort tot de belangrijkste resultaten besproken in deel I en heeft brede aandacht gekregen na publicatie. Ook opmerkelijk is de ontdekking van de laagste karakteristieke variabiliteits-frequenties die tot dusverre zijn waargenomen bij neutronensterren in LMXBs. Dit wordt gepresenteerd in deel I in een studie van een andere AMP.

Accretie in LMXBs kan op verschillende manieren plaatsvinden. Verschillende configuraties van de accretiestroom geven aanleiding tot verschillende accretietoestanden, zoals duidelijk wordt aan de hand van verschillen in röntgen spectrum en variabiliteit. Het tweede deel van dit proefschrift bespreekt de breedband röntgenhelderheid van deze verschillende röntgen-toestanden voor een groot aantal bronnen, welke de twee belangrijkste subklassen van neutronensterren in LMXBs omvat: Z en atoll bronnen. Er wordt aangetoond dat toestanden met harde spectra niet noodzakelijk een lage helderheid hebben, zoals gewoonlijk werd aangenomen. Omgekeerd blijken toestanden met zachte, voornamelijk thermische, spectra opvallend lage helderheden te hebben. Ik ontdekte ook, zoals gepresenteerd in deel II, een correlatie tussen de helder-

heid en spectrale hardheid van bronnen, welke optreedt wanneer bij een vaste waarde van hun variabiliteits-frequenties wordt gekeken. Dit nieuwe resultaat is geheel in tegenstelling met het gebruikelijke beeld dat hardere bronnen minder helder zijn.

Het derde deel van dit proefschrift bestudeert thermonucleaire explosies van accreterende neutronensterren. Ik presenteer de eigenschappen van een langdurige type-I röntgenuitbarsting, die ik vond in waarnemingen van een nieuwe 'transient' (plotseling opvlammende) röntgenbron. Tot op heden is slechts een dozijn van dergelijke uitbarstingen gevonden, in tegenstelling tot de duizenden gewone type-I röntgenuitbarstingen die zijn waargenomen. De langdurige type-I röntgenuitbarstingen representeren daarom vrij ongebruikelijke nucleaire verbrandingsregimes. In het laatste hoofdstuk bespreek ik de ontdekking van oscillaties in een type-I röntgenuitbarsting van een onderbroken ('intermittent') AMP welke eigenschappen heeft die meer op die van de niet-pulserende systemen lijken dan op die van de andere AMPs.

Resumen

¿Qué es la vida? Un frenesí.
¿Qué es la vida? Una ilusión;
una sombra, una ficción
y el mayor bien es pequeño.
¡Que toda la vida es sueño
y los sueños, sueños son!

Pedro Calderón de la Barca (1600-1681)

La acreción, el proceso a través del cual la materia cae sobre un cuerpo celeste bajo la influencia de su gravedad, juega un papel importante en muchas áreas de la astrofísica. Por consiguiente, el estudio de los flujos de acreción es un tema de investigación extenso y de gran interés. En las binarias X de baja masa con estrella de neutrones (NS-LMXBs; del inglés 'neutron star low-mass X-ray binaries') la estrella compañera, poco masiva, transfiere masa hacia la estrella de neutrones y "alimenta" el flujo de acreción. Esta masa se acerca paulatinamente al objeto compacto. La acreción sobre una estrella de neutrones constituye una de las maneras más eficientes de convertir energía en reposo en radiación, y da lugar a fuentes de rayos X extremadamente intensas. Los destellos de rayos X de tipo I ('type I X-ray bursts'), producidos por explosiones termonucleares sobre la superfície de estrellas de neutrones, constituyen una consecuencia habitual del proceso de acreción en NS-LMXBs, y proporcionan una oportunidad única para estudiar las propiedades de la materia ultra-densa.

Esta tesis presenta una visión amplia de los fenómenos de altas energías asociados con estrellas de neutrones que acrecen en LMXBs. Esta basada en observaciones tomadas por dos observatorios que operan en la actualidad, el *Rossi X-ray Timing Explorer* y el *Swift Gamma-ray Burst Mission*. El análisis de la distribución espectral y la variabilidad de los rayos X son las técnicas empleadas más frecuentemente en esta tesis.

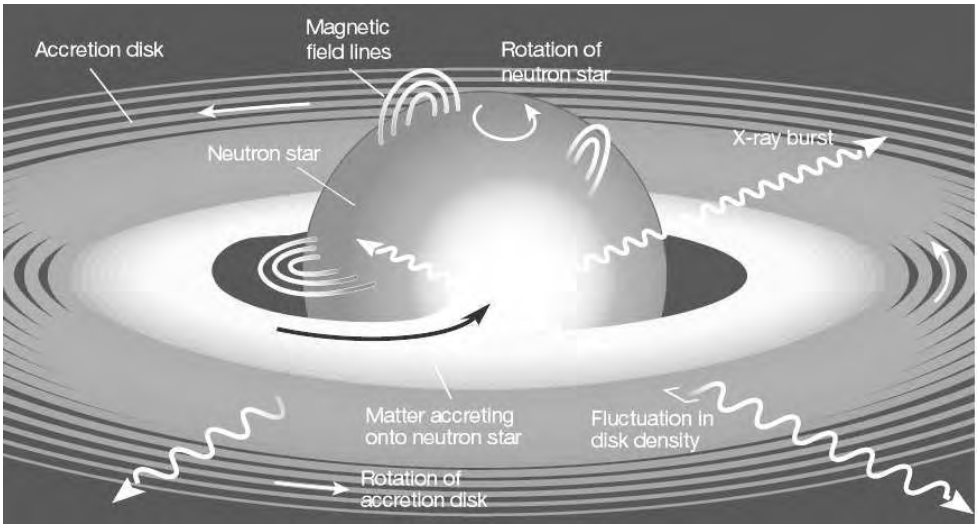

Figura 1: Vista esquemática de un disco de acreción alrededor de una estrella de neutrones poco magnética, destacando algunas de las causas de variabilidad en rayos X: rotación y fluctuaciones de densidad en el disco, rotación de la estrella de neutrones y explosiones termonucleares. De Wagoner (2003).

En la primera parte expongo los resultados obtenidos del estudio de tres pulsares milisegundo en acreción (AMPs; del inglés 'accreting millisecond pulsars'), una clase de NS-LMXBs particular que presenta pulsaciones de milisegundos en su emisión persistente. El descubrimiento de oscilaciones kHz cuasi-periódicas (kHz QPOs) en uno de los AMPs, con frecuencias separadas aproximadamente por la frecuencia de rotación, es uno de los resultados principales de la parte I, y ha recibido amplia atención desde que fué publicado. También es digno de mención el hallazgo de variabilidad con las frecuencias características más bajas observadas hasta la fecha en una NS-LMXB, tal como detalla el último Capítulo de la parte I.

La acreción en LMXBs puede ocurrir de diversos modos. Configuraciones distintas del flujo de acreción dan lugar a estados de acreción distintos, tal y como testifican los cambios en las propiedades espectrales y de variabilidad en LMXBs. La segunda parte de esta tesis estudia la luminosidad de estos distintos estados de acreción en una numerosa muestra de fuentes, que incluye las dos clases de NS-LMXB principales: fuentes 'Z' y fuentes 'atoll'. Muestro que los estados con espectro "duro" ('hard states') no presentan necesariamente luminosidades bajas. A la inversa, los estados con espectro "blando" ('soft states') pueden tener luminosidades muy bajas. En la parte II también

se presenta una correlación entre la luminosidad y la dureza espectral de varias fuentes, que encuentro al considerar un valor fijo de sus frecuencias de variabilidad. Este nuevo resultado contradice la percepción común de que las fuentes más "duras" son menos luminosas.

La tercera parte de esta tesis estudia explosiones termonucleares en estrellas de neutrones. Presento las propiedades de un destello de rayos X de tipo I de larga duración que encontré en observaciones de una nueva fuente. Sólo alrededor de una docena de eventos similares se han observado hasta la fecha y por lo tanto permiten estudiar régimenes de reacciones nucleares bastante atípicos, en contraste con los miles de destellos normales de rayos X que han sido observados. En el capítulo final presento el descubrimiento de oscilaciones durante un destello de rayos X de un AMP ('burst oscillations' en inglés), con propiedades más parecidas a las de los sistemas que no emiten pulsaciones que a las de los AMPs.

Bibliography

Abramowicz M.A., Karas V., Kluzniak W., Lee W.H., Rebusco P., 2003, PASJ, 55, 467

Alpar M.A., Cheng A.F., Ruderman M.A., Shaham J., 1982, Nature, 300, 728

Altamirano D., Casella P., 2008, In: Wijnands R., Altamirano D., Soleri P., et al. (eds.) American Institute of Physics Conference Series, vol. 1068 of American Institute of Physics Conference Series, 63–66

Altamirano D., van der Klis M., Mendez M., et al., 2005, ApJ, 633, 358

Altamirano D., Casella P., Patruno A., Wijnands R., van der Klis M., 2008a, ApJ, 674, L45

Altamirano D., van der Klis M., Méndez M., et al., 2008b, ApJ, 687, 488

Altamirano D., van der Klis M., Méndez M., et al., 2008c, ApJ, 685, 436

Arnaud K.A., 1996, In: Jacoby G.H., Barnes J. (eds.) Astronomical Data Analysis Software and Systems V, vol. 101 of Astronomical Society of the Pacific Conference Series, 17–+

Axelsson M., Borgonovo L., Larsson S., 2005, A&A, 438, 999

Barret D., Olive J.F., 2002, ApJ, 576, 391

Barret D., Olive J.F., Boirin L., et al., 2000, ApJ, 533, 329

Barret D., Boutelier M., Miller M.C., 2008, MNRAS, 384, 1519

Barthelmy S., et al., 2008, GRB Coordinates Network, 7985, 1

Barthelmy S.D., Barbier L.M., Cummings J.R., et al., 2005, Space Science Reviews, 120, 143

Belian R.D., Conner J.P., Evans W.D., 1976, ApJ, 206, L135

Belloni T., Hasinger G., 1990, A&A, 227, L33

Belloni T., Psaltis D., van der Klis M., 2002, ApJ, 572, 392

Belloni T., Homan J., Motta S., Ratti E., Méndez M., 2007, MNRAS, 379, 247

Beloborodov A.M., 1999, MNRAS, 305, 181

Berger M., van der Klis M., van Paradijs J., et al., 1996, ApJ, 469, L13+

Berkhout R.G., Levin Y., 2008, MNRAS, 385, 1029

Bhattacharya D., van den Heuvel E.P.J., 1991, Phys. Rep., 203, 1

Blandford R.D., Begelman M.C., 1999, MNRAS, 303, L1

Bloser P.F., Grindlay J.E., Kaaret P., et al., 2000, ApJ, 542, 1000
Boutelier M., Barret D., Miller M.C., 2008, In: Charbonnel C., Combes F., Samadi R. (eds.) SF2A-2008: Proceedings of the Annual meeting of the French Society of Astronomy and Astrophysics Eds.: C. Charbonnel, F. Combes and R. Samadi. Available online at http://proc.sf2a.asso.fr, p.175, 175–+
Bradt H.V., Rothschild R.E., Swank J.H., Jan. 1993, A&AS, 97, 355
Burderi L., Di Salvo T., Riggio A., et al., 2005, astro-ph/0509224
Burderi L., Testa V., Menna M.T., et al., 2007, The Astronomer's Telegram, 1132, 1
Burrows D.N., Hill J.E., Nousek J.A., et al., 2000, In: Flanagan K.A., Siegmund O.H. (eds.) Society of Photo-Optical Instrumentation Engineers (SPIE) Conference Series, vol. 4140 of Society of Photo-Optical Instrumentation Engineers (SPIE) Conference Series, 64–75
Cackett E.M., Wijnands R., Linares M., et al., 2006, MNRAS, 372, 479
Campana S., Colpi M., Mereghetti S., Stella L., Tavani M., 1998a, A&A Rev., 8, 279
Campana S., Stella L., Mereghetti S., et al., 1998b, ApJ, 499, L65+
Campana S., Ferrari N., Stella L., Israel G.L., 2005, astro-ph/0503529
Campana S., Romano P., Kennea J., et al., 2007, The Astronomer's Telegram, 1117, 1
Campana S., Panagia N., Lazzati D., et al., 2008, ApJ, 683, L9
Casella P., Belloni T., Stella L., 2005, ApJ, 629, 403
Casella P., Altamirano D., Wijnands R., van der Klis M., 2008, ApJ, 674, L41
Chakrabarty D., Morgan E.H., Muno M.P., et al., 2003, Nature, 424, 42
Chakrabarty D., Krauss M.I., Jonker P.G., Juett A.M., Markwardt C.B., 2007, The Astronomer's Telegram, 1096, 1
Chelovekov I.V., Grebenev S.A., Sunyaev R.A., Jul. 2006, Astronomy Letters, 32, 456
Chen X., Taam R.E., 1994, ApJ, 431, 732
Chenevez J., et al., Jul 2007, A&A, 469, L27
Christian D.J., Swank J.H., 1997, ApJS, 109, 177
Churazov E., Gilfanov M., Revnivtsev M., 2001, MNRAS, 321, 759
Church M.J., Balucińska-Church M., 2001, A&A, 369
Church M.J., Halai G.S., Bałucińska-Church M., 2006, A&A, 460, 233
Cooper R.L., Narayan R., May 2007, ApJ, 661, 468
Cui W., Zhang S.N., Chen W., Morgan E.H., 1999, ApJ, 512, L43
Cumming A., 2004, Nuc. Phys. B. Proc. Supp., 132, 435
Cumming A., 2005, ApJ, 630, 441
Cumming A., 2008, In: Wijnands R., Altamirano D., Soleri P., et al. (eds.)

American Institute of Physics Conference Series, vol. 1068 of American Institute of Physics Conference Series, 152–159
Cumming A., Macbeth J., Mar 2004, ApJ, 603, L37
Cumming A., Zweibel E., Bildsten L., 2001, ApJ, 557, 958
Cumming A., Macbeth J., in't Zand J.J.M., Page D., Jul 2006, ApJ, 646, 429
de Martino D., Matt G., Belloni T., Haberl F., Mukai K., 2004, A&A, 415, 1009
De Villiers J.P., Hawley J.F., Krolik J.H., 2003, ApJ, 599, 1238
Degenaar N., Wijnands R., 2008, The Astronomer's Telegram, 1572, 1
Degenaar N., Wijnands R., 2009, A&A, 495, 547
Degenaar N., Wijnands R., Campana S., et al., 2007, The Astronomer's Telegram, 1098, 1
Di Salvo T., Iaria R., Burderi L., Robba N.R., 2000, ApJ, 542, 1034
Di Salvo T., Méndez M., van der Klis M., Ford E., Robba N.R., 2001, ApJ, 546, 1107
Di Salvo T., Méndez M., van der Klis M., 2003, A&A, 406, 177
di Salvo T., Santangelo A., Segreto A., 2004, Nuclear Physics B Proceedings Supplements, 132, 446
Dib R., Ransom S., Ray P., Kaspi V., Archibald A., 2004, astro-ph/0407629
Dickey J.M., Lockman F.J., 1990, ARA&A, 28, 215
Done C., Życki P.T., Smith D.A., 2002, MNRAS, 331, 453
Done C., Gierliński M., Kubota A., 2007, A&A Rev., 15, 1
Eckert D., Walter R., Kretschmar P., et al., 2004, The Astronomer's Telegram, 352, 1
Esin A.A., McClintock J.E., Narayan R., 1997, ApJ, 489, 865
Falanga M., Bonnet-Bidaud J.M., Poutanen J., et al., 2005a, astro-ph/0503292
Falanga M., Bonnet-Bidaud J.M., Suleimanov V., 2005b, A&A, 444, 561
Falanga M., Kuiper L., Poutanen J., et al., 2005c, A&A, 444, 15
Falanga M., Chenevez J., Cumming A., et al., Jun 2008, A&A, 484, 43
Falcke H., Körding E., Markoff S., 2004, A&A, 414, 895
Fender R., 2006, Jets from X-ray binaries, 381–419
Fender R., De Bruyn G., Pooley G., Stappers B., 2004a, The Astronomer's Telegram, 361, 1
Fender R.P., Belloni T.M., Gallo E., 2004b, MNRAS, 355, 1105
Fiocchi M., Bazzano A., Ubertini P., Jean P., 2006, ApJ, 651, 416
Ford E., Kaaret P., Tavani M., et al., 1997, ApJ, 475, L123+
Ford E.C., van der Klis M., Méndez M., et al., 2000, ApJ, 537, 368
Fox D.B., 2005, The Astronomer's Telegram, 526, 1
Fox D.B., Kulkarni S.R., 2004, The Astronomer's Telegram, 354, 1
Frank J., King A., Raine D.J., 2002, Accretion Power in Astrophysics: Third

Edition
Fujimoto M.Y., Hanawa T., Miyaji S., Jul 1981, ApJ, 247, 267
Gallo E., Fender R., Kaiser C., et al., 2005, Nature, 436, 819
Galloway D.K., Chakrabarty D., Muno M.P., Savov P., 2001, ApJ, 549, L85
Galloway D.K., Markwardt C.B., Morgan E.H., Chakrabarty D., Strohmayer T.E., 2005, ApJ, 622, L45
Galloway D.K., Psaltis D., Muno M.P., Chakrabarty D., 2006, ApJ, 639, 1033
Galloway D.K., Morgan E.H., Krauss M.I., Kaaret P., Chakrabarty D., 2007, ApJ, 654, L73
Galloway D.K., Morgan E.H., Chakrabarty D., 2008a, In: Wijnands R., Altamirano D., Soleri P., et al. (eds.) American Institute of Physics Conference Series, vol. 1068 of American Institute of Physics Conference Series, 55–62
Galloway D.K., Muno M.P., Hartman J.M., Psaltis D., Chakrabarty D., 2008b, ApJS, 179, 360
Garcia M.R., McClintock J.E., Narayan R., et al., 2001, ApJ, 553, L47
Gavriil F.P., Strohmayer T.E., Swank J.H., Markwardt C.B., 2007, ApJ, 669, L29
Gehrels N., 1986, ApJ, 303, 336
Gehrels N., Chincarini G., Giommi P., et al., 2004, ApJ, 611, 1005
Ghosh P., Lamb F.K., 1978, ApJ, 223, L83
Giacconi R., Gursky H., Paolini F.R., Rossi B.B., 1962, Physical Review Letters, 9, 439
Gilfanov M., Revnivtsev M., Sunyaev R., Churazov E., 1998, A&A, 338, L83
Gilfanov M., Revnivtsev M., Molkov S., Oct. 2003, A&A, 410, 217
Gladstone J., Done C., Gierliński M., 2007, MNRAS, 378, 13
Göğüş E., Alpar M.A., Gilfanov M., 2007, ApJ, 659, 580
Grebenev S.A., Molkov S.V., Sunyaev R.A., Mar. 2005, The Astronomer's Telegram, 446, 1
Grindlay J., Gursky H., Schnopper H., et al., 1976, ApJ, 205, L127
Gupta S., Brown E.F., Schatz H., Möller P., Kratz K.L., Jun. 2007, ApJ, 662, 1188
Haberl F., Motch C., 1995, A&A, 297, L37+
Haensel P., Zdunik J.L., Jan. 1990, A&A, 227, 431
Haensel P., Zdunik J.L., Jun. 2003, A&A, 404, L33
Haensel P., Zdunik J.L., Mar. 2008, A&A, 480, 459
Hasinger G., van der Klis M., 1989, A&A, 225, 79
Heinz S., Schulz N.S., Brandt W.N., Galloway D.K., 2007, ApJ, 663, L93
Hertz P., Vaughan B., Wood K.S., et al., 1992, ApJ, 396, 201
Hessels J.W.T., Stappers B.W., 2007, The Astronomer's Telegram, 1129, 0
Hewish A., Bell S.J., Pilkington J.D.H., Scott P.F., Collins R.A., 1968, Nature,

217, 709
Heyl J.S., 2004, ApJ, 600, 939
Hoffman J.A., Marshall H.L., Lewin W.H.G., 1978, Nature, 271, 630
Homan J., Belloni T., 2005, Ap&SS, 300, 107
Homan J., van der Klis M., Jonker P.G., et al., 2002, ApJ, 568, 878
Homan J., van der Klis M., Wijnands R., et al., 2007, ApJ, 656, 420
Horowitz C.J., Dussan H., Berry D.K., Apr. 2008, Physical Review C, 77, 045807
Jahoda K., Swank J.H., Giles A.B., et al., 1996, In: Siegmund O.H., Gummin M.A. (eds.) Society of Photo-Optical Instrumentation Engineers (SPIE) Conference Series, vol. 2808 of Presented at the Society of Photo-Optical Instrumentation Engineers (SPIE) Conference, 59–70
Jahoda K., Markwardt C.B., Radeva Y., et al., 2006, ApJS, 163, 401
Jonker P.G., Nelemans G., 2004, MNRAS, 354, 355
Jonker P.G., van der Klis M., Wijnands R., et al., 2000, ApJ, 537, 374
Jonker P.G., Méndez M., van der Klis M., 2002, MNRAS, 336, L1
Jonker P.G., Méndez M., Nelemans G., Wijnands R., van der Klis M., 2003, MNRAS, 341, 823
Jonker P.G., Campana S., Steeghs D., et al., 2005, MNRAS, 361, 511
Juett A.M., Psaltis D., Chakrabarty D., 2001, ApJ, 560, L59
Kaaret P., Zand J.J.M.i., Heise J., Tomsick J.A., 2002, ApJ, 575, 1018
Kaaret P., Morgan E.H., Vanderspek R., Tomsick J.A., 2006, ApJ, 638, 963
Kalemci E., Tomsick J.A., Rothschild R.E., Pottschmidt K., Kaaret P., 2004, ApJ, 603, 231
Kaplan D.L., Chakrabarty D., 2008, The Astronomer's Telegram, 1630, 1
Kaspi V.M., Roberts M.S.E., Harding A.K., 2006, Isolated neutron stars, 279–339
Klein-Wolt M., 2004, Thesis, Universiteit van Amsterdam
Klein-Wolt M., van der Klis M., 2006, in prep.
Klein-Wolt M., Homan J., van der Klis M., 2004, Nuclear Physics B Proceedings Supplements, 132, 381
Klein-Wolt M., Wijnands R., Markwardt C.B., Swank J.H., 2007a, The Astronomer's Telegram, 1025, 1
Klein-Wolt M., Wijnands R., Swank J.H., Markwardt C.B., 2007b, The Astronomer's Telegram, 1065, 1
Klein-Wolt M., Wijnands R., Swank J.H., Markwardt C.B., 2007c, The Astronomer's Telegram, 1075, 1
Kluźniak W., Abramowicz M.A., Kato S., Lee W.H., Stergioulas N., 2004, ApJ, 603, L89
Krimm H.A., Barthelmy S.D., Barbier L., et al., 2007a, The Astronomer's

Telegram, 1105, 1
Krimm H.A., Markwardt C.B., Deloye C.J., et al., 2007b, ApJ, 668, L147
Kuulkers E., et al., 2009, in preparation
Kuulkers E., van der Klis M., 2000, A&A, 356, L45
Kuulkers E., van der Klis M., Oosterbroek T., et al., 1994, A&A, 289, 795
Kuulkers E., den Hartog P.R., in't Zand J.J.M., et al., 2003, A&A, 399, 663
Kuulkers E., Shaw S., Chenevez J., et al., 2007a, The Astronomer's Telegram, 1008, 1
Kuulkers E., Shaw S.E., Paizis A., et al., 2007b, A&A, 466, 595
Lamb F.K., Miller M.C., 2001, ApJ, 554, 1210
Lamb F.K., Miller M.C., 2003, astro-ph/0308179
Lamb F.K., Pethick C.J., Pines D., 1973, ApJ, 184, 271
Lamb F.K., Boutloukos S., Van Wassenhove S., et al., 2008, ArXiv e-prints
Lasota J.P., 2001, New Astronomy Review, 45, 449
Lee W.H., Abramowicz M.A., Kluźniak W., 2004, ApJ, 603, L93
Levine A.M., Bradt H., Cui W., et al., 1996, ApJ, 469, L33+
Lewin W.H.G., van Paradijs J., Taam R.E., 1993, Space Science Reviews, 62, 223
Lin D., Remillard R.A., Homan J., 2007, ApJ, 667, 1073
Linares M., van der Klis M., 2009, ApJ, submitted
Linares M., van der Klis M., Altamirano D., Markwardt C.B., 2005, ApJ, 634, 1250
Linares M., van der Klis M., Wijnands R., 2007, ApJ, 660, 595
Linares M., Degenaar N., Wijnands R., Altamirano D., 2008a, The Astronomer's Telegram, 1777, 1
Linares M., Soleri P., Curran P., et al., 2008b, The Astronomer's Telegram, 1618, 1
Liu Q.Z., van Paradijs J., van den Heuvel E.P.J., 2007, A&A, 469, 807
London R.A., Howard W.M., Taam R.E., 1984, ApJ, 287, L27
Long M., Romanova M.M., Lovelace R.V.E., 2008, MNRAS, 386, 1274
Méndez M., van der Klis M., 1999, ApJ, 517, L51
Méndez M., van der Klis M., Ford E.C., Wijnands R., van Paradijs J., 1999, ApJ, 511, L49
Maccarone T.J., 2003, A&A, 409, 697
Maccarone T.J., Coppi P.S., 2003, MNRAS, 338, 189
Maitra D., Markoff S., Brocksopp C., et al., 2009, MNRAS, accepted
Manmoto T., Takeuchi M., Mineshige S., Matsumoto R., Negoro H., 1996, ApJ, 464, L135+
Markwardt C.B., 2004, In: AIP Conf. Proc. 714: X-ray Timing 2003: Rossi and Beyond, 217–223

Markwardt C.B., Krimm H.A., 2007, The Astronomer's Telegram, 1114, 1
Markwardt C.B., Swank J.H., 2003, IAU Circ., 8144, 1
Markwardt C.B., Strohmayer T.E., Swank J.H., 1999, ApJ, 512, L125
Markwardt C.B., Swank J.H., Strohmayer T.E., Zand J.J.M.i., Marshall F.E., 2002, ApJ, 575, L21
Markwardt C.B., Juda M., Swank J.H., Mar. 2003a, IAU Circ., 8095, 2
Markwardt C.B., Smith E., Swank J.H., 2003b, IAU Circ., 8080, 2
Markwardt C.B., Galloway D.K., Chakrabarty D., Morgan E.H., Strohmayer T.E., 2004a, The Astronomer's Telegram, 360, 1
Markwardt C.B., Swank J.H., Strohmayer T.E., 2004b, The Astronomer's Telegram, 353, 1
Markwardt C.B., Klein-Wolt M., Swank J.H., Wijnands R., 2007a, The Astronomer's Telegram, 1068, 1
Markwardt C.B., Krimm H.A., Swank J.H., 2007b, The Astronomer's Telegram, 1108, 1
Markwardt C.B., Cummings J., Krimm H., 2008a, The Astronomer's Telegram, 1616, 1
Markwardt C.B., Pereira D., Swank J.H., 2008b, The Astronomer's Telegram, 1569, 1
McHardy I.M., Papadakis I.E., Uttley P., Page M.J., Mason K.O., 2004, MNRAS, 348, 783
Méndez M., Belloni T., 2007, MNRAS, 381, 790
Mendez M., van der Klis M., van Paradijs J., et al., 1998a, ApJ, 494, L65+
Mendez M., van der Klis M., Wijnands R., et al., 1998b, ApJ, 505, L23+
Méndez M., van der Klis M., Ford E.C., 2001, ApJ, 561, 1016
Merloni A., Di Matteo T., Fabian A.C., 2000, MNRAS, 318, L15
Meyer-Hofmeister E., Liu B.F., Meyer F., 2005, A&A, 432, 181
Migliari S., Fender R.P., 2006, MNRAS, 366, 79
Migliari S., Miller-Jones J.C.A., Fender R.P., et al., 2007, ApJ, 671, 706
Miller J.M., 2009, The Astronomer's Telegram, 1966, 1
Miller J.M., Homan J., Miniutti G., 2006, ApJ, 652, L113
Miller J.M., Reynolds C.S., Fabian A.C., Miniutti G., Gallo L.C., 2009, ApJ, 697, 900
Miller M.C., Lamb F.K., Psaltis D., 1998, ApJ, 508, 791
Mineshige S., 1996, PASJ, 48, 93
Molkov S., Revnivtsev M., Lutovinov A., Sunyaev R.A., 2005, A&A, 434, 1069
Morrison R., McCammon D., 1983, ApJ, 270, 119
Muno M.P., Chakrabarty D., Galloway D.K., Savov P., 2001, ApJ, 553, L157
Muno M.P., Chakrabarty D., Galloway D.K., Psaltis D., 2002a, ApJ, 580, 1048

Muno M.P., Özel F., Chakrabarty D., 2002b, ApJ, 581, 550
Muno M.P., Remillard R.A., Chakrabarty D., 2002c, ApJ, 568, L35
Muno M.P., Özel F., Chakrabarty D., 2003, ApJ, 595, 1066
Muno M.P., Galloway D.K., Chakrabarty D., 2004, ApJ, 608, 930
Narayan R., 1996, ApJ, 462, 136
Narayan R., Yi I., 1995, ApJ, 452, 710
Norton A.J., Beardmore A.P., Allan A., Hellier C., 1999, A&A, 347, 203
Olive J.F., Barret D., Boirin L., et al., 1998, A&A, 333, 942
Olive J.F., Barret D., Gierliński M., 2003, ApJ, 583, 416
Oosterbroek T., van der Klis M., Kuulkers E., van Paradijs J., Lewin W.H.G., 1995, A&A, 297, 141
Paltani S., Barret D., Olive J.F., Skinner G.K., 2004, In: Combes F., Barret D., Contini T., Meynadier F., Pagani L. (eds.) SF2A-2004: Semaine de l'Astrophysique Francaise, 381–+
Patruno A., Watts A.L., Klein-Wolt M., Wijnands R., van der Klis M., 2009, ApJ, submitted; ArXiv 0904.0560
Patterson J., Mar. 1994, PASP, 106, 209
Peng F., Brown E.F., Truran J.W., Jan 2007, ApJ, 654, 1022
Penninx W., Damen E., van Paradijs J., Tan J., Lewin W.H.G., 1989, A&A, 208, 146
Piro A.L., Bildsten L., 2005, ApJ, 629, 438
Pooley G., 2004, The Astronomer's Telegram, 355, 1
Possenti A., Murgia M., Reynolds J., et al., 2007, The Astronomer's Telegram, 1128, 1
Pottschmidt K., Wilms J., Nowak M.A., et al., 2003, A&A, 407, 1039
Poutanen J., Fabian A.C., 1999, MNRAS, 306, L31
Press W.H., Teukolsky S.A., Vetterling W.T., Flannery B.P., 1992, Numerical recipes in FORTRAN. The art of scientific computing, Cambridge: University Press, —c1992, 2nd ed.
Priedhorsky W., Garmire G.P., Rothschild R., et al., 1979, ApJ, 233, 350
Pringle J.E., Rees M.J., 1972, A&A, 21, 1
Psaltis D., Chakrabarty D., 1999, ApJ, 521, 332
Psaltis D., Lamb F.K., Miller G.S., 1995, ApJ, 454, L137+
Psaltis D., Belloni T., van der Klis M., 1999, ApJ, 520, 262
Rappaport S.A., Fregeau J.M., Spruit H., 2004, ApJ, 606, 436
Reerink T., 2005, Thesis, Universiteit van Amsterdam
Reig P., van Straaten S., van der Klis M., 2004, ApJ, 602, 918
Remillard R., 2004, The Astronomer's Telegram, 357, 1
Remillard R.A., 2002, IAU Circ., 7888, 2
Revnivtsev M., Sunyaev R., Borozdin K., 2000, A&A, 361, L37

Revnivtsev M.G., Gilfanov M.R., 2006, A&A, 453, 253
Romanova M.M., Ustyugova G.V., Koldoba A.V., Wick J.V., Lovelace R.V.E., 2003, ApJ, 595, 1009
Romanova M.M., Ustyugova G.V., Koldoba A.V., Lovelace R.V.E., 2004, ApJ, 610, 920
Roming P.W.A., Kennedy T.E., Mason K.O., et al., 2005, Space Science Reviews, 120, 95
Rothschild R.E., Blanco P.R., Gruber D.E., et al., 1998, ApJ, 496, 538
Rupen M.P., Dhawan V., Mioduszewski A.J., 2004, The Astronomer's Telegram, 364, 1
Russell D.M., Fender R.P., Jonker P.G., 2007, MNRAS, 379, 1108
Sakamoto T., et al., 2008, GRB Coordinates Network, 8034, 1
Schulz N.S., 1999, ApJ, 511, 304
Shafee R., McClintock J.E., Narayan R., et al., 2006, ApJ, 636, L113
Shahbaz T., Watson C.A., Zurita C., Villaver E., Hernandez-Peralta H., 2008, PASP, 120, 848
Shakura N.I., Syunyaev R.A., 1973, A&A, 24, 337
Shaw S.E., Mowlavi N., Rodriguez J., et al., 2005, A&A, 432, L13
Shklovsky I.S., 1967, ApJ, 148, L1+
Sidoli L., Parmar A.N., Oosterbroek T., et al., 2001, A&A, 368, 451
Starling R., Evans P., 2008, The Astronomer's Telegram, 1621, 1
Steeghs D., Blake C., Bloom J.S., et al., 2004, The Astronomer's Telegram, 363, 1
Stella L., Vietri M., 1998, ApJ, 492, L59+
Strohmayer T., Bildsten L., 2006, New views of thermonuclear bursts, 113–156
Strohmayer T., Zhang W., Swank J., Feb. 1996a, IAU Circ., 6320, 1
Strohmayer T.E., 2001, Advances in Space Research, 28, 511
Strohmayer T.E., Markwardt C.B., 1999, ApJ, 516, L81
Strohmayer T.E., Markwardt C.B., 2002, ApJ, 577, 337
Strohmayer T.E., Zhang W., Swank J.H., et al., 1996b, ApJ, 469, L9+
Strohmayer T.E., Markwardt C.B., Swank J.H., in't Zand J., 2003, ApJ, 596, L67
Strohmayer T.E., Markwardt C.B., Kuulkers E., 2008a, ApJ, 672, L37
Strohmayer T.E., Markwardt C.B., Swank J.H., 2008b, The Astronomer's Telegram, 1635, 1
Sunyaev R., Revnivtsev M., 2000, A&A, 358, 617
Sunyaev R.A., Arefev V.A., Borozdin K.N., et al., 1991, Soviet Astronomy Letters, 17, 409
Swank J., Markwardt K., 2001, in ASP Conf. Ser. 251, New Century of X-ray Astronomy, eds. H. Inoue & H. Kunieda (San Francisco: ASP), 94

Swank J.H., 1999, Nuclear Physics B Proceedings Supplements, 69, 12
Swank J.H., Markwardt C.B., Smith E.A., Mar. 2005, The Astronomer's Telegram, 449, 1
Swank J.H., Markwardt C.B., Klein-Wolt M., Wijnands R., 2007, The Astronomer's Telegram, 1022, 1
Tananbaum H., Gursky H., Kellogg E., Giacconi R., Jones C., 1972, ApJ, 177, L5+
Tauris T.M., van den Heuvel E.P.J., 2006, Formation and evolution of compact stellar X-ray sources, 623–665
Thompson T.W.J., Galloway D.K., Rothschild R.E., Homer L., 2008, ApJ, 681, 506
Titarchuk L., Fiorito R., 2004, ApJ, 612, 988
Titarchuk L., Muslimov A., 1997, A&A, 323, L5
Titarchuk L., Shaposhnikov N., 2008, ApJ, 678, 1230
Titarchuk L., Cui W., Wood K., 2002, ApJ, 576, L49
Tudose V., Fender R.P., Linares M., et al., 2009, MNRAS, submitted
Turler M., Balman S., Bazzano A., et al., 2007, The Astronomer's Telegram, 1021, 1
Uttley P., McHardy I.M., 2005, MNRAS, 363, 586
Uttley P., McHardy I.M., Papadakis I.E., 2002, MNRAS, 332, 231
van der Klis M., 1994, ApJS, 92, 511
van der Klis M., 1995a, In: Lewin W.H.G., van Paradijs J., van den Heuvel E.P.J. (eds.) X-ray binaries, p. 252 - 307, 252–307
van der Klis M., 1995b, Proceedings of the NATO Advanced Study Institute on the Lives of the Neutron Stars, held in Kemer, Turkey, August 19-September 12, 1993. Editor(s), M. A. Alpar, U. Kiziloglu, J. van Paradijs; Publisher, Kluwer Academic, Dordrecht, The Netherlands, Boston, Massachusetts, 301
van der Klis M., 2000, ARA&A, 38, 717
van der Klis M., 2001, ApJ, 561, 943
van der Klis M., 2006, in "Compact Stellar X-ray Sources", ed. W. H. G. Lewin & M. van der Klis (Cambridge Univ. Press) (astro-ph/0410551), 39–112
van der Klis M., 2008, In: Wijnands R., Altamirano D., Soleri P., et al. (eds.) American Institute of Physics Conference Series, vol. 1068 of American Institute of Physics Conference Series, 163–173
van der Klis M., Hasinger G., Damen E., et al., 1990, ApJ, 360, L19
van der Klis M., Swank J., Zhang W., et al., 1996, IAU Circ., 6319, 1
van der Klis M., Wijnands R.A.D., Horne K., Chen W., 1997, ApJ, L97+
van Paradijs J., 1982, A&A, 107, 51
van Paradijs J., van der Klis M., 1994, A&A, 281, L17
van Paradijs J., Verbunt F., Shafer R.A., Arnaud K.A., 1987, A&A, 182, 47

van Straaten S., Ford E.C., van der Klis M., Méndez M., Kaaret P., 2000, ApJ, 540, 1049
van Straaten S., van der Klis M., di Salvo T., Belloni T., 2002, ApJ, 568, 912
van Straaten S., van der Klis M., Méndez M., 2003, ApJ, 596, 1155
van Straaten S., van der Klis M., Wijnands R., 2005, ApJ, 619, 455
Vanderspek R., Morgan E., Crew G., Graziani C., Suzuki M., 2005, The Astronomer's Telegram, 516, 1
Vaughan B.A., van der Klis M., Wood K.S., et al., 1994, ApJ, 435, 362
Vignarca F., Migliari S., Belloni T., Psaltis D., van der Klis M., 2003, A&A, 397, 729
Vikhlinin A., Churazov E., Gilfanov M., 1994, A&A, 287, 73
Wagoner R.V., 2003, Nature, 424, 27
Watts A., Altamirano D., Casella P., et al., 2009a, The Astronomer's Telegram, 2004, 1
Watts A.L., 2008, In: Wijnands R., Altamirano D., Soleri P., et al. (eds.) American Institute of Physics Conference Series, vol. 1068 of American Institute of Physics Conference Series, 199–206
Watts A.L., Strohmayer T.E., 2006, MNRAS, 373, 769
Watts A.L., Strohmayer T.E., Markwardt C.B., 2005, ApJ, 634, 547
Watts A.L., Krishnan B., Bildsten L., Schutz B.F., 2008a, MNRAS, 389, 839
Watts A.L., Patruno A., van der Klis M., 2008b, ApJ, 688, L37
Watts A.L., Altamirano D., Linares M., et al., 2009b, ApJ, 698, L174
Wijnands R., 2005, astro-ph/0501264
Wijnands R., van der Klis M., 1998, Nature, 394, 344
Wijnands R., van der Klis M., 1999a, ApJ, 514, 939
Wijnands R., van der Klis M., 1999b, ApJ, 522, 965
Wijnands R., van der Klis M., Mendez M., et al., 1998, ApJ, 495, L39+
Wijnands R., van der Klis M., Homan J., et al., 2003, Nature, 424, 44
Wijnands R., Homan J., Miller J.M., Lewin W.H.G., 2004, ApJ, 606, L61
Wijnands R., Altamirano D., Soleri P., et al. (eds.), 2008, A Decade of Accreting Millisecond X-Ray Pulsars, vol. 1068 of American Institute of Physics Conference Series
Wijnands R.A.D., van der Klis M., 1997, ApJ, 482, L65+
Wijnands R.A.D., van der Klis M., Psaltis D., et al., 1996, ApJ, 469, L5+
Wijnands R.A.D., van der Klis M., van Paradijs J., et al., 1997, ApJ, 479, L141+
Wilms J., Nowak M.A., Dove J.B., Fender R.P., di Matteo T., 1999, ApJ, 522, 460
Woods P.M., Thompson C., 2006, Soft gamma repeaters and anomalous X-ray pulsars: magnetar candidates, 547–586

Yin H.X., Zhang C.M., Zhao Y.H., et al., 2007, A&A, 471, 381
in't Zand J.J.M., Cumming A., van der Sluys M.V., Verbunt F., Pols O.R., 2005, A&A, 441, 675
in't Zand J.J.M., Jonker P.G., Markwardt C.B., Apr 2007, A&A, 465, 953
Zhang W., Giles A.B., Jahoda K., et al., 1993, In: Proc. SPIE Vol. 2006, p. 324-333, EUV, X-Ray, and Gamma-Ray Instrumentation for Astronomy IV, Oswald H. Siegmund; Ed., 324–333
Zhang W., Jahoda K., Swank J.H., Morgan E.H., Giles A.B., 1995, ApJ, 449, 930
Zhang W., Jahoda K., Kelley R.L., et al., 1998a, ApJ, 495, L9+
Zhang W., Smale A.P., Strohmayer T.E., Swank J.H., 1998b, ApJ, 500, L171+

List of publications

Refereed journal papers

- *"Accretion states of neutron stars: luminosity, variability and spectra of atoll sources"*
  Linares, M.; van der Klis, M.
  ApJ, submitted (2009).

- *"Type I X-ray bursts, burst oscillations and kHz quasi-periodic oscillations in the neutron star system IGR J17191–2821"*
  Altamirano D., **Linares M.**, Patruno A., Degenaar N., Wijnands R., Klein-Wolt, M., van der Klis M., Markwardt C. B., Swank J.
  MNRAS, submitted (2009).

- *"Discovery of burst oscillations in the intermittent accretion-powered millisecond pulsar HETE J1900.1-2455"*
  Watts A., Altamirano D., **Linares M.**, Patruno A., Casella P., Cavecchi Y., Degenaar N., Rea N., Soleri P., van der Klis M., Wijnands R.
  ApJ-Letters, 698, 174 (2009).

- *"SAX J1808.4-3658: high resolution spectroscopy and decrease of pulsed fraction at low energies"*
  Patruno A., Wijnands R., Rea N., Altamirano D., **Linares M.**, van der Klis M.
  MNRAS-Letters, 396, 51 (2009).

- *"The Swift capture of a long X-ray burst from XTE J1701-407"*
  Linares M., Watts A. L., Wijnands R., Soleri P., Degenaar N., Curran P. A., Starling R. L. C., van der Klis M.
  MNRAS-Letters, 392, 11 (2009).

- *"Broad relativistic iron emission line observed in SAX J1808.4-3658"*
  Cackett E., Altamirano D., Patruno A., Miller J., Reynolds M., **Linares M.**, Wijnands R.
  ApJ-Letters, 694, 21 (2009).

- *"The disc-jet coupling in the neutron star X-ray binary Aquila X-1"*
  Tudose V., Fender R., **Linares M.**, Maitra D., van der Klis M.
  MNRAS, submitted (2008).

- *"Timing and Spectral Properties of the Accreting Millisecond Pulsar SWIFT J1756.9-2508"*
  Linares M., Wijnands R., van der Klis M., Krimm H., Markwardt C. B., Chakrabarty D.
  ApJ, 677, 1, 515 (2008).

- *"An Accreting Millisecond Pulsar with Black Hole-like X-Ray Variability: IGR J00291+5934"*
  Linares M., van der Klis M., Wijnands R.
  ApJ, 660,1, 595 (2007).

- *"Cooling of the quasi-persistent NS X-ray transients KS 1731-260 and MXB 1659-29"*
  Cackett E. M., Wijnands R., **Linares M.**, Miller J. M., Homan J., Lewin W. H. G.
  MNRAS, 372, 1, 479 (2006).

- *"Discovery of Kilohertz Quasi-periodic Oscillations and Shifted Frequency Correlations in the Accreting Millisecond Pulsar XTE J1807-294"*
  Linares M., van der Klis M., Altamirano D., Markwardt C. B.
  ApJ, 634, 2, 1250 (2005).

Conference proceedings

- *"The disk jet coupling in Aql X-1"*
  Tudose, V.; Fender, R.; **Linares, M.**; Maitra, D.
  PoS Conf. Proc., in press. "VII Microquasar workshop: Microquasars and beyond", Foca, Turkey (2008).

- *"Timing the accretion flow around accreting millisecond pulsars"*
  Linares, M.
  AIP Conf. Proc., in press. "A decade of accreting millisecond X-ray pulsars", Amsterdam (2008). Astro-ph 0809.3368.

- *"Accreting millisecond pulsars: one on each hand"*
  Linares M., van der Klis M., Wijnands R.
  AIP Conf. Proc., 924, 629-634. "The Multicolored landscape of compact objects and their explosive origins", Cefalu (2007). Astro-ph 0610902.

Astronomer's telegrams

- *"New NGC 6440 transient declining rapidly"*
  Heinke, C. O.; Budac, S. A.; Altamirano, D.; Linares, M.; Wijnands, R.; Cohn, H. N.; Lugger, P. M.; Strohmayer, T. E.; Servillat, M.; Grindlay, J. E.; *ATel* 2143 (2009).

- *"ATCA radio observations of Swift J1756.9-2508 in outburst"*
  Tudose, V.; Tzioumis, A.; Patruno, A.; **Linares, M.**; Soleri, P.; Russell, D.; *ATel* 2138 (2009).

- *"Discovery of burst oscillations near the spin frequency in the intermittent accreting millisecond pulsar HETE J1900.1-2455"*
  Watts, A.; Altamirano, D.; Casella, P.; Cavecchi, Y.; Degenaar, N.; **Linares, M.**; Patruno, A.; Rea, N.; Soleri, P.; van der Klis, M.; Wijnands, R.; *ATel* 2004 (2009).

- *"Discovery of the shortest recurrence time between thermonuclear X-ray bursts"*
  Linares, M.; Watts, A.; Altamirano, D.; Patruno, A.; Casella, P.; Rea, N.; Soleri, P.; van der Klis, M.; Wijnands, R.; Belloni, T.; Homan, J.; Mendez, M. *ATel* 1979 (2009).

- *"Broad relativistic iron line observed in SAX J1808.4-3658 by Suzaku"*
  Cackett, E.; Altamirano, D.; Miller, J.; Reynolds, M.; Blum J.; **Linares, M.**; Patruno, A.; Wijnands, R.; *ATel* 1844 (2008).

- *"Swift detects increased activity of the neutron star transient SAX J1750.8-2900"*
  Linares, M.; Degenaar, N.; Wijnands, R.; Altamirano, D.; *ATel* 1777 (2008).

- *"Radio non-detection of SAX J1808.4-3658"*
  Tudose, V.; Tzioumis, T.; Maitra, D.; **Linares, M.**; Patruno, A.; Russell, D.; Casella, P.; Altamirano, D.; Wijnands, R.; *ATel* 1748 (2008).

- *"Near-IR and Optical Observations of the Ongoing Outburst of SAX J1808.4-3658"*
  Maitra, D.; Buxton, M.; Tourtellotte, S.; Altamirano, D.; Patruno, A.; Casella, P.;
  Linares, M.; Tudose, V.; Russell, D.; Wijnands, R.; Bailyn, C.; *ATel* 1733 (2008).

- *"Renewed optical and X-ray activity in IGR J00291+5934"*
  Lewis, F..; **Linares, M.**; Russell, D. M.; Wijnands, R.; Roche, P.; *ATel* 1726 (2008).

- *"Improved position of the new X-ray transient XTE J1637-498"*
  Wijnands, R.; **Linares, M.**; Degenaar, N.; Markwardt, C. B.; *ATel* 1700 (2008).

- *"A WSRT radio observation of IGR J00291+5934 in outburst"*
  Linares, M.; Tudose, V.; Migliari, S.; *ATel* 1667 (2008).

- *"Faulkes Telescope monitoring of the current outburst of IGR J00291+5934"*
  Russell, D. M.; Lewis, F..; **Linares, M.**; Roche, P.; Maitra, D.; *ATel* 1666 (2008).

- *"SAX J1750.8-2900 is returning to quiescence"*
  Linares, M.; Degenaar, N.; Altamirano, D.; Wijnands, R.; van der Klis, M.; Markwardt, C.; *ATel* 1662 (2008).

- *"The cooling tail of a long X-ray burst from XTE J1701-407"*
  Linares, M.; Soleri, P.; Curran, P.; Wijnands, R.; Degenaar, N.; van der Klis, M.; Starling, R.; Markwardt, C.; *ATel* 1618 (2008).

- *"The neutron star transient SAX J1810.8-2609 going back to quiescence"*
  Linares, M.; Degenaar, N.; Wijnands, R.; *ATel* 1260 (2007).

- *"XTE J1751-305 going back to its quiescent state"*
  Linares, M.; Wijnands, R.; van der Klis, M.; *ATel* 1055 (2007).

- *"A Swift/XRT observation of Aql X-1 during its recent outburst"*
  Wijnands, R.; Maitra, D.; Bailyn, C.; **Linares, M.**; *ATel* 871 (2006).

- *"Pointed RXTE observations of SAX J1808.4-3658"*
  Wijnands, R.; Wolt, M. Klein; **Linares, M.**; van der Klis, M.; Chakrabarty, D.; Morgan, E. H.; Markwardt, C. B.; *ATel* 507 (2005).

Observing proposals

Listed those accepted where I am the principal investigator

- Accretion disks in strong gravity: Fe lines vs. kHz QPOs and spectral states.
  Suzaku, AO-4, Scheduled September 2009. **100 ksec**.
- XMM observation of IGR J00291+5934.
  X-ray Multi-mirror Mission, DDT, August 2008. **30 ksec**.
- WSRT observation of an accreting millisecond pulsar in outburst: IGR J00291+5934.
  Westerbork Synthesis Radio Telescope, ToO, August 2008. **36 ksec**.
- Swift observations of neutron star transients in the decay to quiescence.
  Swift, three ToO programs, 2007-2008. Total of **50 ksec**.
- Swift observations of accreting millisecond pulsars in outburst.
  Swift, two ToO programs, 2008. Total of **14 ksec**.
- Extended timing observations of the accreting millisecond pulsar IGR J00291+5934.
  Rossi X-ray Timing Explorer, AO-11. **400 ksec**.

Acknowledgements

Grant me chastity and continence,
but not yet.

Saint Augustine (354-430)

Hello world, welcome to this book. It's been a long way to write it, and it's been great fun. *This* would have not happened without many of you. It sounds like a cliché but it is a very true one. I'll explain why in the following lines. Given that the acknowledgements are one of the "most frequently read" Sections of a PhD thesis, and often the first and only pages glanced by the rushed reader, let me encourage you to sit back and have a look also at Chapter 1, which gives an overview of the research topics presented herein.

Thanks Michiel. Once again, many thanks for giving me this job and for these fruitful and enjoyable years working together. In science, one of the first and many things I learned from you is to recognize the sometimes thin line that separates facts from interpretations, and to work with both sides of it. I have also much appreciated your positive attitude and learned from your skills of turning things the right way. When I landed in Amsterdam it took me a while to get acquainted with the timing jargon[2]. Back then, however, I was happy to see that I was not alone in the dark:

> *Michiel's second Sco observation showed a narrow peak at 1100 Hz. The signal is clear, but weak. In this case, the large collecting area of the PCA was crucial. (...) A shorter VLE window improved observation by extending frequency range (I DIDN'T GET ALL OF THIS). The data also show a normal 6 Hz QPO.*
>
> From the RXTE Users' Group Minutes, April 2-3, 1996

[2]Which later turned out to be much easier to understand than certain Dutch behaviours like, e.g., stuffing a few dry bread and cheese slices into a tiny red plastic box, adding some chocolate sprinkles and calling this "lunch".

And then there was light, and I was proud to hear that incredulous "Did you write this?" when I gave you the draft of our first paper. During these years you always left room for all my interests, and at the same time you were always there when needed. In short, you have been an excellent advisor and promoter. We will continue to collaborate on the ongoing projects and, I hope, on the future ones.

Rudy, much of *this* happened thanks to you. It's been a privilege to work with you, and I hope we keep doing so. It was a great pleasure to learn from you from the very moment I could understand what you were saying. We've also had fun. Everything changed when I saw you inhaling Helium and I heard that high-pitched voice coming out of your belly (I can still hear it). I just couldn't stop laughing. I really appreciate your help (and Anna's) in the job search and the many conversations about life and science. The rest of the group has been almost a family, to which I am thankful. To Mariano and Rob for sharing their wisdom when they were around, Diego for the initial help, Marc for the script support, Simone for so many things that I won't pick one here, Elena for her jet ways and Boston tips, Alessandro for the gusty winds, Paolo for our good office times, Pg for the tagliatelle in brodo, Nanda for so many things that I won't pick one here, Nathalie for the swift and gentle translations, Yuri for his tex mastery and proof reading, Dipankar for the great rallies, Anna for her burst expertise and the projects together, and the newcomers for bringing new blood. I also want to thank sincerely all the collaborators involved in every Chapter of this thesis for their contribution, and Deepto in particular for his support in my new position.

En Barcelona, quiero agradecer especialmente a Carlos Castel el haberme descubierto la pasión por la Física. Esta tesis empezó en cierta manera en l'Alzina. I va continuar a la Universitat de Barcelona. Gràcies Ramón per les xerrades al departament, Javier por el flash del Helio, Valentí i Josep Maria per parlar-me de la plaça a Amsterdam, Margarita i Jordi per l'hospitalitat al IEEC. Y a la peñica en su sentido más amplio por el coleguismo y las risas. Jaume, gràcies per la portada més molona del segle i per aguantar el ritme durant les visites llampec. Jodeeeer, ya me estoy animando. Elías te quiero a ti y a cada uno de tus pelos. Borja estas looooooco tío. Joan-ample-d'espatlles et trobo a faltar. Xavi, supertortugón, no pot ser que et perdi el compte de la descendència. Carol, Dani, Marc, Altiman, Ricard, Natja, Gerard, Rocco, Mario, Ruben, Annusca, Adri, Pek, Lluís, Pol, Titus, Barba en el Pie... aahhhh! Prou! He venido a hablar de mi libro!

Arriving to the cold Amsterdam autumn from the warm Spanish summer was not that painful thanks to the API and its warm atmosphere. The API is a very special place and I proudly belong to it. The first week I thought

"Do these guys only eat cake and drink coffee?". While this might be true for Martin, in general there is much more than cake and coffee, and from the first moment Lide, Minou, and many others were helpful, kind and open. I will never forget the great ping-pong moments with big-Al, Ato, Diego, Simo, Gemma, Valeriu, Martin (remember when you used to beat me?), Dipankar et al., the heerlijk pierogi of Maciej's grandma and Eduardo's laughs and lectures on Guatemalan history. Martin, you've appeared twice in this paragraph but you deserve more text as I have to admit, here, now, publicly, that I will miss you. As much as I miss Peter, my dear Pedro Curranino, since he embarked on a boat trip to the wild side with crazy-Agnieszka. And as much as I'll miss sweet-Nicole and her gekke stories. But I'm quite sure we'll get together to drink two-many beers again, maybe talking nonsense, burning noses or biting arms. And hopefully my dear Atakan will also be there. Thanks for all the fish duude, we should get our winery-brewery plans going. Special thanks to Samia for the brief office-sharing period and the great API logo! To Arjan, Alícia, Eva, Esther, Dave, Ton, Nick, Evert, Atish, Raman... for these wonderful years, to all of you APIs!

And needless to say, I will miss Amsterdam. Crossing the Amstel by bike every day, having a couple of (well maybe three) biertjes next to the canal, and all the good friends I've made here. Ewa, thanks for being the almost-perfect flatmate for so many years, it really felt like home. My dear Spanish crowd welcomed me since the very first evening in the Plantage Muidergracht, when they still thought I was an innocent guy, and has been my beloved family in the Netherlands. Uncles Ruben and Nacho, with their wise ad-vice on how to pick up girls, my dear bros Dieguito and Tury (yes, both in the Spanish crowd after all), auntie Miriam and her irresistible profiteroles, Jorge and Maria and their smoothie-and-cake-based parental care, the unforgettable Barça nights with my cousins Jordi and Annemarieke, Juan-Gurrix-the-crazy-grandpa letting me drive his car through the Vondelpark, Juan-the-boquerón, the uncle who lives on the mountain[3] with Vero-vasca-de-altos-vuelos and who kills a cow every time we visit them, my cousins Nacho G. and Raul, the real party animals together with Timi the French auntie and the squat-cousin Maria Z., uncle Javier from Colombia, and I start to lose track here but that's the good thing of a family, you don't really know where it ends. The same happens with my dear Italian crowd; grazie mille a tutti per tutte le serate e il buon cibo, and for reminding me that even where things are arranged at least two months in advance you can actually plan something half an hour *after* it started, and

[3]For the Dutch readers: *mountain: a natural elevation of the Earth's surface rising more or less abruptly to a summit, and attaining an altitude greater than that of a hill, usually greater than 610 m.* From `http://dictionary.reference.com`.

it is usually much more fun. Thanks to those who defy classification and have shared so many good things with me: Leslie, Phil, Keshri, Viney, Zuli, Gabriele, Paola, Bill, Alessia, Daniele, Busy, José, and many others that would make this list hard to read. Y a mis queridos latin-american-splash friends, Pauli, Nuri, Matthieu (jusqu'à présent plus latin qu'américain), Viole, Beins, Cas, Cons y compañía, gracias por las parrandas y las jodas, los quilombos, las juntadas, las tocadas, los asados y los momentos recopados/chidos/chévere.

Thanks to those who kept me alive with their music and helped me keeping my music alive. This means in the first place *The Silk Roads*[4], the one and only, the cult band from the lowlands formed by three very good friends. Stefano, the greatest (cheer)leader; Nanda, my cara paranimfa, and Simone, the hottest sax-player wherever he goes (here you are again, see what I mean?). È stato bello carissimi, I hope we'll keep filling concert halls and rocking in the studios. To Sahand and his Mezrab for the sparkling moments, and to Carles (who refers to my PhD as 'el título de astronauta flamenco') for giving me the opportunity to play what I like the most, flamenco, in no less than Het Concertgebouw. Cesar, Pastora, Haik, Ermínia, Arturo, Nuri, Babak, Branko... for the beats and notes and chords we shared.

Familia[5], muchas gracias por vuestro apoyo y vuestro cariño constante. Per les visites; pels queviures. Gracias a los Linares. Gràcies als Alegrets. Y gracias a Isa y los Cárdenas, a Kike y a los garbancitos más hermosos: Bruna, Joan y Leo. Durante estos años os he llevado cerquita, me habéis dado vuestros sabios consejos en el momento oportuno y me habéis seguido llenando de orgullo y de amor. Molt especialment a vosaltres, pare, mare, germana, per ser com sou i fer-me el que sóc.

This is the end
Beautiful friend
This is the end
My only friend, the end.

Jim Morrison (1943-1971)

[4] `http://www.myspace.com/thesilkroads`.
[5] También llamada "sistema" en ciertos ambientes.

Notes